Design, Analysis, and Test of a High-Powered Model Rocket

A Major Qualifying Project Report
Submitted to the Faculty of the
WORCESTER POLYTECHNIC INSTITUTE
in Partial Fulfillment of the Requirements for the
Degree of Bachelor of Science
in Aerospace Engineering

by

_____
Nicolas Amato

_____
Zachary Huamán

_____
Alicea Hyland

_____
Jacob Koslow

_____
Jordan Pickunka

_____
Jack Procaccini

_____
Saiyab Ranjit

_____
William Roe

_____
Jarod Romankiw

_____
David Santamaria

_____
Jake Scarponi

_____
Braden St.Jacques

_____
Jake Tappen

April 2020

Approved by: _____

John J. Blandino, Advisor
Professor, Aerospace Engineering Program
Worcester Polytechnic Institute

Abstract

This paper describes the design, analysis, assembly and test of two High-Powered Model Rocket systems, one designed with traditional subsystems for recovery, separation, and flight stabilization while a second incorporated innovative subsystems. An analysis of the composite motor was completed using Cantera and COMSOL to model the chemical equilibrium reaction and evaluate the temperature distribution in the motor during flight. These results were used to provide chamber conditions in a MATLAB model for ideal rocket performance. For the separation system, a comparison of black powder separation charges and a spring-loaded ejection mechanism was investigated. Aerodynamic loads, spin stabilization, and rocket performance were evaluated using a combination of models created for this project in MATLAB and standard computational fluid dynamic (CFD) tools in ANSYS Fluent. Data from a successful test launch is presented. The design of a second rocket, incorporating a three-blade autorotation recovery system, dual stage motors, a spring separation system, and stabilized flight control surfaces is also presented.

Acknowledgements

The MQP team would like to thank and recognize the following individuals and groups for their help and support throughout the project.

Table of Contents

List of Figures

List of Tables

Table of Authorship

1.	Introduction	ALL
1.1.	Literature Review	
1.1.1.	ARS	ALL ARS
1.1.2.	PTSS	ALL PTSS
1.1.3.	FDA	ALL FDA
1.2.	Program Goals	Jarod Romankiw
1.3.	Overall Project Design Requirements, Constraints and Other Considerations	Jarod Romankiw
1.4.	Tasks and Timetable	Jarod Romankiw
2.	**Airframe and Recovery Systems – Design and Analysis**	
	Introduction	Jordan Pickunka
2.1.	Methodology	Jarod Romankiw
2.1.1.	Airframe Mechanical Design	Zach Huaman/Jake Tappen
2.1.2.	Payload Bay	Jordan Pickunka
2.1.3.	Electronics Bay	Jarod Romankiw
2.1.4.	Motor Bay	Jarod Romankiw
2.1.5.	Nosecone	Zach Huaman
2.1.6.	Autorotation Recovery System	Jordan Pickunka
2.2.	Analysis	Zach Huaman
2.2.1.	Airframe Stress Distribution (ARS Analysis Task 1)	Jake Tappen
2.2.2.	Fin Analysis (ARS Analysis Task 2)	Jarod Romankiw
2.2.3.	Stresses on U-Bolt-Bulkhead Coupling (ARS Analysis Task 3)	Zach Huaman
2.2.4.	Parachute Sizing Model (ARS Analysis Task 4)	Jake Tappen
2.2.5.	Autorotation Blade Model (ARS Analysis Task 5)	Jordan Pickunka
3.	**Propulsion, Thermal, and Separation Systems – Design and Analysis**	
	Introduction	Jack Procaccini
3.1.	Methodology	Jack Procaccini
3.1.1.	Propulsion	Jack Procaccini
3.1.1.1.	Engine Systems	Jack Procaccini
3.1.1.2.	Ignition/Mounting Systems	Dave Santamaria
3.1.1.3.	Temperature Distribution Model	Dave Santamaria
3.1.1.4.	Motor Performance Analysis	Jack Procaccini
3.1.1.5.	One-Dimensional Isentropic Nozzle Flow Analysis	Jack Procaccini
3.1.2.	Separation	Braden St.Jacques
3.1.2.1.	Black Powder Charges	Braden St.Jacques
3.1.2.2.	Nosecone Separation System Model (PTSS Analysis Task 3)	Jacob Koslow
3.2.	Analysis	Jack Procaccini
3.2.1.	Temperature Distribution (PTSS Analysis Task 1)	Dave Santamaria
3.2.2.	Motor Performance Model (PTSS Analysis Task 2)	Jack Procaccini
4.	**Flight Dynamic Analysis – Design and Analysis**	
4.1.	Baseline Fin Design and Production	Saiyab Ranjit
4.2.	Avionics and the E-Bay	Greg Roe
4.2.1.	Avionics Selection	Greg Roe
4.2.2.	Avionics Testing	Greg Roe
4.3.	Aerodynamic Load Analysis	Alicea Hyland, Nick Amato
4.3.1.	Aerodynamic Loads – Simple Model (FDA Analysis Task 1)	Nick Amato
4.3.2.	Aerodynamic Loads – Simulation (FDA Analysis Task 2)	Alicea Hyland
4.3.3.	Fin Design for Vehicle Spin Stabilization (FDA Analysis Task 3)	Greg Roe/Saiyab Ranjit/Nick Amato
4.4.	Vehicle Dynamics and Performance Model (Analysis Task 4)	Greg Roe/Saiyab Ranjit/Nick Amato
4.5.	Baseline Rocket Launch Results	Jake Scarponi
5.	**Summary, Conclusions and Recommendations (Overall)**	
5.1.	Airframe and Recovery Systems	ALL ARS
5.2.	Propulsion, Thermal, and Separation Systems	ALL PTSS
5.3.	Flight Dynamic Analysis	ALL FDA
5.4.	Broader Impacts	Jarod Romankiw
6.	**References**	Nick Amato
7.	**Appendices**	ALL

1 Introduction

1.1. Literature Review

We conducted a literature review to learn about different methods of High-Powered Model Rocketry. The team focused on the main topics for different systems within the rocket including airframe, recovery system, propulsion system, as well as flight dynamics and avionics. The following review supports the design decisions made for this MQP.

1.1.1 Airframe and Recovery System

As one of the three subteams of the Design, Analysis, Assembly, and Test of a High-Powered Model Rocket Major Qualifying Project, the Airframe and Recovery Systems (ARS) team was responsible for the airframe design and integration of the overall mechanical structure of the High-Powered Model Rocket (HPMR). This includes the integration of an innovative recovery system to be used for a flight ready rocket. This literature review discusses the multiple components of the airframe of a model rocket, including the history of rocket airframes and recovery systems used in modern model rocketry.

1.1.1.1 The Airframe of a Model Rocket

The airframe serves as the body of the model rocket, and "provides the main structure" [1]. It encompasses the housing of the motor bay, the electronics bay, any payloads that may be integrated in the rocket design, and a space for the nose cone. The airframe is generally made up of multiple sections of material that are joined using bulkheads, couplers, and epoxy. The airframe materials can be purchased from model rocketry hobby shops, and the material itself is easy to cut with a Dremel tool. An example of a typical model rocket airframe can be seen in Figure 1: "Parts of a Rocket," where the parts and locations of a model rocket are shown. Airframes usually have "high

length to diameter ratios" [2] for model rockets. The walls of the airframe are thin, with the motor of the model rocket being located at the aft end of the airframe, while the payload and electronics bay are typically closer to the center of gravity. A coupler is fitted to the aft end of the nose cone of a rocket, then the coupler is fitted to the aft end of the airframe tube.
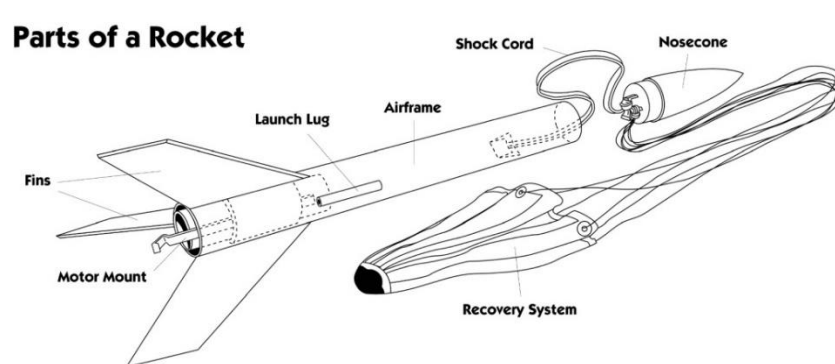
Figure 1: Parts of a model rocket [3]. © National Association of Rocketry

In model rocketry, the most used material for airframe construction is spiral wound paper [3]. This lightweight material acts as the support that protects the payload and other systems inside from forces that act on the model rocket during launch, flight, and recovery. Some other common airframe materials include phenolic tubes, carbon fiber, or fiberglass [1], which easily support the large force from the motor at lift off. NASA provides recommendations for the types of materials to use in model rocketry, and advises to steer clear of "metallic tubing" [4] as it can cause harm to any individuals in the surrounding area if the model rocket were to be launched incorrectly or if an accident were to occur during flight. Furthermore, the airframe materials for high-powered model rocketry are usually high strength to weight composite materials [2]. This means that the material must be durable enough to withstand the forces from the motor upon ignition, aerodynamic forces during flight, and contact forces during recovery. Figure 2 from *Rocketarium*, a company that sells model rocket materials, shows the phenolic tubing used for most model rockets.

Figure 2: Phenolic Tubing [5]. © Rockertarium

An airframe material needs to be chosen so the rocket will not crush or break under the extreme forces that the rocket experiences. Due to these requirements, the ARS subteam chose Blue Tube 2.0 material from AlwaysReadyRocketry. Blue Tube 2.0 is a vulcanized fiber (cardboard) with a 0.062in wall thickness and a density of 1.25 g/cm³. Blue Tube 2.0 was also used by the 2018 –2019 MQP team for their model rocket project [1]. An image of the Blue Tube 2.0 material, taken from Apogee Rockets, can be seen in Figure 3.

Figure 3: Blue Tube 2.0 [2]. © Always Ready Rocketry, LLC

1.1.1.2   Payload Bay

The payload bay is typically located in the upper airframe section of a model rocket. Its purpose is to fasten the nose cone to the rocket as well as hold the payload (if any) on the inside

of the airframe. Depending on the size of the rocket, the payload bay may be integrated into the airframe tube, such as in Figure 4, or a separate subsystem of the rocket, as in Figure 5.
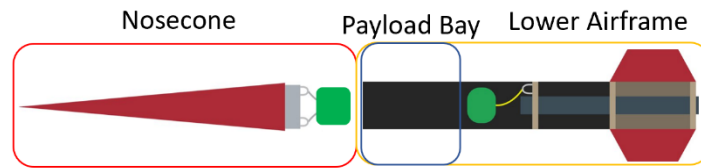
Figure 4: Model rocket with payload bay integrated into lower airframe
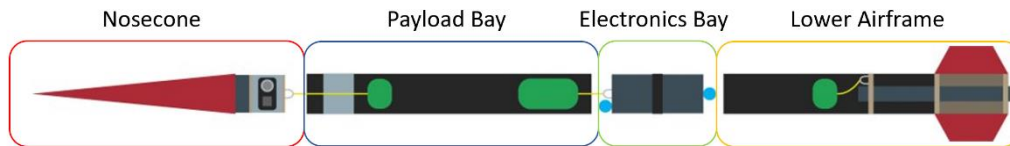
Figure 5: Model rocket with payload bay subsystem

For high-powered model rockets, most designs have the payload bay as a separate subsystem to allow for an easier assembly and to have a separate electronics bay. The size of the payload bay is determined by the size of the payload. The payload of a model rocket may consist of many different objects, including, but not limited to, a recovery system, a camera, and in some rocketry competitions, a small robotic rover or UAV. Some rocket designers may choose to implement more innovative systems such as a glider system [6].

1.1.1.3 Electronics Bay

The purpose of the electronics bay, or "e-bay," is to house the processor (if included), altimeter, gyroscopes, accelerometer, battery, and wiring in the HPMR. For this project, MQP members had experience designing e-bays for other WPI rocketry teams such as Battle of the Rockets (BOR) [7]. The WPI BOR team from 2018 used a coupler tube with an outer diameter that was equal to the inner diameter of the airframe. A coupler tube is a section of tube which fits

between the upper and lower airframe to attach the two. A thin band was then fixed to the outside of the coupler tube to prevent the e-bay from sliding within the airframe [8]. An e-bay is pictured in Figure 6. The blue portion of the e-bay is the coupler tube, and gold portion is the e-bay band.

Figure 6: Electronics bay example

The ends of the airframe were capped with bulkheads made of plywood. A previous MQP team (NAG-1901) used 0.5 in. thick plywood to increase strength as compared to a 0.25 in. thick plywood [8]. The 2012 MIT Rocketry team used a similar technique, in which a coupler tube was capped by two pieces of plywood serving as a bulkhead [9].

An arming switch is fixed to the outside of the band which allows the electronics to be armed when on the launch pad as shown in Figure 7. It is easiest to use a round switch as opposed to a rectangular switch. Round switches can be installed by using a drill to bore a hole in the airframe, while a rectangular switch requires a knife [10].

Off-the shelf e-bays are available through online vendors, but previous MQP and BOR teams have opted to make their own to allow for as much customization as possible.

Figure 7: E-bay switch

1.1.1.4 Motor Bay

The motor bay is located at the aft end of the HPMR. It is designed to house the motor, retain

it in the bay after burnout, and provide structural support for the fins. The size of the motor bay is

heavily dependent on the size of the motor. Motors are geometrically defined by two dimensions:

the diameter of the motor and the length. Knowing these two dimensions is required to determine

the size of the motor bay. A typical motor bay design is a central tube (motor tube), which has an

inner diameter equal to the outer diameter of the motor. The motor tube is fitted with three equally

spaced centering rings which span the annular gap between the motor tube and the airframe. The

centering rings are made of circular plywood bulkheads with a hole bored through the middle fitted

to the motor tube diameter. All components are fixed with West Systems Epoxy Resin and

Hardener. This design helps the rocket maintain its center of pressure within the rocket body. The

center of pressure is defined as the sum of all normal forces along the rocket body surface. It is a

single point where the aerodynamic forces are balanced on the rocket.
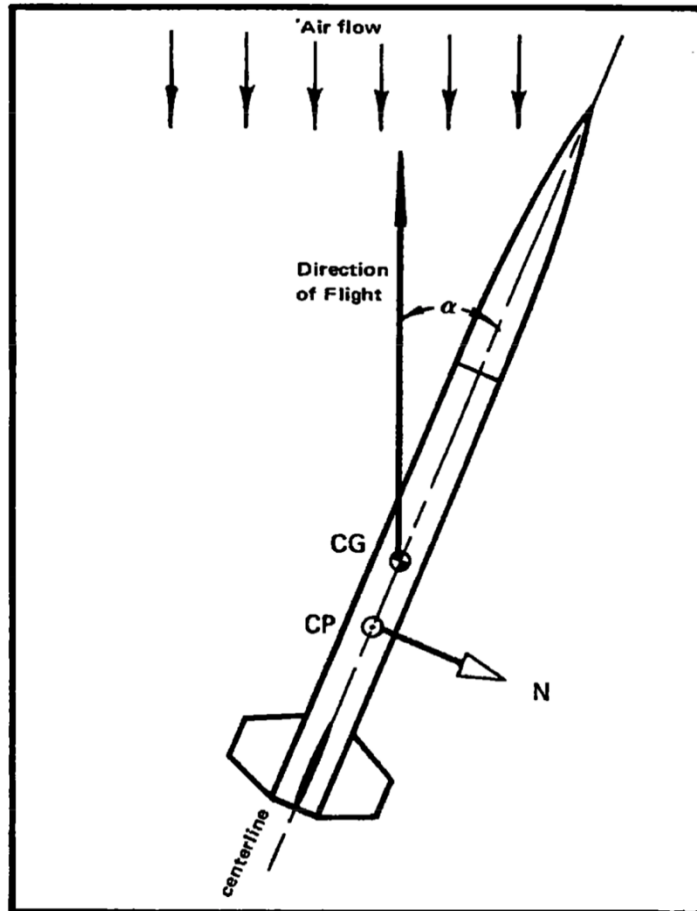
Figure 8: Center of pressure diagram [11]

Previous MQP teams including NAG-1901 [8] and WPI Rocketry Teams like the 2018 BOR, have exposed a small portion of the motor out of the bottommost bulkhead of the rocket. The WPI teams did this for several reasons, mainly focused on two ideas: previous experience, and easy integration of retention systems for the motor. The fins are typically integrated in between two bulkheads. Fin tabs extend the span of the fins through the outer airframe up to the motor bay, increasing the structural integrity of the fins.

1.1.1.5 Nose cone

The nose cone of the rocket is located at the forward end of the rocket and is the main aerodynamic surface used for drag reduction. As shown in Figure 9, nose cones are made in many different shapes, including but not limited to: parabolic, long elliptical, long cone, and solid cylinder. All nose cones designed for model rockets have a smaller diameter section at their base, so they can better connect to the airframe and eject more reliably when the time comes. In the newsletter "Peak of Flight", published by Apogee Components, journalist, Ashley Van Milligan describes a study she performed to find the wind speed and drag force associated with each of the designs [12]. Van Milligan ran tests using a wind tunnel to find the drag force on each nose cone shape and her findings are displayed in Figure 9.

Drag of Nose Cones
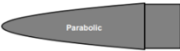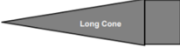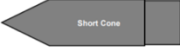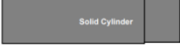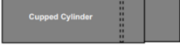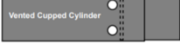
Nose Shape	Wind Speed	Temp	Drag Force
Parabolic	39.28 mph	72.0° F	4.477 g
Ogive	39.28 mph	72.0° F	4.942 g
Long Eliptical	39.27 mph	72.0° F	4.149 g
Short Eliptical	39.27 mph	72.0° F	4.791 g
Long Cone	39.26 mph	72.5° F	4.561 g
Short Cone	39.25 mph	72.0° F	5.248 g
Solid Cylinder	39.24 mph	72.0° F	8.659 g
Cupped Cylinder	39.26 mph	72.0° F	10.459 g
Vented Cupped Cylinder	39.19 mph	72.5° F	10.399 g

Figure 9: Drag force of varying nose cone shapes [12]. © Apogee Components, Inc.

This study suggests that the long elliptical nose cone shape is the best for reaching the highest apogee during flight due to its low drag force [12].

1.1.1.6   Recovery System

A major goal in model rocketry is to safely retrieve a rocket after it has been launched. A recovery system is defined as "any device that is incorporated into the model rocket to return it safely to the ground" [13]. Recovery systems work by inducing an upward drag force to overcome the force of gravity and subsequently cause the rocket to slowly descend. Aside from improving safety, integrating a recovery system into model rockets allows the rocket to be re-used if undamaged upon landing.

Parachutes are the traditional recovery method within model rocketry. The system functions by deploying a parachute from the airframe at apogee, which allows the rocket to make a safe descent. The ARS subteam decided to use parachute recovery in one of their rocket designs, since it's the most common recovery method.

Parachute recovery is an important system that is implemented not just in model rocketry, but also in actual launch vehicles stage and spacecraft recovery. NASA and commercial launch providers routinely use parachute recovery. One example of parachute recovery being used in full-scale rocketry is the Ares I Recovery system. In 2009, NASA successfully tested the "largest rocket parachute ever manufactured" for the Ares I Rocket, which was intended to launch astronauts to the international space station [14]. With a diameter of 150 ft, this major feat allowed for the expansion of parachute recovery on a large scale.

We define a baseline recovery approach for a model rocket as one which uses a simple parachute recovery system. Typically, in model rocketry, there are three parachutes (refer to Figure 10) that are deployed after reaching apogee. The first parachute, the drogue parachute, is deployed to slow down the model rocket during descent. Drogue parachutes are typically smaller than the main parachutes to control the descent of the model rocket, and "stabilize the rocket so that the main parachute can open without failing" [15]. The drogue parachute, which can be seen in Figure

10 from NASA's testing of an Ares drogue chute [16], deployed from the lower airframe section of the rocket.

Figure 10: Image of Ares drogue parachute take from NASA [16]. © NASA

The main parachute is typically attached to the bulkhead of the electronics bay. The main parachute is responsible for reducing the descent velocity of the entire airframe. The ARS subteam was responsible for calculation of the rocket descent velocity in order to determine the diameter of the parachute needed to safely recover this rocket. The methodology for this analysis and results are presented in Section 2.2.4.
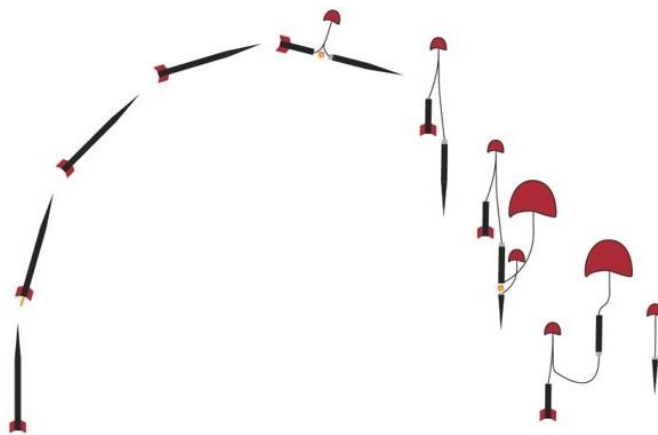
Figure 11: Illustration of parachute recovery

An illustration of a rocket flight profile using a parachute recovery system can be seen in Figure 11. The figure demonstrates the drogue parachute being deployed at apogee, with the nose cone parachute and main airframe parachute deployed afterwards. The main parachute is attached to the drogue parachute, which work in tandem to return the rocket safely to the ground. Note that the nose cone completely detaches from the rest of the airframe and descends separately than the rest of the model rocket. There is a considerable amount of planning when it comes to designing a parachute for a model rocket. Typically, parachutes are designed so that the descent velocity is 3.5 to 4.5 m/s [17].

When it comes to using a parachute, Apogee Rockets suggest using materials such as cotton, silk, polyester, or nylon for model rockets with a mass greater than 300 g [17]. Finding the parachute size required for our model rocket is extremely important, as a parachute too small will not produce enough upward drag for a given inflated diameter size. With insufficient upward drag, the model rocket will fall with too high a velocity, causing it to crash land, and not be able to be reused for subsequent launches.

While parachutes are a traditional way to recover a model rocket, there are different recovery methods that can be used such as streamers, a glider, a helicopter or autorotational system, and more [13]. Streamer recovery works by deploying strips of material to induce a drag and slow the descent velocity of the rocket. This method is only used on rockets or sections of a rocket that weigh less than two ounces because the streamers are unable to create enough drag [13]. The glider recovery system either has wings attached to the airframe or deployed wings that enable the model rocket to safely glide down to the ground. Gliders are hard to control during descent and for high apogee rockets, the glider may sore for a long distance, which increases the risk of the rocket landing in a road, house, or other places where it could damage property or injure a person. The

autorotation or helicopter recovery system involves deploying rotor blades to create an upward force from lift and drag, which slows the descent of the rocket [13]. The rotor blades of the recovery system must be properly designed to produce enough upward force otherwise the rocket will crash down to earth. This is a safety hazard to people in the vicinity of the launch site. Using the information from above, the ARS subteam decided to investigate using an autorotation recovery system as another potential recovery system for the HPMRs since a streamer system would not be able to produce enough drag to slow the descent of a large model rocket to a safe speed and the guilder system would require a great deal of manufacturing and design of a control system. Additionally, the team wanted to continue the research performed by the Design and Integration of a High-Powered Model Rocket – III MQP team [JB3 1901] [18].

Autorotation refers to the state of a helicopter in free fall where the rotor blades are only rotating due to the aerodynamic forces from the resultant wind velocity with no power from the engine [19]. During flight, helicopter rotor blades are angled to create lift, drag, and thrust based on the resultant relative air velocity. These relative wind velocity components are shown Figure 12.
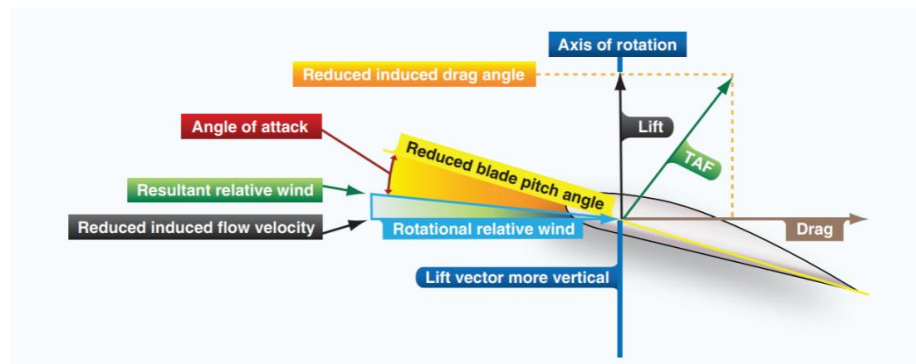
Figure 12: Aerodynamic force of an airfoil [20]. © Federal Aviation Administration

The resultant relative wind velocity is determined by the addition (or subtraction) of the wind speed relative to the aircraft and the wind velocity relative to the rotating blade [20]. The relative wind velocity and angle are determined by the flight path of the aircraft. The wind velocity due to rotational motion is equal to the rotational velocity of the rotor blade times the distance along the span of the rotor blade [20]. This means that the wind velocity long the span of the blade is a function of the spanwise coordinate. Since the relative wind velocity is a combination of the speed relative to the aircraft and the wind velocity due to the rotation of the blades, it will also change along the span of the rotor blades. These changes cause the angle of attack (AOA) to vary [20]. The AOA is the angle between the resultant wind velocity and the chord line of an airfoil, and it directly affects the lift and drag forces [21]. As the AOA increases, the lift and drag forces also increase. If the AOA increases past the critical angle, then the lift and drag forces become unsteady, causing the rotor blades to stall and the helicopter to lose control [22]. Therefore, as the angle of the resultant wind velocity changes, such as in autorotation, the drag and lift force also change.

When the rotor blades experience autorotation, the direction of the wind velocity relative to the aircraft becomes vertical. The vertical and rotational wind components cause significant changes in the AOA, which could cause the rotor blades to stall if the new AOA is greater than the airfoil's critical AOA. In such a situation, the lift and drag forces would become unpredictable causing the rotor blades to stall [20].

Altering the pitch angle of the rotor blade changes the direction of the lift and drag force vectors, which changes the horizontal and vertical force components they produce. The vertical components add together to create the total upward force, which is acting against gravity. The horizontal components supply the rotational force to the rotor blades. It is important that the

horizontal component of the lift force be greater than the drag force component otherwise the rotor blade will rotate in the incorrect direction [19].

Once the rotor blades begin autorotation, the circular area covered by the rotation of the blades, or "rotor disk," is divided into three sections: the driven, driving, and stall regions [20]. The driven section of the rotor blades usually consists of the outer 30% of the span of the rotor blade. Within this section, the lift and drag forces tend to offset each other, which often leads to the deceleration of the rotor blade [20]. The driving region is the most important section because it creates the necessary aerodynamic forces to turn the blades. This region makes up 25-70% of the rotor blades. The last region, the stall region, makes up the remaining 25% of the rotor blades. This region experiences AOAs higher than the critical AOA, so it is under stall conditions. These conditions cause large amounts of drag that tend to slow the rotation of the rotor blades. These three regions exist due to the change in force vectors caused by increasing rotational relative wind velocity from the blade root to tip [20]. Figure 13 and Figure 14 illustrate the distribution of these three sections on the rotor blades during rotation.
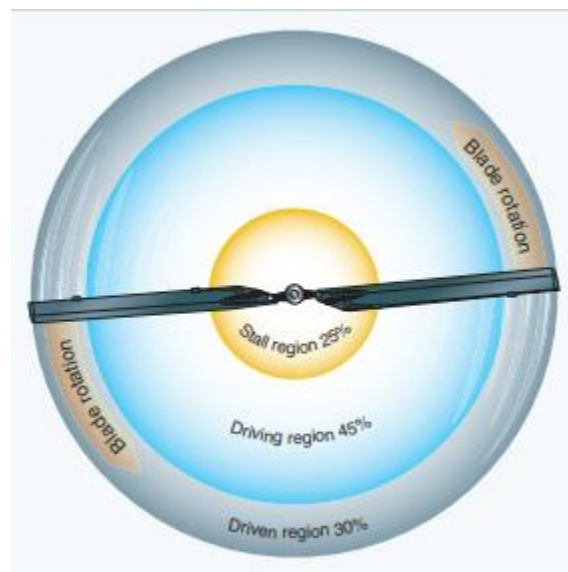
Figure 13: Blade regions during autorotation descent [20]. © Federal Aviation Administration
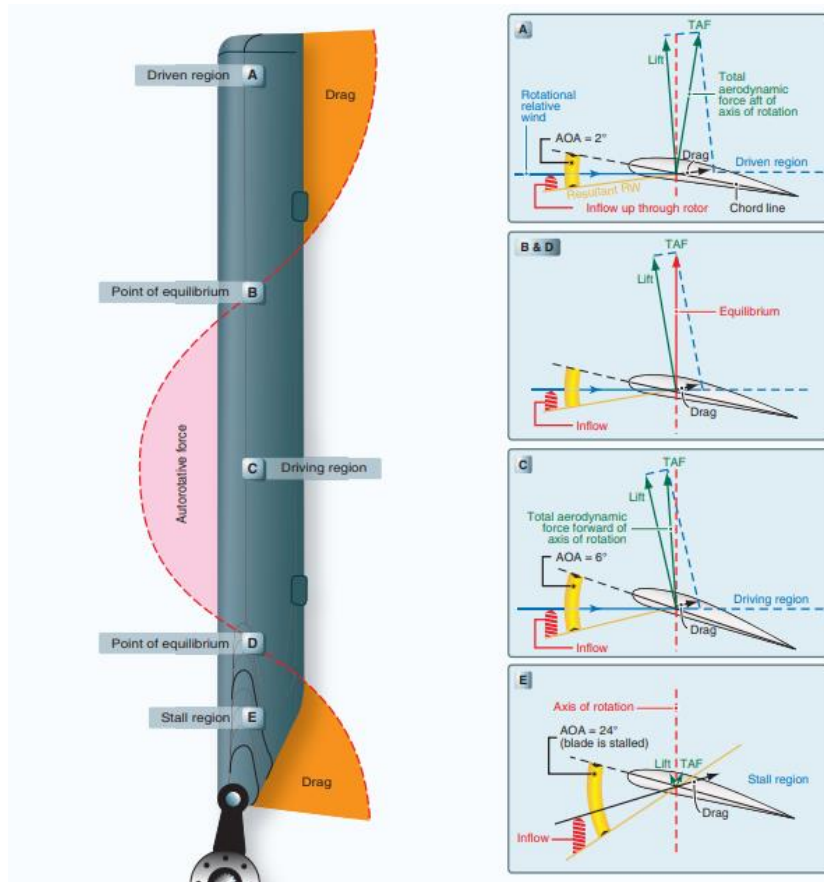
Figure 14: Force vectors in vertical autorotation descent [20]. © Federal Aviation Administration

The average percent area of the three regions is given in Figure 13, but the areas are subject to change depending on the blade pitch, rate of descent, and rotor revolution per minute (rrpm) [20]. Figure 14 shows the aerodynamic forces acting on each of the three regions while considering the effects of the angle of twist on the AOA. Each of the three regions have their own lift and drag properties that affect the rotation and descent of the autorotation system. Both the driven and driving region produce a total upward aerodynamic force that helps to decelerate the aircraft while the stall region produces no significant forces, which is seen in Figure 14. The driven region produces a drag force that is higher than its lift force, which results in a deceleration of the rotation of the blades. The driving region has a greater lift force than drag force, which leads to an

acceleration of the rotor blades. The areas of the three regions can be altered through changes of the pitch angle in such a way that the deceleration of the driven region and the acceleration of the driving region cancel, so the autorotation system has a constant rpm. Figure 15 shows an airfoil at the ideal pitch angle, where the horizontal lift and drag force components cancel, leaving only the vertical component. This would cause a constant angular velocity if the entire blade experienced the same conditions or horizontal force components along the span of the blade cancelled. The vertical force component is very important because it causes the aircraft to slowly descend.
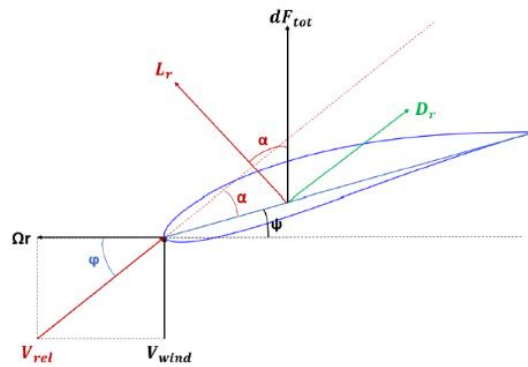
Figure 15: Relative wind reference frame of airfoil in autorotation [18]. © Worcester Polytechnic Institute

The ARS subteam researched different commercially off the shelf (COTS) model rockets that utilize autorotation as the main recovery system. Some of these rockets included Apogee components' Gyro Chaser, Heli-Rocm, and Mini-Copter or Estes' Mini "A" Heli and Flip Flyer [23] [24]. Most of these rockets utilize the rotor blades as the airframe or attach the blades to the sides of the airframe. These methods increase the drag forces of the model rocket due the increase in surface area, which lowers the height of apogee. The largest of these rockets is the Flip Flyer, shown in Figure 16, at 19.2 in long, 0.98 in diameter and weighing 3.2 oz [25]. This rocket is

significantly smaller than most HPMRs, which means these methods of autorotation recovery may not be viable options for larger scale rockets.

Figure 16: Estes's Flip-Flyer [25]. © Estes

Attaching the rotor blades to the outer airframe of the model rocket is a more viable option for a high-powered rocket as it was studied by students working on Project Hummingbird at Embry-Riddle Aeronautical University [26]. The recovery system of their model rocket operated by deploying a drogue parachute from the nose cone at apogee to orient the rocket vertically. After the rocket was oriented vertical, the nose cone separated from the rocket and the rotor blades folded out from the sides of the airframe, as seen in Figure 17.
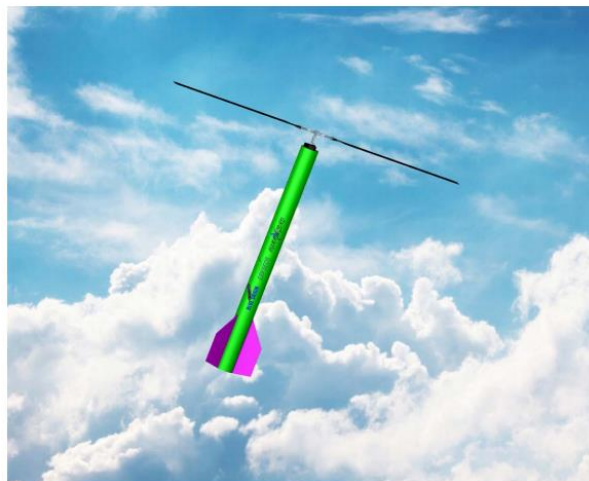
Figure 17: Project Hummingbird autorotation helicopter [26]. © Embry-Riddle Aeronautical University

1.1.2 Propulsion, Thermal, and Separation Systems

The propulsion, thermal and separation system (PTSS) team was responsible for the motor selection and stage separation of the HPMR. This includes the design and implementation of an innovative stage separation system. This literature review discusses the various design considerations for a model rocket's propulsion system including mounting systems, staging and modelling techniques.

1.1.2.1 Propulsion

The purpose of a propulsion system is to change the motion of a body through the production of a force. There are many applications using a propulsion system including aircraft, missiles, assisted takeoff vehicles, space vehicles and more. These applications can be separated into two main groups by their propulsion type: jet and rocket propulsion. The difference between the two is that jet propulsion utilizes the oxygen within Earth's atmosphere as an oxidizer whereas rocket propulsion must carry an oxidizer onboard since there is no oxygen in space [27]. Despite these two major differences between jet and rocket propulsion, all propulsion systems operate on the same fundamental principles. Thrust is the force provided by the propulsion system responsible for changing the motion of a body. Thrust is produced by the ejection of particles called propellant. Each particle being ejected has a mass and a velocity and hence a corresponding momentum. In turn, the conservation of momentum results in a reaction force that changes the motion of a body [28].

The relationship between thrust and momentum can be seen in Eq. 1-1, where mv is the momentum and T is the thrust.

$$T = \frac{d(mv)}{dt} \qquad \qquad 1\text{-}1$$

Focusing specifically on model rockets, thrust is produced by a motor that ejects burning propellant at high velocities out of the motor nozzle. This creates a reaction force that accelerates the rocket upward.

Most model rocket engine contain the same essential components. Figure 18 below shows the primary components in a commercially available model rocket motor.
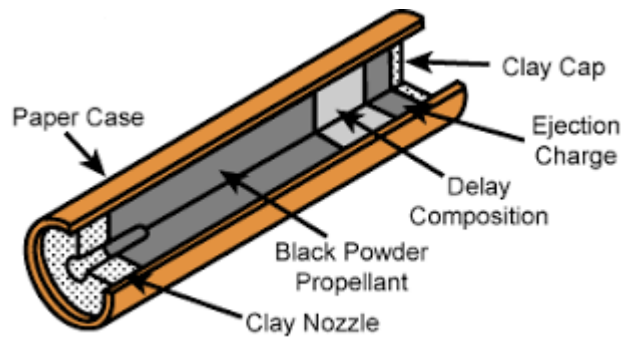
Figure 18: Cutaway of model rocket motor [29]. © 2019 Apogee Components

As shown in the diagram, the first component is the propellant. Solid propellant is typically used in model rocketry however, liquid and hybrid propellants for model rockets do exist. As the propellant is being burned, it is accelerated out of the back end of the motor through a nozzle. Due to the extreme temperatures caused by the burning propellant, the nozzle is typically made of clay or ceramic material. The next component in a motor is a delay charge. The delay charge burns immediately following the burn of the solid propellant. The delay charge produces no thrust thus allowing the rocket to coast after the propellant has finished burning. This enables the rocket to achieve a maximum altitude before deployment of a recovery device. Once the delay charge has finished burning, an ejection charge is ignited. The ejection charge creates a controlled explosion which accelerates hot gas towards the front of the rocket. The purpose of the ejection charge is to

create enough pressure to eject a nose cone and recovery device. In some scenarios, such as during staging, the delay charge and ejection charge are removed. All engine parts are enclosed within a cylindrical engine casing made of either cardboard or aluminum [30].

In some cases, a user may desire a reloadable motor. Reloadable motors utilize reusable motor casings thus requiring the user to replace only the propellant kit for each launch which saves the user money over multiple launches. Reloadable motors have two additional components: the aft closure and forward closure. The function of the aft closure is to secure the rocket nozzle while also providing a seal to ensure that the gases from the burning propellant escape only through the nozzle. Likewise, the forward closure prevents the hot gases from escaping out of the front of the motor [31].

The propellant within a model rocket motor consists primarily of a fuel-and-oxidizer mix. In a process called combustion, propellant is burned in order to create hot gases that are subsequently accelerated through the motor nozzle creating thrust. Model rocket motors are typically made of a solid propellant mix. There are two common types of solid propellant engines: black powder and composite. A black powder engine consists of exclusively charcoal, potassium nitrate and sulfur [29]. These types of motors can be found in hobby shops and are generally cheaper in comparison to other motor types. Black powder engines only require intense heat to ignite, as opposed to a direct flame, therefore making them very practical as an upper stage motor requiring a separate ignition system [29]. Alternatively, composite motors are made of a mixture containing fuel (commonly aluminum) and oxidizer (commonly ammonium perchlorate), as well as a binder substance responsible for holding the mixture together (commonly polyurethane or polybutadienes) [32]. These types of motors are typically more expensive in comparison to black powder motors. Unlike black powder motors, composite motors require a direct flame to ignite

[29]. This makes tasks such as staging difficult to accomplish without the use of onboard electronics.

Solid model rocket motors can be distinguished by understanding their unique motor code system that was created by the National Association of Rocketry (NAR) [33]. Understanding of this motor code provides important performance parameters specific to the motor. In general, all motor codes utilize the same format. For example, a typical model rocket code may be C6-3. The first letter represents the total impulse of the motor. In the example, "C" corresponds to an impulse range between 5-10 N-s of total impulse in the motor. Table 1 shows the corresponding impulse range for each letter designation. Similarly, the total impulse can be calculated by plotting thrust as a function of burn time. These plots are typically provided by the motor manufacturer. The area under the curve would equal the total impulse. The number immediately following the letter denotes the approximate average thrust of the motor in newtons. In the example provided, the number "6" signifies an average thrust of approximately six newtons. The average thrust can also be calculated by dividing the total impulse by the burn time. Finally, the number immediately following the dash in the motor code represents the time delay, in seconds, between burnout of the propellant and firing of the ejection charge. In the example, the number "3" corresponds to a time delay of three seconds. In some cases, there will be a zero following the dash or there will not be a number at all. This indicates that there is no delay time or ejection charge in the motor. These dash-zero motor types are utilized as lower stage motors which do not require an ejection charge. There are also instances when the motor code will have a letter either after the average thrust or after the dash. This letter simply corresponds to propellant type and has no impact on engine performance [33].

Table 1 shows the classification for each rocket motor and the corresponding impulse range and limit. In addition, the column labeled "Category" indicates the level of power the motor provides and whether a certification is required to fly the motor. A certification is given to an individual by the NAR for demonstrating the ability to build and successfully launch a model rocket using certain level motor [33]. Any motor with an impulse limit less than or equal to 160 N-s is available to anyone in the public who wants to purchase them. Anything above 160 N-s requires the appropriate Level 1, 2 or 3 certifications to fly [34].

The NAR standards and Testing Committee performs intense testing of every rocket motor available to the public to ensure the safety of each motor and quality assurance. These tests are conducted to determine accurate motor codes in addition to other critical motor characteristics such as sensitivity to shock and temperature. NAR also creates a thrust-time curve based on these tests [33]. For each motor, the results of the test can be found on the NAR website.

1.1.2.2 Ignition/Mounting Systems

The ignition system must be able to ignite the rocket motor propellant. Along with a launch pad, ignition systems are all part of what is known as ground support equipment (GSE) in professional rocketry [35]. With various types of igniters, electronic ignition systems are safe and dependable options for launching a rocket [35]. Alternative methods used for ignition systems by hobby rocketeers include pyrogens, mini-bulbs, low current systems, hot particle igniter compounds and nitrate-based igniters for composite propellants [36].

Electric ignition systems rely on the fact that almost all materials have a resistance to the conduction of electrical currents [35]. The ignition system has multiple components that include lead wires, igniter wires, and an element of the wire that is dipped in a pyrogen [37]. In a manner similar to an old-style light bulb, which use tungsten wire heated to the point of incandescence,

Table 1. Rocket motor classification [33].

Classification	Impulse Range	Impulse Limit	Category
Model Rocket	1/8A	0.3125	Micro
	1/4A	0.625	Low Power
	1/2A	1.25	
	A	2.5	
	B	5	
	C	10	
	D	20	
	E	40	Mid Power
	F	80	
	G	160	
High-Power	H	320	Level 1 (certification)
	I	640	
	J	1280	Level 2 (certification)
	K	2560	
	L	5120	
	M	10240	Level 3 (certification)
	N	20480	
	O	40960	

the ohmic heating in an igniter results in very high localized heating that can either ignite a black powder motor, or if dipped in a flammable pyrogenic mixture (pyrogen), results in a flame that can ignite [37]. For composite motors, the propellant itself is lit from pyrogenic material that is ignited and dispersed in all directions, which then lands on the fuel to ignite the motor [37].

The heating element of the igniter wire, typically made from a nickel-chromium mixture known as nichrome, requires a material with a high electric resistance [35]. Nichrome's high resistance makes it a suitable material for effectively dissipating sufficient heat from the lead wire to ignite the pyrogen compared to other materials such as iron, stainless steel, copper, and aluminum [37]. Considering the high ignition temperatures of model rocket motors, various parameters of the nichrome wire affect operation of the ignition system itself. With ignition temperatures in excess of 550 F (288 C), wire diameter and length are important to ensure that nichrome possesses a high enough electrical resistance to produce the heat required for ignition [35]. Similarly, the material choice for the igniter wire is determined in part by the amount of current it needs to carry to produce the required heating for a given applied voltage (usually 12 V DC for model rockets). Along with the igniter wire, the lead wire is another important element that carries current from the control box supplying the electric power to the igniter wire. This means that the lead wires require as low a resistance as possible to ensure most of the voltage drop occurs across the igniter wire [37]. With a high conductivity, copper is a common material that has a low enough resistance to prevent any significant heating [37]. Due to NAR Model Rocket Safety Code regulations, a person is required to be at least 30 ft from the launch pad [35]. This is an important factor that requires durable wiring and connections to minimize the resistance of the system to prevent heating of the lead wires and other components other than the igniter [35].

Motor mounts are another crucial component rocket propulsion system component. These mounts provide stability for the propulsion system, securing the motor in place to prevent it from moving forward or backward in the rocket during flight. Additionally, the motor mounts assist in aligning the motor with the main airframe of the rocket [35]. The motor mounting system is comprised of multiple parts including a motor mounting tube, centering rings, a thrust ring or mount, and a motor retainer. These components can be seen in Figure 19. The retainer usually consists of an engine hook or a threaded endcap.
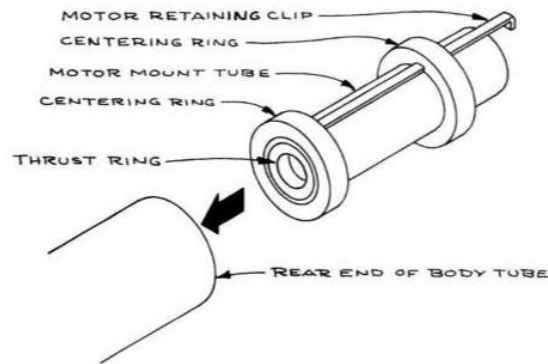
Figure 19: Motor mounting system diagram [35]. © 2004 George W. Stine

To prevent any difficulties from occurring during assembly of the rocket, the motor tube is made to have a smaller diameter than the airframe tube, which also allows for a snug fit. With regards to the centering rings, the outer diameter is equal to the inner diameter of the airframe tube and a cutout inner diameter equal to that of the motor to ensure that there is no movement during flight caused by thrust produced from the motor. This also ensures that the motor is aligned with the central axis of the main airframe of the rocket. Additionally, a thrust ring, which is equivalent to the diameter of the motor, is needed to prevent the motor from flying forward in the motor tube. It is placed either on the nozzle end of the motor or on the aft end of the motor and has a center hole that allows for an ejection charge to pass through if placed inside the motor tube [35].

25
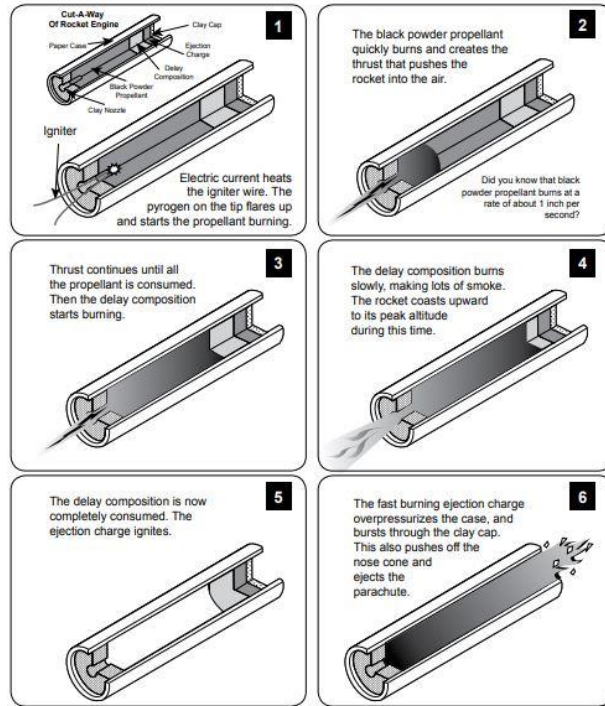
Figure 20. Rocket engine cut-a-way [38]. © 2007 Apogee Components

Motor ejection charges are also frequently used as backup charges in the case of a misfire in the separation systems. This ensures that in the case of a faulty separation charge, igniter wire, or other failure, the rocket still deploys a recovery device and does not enter a free fall. This process is used when the user needs a payload or parachute to be ejected at a time prior to the regular delay time of the motor. The operation of a motor ejection charge is illustrated in Figure 20 from Apogee Rockets [36].

Motors come with a specified time delay between burnout and ejection events, however a drill can be used to drill out the top of the motor and decrease the time delay to a specified amount [39].

1.1.2.3 Staging

One method for achieving a maximum altitude when launching a rocket is to use a technique called staging. Staging refers to the use of two or more motors that are ignited in succession

followed by separation of the first motor from the main body of the rocket once it has completed its main (first stage) engine burn. This technique enables the upper stages of the rocket to propel a reduced overall mass thus allowing it to fly to a greater altitude [28].

There are two types of staging, direct and indirect. For direct staging, the first stage ignites the stage directly above it. In this case, as the first stage finishes its burn, the hot gases from the burning propellant ignite the second stage located directly above it [40]. It is important to note that within the motors of the first stage, also known as booster stages, there is no delay charge or ejection charge. The removal of material comprising these charges allows the hot gases to travel unobstructed into the second stage for ignition. One of the benefits of direct staging is that it only requires one ignition system (to ignite the booster). However, direct staging can only be accomplished with black powder propellant due to the linear progression in which the propellant burns within the motor. Since black powder propellant burns from the nozzle end of the motor towards the forward end, ignition of the second stage is easily attainable [40]. On the other hand, the propellant within a composite motor is aligned so that there is a hole down the middle of the propellant grain in order to increase the surface area of the propellant being burned [41]. Direct staging would not work properly if using a composite motor because the hot gases would travel up the hole in the propellant grain and ignite the second stage before the first stage has finished burning.

A solution to this problem is indirect staging. Indirect staging uses additional onboard electronic ignition systems as a technique to fire the second stage. This electronic ignition requires a power source, an igniter and a component capable of determining when the igniter will fire. These additional components are typically either timers, radio control systems or some alternate onboard flight computer capable of sensing an event that would activate the ignition [42]. Although

indirect staging is more complicated in comparison to direct staging, it allows for the use of higher power motors containing composite propellant.

Overall, staging allows for a rocket to fire multiple motors in series while reducing the overall weight after each stage. This method requires the use of multiple separation and ignition systems as well as changes to other subsystems outside of the propulsion system. Despite this technique being more complex in comparison to a single stage rocket, it allows the rocket to reach a greater altitude.

1.1.2.4 Motor Performance Analysis

Combustion is the rapid chemical reaction that occurs when a fuel and oxidizer mixture is ignited [28]. For example, in a solid composite rocket motor, the fuel is premixed with the oxidizer and reacts in the combustion chamber before the pressure drop across the nozzle accelerates the burning gas out the nozzle, hence producing thrust. Oftentimes, it is desired to know the properties of the combustion reaction mixture once it has reached chemical equilibrium because these represent the initial state for the fluid flow through the motor nozzle. A chemical equilibrium problem can quickly become complex, especially if there are many unknown product species. Fortunately, there is reliable software available that can solve a chemical equilibrium problem for a user.

In a paper written by Youngblood, Hargather, Grubelich and Saul, the equilibrium properties for a nitrous oxide and ethanol reaction in a liquid rocket engine were calculated using both NASA's Chemical Equilibrium with Applications (CEA) computational program and the open-source software, Cantera [43]. The researchers varied the mixture ratios of the fuel and oxidizer, the operating pressure and outlet nozzle configurations, while calculating the adiabatic chemical equilibrium temperature as well as the product mixture enthalpy, density and specific heat C_p.

After completion of all trials, Cantera produced nearly identical equilibrium properties to that of CEA. This comparative study further validated that Cantera software can produce reliable and accurate results for chemical equilibrium [43].

1.1.2.5 Temperature Distribution Analysis

Calculating an estimate of the temperature distribution surrounding the motor during flight can provide more information on any structural degradation due to heat produced from the motor during the rocket in flight. This is important to identify parts of the structure where there is a potential increase in the risk of structural failure due to an excess of heat melting any surrounding components of the motor. COMSOL Multiphysics software serves as a tool to conduct finite element analysis by using various add-on physics module options that can be coupled together to provide solutions for an array of engineering problems [44]. The software provides modules for electromagnetics, structural mechanics and acoustics, fluid flow and heat transfer, and chemical engineering [44]. For the purposes of modeling a rocket nozzle, the fluid flow and heat transfer is the most appropriate module to be used as it can simulate "conjugate" heat transfer. A conjugate heat transfer simulation incorporates heat transfer through both solid and fluids. Heat transfer through fluids consists primarily of convection (advection due to bulk motion and conduction due to temperature gradients) whereas in solids the main form of internal heat transfer occurs through conduction [45]. Conduction specifically refers to the transmission of heat through the collision of molecules in a solid or fluid, from high thermal energy areas to lower energy areas. The flow of heat is characterized by Fourier's Law heat flux through conduction can be expressed as Eq. 1-2.

$$\boldsymbol{q} \ = \ - \ k \nabla T \qquad\qquad 1\text{-}2$$

where q is the heat flux (W/m^2) or energy per unit area per unit time), k is the thermal conductivity, and ∇T is the temperature gradient.

Convection is characterized by heat transfer caused through the bulk movement of a fluid (advection) as well as the diffusive transport of heat because of temperature gradient (conduction) [45]. In a fluid, heat transfer effects are largely dependent upon the Reynolds number. If the Reynolds number is zero that means the fluid is at rest, resulting in heat transfer being purely conductive. Both convection and advection can play a major role for a Reynolds numbers much greater than one. Fluid heating produced by viscous effects is another aspect that is often negligible for low velocity flows. A time-independent equation that describes both conductive and convective heat transfer, known as the heat equation, can be written as Eq. 1-3

$$\rho Cp(\boldsymbol{u} \bullet \nabla T) = \alpha p\ T(\boldsymbol{u} \bullet \nabla Pa) + \nabla \bullet (k\nabla T) + Q \qquad \text{1-3}$$

where ρ signifies density, C_p is constant pressure specific heat, u is velocity, p is the thermal expansion coefficient, ∇Pa is the absolute pressure gradient and Q is the heat source [45].

For a conjugate heat transfer analysis to be made, the COMSOL laminar flow module must also be utilized in conjunction with heat transfer within a solid. This module uses the Navier-Stokes equations, which represent the conservation of momentum and can be expressed as Eq. 1-4.

$$\rho(\boldsymbol{u} \bullet \nabla \boldsymbol{u}) = -\nabla p + \nabla \bullet (\mu(\nabla \boldsymbol{u} + (\nabla \boldsymbol{u})^T) - \frac{2}{3}\mu(\nabla \bullet \boldsymbol{u})\boldsymbol{I}) + \boldsymbol{F} \qquad \text{1-4}$$

where $\boldsymbol{u}$ is velocity, is density, p is pressure, $\boldsymbol{I}$ is the identity matrix, μ is dynamic viscosity and $\boldsymbol{F}$ represents external forces on the fluid. The steady continuity equation is coupled with these equations and can be written as

$$\nabla(\rho\boldsymbol{u}) = 0 \qquad \text{1-5}$$

In addition to these equations, boundary conditions such as inlets, outlets, and walls can be used to solve for and predict characteristics of the fluid flow, such as velocity and pressure within a predefined geometry [45].

1.1.2.6 Existing Methods of Separation

Any rocket, no matter how complex, must undergo certain processes during flight to ensure it performs successfully. One of these processes is separation of sections, where a force is exerted inside the rocket that breaks it into two or more parts. Separation normally occurs when a rocket has reached apogee (its maximum height) and starts to descend. Oftentimes the nose cone of the rocket is pushed outward, allowing a parachute to exit the rocket body and create drag. In more advanced rockets, a separation event can also be used to either deploy an internal payload or detach a stage of the rocket when using a multi-staged system. There are many methods used exert the force required for separation events, however the most common is pressurization of an internal compartment produced by ignition of black powder.

Combustion of black powder can be used to create a high-pressure difference between the inside of the rocket and the ambient pressure. This is easily accomplished by loading a calculated amount of powder into a black powder cap [46], which can then be mounted to a bulkhead inside the rocket.
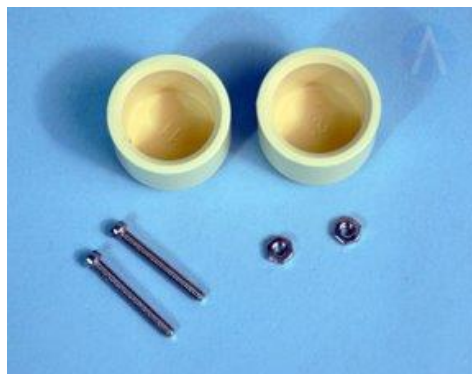
Figure 21: Black powder caps [46]. © 2019 Apogee Components Inc.

A "firewire" [45], or igniter wire with a pyrogen coated end, is led from the on-board electronics to the blast cartridge.

Figure 22: Firewire igniter [45]. © 2019 Apogee Components Inc.

Once the electronics detect that certain conditions are met, a current is sent through the wire igniting the pyrogen end, which combusts the black powder and ejects the necessary components. Due to the simple implementation of this system, black powder cartridges can be used in simple unibody model rockets as well as in more complex rockets that require multiple separation events. The amount of black powder needed for separation can be easily calculated using the equations presented in Section 3.1.2.1. These equations are based on the dimensions of the rocket, specifically the diameter and length of the internal body tube being pressurized [47]. Multiple hobbyist groups [47] [48] have created online calculators using the equations presented in Section 3.1.2.1 to aid in calculating the amount of black powder required for separation. Other sources also recommend the maximum number of shear pins needed to hold the nose cone and rocket body together [48]. When stronger pins are chosen, a smaller quantity is required [48].

1.1.2.7 Carbon Dioxide (CO$_2$) Separation

Carbon dioxide separation is an innovative system used for separation and ejection mechanisms in model rocketry. While it has seen limited use so far because of the level of complexity it adds to a model rocket, CO$_2$ separation offers increased safety, flexibility, and testability compared to black powder charges.

CO$_2$ separation systems function by pressurizing the rocket body with gaseous CO$_2$ in order to jettison the nose cone and release the recovery system. The cartridge is meant to be mounted behind the bulkhead in the electronics bay. Unlike black powder, CO$_2$ separation is clean, meaning that there is no flame or residue that gets pushed into the body of the rocket and onto its components. This removes the need for flame-retardant cloths to protect the interior components such as parachutes from high temperature flames and debris. In addition, CO$_2$ systems are suited for high altitude flights because the small charge used to puncture the CO$_2$ cartridge is sealed and does not rely on the oxygen in the air to burn. Typically, black powder burns inconsistently above 20,000 ft and not at all above 50,000 ft while certain commercial CO$_2$ kits such as the Peregrine are capable of deployment at any altitude and have been tested at simulated altitudes equivalent to 80,000 ft [39].
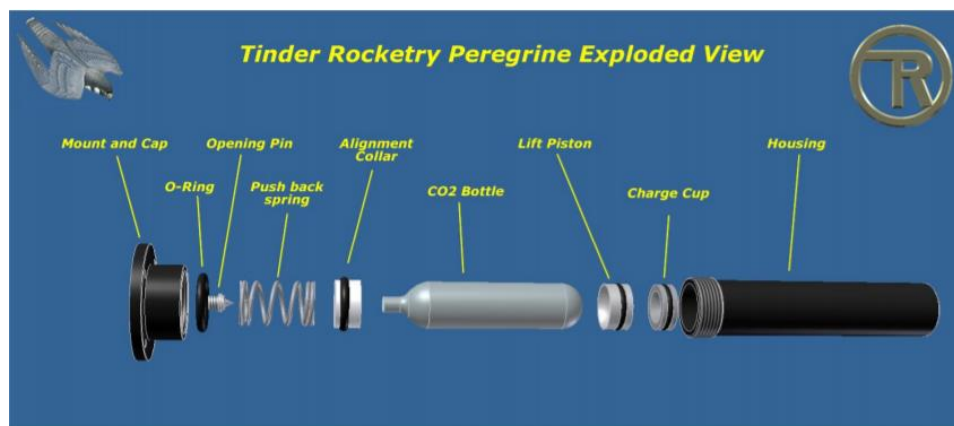
Figure 23: Tinder rocketry peregrine exploded view [49]. © 2016 Tinder Rocketry.

Commercial separation kits such as the Peregrine in Figure 23 are reusable and include different sized CO_2 cartridges. These kits consist of three main components; the CO_2 cartridge, a housing for the cartridge, and a mechanism to seal, load, and puncture the cartridge. The system is usually triggered by some flight event, for example, when the altimeter reads that the rocket is at apogee. The commercial CO_2 kit would be prepared according to the manufacturer's instructions which should explain both assembly and disassembly of the system. CO_2 cartridges are not specific to model rocketry, and canisters used for other applications such as filling bicycle tires can also be used interchangeably [39]. These cartridges come in several sizes, ranging from 8 to 85 grams of CO_2. The general rule of thumb for calculating the needed amount of CO_2 to properly pressurize the rocket tube for nose cone jettisoning is to multiply the recommended mass of the black powder charge by five [48].

1.1.3   Flight Dynamic Analysis

1.1.3.1   Control Systems and Fin Design

In model rocketry, stability plays a vital role as it keeps the rocket oriented to the right flight path. This can be achieved by having control systems incorporated on the rocket. The control system can be either active or passive. Active control consists of sensors that measure various parameters and through some onboard processor, provide control signals to actuators as necessary. Some examples of active control systems are actuated fins, cold gas jets, and gimbaled thrust. The sensors in the system will be used to keep track of acceleration, altitude, position, and the rocket attitude (orientation). If the sensors detect the rocket is deviating from the desired path, the actuators can be controlled to keep the rocket in the desired orientation. Active controls require a source of power to move the actuators. Passive control on the other hand does not have moving parts and depends entirely on the geometry of the body. A rocket can be designed using both

passive and active control system. One of method to attain passive control system on a model rocket is to design stationary fins, which provide stability and orientation in rockets using the aerodynamic forces around it.

The purpose of the fin is to provide dynamic stability in rocket during its flight. Generally, model rockets have three or four fins to provide better stability. Three fins are placed 120 deg apart and four fins are placed 90 deg apart from one another. Fins create a lift force that produces a torque(moment) about the center of gravity, which makes the rocket fly in the desired direction. The lift force produced by the fins will exert a torque at the center of gravity and restore the rocket at an angle of 0 deg [50]. This force is also known as restoring force as it helps to restore the rocket to its initial condition, hence making it stable. If the center of pressure is before the center of gravity, the torque generated by the lift and drag forces gets reversed. This will make the rocket's motion unstable. For a stable rocket, the center of pressure needs to be closer to the tail end than the center of gravity. Keeping the center of pressure behind the center of gravity ensures the rocket will tend to fly with its longitudinal axis aligned into the wind and have some stability during wind disturbances. The stability of a rocket can be measured by a stability margin. The stability margin is defined as the difference between the center of pressure and center of gravity divided by the diameter of the body. For an ideal rocket, the stability margin is between 1.5-2.5.

Designing the right size and shape of fin plays an integral part in model rocketry as it contributes to the performance of the rocket. Fins can be designed in variety of shapes, some of the most common shapes are elliptical, delta, clipped delta, trapezoid, parallelogram and rectangular. The most aerodynamically efficient shape for the fin is an elliptical shape as they produce less drag compared to other shapes, however, elliptical shapes are not practical to fabricate [51]. The most used shapes in model rocketry, then, are clipped delta and trapezoid shapes. These

shapes are aerodynamically efficient as they induce low drag and can be designed with a control surface (aileron) for active control. Adding an airfoil to the fins will make the rocket more stable and aerodynamically efficient.

RECTANGULAR
Simple to make, least aerodynamic

CLIPPED DELTA
Good aerodynamic fin, used on low-drag, high-performance rockets

SWEPT
Simple to make, slightly better aerodynamics

TRAPEZOIDAL
Good aerodynamic fin for payload rockets, moves the Center of Pressure forward.

TAPERED SWEPT
Moves Center of Pressure back, good design for fast moving rockets.

ELLIPTICAL
Best aerodynamic fin, difficult to construct.

FIN SHAPES

2009 Tom Sarradet

Figure 24: Fin shapes [52]. © 2019, AIAA.

The size of the fin is determined based on the diameter of the rocket airframe. The root chord and the semi-span will be twice the airframe diameter, and the tip chord will have a length equal to the diameter. This is generally the rule of thumb that is followed for designing rocket fins [52]. However, this rule can give fins that will make the rocket unstable. To check the rocket's stability, software like OpenRocket can be used. OpenRocket is an open-source software that allows the user to input rocket's geometry and determine whether the rocket is stable or not. As mentioned above, the stability margin should be between 1.5-2.5, and if the stability is not within the given range, the size of the fins needs to be re-designed.

The fins can be made from various materials. One of the main concerns while choosing the material for the fin is that they need to be able to withstand the various forces while on flight. Typical model rockets fins are made from balsa wood, plastic, fiberglass, carbon-fiber, plastic and even hard cardboards [52]. Balsa woods are generally used for smaller rockets. They are light

36
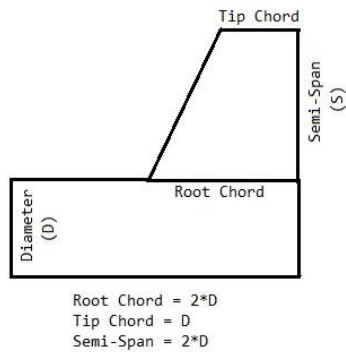
Figure 25: Fin dimensions

and can be broken easily if it's not handled properly. Basswood can be used as an alternative wood

as it is stronger than the balsa wood. Another consideration to be taken in account is the method

of attachment. Attaching fins on the rocket can be challenging if the proper material is not selected.

For instance, plastics and fiberglass are difficult to glue to the rocket tube made from cardboard.

Therefore, choosing the right shape, size and material for the fin are important factors for designing

a better rocket.

1.1.3.2   Avionics

A typical model rocket uses an avionic system housed in a single electronics bay, or e-bay.

Among the components of the system, a flight computer, ranging from a simple microcontroller

to a sophisticated computer board is at the heart of the e-bay. The flight computer receives

measurements from sensors and determines when to send electrical signals to other parts of the

rocket to trigger events such as parachute deployment and engine staging. These sensors include

an inertial measurement unit (IMU) that gathers accelerometer data at a specified frequency

measured in hertz. Hertz (Hz) is a unit derived from time which measures the frequency of how

often something happens. The IMU communicates acceleration data to the flight computer where

the accelerometer data is filtered through a program on the flight computer to filter out noise. This acceleration data is then used by the flight computer to determine the moment at which the rocket reaches apogee. The flight computer establishes when apogee is reached by performing basic calculations to detect a decrease in the rocket's vertical acceleration. When the acceleration reaches a preprogrammed threshold, the flight computer sends an event-triggering signal to release a recovery system. The IMU can also be used to time engine staging in model rockets with multiple stages by communicating with the flight computer to detect a decrease in acceleration. An altimeter is also typically included to measure and record the atmospheric pressure. This information is then sent to the flight computer and compared to predetermined values to establish the altitude of the rocket. Should the IMU fail to detect an event, altimeter data can also be useful in creating a backup signal to trigger staging events. Finally, many model rockets are built with a GPS or RF tracker to determine absolute location throughout flight to aid in post-landing recovery of the rocket if it has fallen outside the line of sight.

1.1.3.3   *Innovative Stabilization and Rocket Rotation*

The FDA subteam discussed and researched multiple methods of attitude stabilization. There were several stabilization options of various complexity contemplated for implementation. The subteam considered active control stabilization methods including cold-gas attitude thrusters, reaction wheels, jet vanes, and gimballed engines. Diagrams of these active control systems are found in Figure 26.

In terms of model rockets, cold-gas attitude thrusters work by releasing pressurized gas, typically carbon dioxide, through small nozzles oriented perpendicular to the rocket's long axis. Given the rocket is perturbed by a gust of wind, a cold-gas thruster fires to provide control moments to counteract the rocket's change in attitude. Reaction wheels are heavy flywheels,

aligned to a specific axis, that are spun and de-spun to provide control moments. A jet vane is a control surface located in the exhaust plume of the rocket that redirects the exhaust, providing a torque to change the attitude of the rocket. A gimballed engine can alter the direction of its thrust vector and thus counteract changes in the rocket's orientation [53]. These active attitude control systems were deemed too complex to implement, however, especially considering the team's relative inexperience with developing control law. The subteam felt they could provide a more thorough analysis of the aerodynamic loads on and the performance of both the baseline and innovative rockets if time and resources were not focused on complex active control systems. Also, if the FDA sub teams' innovative design component did not use space within the rocket for an active attitude control system, such as gas canisters, pipes, and actuators for cold-gas attitude control, there would be more room for the ARS and PTSS sub teams' innovative systems.
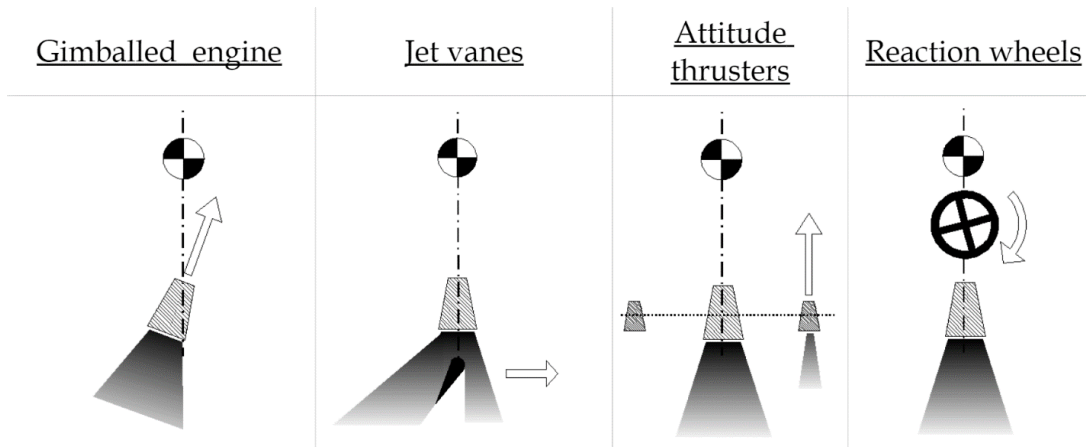
Figure 26: Diagram of active control stabilization options [53]. © 2006/2007, Wyatt.

Information and research regarding spin-stabilized rockets within the atmosphere, model and full scale alike, are relatively scarce. The lack of technical papers that cover spin-stabilized, high-powered model rockets appears to be the result of primarily trial-and-error testing in lieu of aerodynamic analysis using computer simulation or theoretically derived formulas. Lack of

research could also be a result of a lack of interest due to advancements of fixed fin performance. Early model rocket flights using spin-stabilization provide promising evidence that spin-stabilized rockets are in fact stable during flight. However, these early model rockets were designed without fins and did not reach a high altitude [54]. The most common and publicized rocket projects that include spin-stabilization do so with their launch vehicles' upper stages and payloads in deep space missions. Examples of spin-stabilized spacecrafts can be found in upper stages that use the Star 48 motor. Using what is known as a "Payload Assist Module" the Star 48 and its cargo are spun to 60 rotations per minute prior to separation [55].

Spacecraft that use spin-stabilization may perform a "yo-yo de-spin" if some sort of mission/sensor requires the spacecraft rotate under a certain rate. Such a maneuver could be avoided in a model rocket if a descent system could be designed so that the rocket's rotation does not entangle parachutes or recovery devices [56]. A recovery device could be attached to the rocket using a connection that allows a rotational degree of freedom compared to the case where a parachute is fixed to the rocket's body in such a way that it could become tangled if the rocket is spinning during descent. The freedom of the upper limit of the rate of spin rate and the lack of de-spinning techniques necessary results in fins that induce a faster and thus more stabilizing spin.

Although this example of spin stabilization is implemented differently than it would be for a model rocket, the fundamental principles between the two cases are similar. Stabilizing a rocket by imparting a spin on its roll axis is conceptually like the behavior of a bullet shot from a rifled gun barrel. Both rotating axisymmetric projectiles, such as a bullet or model rocket, have an angular momentum. The angular momentum causes the rocket to react more sluggishly to attitude disturbances. Aerodynamic forces, acting on the rocket's center of pressure, act as a "restoring force," keeping the rocket pointed straight and, in this case, vertical. Since the rocket reacts to

disturbances more slowly, the disturbances will have a smaller overall effect on its flight performance, such as how well the rocket stays vertical, and the magnitude of the rocket's reaction to disturbances is generally lower [36]. The main difference between the cases above and a model rocket case, however, is the presence of an atmosphere. For a model rocket, the presence of the atmosphere requires the rotation of the rocket to be stronger in order to counteract the air friction's resistance to motion and provide a comparable stabilizing effect to spin induced in the vacuum of space. This is also true because the disturbances a model rocket faces have greater magnitudes and effects, thanks to the rocket's susceptibility to potential wind gusts.

Due to simplicity, weight savings, and real estate benefits, the FDA subteam selected passive stabilization methods for analysis. Considering flights within the Earth's atmosphere, a rocket will spin naturally due to minor asymmetries in its external geometry such as camera housings or bolts [57]. A slow rotation will have relatively no stabilization effects, though, outside of the restoring moment generated by the fins. Induction of a rotation on a rocket or spacecraft can be achieved using either active or passive control systems. The subteam seek to induce a fast-enough rotation on the rocket such that under normal atmospheric conditions, flight perturbations would have very limited effects on the rocket's performance.

The FDA subteam decided to induce spin on the innovative rocket by applying a camber to the airfoil of each fin. This creates a pressure difference between the two planform sides of each fin, generating lift that causes the rocket to rotate in one direction. The subteam was interested to investigate the performance of the rocket using various simulated fin designs, in order to try to find the most efficient one.

1.1.3.4   Aerodynamic Analysis

Aerodynamics play a critical role in the design of all HPMRs. Knowing how the airflow around a rocket will behave in the air is essential to designing a stable vehicle. For any hobbyist, a finished rocket represents a significant investment of both money and time that would be wasted if a loss of stability were to lead to a crash landing. Therefore, when building an HPMR, it is important to analyze the rocket's passively controlled stability by conducting a thorough analysis of its aerodynamic behavior.

Several rocket design projects have been conducted by Worcester Polytechnic Institute students, each employing a variety of approaches to aerodynamic analysis. The WARRIORS I project from 2006 [58] intended to assess the aerodynamic stability of their rocket through direct wind tunnel testing. Due to time constraints, no data was gathered, but their experiment would have attached a scale model of the WARRIORS I rocket to a free-pitching test stand fitted to the test section of a small open-circuit wind tunnel. For each iteration of their experiment, the team planned to observe the pitching behavior of the rocket model after disturbing it with a simulated wind gust. This experiment would have determined if the WARRIORS I rocket had acceptable stability based on whether or not the rocket's flight angle tended back to zero [58].

The WARRIORS II team of 2007 [6] chose to conduct aerodynamic stability analysis using the rocket design program RockSim (Apogee Components Inc., Colorado Springs, Colorado). RockSim simulates HPMR behavior based on a number of parameters given by the user. The rocket's weight, body shape and size, and fin geometry are the main input parameters used in RockSim's numerical calculations. Through an iterative process of adjusting their fin design, the WARRIORS II team was able to use aerodynamic analysis to select a fin size and shape optimized for stability. Additional analysis was required to determine if this team's innovative glider recovery system would be effective. A scale model of this rocket was constructed, as WARRIORS

I had planned. This time, however, the WARRIORS II team chose not to use a wind tunnel. Instead, they conducted a series of drop tests to qualitatively evaluate the performance of the glider system. From these tests, the team successfully concluded that the glider system was capable of maintaining steady level flight [6].

Aerodynamic analysis of the 2008 WARRIORS III [59] rocket focused primarily on characterizing dynamic instability of its fins, a phenomenon known as fin flutter. This was the focus of their analysis due to the risk excessive occilations pose to the structral inegrity of the fins. Of the three WARRIORS projects, this team used the widest range of aerodynamic analysis methods. Preliminary flutter predictions were made using a model implemented using MATLAB. The model's results were verified in FinSim (AeroRocket and WarpMetrics, Ocala, Florida), a program similar to RockSim, but specifically created for rocket fin design and analysis. This team then turned to wind tunnel testing to verify their analytical predictions with experimental data. Prototypes of several fin shapes were fitted with strain gauges and placed in a wind tunnel at the flutter velocities estimated by FinSim. Strain data recorded over time created a picture of how much each fin type fluttered during the experiment which closely matched the model predictions. Finally, in order to further understand the mechanisms behind fin flutter, the WARRIORS III team conducted two-dimensional computational fluid dynamics (CFD) analysis on each fin type using ANSYS Fluent. Velocity, pressure, and vorticity contours generated from the Fluent simulations were all used to visualize the flow of air around the fins. These contours helped the team visualize the aerodynamic disruptions and unbalanced flows that induced fin flutter in the wind tunnel [59].

The most recent HPMR project by students at WPI conducted aerodynamic analysis primarily through analytical calculations, CFD simulation, and predictive modeling. The 2019 HPMR Design MQP team began by calculating force and moment coefficients by analytical calculation

in Excel [60]. These results were then compared to values generated by OpenRocket (Helsinki University of Technology, Helsinki, Finland), a rocket design program similar to RockSim, for verification. A similar analysis of aerodynamic coefficients was conducted using the CFD programs ANSYS Fluent (ANSYS Inc., Canonsburg, Pennsylvania) and SimScale (SimScale GmbH, Munich, Germany). Fluent allows the user nearly full control over the design of meshing geometry and simulation parameters. However, the user interface is complex and requires a significant learning period by a new user. For this reason, the HPMR Design team struggled with meshing their rocket geometry in Fluent, resulting in unreliable aerodynamic coefficient results. The team turned to SimScale, which is less complex, as a secondary tool for running aerodynamic simulations. SimScale has a simpler user interface than Fluent and provided the HPMR Design team enough control over the simulation variables to generate reliable coefficient results [60].

Instead of adjusting fin shape and size, the team modeled the wind profile for their chosen launch location in MATLAB. Gusts of wind at velocities comparable to flight velocity can cause a rocket to become unstable. The HPMR Design team's model estimated wind velocity over the rocket's expected altitude range and produced plots showing altitude, wind velocity, and rocket velocity as functions of each other. From these plots, the team predicted the altitudes and wind velocities at which their rocket was most likely to become unstable [60].

The variety of approaches taken by WPI's past HPMR projects illustrate that different approaches to aerodynamic analysis vary in complexity and can serve several different functions in the process of rocket design. While qualitative analysis is not usually as precise, it is generally simple. Experiments such as drop tests require minimal set up and produce straightforward results that are easy to record in pictures or videos. If the time and resources are available to build a sturdy scale model, qualitative analysis is best for testing recovery systems. Analytical calculations and

calculations using basic design software are relatively simple as well, provided that all the necessary input parameters are available. Due to simplifying assumptions made in the derivation process, analytical results may not be exact. However, they can still serve as reasonable estimates for fin design and fin-based stability analysis.

Wind tunnel testing (WTT) is typically more precise than analytical solutions but involves significantly more preparation. Wind tunnel experiments require an accurate scale model of the rocket body, in addition to a well-planned experimental setup to measure forces and moments. Therefore, as with other qualitative experiments, WTT is an acceptable method for fluid loads analysis only if the time and resources are available. Investigating more forces requires additional measurement devices. In comparison, CFD can produce results equally as precise as WTT. Since human and equipment errors are less of a concern in computer simulations, CFD results could potentially be more reliable than WTT. Overall, CFD simulations save time and resources. Preparation is limited to geometry meshing and setting flow parameters and if the setup is done well, multiple simulations can be run back-to-back in a relatively short amount of time. This method is also best for investigating a large series of forces acting on a rocket since no specialized measurement equipment is needed. The greatest time commitment CFD requires is the time to learn how to use a given software tool. While some programs may be complex, there are simpler options available to beginners who want to learn the basics quickly.

1.1.3.5 *ANSYS Fluent Solvers and Models*

The solver used by a simulation determines what inputs are necessary for the rest of the set up process. Therefore, choosing an appropriate solver is critical to obtaining acurate results. Fluent offers two solver options for fluid flow modeling; pressure-based and density-based. Acording to the ANSYS Fluent Users Guide, the pressure-based solver is best suited for incompressable and

low speed compressible fluid flows. The density-based solver, however, was designed for high-speed compressible flows [61]. The algorithhim for each solver is shown below in Figure 27 and Figure 28.
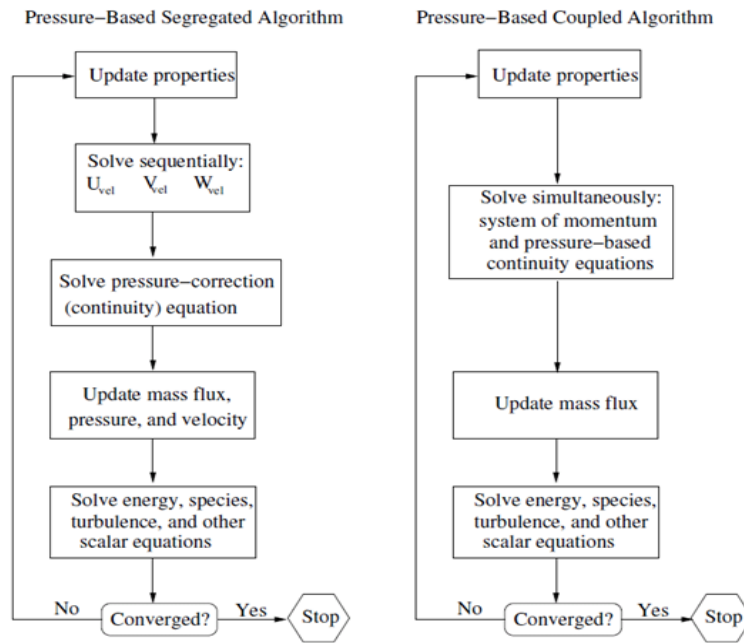
Figure 27: Algorithms for segregated and coupled presure-based solver [62]
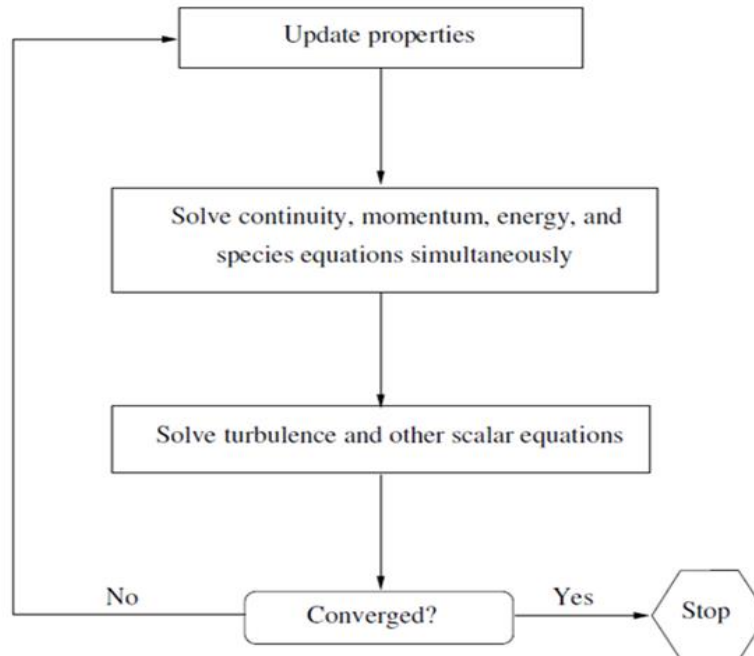
Figure 28: Solution method for density based solver. [62]

While the segregated algorithm evaluates the momentum and contiuniy equations in sequence, the coupled algorithm evelauates them simultaniously. Both versions of the pressure-based solver can be applied to steady-state and transient solutions. The only version of the density-based solver available uses a coupled algorithm [62].

Based on user defined initial flow properties, each solver iterativly evaluates a set of fluid flow equations and checks for convergence. Convergence occures when the residuals of the those equations are found to be less than or equal to a user defined value. Residuals are defined as the error between results of consecutive interations. Where $m(n)$ is the result of the nth iteration and $m(n-1)$ is the result of the interation before it, the resdual value R_1 is calculated from

$$R_1 = \frac{|m(n) - m(n-1)|}{m(n)} \qquad \text{1-6}$$

The default setting in Fluent defines convergence as when the residuals of the continuity, energy, and momentum equations are all less than or equal to 0.001. Once the solutions converge, the calculation is complete. If the solution does not converge, the initial properties are updated and the equations are evaluated again [62] [61].The user must specify a desired limiting number of iterations to prevent the software from running for an excessive period of time. If convergence is not achieved by the final iteration, the user should consider increasing the maximum number of iterations or changing their meshing strategy [61]. Refer to the "ANSYS Fluent User Guide" for details on using the ANSYS meshing tool.

The specific equations evaluated by each solver are determined by the type of model chosen. A variety of models are available, each making specific assumptions about the flow to be analysized. The viscous model in particular is useful for turbulence modeling as it takes into account fluid viscosity and wall roughness. Several types of viscous solver can be applied to match

the type of viscous flow being analyzed. The most common types for turbulence modeling are two-equation models which, according to the Fluent User guide, "solve two transport equations and model the Reynolds Stresses using the Eddy Viscosity approach" [61]. Two of these two-equation models, k-ε and k-ω, are available in Fluent. The k-ε model has long been the indusrty standard simulating practical flow and heat transfer problems. However, it tends to drastically underestimate boundary layer separation resulting in very optimistic assesment of flows over smooth surfaces, such as aerodynamic bodies. For this reason the k-ε model is not well suited for aerodynamics [61]. The k-ω model, however, was designed to predict boundary separtaion better. Unlike the k-ε, the k-ω model "can be integrated without additional terms through the viscous sublayer" [61]. This means the k-ω model is a much better choice for simulating external aerodynamic flows.

Defining boundary conditions properly is also a critical step when setting up a simulation in Fluent. Boundary conditions define how the flow around the object of interest behaves as it enters, exist, and interacts with objects within user specified domains. Table 2 lists and describes the various boundary types available in Fluent.

Table 2: Boundary types available in ANSYS Fluent [61].

Boundary Type	Description
Pressure Inlet	Defines total pressure and scalar fluid properties where flow enters the domain.
Pressure Outlet	Defines static pressure where flow exits the domain. Can also define scalar fluid properties in case of backflow.

Pressure Far Field	Defines free-stream Mach number and static pressure at infinity for compressible flows.
Velocity Inlet	Defines velocity and scalar fluid properties where flow enters the domain.
Mass-Flow Inlet	Used in compressible flows to define mass flow rate where flow enters the domain.
Mass-Flow Outlet	Imposes a prescribed mass flow out of a domain. Used when it is more important to match a prescribed mass flow rate than to match an outflow stream static pressure.
Outflow Boundary	Assumes zero stream wise gradient for all variables except pressure. Used when details of flow velocity and pressure at exit are unknown. Only appropriate when exit flow is assumed to be fully developed.
Inlet Vent	Specifies loss coefficient, flow direction, and ambient total pressure and temperature for a vent intake.
Outlet Vent	Specifies loss coefficient, ambient static pressure and temperature for a vent discharge
Intake Fan	Specifies pressure jump, ambient total pressure and temperature for a fan intake.
Exhaust Fan	Specifies pressure jump and ambient static pressure for a fan discharge
Degassing Boundary	Models free space in which dispersed gas bubbles can escape, but continuous liquid phase cannot. Only available for two-phase liquid-gas flows using the Eulerian multiphase model.
Wall Boundary	Bounds fluid and solid regions. Assumes no-slip condition for viscous flows.
Symmetry Boundary	Mirrors geometry and pattern of flow and thermal solutions. Can also act as a zero shear slip wall in viscous flows
Periodic Boundary	Periodically repeats geometry and pattern of flow and thermal solutions. Two types: Cyclic does not allow pressure drop between periodic planes. Periodic allows the pressure drop.
Axis Boundary	Defines the centerline of an axisymmetric geometries.

Fan Boundary	Models effect of a fan with unknown characteristics upon the larger flow field. Defines pressure rise, flow rate, and components of swirl velocity for fan element. Typically used as a flow source
Radiator Boundary	Models effect of a heat exchange element on flow. Specifies pressure drop and heat transfer coefficients as functions of flow velocity.
Porous Jump Boundary	Models a thin membrane with known velocity and pressure drop characteristics.

1.1.3.6 *Flight Dynamics and Performance*

A rocket's current state, defined by its position, velocity, attitude, etc. at some moment in time can be represented mathematically by a set of state vectors and their derivatives whose elements change over time as the rocket flies. One set that could be used in a complete solution that couples differential equations describing both the rocket's trajectory and orientation are summarized in Table 3 below. Vector quantities shown in this table are defined in the rocket's body frame. One solution for this system is presented in Box et. al.'s "Stochastic Six-Degree of Freedom Flight Simulator for Passively Controlled High-Power Rockets" [63]. It is assumed that: the rocket is an axisymmetric body; moments of inertia are constant during flight; gravity does not change with altitude and acts only at the center of mass; and that the center of pressure on the rocket does not move over time. Any gravity gradient present is considered negligible with a rocket flying under comparatively large aerodynamic drag forces to an altitude of approximately 2,000 feet. Obtaining a rocket's current state and state derivatives can be done numerically at regular intervals over a range of flight time, producing a simulation of its trajectory.

Table 3: State period vectors representing the rocket's current state at some time [63].

Vector symbol	Elements	Vector quantity
P	$[P_x, P_y, P_z]$	Linear momentum
L	$[L_x, L_y, L_z]$	Angular momentum
Q	$[s, v_x, v_y, v_z]$	Quaternion
X	$[x, y, z]$	Position

The linear and angular momentum velocity vectors **P** and **L** originate at the rocket's center of mass. The position vector **X** places the rocket's center of mass in Cartesian coordinates; the origin of this coordinate system lies on a plane tangent to the surface of the Earth at the launch site. The quaternion **Q** describes the rocket's rotational orientation (i.e. attitude) as a rotational transformation between a reference orientation and the current one. Its elements—s being real and the v vector being an imaginary part—mathematically describe a rotation of θ radians about an axis which passes through the rocket's center of mass. The unit vectors pointing in the direction of the rocket's current roll, pitch, and yaw axes can be calculated if the quaternion vector is converted into a rotation matrix populated with combinations of its vector elements. An explicit description of the quaternion's components and this rotation matrix can be found in Box et. al.'s work [63], but these quantities are not relevant towards this project's solution. The analysis presented in this work (Section 4.4), represents a method for summing thrust, gravity, and aerodynamic forces on the rocket over time. These forces are numerically integrated to produce the rocket's trajectory during flight and under parachute descent.

This project's solution makes several assumptions in order to produce a greatly simplified solution of the rocket's trajectory. The most important simplification is that the attitude of the rocket (relative to the relative airflow) is assumed constant. The Euler equations for the rocket's rigid body motion are not solved. This implies the rocket angle of attack is constant (and assumed in this case to be zero). This implies that the rocket's velocity vector is always in line with its primary axis which points from the center of its base to the tip of the nose cone. Thrust and drag forces must also act along this axis. If we also assume that lift forces acting on the symmetric-airfoil, zero-angle-of-attack fins on this solution's rocket are zero, the rocket has no angular momentum and travels only in one plane without wind. Gravity gradients have already been assumed negligible. The culmination of these assumptions is that this solution treats the rocket as a point mass with no orientation to solve for rather than a rigid body whose orientation and trajectory are related. Section 4.4 presents a set of differential equations describing the rocket's motion under these assumptions and how they are implemented into this project's solution for a flight simulator.

1.2. Overall Project Goals

The requirements for the entire HPMR program were shared between three subteams:

- Airframe and Recovery System (ARS)

- Flight Dynamics Analysis (FDA)

- Propulsion, Thermal, and Separation Systems (PTSS)

The overall project goals were to:

- Design, build, and fly two reusable rockets. One rocket called the 'Baseline Rocket' could be a typical HPMR and could be easily constructed and flown at a local rocketry launch.

The other rocket called the 'Innovative Rocket' which would a more advanced design and potentially not be permitted to fly at local rocketry launches.

- o The baseline rocket was a dual deployment, single stage Class I High-Powered Rocket using parachutes as a recovery device.

- o The innovative rocket was a dual deployment, dual stage Class I High-Powered Rocket using autorotational blades as a recovery device.

- Provide the 13 members of the MQP with the opportunity to work as a team to design, build and test a moderately complex aerospace system in which the overall vehicle performance is critically tied in with the mass and performance of the individual components and assemblies.

- Provide the 13 members of the MQP with specialized training in and opportunity to apply software tools: MATLAB, ANSYS – Static Structural Analysis, ANSYS - Fluent, ANSYS Dynamic Analysis, Cantera, others.

Each individual subteam had its own set of objectives to complete. They are:

- Airframe and Recovery System (ARS)

  1. Design and fabricate airframe structure.

  2. Lead integration of subsystems: payload, recovery, staging, avionics, and propulsion.

  3. Design, fabricate, and test both baseline and innovative recovery system.

- Flight Dynamics Analysis (FDA)

  1. Perform analysis of aerodynamics loads on vehicle in flight.

  2. Lead selection and integration of avionics, including processor (if any), accelerometers, gyros, and altimeter.

3. Perform analysis of rocket performance (altitude, range, etc.) in support of design activities and flight planning.

4. Support integration of other subsystems: payload, recovery, staging, avionics, and propulsion.

- Propulsion, Thermal, and Separation Systems (PTSS)

   1. Select, model, and test of commercially available motors for single and two stage rocket

      o Evaluate the design considerations involved with motor staging

      o Estimate thrust and impulse by conducting a motor performance analysis using Cantera

      o Model chemical grain configuration and predict heat flux using COMSOL

   2. Design, fabricate, and test both black powder and spring-loaded stage separation systems

      o Calculate the force required to separate all stages of the rocket

      o Design a spring-loaded separation system for nose cone ejection

      o Perform ground tests to validate the feasibility of a spring-loaded stage separation system

   3. Perform analysis of thermal loads from the motor(s) during flight.

   4. Support integration of propulsion and staging subsystem.

A final category of objectives encompasses the flight operations. These are objectives which are mutually shared between all the subteams and while they don't all have a specific technical application, they helped support the success of the MQP.

- Flight Operations (Mutually shared between ARS, FDA & PTSS)

   1. Select and prepare a payload (e.g. camera).

2. Identify candidate CMASS and Tripoli launch events and communicate with organizers as needed

3. Support flight test(s): pre-flight planning, launch operations, and recovery

4. Maintain the MQP Lab with respect to tool and material organization and general cleanliness

1.3. Overall Project Design Requirements, Constraints and Other Considerations

The *design requirem*ents for the entire HPMR project were shared between three subteams (ARS, FDA and PTSS). The design requirements consisted of:

- Use an interchangeable design for a baseline and innovative rocket.

- Use a camera system to record video during flight.

- Use parachutes to recover the baseline rocket and an autorotation system to recover the innovative rocket.

- Use black powder stage-separation charges for a baseline rocket and spring actuated stage-separation for an innovative rocket.

- Use a single Level-1 high impulse main motor for a baseline rocket or dual stage Level-1 medium impulse motors for an innovative rocket to provide an acceptable thrust-to-weight to satisfy the requirements of range safety officers.

- Use an on-board gyroscopic sensor to analyze flight data.

The *design constraints* for the HPMR project were shared between three subteams (ARS, FDA and PTSS). The constraints consisted of:

- The rocket must be lightweight to allow for an acceptable thrust-to-weight of 5:1.

- The rocket must leave the launch rails at a velocity in which the aerodynamics forces have a significant effect on the rockets' stability.

- The internal components must be non-interfering with nearby components and be encompassed by the rocket's airframe.

- The internal components must be easily accessible when rocket is disassembled.

The *design standards* for the HPMR project were shared between three subteams (ARS, FDA and PTSS). The National Association of Rocketry (NAR) has considerations for launching High-Powered rockets. The constraints from the NAR consisted of [64]:

- The rocket must be launched within the certification level of the certified launcher.

- The rocket must be built with lightweight materials (paper, wood, rubber, plastic, fiberglass, or ductile metal when necessary).

- Commercially made rockets motors are the only certified launching motors.

- The rocket must be launched with an electrical launch system and electric motor igniters. They must be installed after the rocket is on the launch pad or in a designated preparation area. The launch system must have a launch switch that has a safety interlock. The switch is installed and tested before launch.

- If the rocket does not launch, the launcher will watch 60 seconds after initial attempt to diagnose the rocket.

- The (baseline) recovery system should be a system like a parachute so that that all parts of the rocket return to the ground safely, undamaged, and ready to be flown again. The rocket will only have flame-resistant or fireproof recovery system wadding.

The *design considerations* for the HPMR project were shared between three subteams (ARS, FDA and PTSS). The considerations consisted of:

- Safety: Primary consideration during development, production and launch for the MQP team and outside parties.

56

- o Simulations of rocket performance to help determine stable and safe flight including a thrust-to-weight ratio of 5:1.

- o Safe handling of explosives like black power and motor to protect nearby persons.

- o Redundant recovery systems to ensure slow descent of rocket and not projectile.

1.4. Tasks and Timetable

A set of specific analysis tasks were identified for each of subteam to inform and support our effort to meet the project goals listed in Section 1.2. Table 4 lists the section in the report where a complete description, solution approach and result of the task is presented. Each of these analysis tasks is described in summary form in Table 5, Table 6, and Table 7 below.

Table 4. Analysis Tasks for each subteam indicating section of report where analysis is described, and results presented

Airframe and Recovery System Subteam	Section
ARS Analysis Task 1: Airframe Stress Distribution	2.2.1
ARS Analysis Task 2: Fin Stress	2.2.2
ARS Analysis Task 3: U-Bolt-Bulkhead Coupler Stress	2.2.3
ARS Analysis Task 4: Parachute Sizing Model	2.2.4
ARS Analysis Task 5: Autorotation Blade Model	2.2.5
Propulsion, Thermal, and Separation System Subteam	**Section**
PTSS Analysis Task 1: Temperature Distribution	3.2.1
PTSS Analysis Task 2: Motor Performance Model	3.2.2
PTSS Analysis Task 3: Nosecone Separation System Model	3.1.2.2
Flight Dynamics Analysis Subteam	**Section**
FDA Analysis Task 1: Aerodynamic Loads – Simple Model	4.3.1
FDA Analysis Task 2: Aerodynamic Loads – Simulation	4.3.2
FDA Analysis Task 3: Fin Design for Vehicle Spin Stabilization	4.3.3
FDA Analysis Task 4: Vehicle Dynamics and Performance Model	4.4

The entire MQP was tracked on the online utility, *TeamGantt*. The Gantt chart can be found in Appendix A: Gantt Chart.

Table 5. Airframe and Recovery System (ARS) Subteam Analysis Tasks

ARS Analysis Task 1: Airframe Stress Distribution
Problem Statement:
Identify critical locations of high stress throughout the airframe and internal structure during peak acceleration loads.
Solution Methodology:
- Tool(s): ANSYS Mechanical Workbench / Dynamic Analysis, SolidWorks Stress Analysis   - Inputs: Airframe solid model including information on materials, joint/bond point models, acceleration due to primary motor, aerodynamic loads (forces and moments), impulse from separation events (black power or spring actuated)
Analysis Products:
- Map of stress distribution   - Identification of critical locations/joints
Use of Results:
- Stress data will be used to determine weak points within airframe design during 1) maximum acceleration and 2) separation events   - Determine method(s) to improve structural integrity of the airframe and internal structures e.g. electronics bay and motor bay

ARS Analysis Task 2: Fin Stress
Problem Statement:
Estimate stresses on the fins at maximum lateral load (when the fins impact the ground).
Solution Methodology:
- Tool: ANSYS Explicit Dynamics   - Required Inputs: Fin geometry and material, landing speed (to determine how much force the ground exerts on the fin)   - Formulate model that can be used to estimate force on fin as a function of landing sped and vehicle orientation
Analysis Products:
Map of stress distribution
Use of Results:
- Results will be used to identify maximum allowable landing speed (as a function of vehicle orientation)   - Determine method(s) to improve structural integrity of fin and fin-airframe attachment method

ARS Analysis Task 3: U-Bolt Bulkhead Coupler Stress
Problem Statement:
Estimate lateral forces of parachute deployment on u-bolt attachment to bulkheads
Solution Methodology:
- Tools: ANSYS Mechanical Workbench and MATLAB   - Required Inputs: parachute characteristics (drag coefficient, surface area), parachute inflation time, rocket decent velocity, shock cord properties (geometry and spring constant)   - Formulate model that can be used to estimate transient load on u-bolt
Analysis Products:
- Maximum force on bulkhead generated by the parachute opening, shock cord extension, and u-bolt attachment   - Stresses on the bulkhead during parachute deployment
Use of Results:
Determine method(s) to improve structural integrity of u-bolt attachment to bulkhead

ARS Analysis Task 4: Parachute Sizing Model
Problem Statement:
Create a simplified model to estimate shape and dimensions of the drogue and main parachutes to insure an acceptable landing velocity (5 m/s)
Solution Methodology:
- Tool(s): MATLAB   - Required Inputs: vehicle mass and airframe geometry   - Formulate model for parachute inflation time (based on literature), drag, and vehicle terminal velocity
Analysis Products:
Estimate of parachute inflation time, drag, and vehicle terminal velocity for different commercially available parachutes
Use of Results:
Results will be used to select drogue and main parachutes

ARS Analysis Task 5: Autorotation Blade Model
Problem Statement:
Create a simplified autorotation blade model to estimate lift forces to decrease the decent velocity
Solution Methodology:
- Tool(s): MATLAB, XFLR5, and SOLIDWORKS   - Required Inputs: vehicle mass and airframe geometry, spanwise blade geometry (assumed for design or from commercially available blades)   - Formulate model for lift as a function of blade design, vehicle weight, and descent velocity
Analysis Products:
Vehicle descent velocity as a function of time after deployment and blade design
Use of Results:
Model results will be applied to original design as well as commercially available blades to estimate velocity at time of impact. Sensitivity to deployment altitude will also be investigated

Table 6. Propulsion, Thermal and Separation Systems (PTSS) Subteam Analysis Tasks

PTSS Analysis Task 1: Motor Performance Model
Problem Statement:
Create a simplified model for the H400 and I212 Cesaroni motors, that can be used to estimate performance (thrust and Isp) that can be compared with published data
Solution Methodology:
- Tools: Cantera, MATLAB   - Major Assumptions: chemical equilibrium in chamber, frozen flow, steady state, isentropic flow in nozzle   - Required Inputs: Propellant composition and properties, chamber and nozzle geometry, ambient conditions (p, T)   - Formulate model that couples equilibrium chemistry with flow through nozzle
Analysis Products:
Composition of combustion products, chamber pressure and temperature, mass flow rate, thrust, specific impulse
Use of Results:
- Compare predicted performance with manufacturer data   - Estimate heat flux for thermal analysis

PTSS Analysis Task 2: Temperature Distribution
Problem Statement:
Estimate the temperature distribution through the propellant grain, motor casing, and rocket body subject to heat flux from the motor
Solution Methodology:
- Tool: COMSOL   - Required Inputs: Material and property data for motor, casing, and rocket body. External, flight boundary conditions (velocity, ambient pressure, temperature, air properties)
Analysis Products:
Temperature and heat flux distribution through motor and airframe structure
Use of Results:
Results can be used to conduct thermal analysis on the motor body tubes to see if there are any points of risk for structural degradation due to overheating (adhesives used for joints, etc.)

PTSS Analysis Task 3: Nosecone Separation System Model
Problem Statement:
Create a simplified model for the spring-based nosecone separation system
Solution Methodology:
- Tools: MATLAB, Excel, force balance (scale)   - Experimentally measure force required for separation   - Formulate simple spring model using Hooke's Law, number and size (length diameter) of springs, spring constant, compression distance   - Required Inputs: Force required to jettison the nosecone, spring constant and geometry (length, coil and wire diameters)
Analysis Products:
Number and compression distance required for selection of commercially available springs
Use of Results:
Results will be used to evaluate design options (number, geometry, and compression distance) for commercially available springs

Table 7. Flight Dynamics Analysis (FDA) Subteam Analysis Tasks

FDA Analysis Task 1: Aerodynamic Loads – Simple Model
Problem Statement:
Estimate the aerodynamic forces and moments on the vehicle as a function of velocity and vehicle attitude
Solution Methodology:
- Tool: MATLAB   - Required Inputs: rocket geometry and inertia properties, center of pressure, center of mass, drag and moment coefficient data for similar vehicles (from literature), Formulate analytical model for lift, drag, and moments on vehicle as a function of airframe geometry, flight velocity, and vehicle attitude
Analysis Products:
Estimates of forces and moments acting on vehicle of given design and flight state (attitude and velocity)
Use of Results:
- For both baseline and innovative rockets: - Provide load estimates to be used in structural stress analysis   - Use as check of results from numerical simulation   - Evaluation of effectiveness of innovative fin design

FDA Analysis Task 2: Aerodynamic Loads – Simulation
Problem Statement:
Estimate the aerodynamic forces and moments on the vehicle as a function of velocity and vehicle attitude
Solution Methodology:
- Tools: SimScale, ANSYS Fluent   - Required Inputs: rocket geometry and inertia properties, center of pressure, center of mass, drag and moment coefficient data for similar vehicles (from literature), initial and boundary conditions, fluid properties, mesh characteristics, wind profile in given topography, avg. wind speed across the rocket's altitude range
Analysis Products:
- Pressure contours, plots of forces and moments acting on vehicle of given design and flight state (attitude and velocity)   - Evaluation of forces and moments acting on vehicle of given design and flight state (attitude and velocity) when subject to wind disturbances
Use of Results:
- For both baseline and innovative rockets: - Provide load estimates to be used in structural stress analysis   - Provide estimates of perturbation on vehicle attitude (angles and rates) when subject to transient wind disturbances.

FDA Analysis Task 3: Fin Design for Vehicle Spin Stabilization
Problem Statement:
Evaluate the effectiveness of three fin options to provide spin stabilization during flight. The three fin options are: (1) symmetric airfoil with non-zero AOA, (2) cambered airfoil, (3) airfoil with moveable control surface
Solution Methodology:
- Tool: ANSYS Fluent   - Required Inputs: rocket geometry and inertia properties, initial and boundary conditions (flight velocity, etc.), fluid properties, mesh characteristics, fin airfoil geometry, number and placement of fins on the airframe
Analysis Products:
Net torque on airframe for each case considered. A case consists of a combination of fin type, placement, number, and flight conditions
Use of Results:
- For each case, the torque generated over a range of flight velocities will be cure-fit to produce a function that can be used as an input in the vehicle dynamics model (FDA Subteam Analysis Task 4)   - Results will be part of a trade study (effectiveness vs. complexity) to downselect option for innovative rocket

FDA Analysis Task 4: Vehicle Dynamics and Performance Model
Problem Statement:
Create an integrated model that can be used to estimate the vehicle attitude dynamics (angles and rates) as a function of time from launch to impact, as well as the rocket trajectory (including max altitude and range)
Solution Methodology:
- Tool: MATLAB   - Required Inputs: rocket geometry and inertia properties; center of pressure, center of mass; thrust, simplified drag and moment models/data from related analysis tasks, wind profile in given topography, avg. wind speed across the rocket's altitude range   - Formulate model consisting of *two, coupled systems* of nonlinear ODEs, one for attitude dynamics (Euler solver) and one for the equations of motion (Newton's 2nd law) describing the vehicle trajectory. Euler equations are solved at each time step as the equations of motion are solved for the trajectory
Analysis Products:
- Simulation of rocket trajectories, capturing statistically randomized variation in wind speed and direction   - Evaluation of forces and moments acting on vehicle of given design and flight state (attitude and velocity) when subject to wind disturbances and their effect on trajectory
Use of Results:
- Landing probability distribution plot (safety plot)   - Data that can be used to compare stability and performance of innovative fin design with baseline   - For both baseline and innovative rockets: - Provide estimates of perturbation on vehicle attitude (angles and rates) when subject to transient wind disturbances.   - Estimate upper limit on wind disturbance to maintain stable flight   - Evaluation of effectiveness of innovative fin design, i.e. compare vehicle's ability to maintain stable flight with baseline design

2 Airframe and Recovery Systems – Design and Analysis

Using the knowledge gained from the literature review, the ARS subteam completed their set of objectives by designing, fabricating, and analyzing the components of the HPMR. The team designed and fabricated the airframe, nose cone, and payload, electronics, and motor bays. Additionally, five analysis tasks were performed to calculate the airframe stress distribution, fin stresses, stresses on the u-bolt bulkhead coupling, parachute sizing model, and to create an autorotation blade model.

2.1.   Methodology

This section outlines the overall design of the HPMR as well as a brief overview of the construction associated with the different subsystems within the rocket. The rocket is essentially five different systems: airframe, payload bay, electronics bay, motor bay, and nose cone. Most of these systems coexist in both the baseline and innovative designs, although minor alterations were made to tailor to the needs of both rockets. Figure 29 and Figure 30 are cross sectional diagrams of both the rockets.
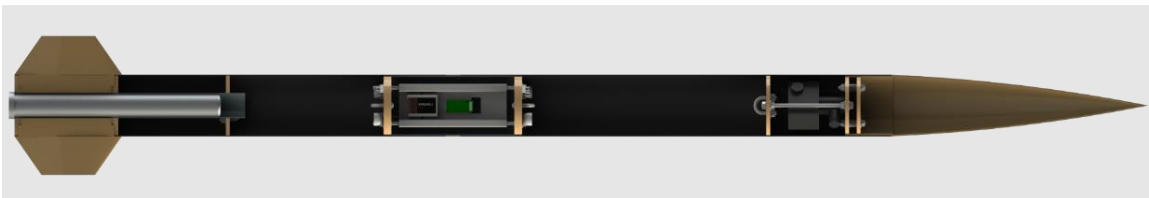
Figure 29: Assembled baseline HPMR
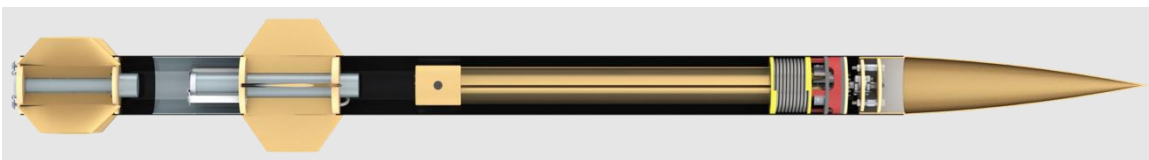
Figure 30: Assembled innovative HPMR

Some of the major design considerations were feasibility of manufacturing, modularity and ease of assembly on launch site among many other things. The three subteams, ARS, PTSS and FDA all worked independently with design parameters based on sizing and weight towards a final design. The subsystems within the rocket can all be disassembled for maintenance or upgrades.

2.1.1 Airframe Mechanical Design

The ARS subteam decided to use Blue Tube 2.0 for the structural material of the airframe of the HPMR. Blue Tube is vulcanized (hardened with chemicals and heat treated) cardboard and was an adequate choice because this material is easy to work with and is light weight. Based on calculations and observations from an OpenRocket model, the ARS subteam decided to split the airframe into two sections. Each section holds different components and serves a different purpose, but when connected by a coupler tube (which is also Blue Tube 2.0) it makes up the entirety of the airframe. There is the upper airframe, which holds the payload, nose cone fitting, and main recovery system of the model rocket, and the lower airframe, which houses the motor tube, motor bay, fins, and drogue parachute. Figure 31 and Figure 32 show two diagrams of these sections.
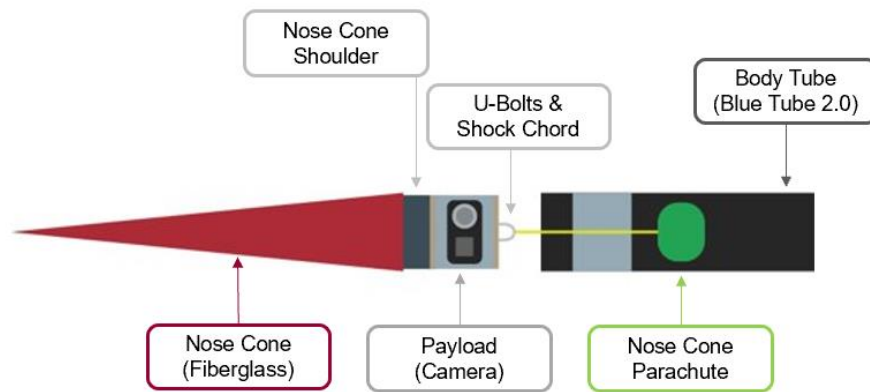
Figure 31: Upper airframe of the HPMR
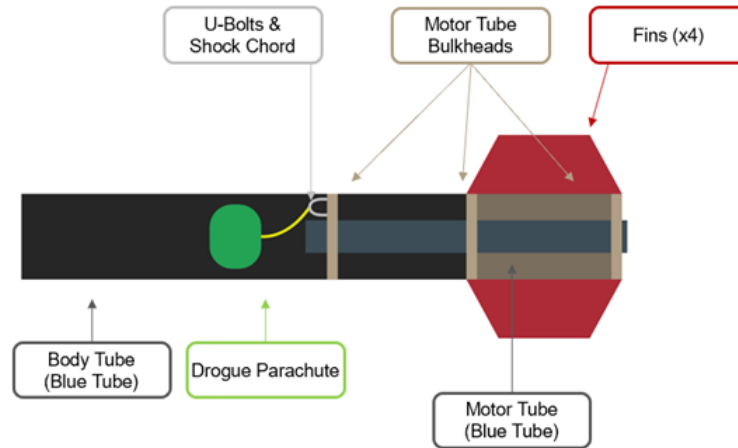
Figure 32: Lower airframe of the HPMR

Both sections are 28 in. in length, with an outer diameter of 4 in. and thickness of 0.062 in. The coupler tube has an outer diameter of 3.9 in. and the same thickness of 0.062 in. A 4 in. diameter was determined to be a sufficient diameter size in order to balance the requirements of achieving flight to the desired altitude, and providing the space needed inside the rocket for the rest of the subsystems, i.e. the motor and electronics bay. A 4 in diameter would allow for a larger motor tube to fit inside the lower airframe, which would increase the altitude the HPMR could reach.

The upper and lower airframes were both cut from one, four-foot long tube with a Dremel in the MQP laboratory. The following process was followed when cutting the airframe sections. Anyone cutting or sanding Blue Tube or other dust-generating materials must wear appropriately rated masks for protection.

1. Using a tape measure, two sections of Blue Tube 2.0, 28 in. in length were measured and marked around the circumference.

2. Using a Dremel, slow passes were made around the circumference of the airframe where the cut was marked.

3. Following the cutting of the airframe, each side was sanded and filed to ensure a level and even finish.

Table 8 is taken from the MQP team bill of material list for reference to the dimensions, pricing, and manufacturer.

Table 8: Qualities and properties of the purchase Blue Tube 2.0 material

Subsystem	Component	Specific Item	Part #	Qty	Price	Total	Vendor	Status	Comment
Airframe									
	Main Tube	4" x 0.062 wall x 48" Airframe / MMT	BT-9848	4	$ 38.95	$ 155.80	Always Ready Rocketry	In Stock	Need 2 to build airframe for baseline and 2 additional for innovative. Scrap can be used for next year's team

In order to attach the fins to the airframe, an alignment tool called a "fin guillotine" (constructed and residing with the AIAA Student Chapter, seen in Figure 33) was used to clamp the bottom section of the airframe in place. Once held, the length of the fin slot was marked on the airframe, then a router was used to cleanly cut the fin slot. This process was repeated three more times, so there were four slots in the lower airframe. These slots were cut to be arranged symmetrically in the body to help decrease drag, maintain the airfoil shape, and for aesthetic reasons. Once the cuts were made for the fins, they were attached to the airframe using West System's epoxy resin and hardener, as well as Aves's apoxie clay. After the epoxy dried, the

airframe was sanded to create a smoother surface around the attachment locations between the airframe and fins.

Figure 33: Fin guillotine

To capture footage of the rocket during launch and descent, a camera was inserted into the airframe and a window was cut from the frame to allow the camera to remain safe within the airframe while capturing the rocket's journey. To create the window, the camera was first loaded within the payload bay, and its position was measured to see how far from the top of the airframe section it would rest while mounted in the rocket. The measurements, in addition to the 107 deg field of view of the camera were then used to create a window area, which was then cut using a Dremel. After being cut, the camera was placed into the payload bay in the airframe, and the team ensured the area cut would be suitable for the camera to capture the rocket's journey.

2.1.2   Payload Bay

The MQP team needed to select a payload when designing the payload bay for the HPMR. The 2019 HPMR team, chose a camera for their payload, so the MQP team decided to continue to

use a camera as the payload [8] [18] [60]. Once this was established, the ARS subteam designed a payload bay to hold the camera and viewing window.

Initially, the ARS subteam designed the payload bay to have a full 360-degree field of view window to allow a pivoting camera to record video during the flight. The design of a full 360-degree view window either required the team to purchase transparent tube with the same outer and inner diameter of the airframe tube or required forming a sheet of transparent material that could be formed to the same outer and inner diameter of the airframe. The transparent tubes readily available on McMaster-Carr did not match the geometry of the airframe, which meant it could not be coupled to the preexisting components. Additionally, the camera purchased was too large to rotate inside the payload bay due to support rails, which can be seen in Figure 34. For these reasons, the ARS subteam redesigned the window of the e-bay and ultimately came to the conclusion that it needed to be molded out of a transparent sheet to the same geometry as the airframe tube, then epoxied into the airframe.

Figure 34: SOLIDWORKS model of the payload bay

The 2019 HPMR teams also designed a window for their camera. Their window design involved securing the window to the inside of airframe with rivets [8] [18] [60]. This airframe

section was fixed to the payload bay and separated from the rest of the rocket. The ARS subteam decided to epoxy the window into the airframe, which allowed the payload bay to separate from the airframe. The two reasons for incorporating the window into airframe were the ARS subteam felt it could be better designed and it was more aesthetically appealing. The ARS subteam installed the window into the side of the rocket by molding a sheet of transparent material to the shape of airframe. The window was then epoxied in place.

Since this method had never been attempted by a previous MQP team, the ARS subteam created a test section to ensure it could be fabricated. First, we cut 3.5 x 1.5 in. section out of a scrap piece of airframe tube. The dimensions of the window were marked on the airframe, then blue painters' tape was placed on these marks to provide a straight line for cutting. The airframe before and after picture of the airframe are below.

Figure 35: Airframe before the e-bay window was cut out

Figure 36: Airframe after the e-bay window was cut out

A piece of polycarbonate was cut, with a hacksaw, so the dimensions were 1/8th in. smaller than the window in the airframe. Since the window was smaller than the cutout within the airframe, it fit within the cutout. This also meant that the window needed to be supported while applying epoxy to hold it in the cutout. Cutting polycarbonate was difficult since it is a flexible material and bent when the hacksaw applied pressure to it. In order to stiffen the polycarbonate, a thin piece of wood was placed under it as seen in Figure 37. The piece of wood was also cut when creating the window.
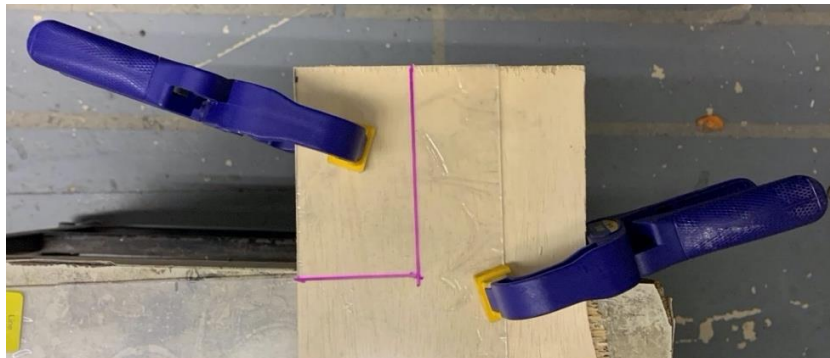
Figure 37: Cutting the polycarbonate window

Next, the polycarbonate cutout was molded to the shape of the airframe by heating up the test window around a section of coupler tube. First, the outer surface of the coupler tube was wrapped with blue painters' tape to prevent the inner surface of the window from getting damaged. The edge of each piece of tape was placed next to each other to provide a smooth transition, so there were no gaps or overlap, which could deform the window during molding. The coupler tube was slid into the airframe in a way that only the painters' tape was visible through the cutout, not the surface of the coupler of tube, as seen in Figure 38. Next, one end of the test window was placed in the cutout of the airframe and clamped to hold it in place for molding, which is demonstrated in Figure 38.
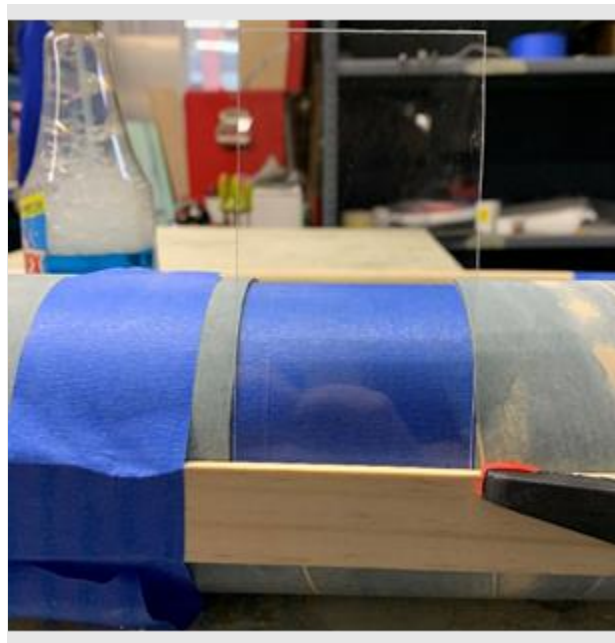
Figure 38: Picture of window clamped in the airframe cutout

Once the window was clamped in place, the Chicago Electric Power Tools – 12 Setting Heat Gun was then used on setting #2 and held at a distance of approximately 6 in. from the surface to heat the window starting at the clamped end of the test window. Once it became malleable, the

edge of another clamp was used to apply force to window to help it form to the coupler tube. Heat was then applied to a section of window above the new molded part. This process was repeated until the entire window was molded, which can be seen in Figure 39

Figure 39: Molding process for the e-bay window

After the window was molded, it needed to be epoxied the airframe. The airframe was put on a section of coupler wrapped in a thin piece of a plastic sheet, which can be seen Figure 40 and Figure 41. The plastic was used to prevent the epoxy from sticking to the coupler tube, which allowed it to slide out after the epoxied cured.

The test window was placed within the cutout of the airframe and epoxy was applied to the seam between the airframe and window, then clamped down. During clamping, epoxy was forced on the inside of the test window, which would be in the field of view of the camera. This can be seen in Figure 41. After curing, the excess epoxy was removed by scoring then gently prying it off to avoid interference with the field of view of the camera. Additionally, the epoxy did not

completely fill the seam because it was too viscous and ran down the airframe as shown in Figure 42 and Figure 43.

Figure 40: Plastic sheet on coupler tube

Figure 41: Coupler tube in airframe

Figure 42: Epoxy seepage behind window
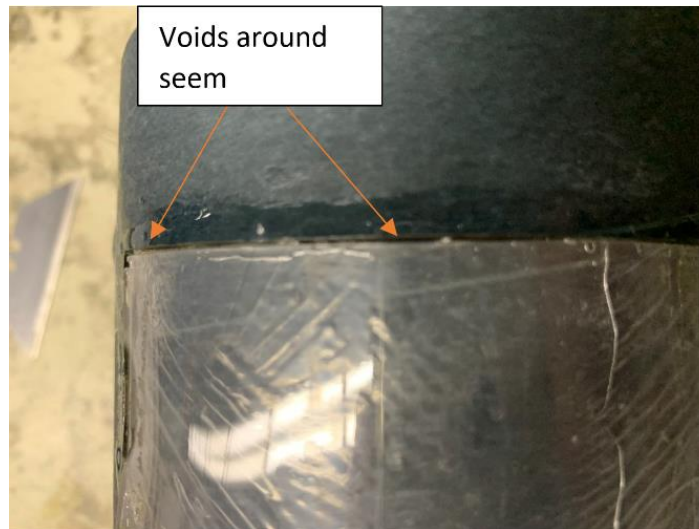
Figure 43: Voids in the seam between the airframe and window

Both problems could be avoided by waiting for the epoxy to slightly cure before application

to the seam. Aside from these two issues, the test window proved that this method could be used

for the fabrication of the HPMR and the clarity of the window was very good as demonstrated in

Figure 44. The only distortion resulting from the fabricated window was that the picture was

slightly hazy.

Figure 44: Comparison of pictures with and without the e-bay window

Before creating the window for the HPMR, the payload bay was designed to determine the location of the camera within airframe. Figure 34 shows the SOLIDWORKS model of the payload bay. The payload bay model consisted of two 0.25 inch thick plywood bulkheads held in place with washers, nuts, and two threaded rods. A u-bolt was attached to the bottom bulkhead to connect a parachute to the payload bay. An additional threaded rod was added to the top bulkhead to connect to the camera mount, which was provided with the camera. This rod was also held in place with washers and nuts and an additional nut was tightened to the top of the camera mount to prevent it from moving or rotating during launch. Two other holes were cut in the top bulkhead, so the payload bay could be attached to the two threaded rods in the nose cone. These two threaded rods were designed as an interchangeable mounting system so different payloads could be attached to the same nose cone. After the payload bay was fabricated, the distance from the contact point from the shoulder of the nose cone to the center of the camera lens was measured to be 5.5 inches.

Once this distance was measured, the required dimensions for the window were calculated using a sketched field of view of the camera in SOLIDWORKS. The field of view of the camera was found to be 107 deg, which came from the specifications listed in its manual. A cone with an angle of 107 deg was created in the SOLIDWORKS model and placed in front of the camera lens to determine the minimum amount for the window cutout. The dimensions of the window were rounded to an even 5.5 x 3.5 inches to make measuring and fabrication easier.

The window was fabricated with a method similar to the one used for the test section, but there were a few differences. After the airframe was cut, the payload bay, with the camera in it, was placed in the airframe while it was recording. The footage was then reviewed to ensure that the airframe did not obstruct the camera's view. The footage validated that the 5.5 x 3.5 inch cutout provided a full field of view. The window of the payload bay took three attempts to mold due to imperfections, such as warping, scratches, and indents, on the polycarbonate, but the final result was a clear and undistorted window with only a minor scratch, which can be seen in Figure 45.

Figure 45: Final window on the GLADIATOR rocket

2.1.3 Electronics Bay

The electronics bay (e-bay) is the central housing unit for all electronic and power systems for the HPMR. The main electronics in the e-bay are the altimeter, power source and gyro that record data and trigger events during the flight (like a separation charge for example). The details of the electronics used for the HPMR are described in Section 4.2.

In the baseline rocket, the e-bay was centrally located in the rocket between the upper and lower airframes as shown in Figure 47. The upper and lower airframes were made of 'Airframe Blue Tube' while the e-bay was made of 'Coupler Blue Tube'. Coupler tube fits inside airframe tube. When assembled, the only portion of the e-bay which is visible is the 1in wide band of outer tube (painted in gold in Figure 48). This band of outer tube, referred to as the 'e-bay band', keeps the electronics bay stationary to restrict sliding up and down inside the airframe.

Figure 46: Model of e-bay   Figure 47: Rocket with e-bolt exposed   Figure 48: Fully assembled rocket

The major components in this system are summarized in Table 9.

Table 9. Major Components in the Electronics Bay

Number	Component	Description
1	Bulkheads (x2)	Caps fixed to each end of the e-bay to enclose the system
2	Coupler Tube	Main body of the e-bay
3	E-Bay Band	Prevents e-bay from sliding throughout the airframe and provides a mounting point for the on/off switch to toggle the electronics
4	U-Bolts (x2)	Mounting points for parachutes
5	Threaded Rod Rails	Mounting point for e-bay sled and holds bulkheads together
6	Sled	3D Printed custom sled to fit inside e-bay and holds all electronics
7	Black Powder Caps (x4)	Canister for the black powder used during stage separation
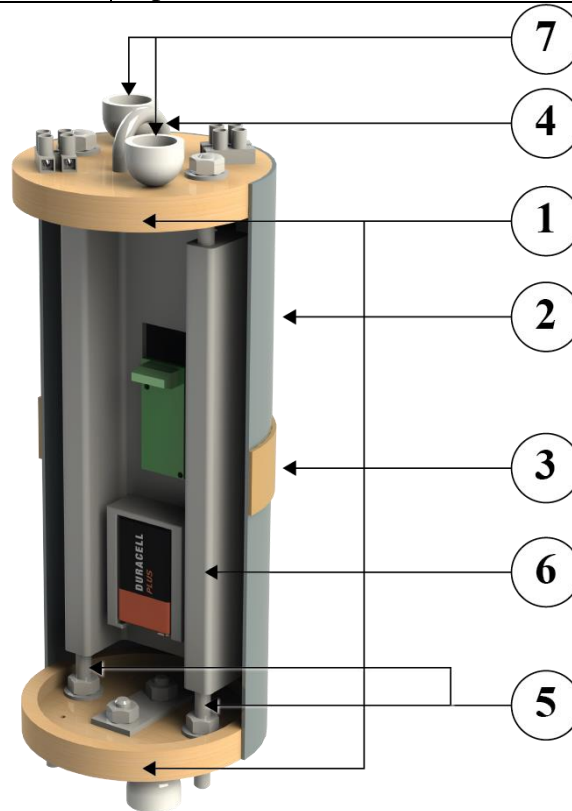
Figure 49: Labeled e-bay cross section

Model rocketry vendors sell e-bays COTS; however, these options were not as configurable as a custom-built model, therefore, the ARS subteam built one from scratch.

The e-bay is one of the main connection points for parachutes. Its design was heavily dependent on the parachutes that attached to it. The drogue parachute attaches to the bottom of the e-bay (the section attached to the lower airframe) and the main parachute attaches to the top of the e-bay (upper airframe). The upper airframe is fixed to the e-bay with a bolt so that does not freefall during a launch since the parachute is attached to the e-bay, to the upper airframe. The lower airframe is attached to the e-bay with a shock cord which has a parachute attached with a swivel linkage. The e-bay during descent is shown in Figure 50.
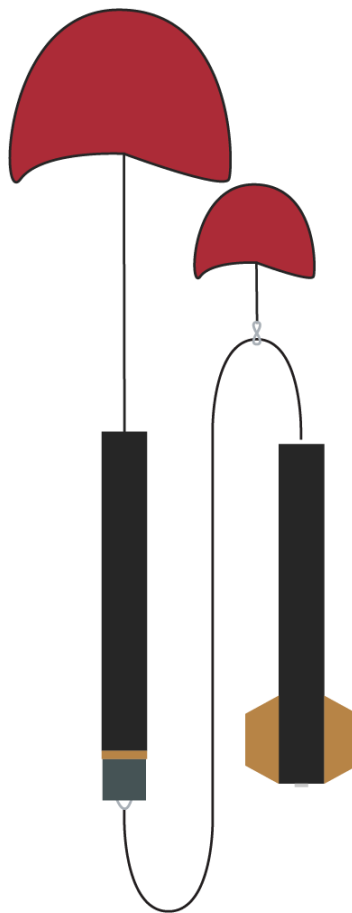
Figure 50: Visual of e-bay deployment

2.1.4 Motor Bay

The motor bay on the baseline rocket is located on the bottommost section of the lower airframe as shown in Figure 51. The motor bay was designed to support the fins and motor during launch. It is comprised of centering rings (also referred to as bulkheads) which are epoxied to a motor tube and then finally epoxied into the inside of the bottom airframe.
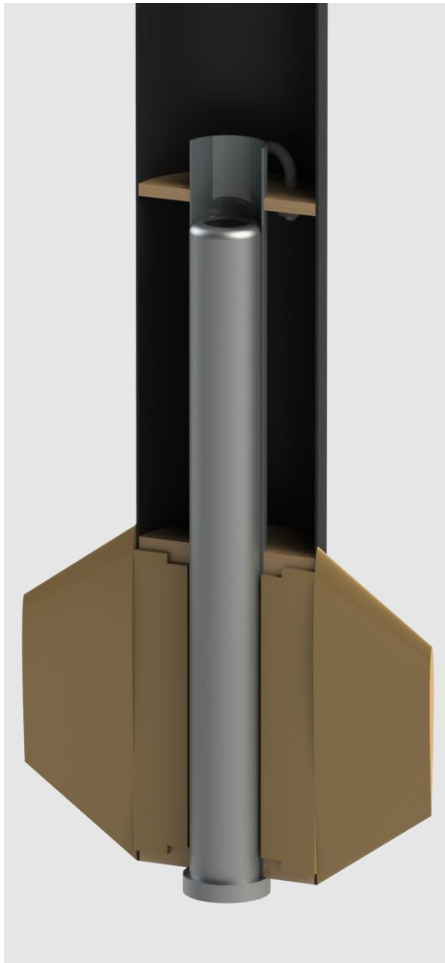
Figure 51: Motor bay
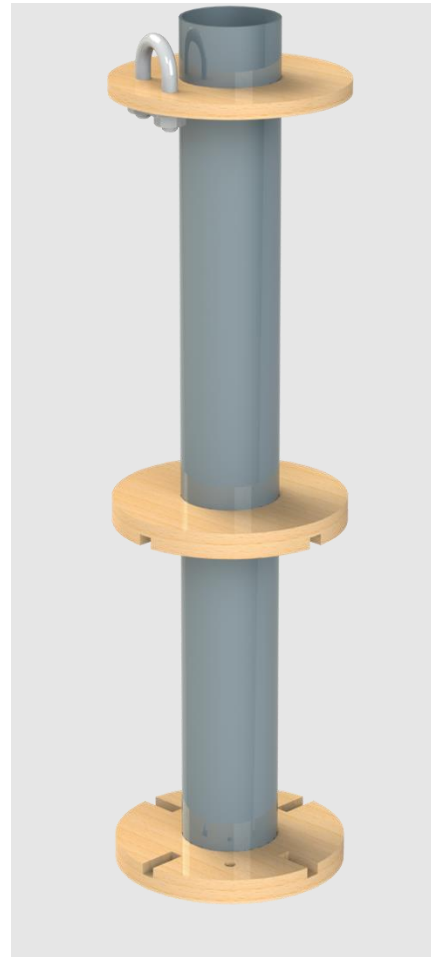
Figure 52: Motor bay exposed

The type of motor used, and the size of the fins were the biggest determining factor when designing the motor bay. The PTSS subteam gave the ARS subteam a list of characteristics

describing the motor including width, height and thrust. The motor the PTSS subteam chose was a Cessaroni I216. The ARS subteam used these parameters to build the motor bay. The major components in the motor bay system are listed in Table 10.

Table 10: Motor bay components

Number	Component	Description
1	Bulkheads(x3)	Spaced along motor tube to transfer thrust from motor to lower airframe
2	Motor tube	Housing for motor casing
3	Motor casing	Detachable tube to house the motor
4	U-Bolt (x1)	Mounting at topmost bulkhead which holds the drogue parachute
5	Fins (x4)	Trapezoidal fins developed by the FDA subteam

In order to have a successful flight, there had to be a form of motor retention. This ensures that the motor does not fall out during flight, especially when the motors ejection charge creates a high-pressure inside the lower airframe. To provide this retention, clips were added to the bottom bulkhead of the rocket to pin the motor against the rocket body. The retention clips were installed after the motor was slid into the motor tube (see Figure 53). The retention clips were designed to be removable, so a new motor could be installed. The entire system was modeled in SOLIDWORKS, laser cut out of plywood, and then epoxied as a full assembly.

As shown in Figure 53, a small portion of motor tube exceeds the length of the motor casing at the forward end. This was designed like this because after the motor burns out, a small ejection charge is fired on the top of the motor. This small detonation could have detrimental effects on the inside of the lower airframe, so this helps guide that explosion up rather than outward.

Figure 53: Motor retention system

2.1.5   Nose cone

A premade, COTS nose cone was ordered by the team after conducting research discussed in the literature review. The nose cone the MQP team purchased has a parabolic shape for its aerodynamic design. When the nose cone arrived, the ARS subteam made sure there were no visible flaws on the nose cone. Then the nose cone's base, where it attaches to the airframe, was cut (Figure 54) to reduce the length of the connection in order to fit another bulkhead within the airframe. The cut would allow the nose cone to be interchangeable with different payloads. The end of the nose cone was then sanded so that the fit was tight, but still removable with a slight amount of force. This was important in ensuring the nose cone would not detach prematurely during the main flight of the rocket. Two shear pins were installed between the upper airframe and nose cone prior to launch to prevent the nose cone from separating midflight unexpectedly.
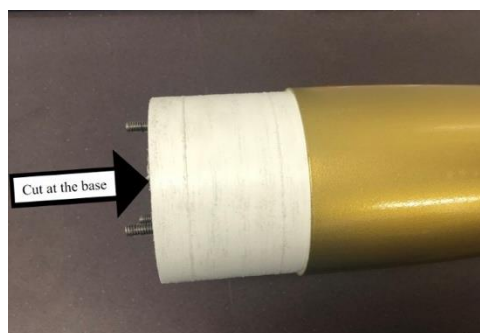
Figure 54: Base of nose cone

2.1.6 Autorotation

Autorotation is a complex landing process performed by helicopters, which is equally as complex when applied to model rocketry due to the lack of active control. Autorotation recovery systems for model rockets are often limited by their fixed blades, which have set pitch angles along the span of the blade. An optimal pitch angle may be calculated to find the AOA that produces the maximum upward force and thus decreases the descent velocity, but this process is complicated since the relative wind angle changes across the span of the blade due to its rotational velocity. During descent, the model rocket could encounter cross winds that change the direction of relative wind velocity, which affects the AOA. As previously stated in Section 1.1.1.6, changes in the AOA could have negative consequences, such as a decrease in the vertical force or even causing the rotor blades to stall. Additionally, the blades have no initial rotational velocity, so the aerodynamic forces initiate the rotation from static conditions, which requires more energy to start rather than a stalled helicopter with its rotor blades already rotating. Also, the autorotation rotor blade dimensions are confined by the length of the payload bay, diameter of the tube, and other systems within the payload bay. These constraints made designing an autorotation system difficult.

When the ARS subteam designed the autorotation system, the first step was to select the design style of the autorotation system. From the literature review, there were three main autorotation designs. The first design uses the airframe as the blades. The second uses blades attached to the outside of the rocket, and the third uses blades stowed within the airframe. The ARS subteam reviewed the pros and cons of each method. The first method that used the airframe as the rotor blades seemed less viable due to the cross-sectional shape of the Blue Tube 2.0 having poor aerodynamic properties compared to an airfoil. The second method of attaching the blades to the

side of the rocket would increase the drag force experienced by the rocket, which would decrease the apogee of the rocket, but it allowed for more space within the airframe. The last method would constrain the size of the rotor blades to the airframe but did not increase the drag force.

The ARS subteam decided that the autorotation blades would be contained within the payload bay of the HPMR because the drag and stability of the rocket would not be affected. In order to release the autorotation system a drogue parachute was incorporated into the nose cone to vertically orient the rocket. After the parachute deployment, the separation system releases the autorotation system. A torsional spring attached to a hinge causes the blades to extend into the deployed position as shown in Figure 55.
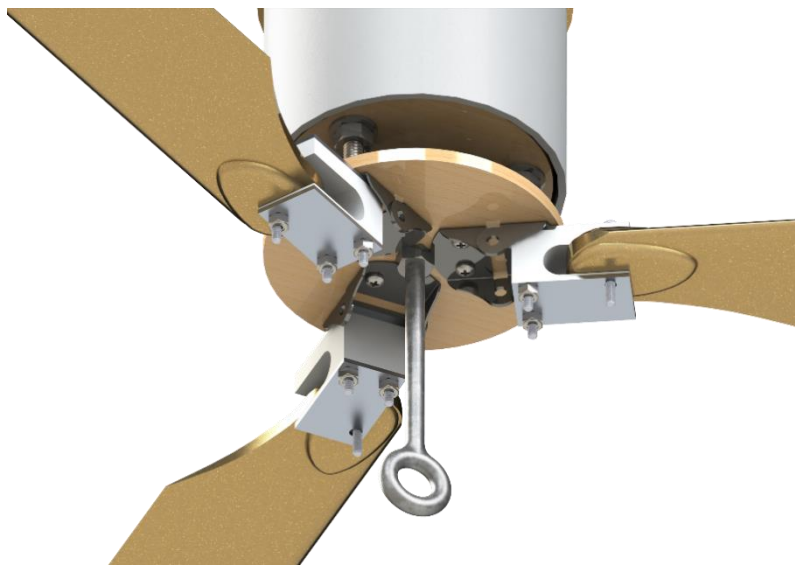
Figure 55: Rendered model of the autorotation deployment system

The design of the mount for the autorotation became very complex due to sizing restrictions within the rocket. As shown in Figure 56, a spring separation system was located near the nose cone (colored in yellow). It fits against the inner surface of the airframe and has a thickness of 0.5 in. More details on the spring separation system can be found in Section 3.1.2.2. For the purpose of designing the autorotation system, the spring separation system was treated as a 0.5 inch thick

pipe, where the outer diameter was equal to the inner diameter of the airframe. This was the simplest case to make sure there were no interfering components.
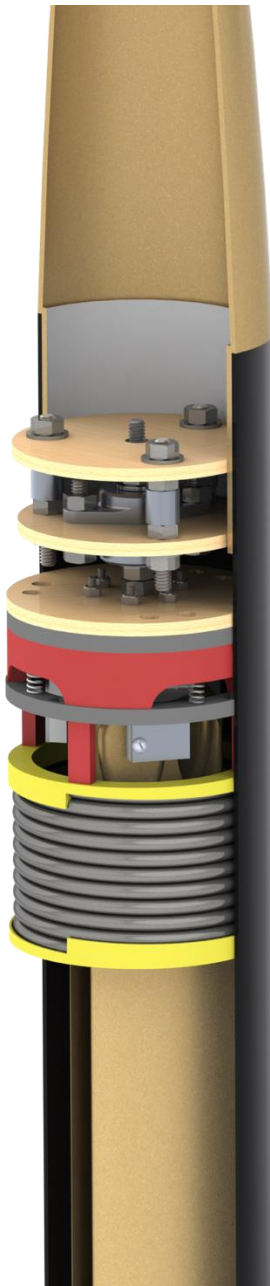
Figure 56: Autorotation system with spring separation system

The overall design of the autorotation system is shown in Figure 57 and Figure 58.

Figure 57. Autorotation
system collapsed

Figure 58. Autorotation system deployed

The autorotation system was designed with modularity in mind. The system is easily removable from the nose cone, with the integration of threaded rods on the topmost bulkhead as shown in Figure 59. Hex nuts can be unthreaded to release the autorotation system from a bulkhead epoxied in the nose cone shoulder. An eyebolt (shown in Figure 55), connects the autorotation system to the upper airframe. A quick link and swivel with shock cord attached to a u-bolt within the upper airframe is linked into the eyebolt on the autorotation system. The purpose of the swivel was to prevent the lower airframe from rotating due to the autorotation system.
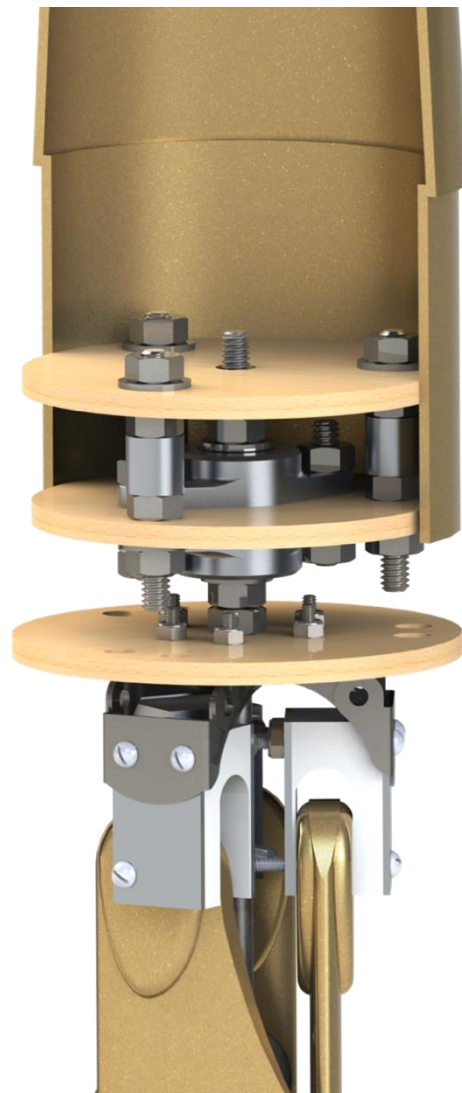
Figure 59. Autorotation system closed up

The middle bulkhead has two bearings mounted to it, with a rod fed through the middle. This allows the bottommost bulkhead to spin freely, enabling the free rotation of the autorotation system. The blades are attached to the bottommost bulkhead with hinges equipped with springs. The springs are under tension when the blades are folded up. This means when the system exits the airframe, the blades automatically are forced to the deployed position. The blades are mounted to the hinge using a 3D printed block (colored in white) and reinforced with aluminum plates.

Many iterations of designs were made with the intent of fitting the autorotation system concentrically within the rocket and spring separation system. Ultimately, the final design was implemented. The minimum clearance between the blades and spring separation system was 0.1 in, which ARS deemed acceptable for tolerances as shown in Figure 60.
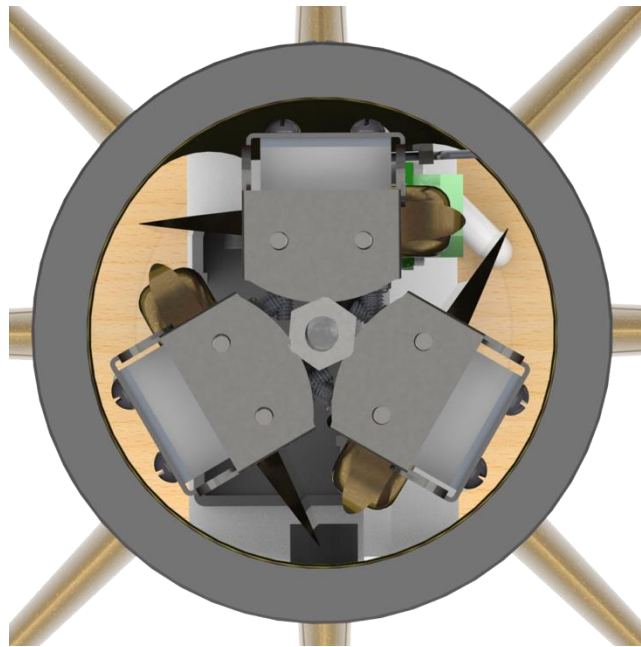
Figure 60. Autorotation integration within spring separation system

The ARS subteam had to decide between manufacturing rotor blades from scratch or purchasing COTS blades. The best option was to buy RC helicopter rotor blades since it is the

easiest method, but their aerodynamic properties needed to be analyzed to determine whether they supplied a sufficient upward force to slow the descent of the rocket. In order to analyze the rotor blades, different specifications, such as blade span, chord length, and airfoil type were required. The ARS subteam researched two main companies that carry three different RC helicopter rotor blade brands. The companies were Align-Trex and BK Hobbies. Align-Trex manufactures a rotor blade, called Align, that is available in blade span ranging from 550-700 mm (21.6-27.5 inches) and a chord length of 50-60 mm (2-2.4 inches), but the airfoil specifications were not specified on their website [65]. The ARS subteam contacted the company but did not receive a response. Next, the ARS subteam researched BK Hobbies, which carries Stefano Andrea Baiardi (SAB) and Switch rotor blades. The data available for the SAB rotor blades only provided information on their span, which ranged from 540-750 mm (21.3-29.5 inches) [66]. The Switch blades data provided information on their spans and chord lengths, which varied from 503-753 mm (19.8-29.6 inches) and 52-65 mm (2-2.6 inches) [67]. Unfortunately, the website did not contain information on the airfoil geometry, so the ARS subteam contacted the company, but they did not provide any useful information in their response. The website stated that their RC helicopter rotor blades were made from a NACA airfoil, but did not include the specific airfoil code [68].

The team decided to purchase the 605 mm long, 55 mm wide Switch rotor blades because the ARS subteam was most confident these would fit well within the HPMR. When the ARS subteam received these rotor blades, they analyzed the cross-section by measuring the chord length, maximum thickness and estimating the location where the maximum thickness occurs. From this data, the airfoil was determined to be similar to a NACA 0012, so the autorotation model used the lift and drag coefficient data of this airfoil for the aerodynamic analysis. The cross section of the rotor blade can be seen in Figure 61.

Figure 61: Photo showing the cross-section of the rotor blade

Before the aerodynamic analysis could be completed, certain assumptions were made to model the RC helicopter rotor blades. The ARS subteam assumed there was no blade twist and a taper ratio of one, therefore the pitch angle and chord length remained constant through the span of blade. The taper ratio is defined as the chord length of the airfoil at the tip of the wing divided by the chord length of the airfoil at the root of the wing and is used to describe the shape of the wing. With these assumptions, the rotor blades were modeled within SOLIDWORKS to find the moment of inertia of the autorotation system. After the moment of inertia was calculated, the ARS subteam had all the required information to start the autorotation blade analysis. If the analysis demonstrated that the blades did not provide sufficient forces to slow the descent of the HPMR, then the ARS subteam changed certain specifications of the recovery system such as the pitch angle or drogue parachute size. If neither of these specifications could be changed to provide a sufficiently low descent velocity of 5 m/s or less, then the team would work to design a rotor blade to provide a slower descent velocity.

If the COTS rotor blades did not slow the descent of the model rocket, then the team intended to design a customized set of rotor blades with no predetermined features. When considering designing a rotor blade "from scratch" for the autorotation system, the ARS subteam considered two main characteristics, which were the airfoil and a blade twist. With the newly found

90

information about the airfoil type, the ARS subteam used the University of Illinois Urbana-Champaign (UIUC) airfoil database to find NACA airfoils of helicopter rotor blades [69]. The team assumed that the airfoils of RC helicopter rotor blades would be similar if not the same as actual helicopter rotor blades. Six NACA airfoils were selected based on the amount of aircraft they were used on. The chosen airfoils included the NACA 0012, 0015, 13112, 23012, 230125, and 63-015.

The ARS subteam chose to analyze the Wortmann FX 69-H-098 as the airfoil for the innovative recovery system blade design. This airfoil was chosen after comparing data for its lift and drag coefficients against the other airfoils. The Wortmann was determined by the ARS subteam to be the best airfoil to use for a future analysis. The Wortmann FX 69-H-098 was designed for Bell attack helicopters, which are used by the military. It has been modified to be used for other flight vehicles, to have a camber added near its trailing edge to shift the moment of the section to zero [70]. The Wortmann FX 69-H-098 is not a traditional airfoil such as the NACA series.

If the team had more time, a non-COTS blade could have been designed; however, the Wortmann was chosen in order to gauge its performance as the airfoil for the recovery system. Using a different airfoil than the COTS NACA 0012 allowed the team to find an airfoil that could provide more lift with less drag. A comparison of the coefficient of lift (C_L) and the coefficient of drag (C_D) vs. the AOA is shown for the NACA 0012 and the Wortmann airfoils for a Reynolds number of 50,000, and varying AOA from –11 deg to 11 deg in Figure 62 (left and right). The data for this figure was gathered from the website called airfoiltools [71]. The Reynolds number of 50,000 was chosen since it was one of the available data sets from the website, airfoiltools, as well is it being within the 1,000 to 100,000 Reynolds number range.
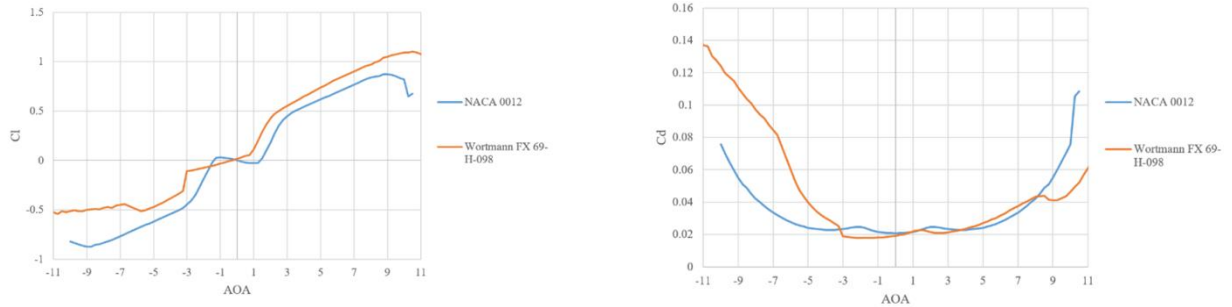
Figure 62 (left and right): NACA 0012 vs. Wortmann FX 69-H-098 for varying AOA from –11 deg to 11 deg and Reynolds number of 50,000

As can be seen in Figure 62, the Wortmann airfoil has a greater maximum and minimum coefficient of lift when compared to the NACA 0012 airfoil. The greater coefficient suggests that the Wortmann would be more useful when applied to the innovative recovery system, since a higher lift force would be produced by the airfoil. The Wortmann would be a good airfoil for the innovative recovery design due to the greater coefficient of lift that would create a greater lift force in the system, and ideally allow the recovery system to bring the rocket to a safe descent velocity. By adding a blade twist, the airfoil could perform at an AOA that provided higher lift and lower drag forces in the driven region of the blade.

2.2. Analysis

The HPMR consists of multiple, different components and sections, all essential to the success of the rocket. The ARS subteam needed to analyze various part of the rocket to ensure no components failed during flight. This section presents analysis of the airframe's stress distribution, what forces act upon the motor bay, stresses on the u-bolt bulkhead couplings, the parachute size, and a discussion of the autorotation blade model designed for the innovative model rocket. The analysis of these essential rocket components was important for understanding physics behind the construction of the rocket.

2.2.1   Airframe Stress Distribution (ARS Analysis Task 1)

The first analysis task for the ARS subteam was to determine the stress distributions on the upper and lower airframes of the model rocket. The team needed to identify critical locations of high stress throughout the airframe and internal structure during peak pressure loads caused by black powder ignitions in the airframe. In order to do this, the team used both SOLIDWORKS modeling software and ANSYS Mechanical Workbench. A transient structural simulation was conducted in ANSYS in order to simulate the impulse from the separation of the black powder charges inside the airframe. A transient structural analysis was the best option for performing this analysis since the black powder charges ignite and burn over a very short period of time.

The Propulsion, Thermal and Separation Systems subteam (PTSS), oversaw calculating the amount of black powder needed to separate the different components of the model rocket from each other, i.e. the nose cone and lower airframe. The pressure resulting from the black powder ignition was calculated to have a maximum pressure of approximately 15 psig (Refer to Section 3.1.2.1 for this calculation). Since the pressure from the ignition of the black powder creates a stress on the inside of the airframe, a static pressure load was applied to the inside of the airframes, with a fixed geometry applied to the base of both airframes. The results of this study can be seen in Figure 63 below. An ANSYS Mechanical Workbench model of both the upper and lower airframes was used to calculate the maximum von Mises stress[1] distribution that Blue Tube 2.0 can withstand at a pressure of 15 psig inside the airframe.

---

[1] The von Mises stress (or the equivalent tensile stress) is defined as the combination of the maximum stress applied on the principal axes of a structure as coordinates in a plane, an equivalent stress that can cause yielding or deformation of the structure [98]. In this application, for the calculations on the airframe of the HPMR, ANSYS calculated the maximum von Mises stress (the combination of the principal axes stress) from the pressure of 15 psig inside the airframe. This was then used in the von Mises Criterion comparing the maximum von Mises stress to the yield stress of Blue Tube 2.0. Since the von Mises stress was not larger than the yield stress, the airframe was determined to not fail or deform.

Note that due to the motor bay being in the lower airframe of the rocket, the lower airframe section that was studied to demonstrate pressure loads in ANSYS was cut to model only the part of the lower airframe above where the motor tube starts. This was because the motor tube did not experience the peak pressure from the separation charges of the black powder, therefore the analysis did not apply to that section.
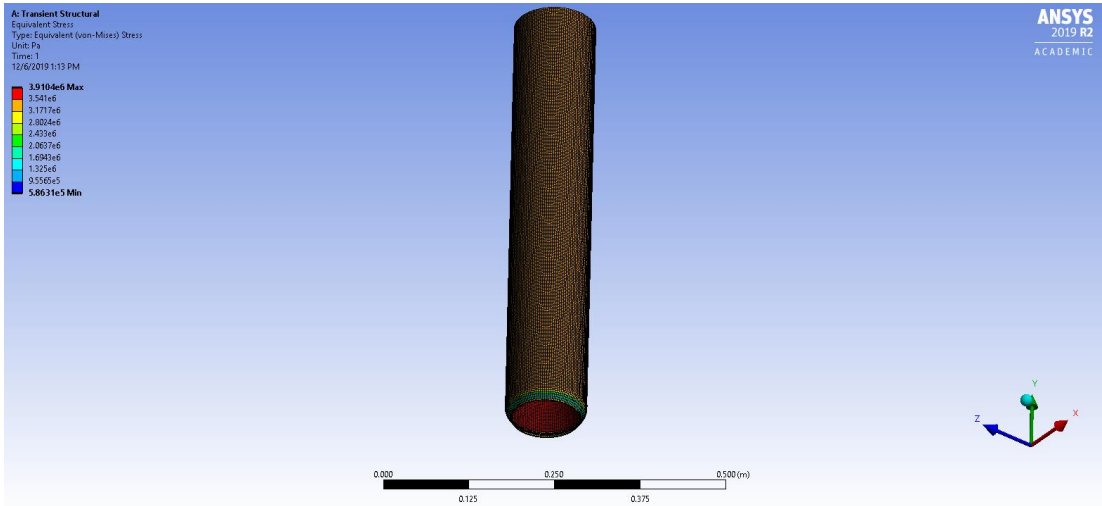
Figure 63. Upper airframe stress distribution

Colors (in the legend) correspond to the stress value in units of Pa, red being the maximum stress and blue being the minimum stress.
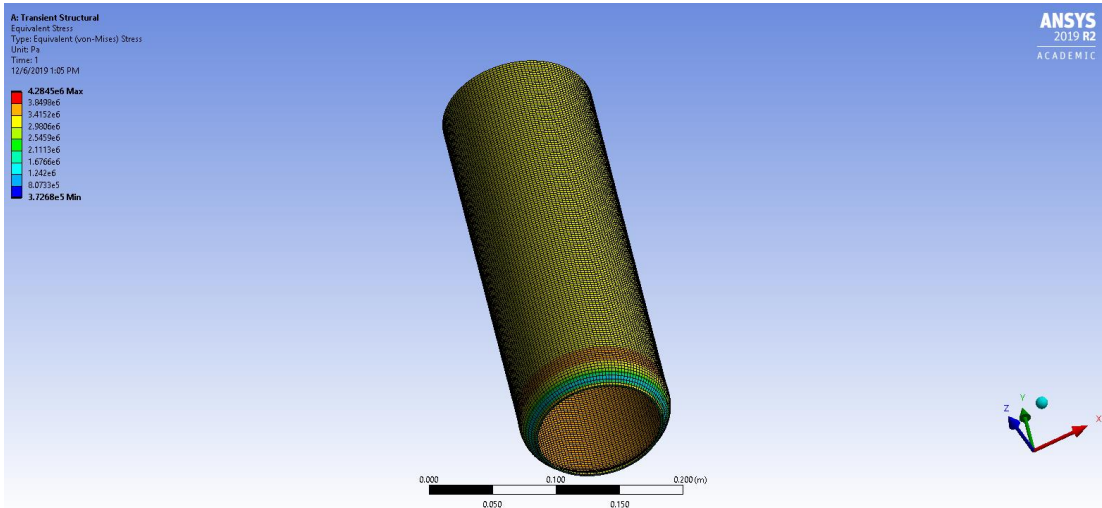
Figure 64. Lower airframe stress distribution

The purpose of this analysis task was to determine if the Blue Tube 2.0 could withstand the impulse pressure resulting from the black powder charge ignition and ensure the integrity of the blue tube during launch and ignition. Depending on the results of the study, ARS would be able to do two things:

- Determine weak points within airframe design during 1) maximum acceleration and 2) separation events
- Determine method(s) to improve structural integrity of the airframe and internal structures e.g. electronics bay and motor bay

Due to the pressure of the black powder charges being 15 psig, the stress analysis yielded results of a maximum von Mises stress on the upper airframe of 3.91 MPa and 4.285 MPa on the lower airframe. The maximum stress Blue Tube 2.0 can withstand is approximately 124.1 MPa [72], confirming that the black powder ignition will not cause deformation or damage to the airframe during launch and ignition. This analysis was critical to the structural integrity of the entire model rocket. If the airframe were to deform or explode from too great a pressure inside, then the entire system would fail, resulting in a destroyed model rocket and failed launch.

The maximum stress of the motor tube was evaluated in SOLIDWORKS using a static load to ensure that during the max thrust condition, that bulkheads would maintain structural integrity. The PTSS subteam calculated that the maximum thrust from the baseline motor was 329N (see Section 3.1.1.1). Therefore, an applied force was simulated on the bottom of the motor bay for the max thrust condition. The study yielded that the max von Mises stress on any bulkhead was approximately 1.5 MPa. The shear modulus of the plywood used in the construction of the rocket ranged from approximately 8.3 – 15.4 MPa [73]. This offers a factor of safety of at least 5, which

the ARS subteam found acceptable. Figure 65 shows the fixture points and applied force in the structural analysis software.
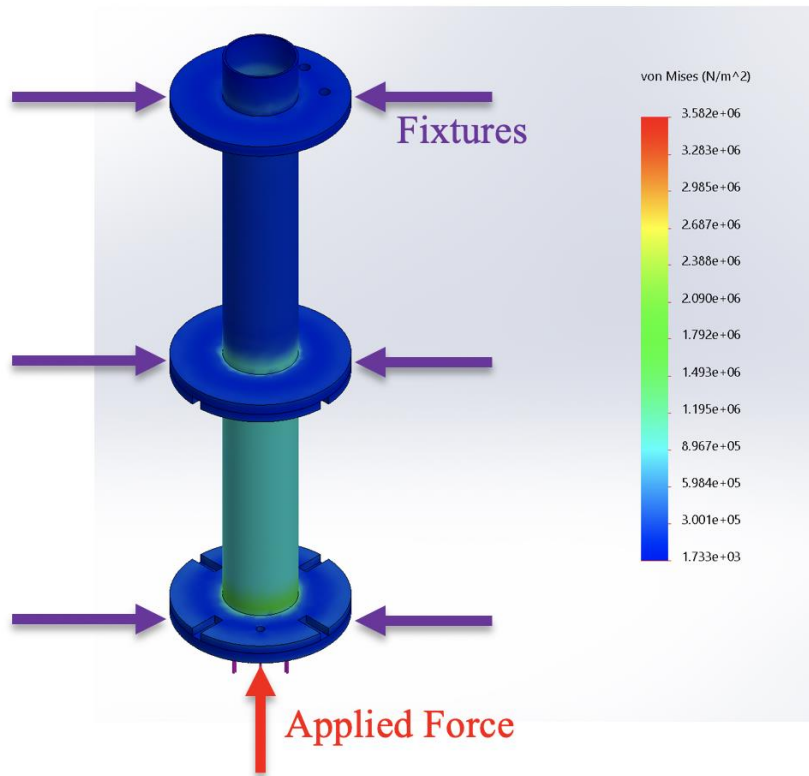
Figure 65. Motor bay structural analysis

2.2.2 Fin Analysis (ARS Analysis Task 2)

One area of the HPMR the ARS subteam found to be of structural importance were the fins. The fins are one of the most important parts of the rocket. Although ARS was not concerned with aerodynamic forces on the fins, the subteam was concerned about their structural integrity upon landing of the rocket. The fins are often the first thing to touch the ground when the rocket lands, meaning all the weight connected to the fins impacts them at one point if the surface is relatively hard. In the case of the baseline rocket, the mass attached to the fins was the lower airframe (refer to Figure 32). In order to ensure that the fins would not break if they experience a high impact force, the ARS subteam performed a structural analysis.

The required inputs for this analysis were fin geometry, material and density, landing velocity and the weight of lower airframe system. The geometry of the fin was imported in ANSYS Mechanical Workbench from a SOLIDWORKS model. Since the fins are a 3D printed structure, the density is not uniform throughout. Therefore, the ARS subteam calculated an average density by measuring the volume in SOLIDWORKS and weight of the physical part. The ARS subteam understood this is not the most accurate way to estimate the geometry of a 3D printed structure, but it was believed to be a good enough approximation. The landing velocity was calculated in Section 2.2.4 and the weight of the lower airframe was known from the SOLIDWORKS model. Therefore, the required inputs were known.

Once all these inputs were determined, the ARS subteam was able to set up an impact analysis. The fin geometry was imported into ANSYS and fixed on the fin tab. The fin tab is the portion of the fin that sits inside the rocket. Figure 66 shows the different setup conditions for the impact analysis. The fixtures remain static during the analysis and the arrows indicating the impact are where the impact load was applied. This setup is very similar to a cantilever beam.
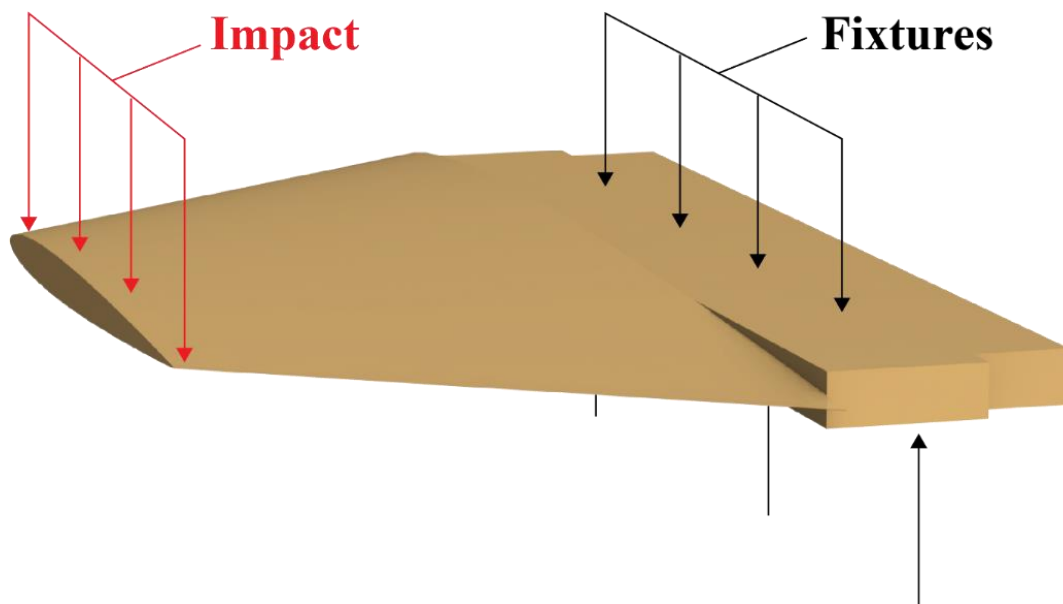
Figure 66. Fin analysis setup

To simulate the applied load, a mass equal to the lower airframe impacts the outer edge of the fin at the calculated landing velocity. The simulation used *explicit dynamics* within ANSYS for the impact. *Explicit dynamics* is used for complex geometries where there is a short-duration impact load. It is similar to *implicit dynamics* except is more compatible with complex geometries like airfoils. The airfoil geometry was unable to be solved using the implicit solver, therefore, the explicit solver was used. A similar test using *explicit dynamics* could include the response of a cantilever beam when impacted with a mass, such as the response of a diver board when a person jumps on it. In the case study of the fin stress on the rocket, the mass of the rocket attached to the fin is added as a block of mass in ANSYS, *Explicit Dynamics* Workbench. This block is then dropped at a velocity of 5 m/s, the landing velocity of the rocket. The block of mass lands on the impact location as defined in Figure 66 over a 0.1 s time period. This user input was an assumption made based on the amount of time the rocket would impact the ground when landing. This block mass distributed its load across the impact location and was analyzed for the equivalent max stress (Von Mises Stress). Figure 67 shows the result of these calculations for the fin displaying its maximum stress.
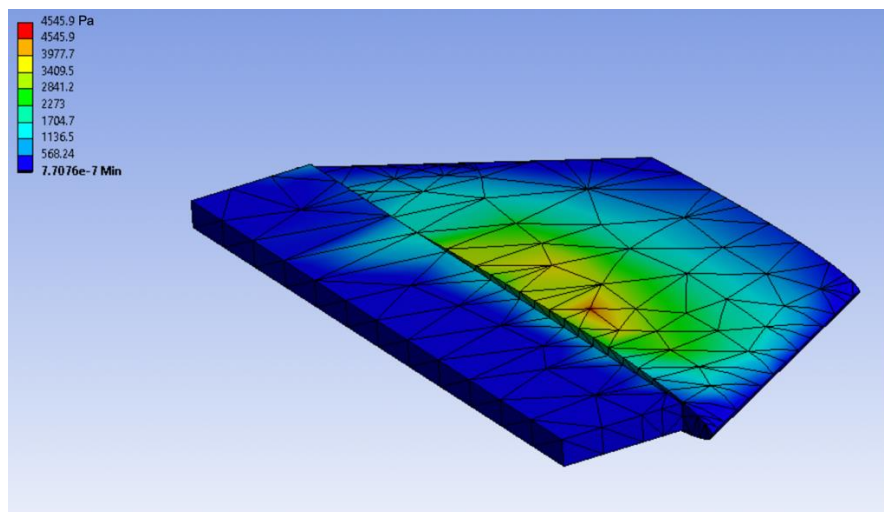
Figure 67. Fin ANSYS analysis max condition

The result of the analysis was a maximum equivalent stress of 4546 Pa. The allowable shear stress of the PLA used to print the fins was 45 MPa [74]. This means there is a factor of safety of approximately 10. The ARS subteam accepted these results, even with the approximation used for the density of the 3D printed fins.

2.2.3 Stresses on U-Bolt Bulkhead Coupling (ARS Analysis Task 3)

The parachutes were necessary for the HPMR to descend at a safe speed. They were attached to the rocket by u-bolt couplings on bulkheads within the airframe. In Figure 68, the green ovals represent the parachutes, and the couplings are located at the end of the yellow connections attached to each of the parachutes.

Figure 68. Parachutes within airframe

The parachute on the forward end of the rocket would be attached to the nose cone and payload bay. The middle parachute represents the main parachute, which is attached to the bottom of the electronics bay and was deployed last. The parachute on the aft end was attached to a u-bolt coupling on the bottom of the airframe. The purpose of this analysis was to determine that, when deployed, the u-bolt couplings on the bulkheads would not break under the force generated by the parachutes opening as the rocket is falling.

In order to calculate the forces generated by the parachutes opening, a MATLAB code was written to calculate the loads following the algorithm shown in Figure 69.
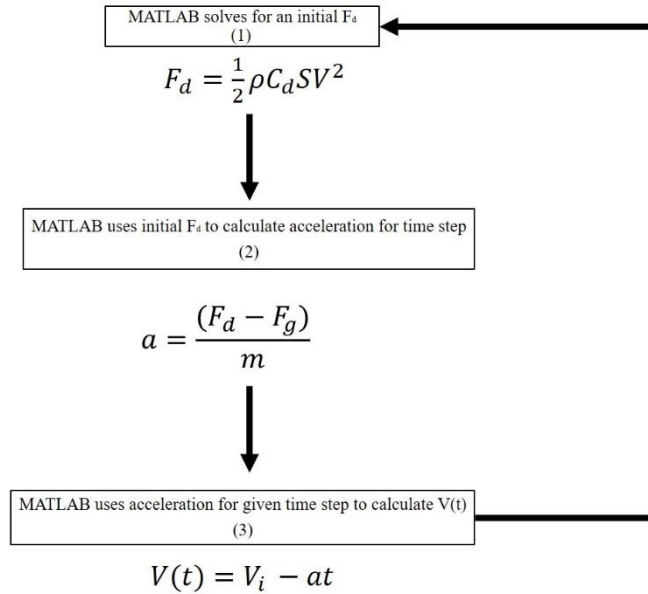
Figure 69: Algorithm used to calculate forces from parachute on bulkhead

Looking in greater detail at the flow chart, the main equation used by MATLAB in the code represents the drag force Eq. 2-1,

$$F_d = \frac{1}{2}\rho C_d S V^2 \qquad\qquad 2\text{-}1$$

In this equation, ρ is the density of air, C_d is the coefficient of drag, S is the surface area of the parachute, and V is the descent velocity of the rocket. The code solves Eq. 2-1 constantly for F_d by changing V, the descent velocity, and then updating F_d for each time step. The time steps are necessary in order to calculate the falling rocket's velocity for every time step (set to 0.01 s), which is then used to calculate a new drag force for that time step. This accounts for the deceleration of the rocket descent assuming the parachute is fully inflated and causes the rocket to slow due to drag. Assuming that the starting velocity is 49.05 m/s due to the rocket falling for 5 s before a parachute being deployed, an initial F_d is calculated, and then used in Eq. 2-2 to solve for

an acceleration for that time step by subtracting the force of gravity, and then dividing by the mass of the rocket.

$$a = \frac{(F_d - F_g)}{m}$$

2-2

That step's acceleration was then used in Eq. 2-3 to calculate the descent velocity for that time step $V(t)$. For this step, it should be clarified that the negative acceleration calculated from the previous step is opposite to the acceleration of gravity, and therefore allows the rocket to decrease velocity as time goes along.

$$V(t) = V_i - at$$

2-3

The velocity, $V(t)$, calculated in Eq. 2-3 is then substituted back into Eq. 2-1, and the process repeated using a time step of 0.01 s, up to a maximum value of 2 s, chosen to see the overall acceleration of the rocket due to the deceleration cause by the parachute. This algorithm is executed in the MATLAB code developed, shown in Appendix B. This process was used for all three parachutes in order to find the forces on all bulkheads. The initial conditions for all three parachutes are shown in Table 11.

Table 11: Initial Conditions for Bulkhead Force Calculations

Component	Parameters	Calculated Value
Nose cone	Parachute Surface Area	0.6567 m²
	Component Mass	0.69 kg
	Initial Velocity	49.05 m/s
Main Body	Parachute Surface Area	1.477 m²
	Component Mass	3.91 kg
	Initial Velocity	49.05 m/s
Lower Body	Parachute Surface Area	0.6567 m²
	Component Mass	4.70 kg
	Initial Velocity	49.05 m/s

The results generated by the MATLAB code are shown in Figure 70 through Figure 72.
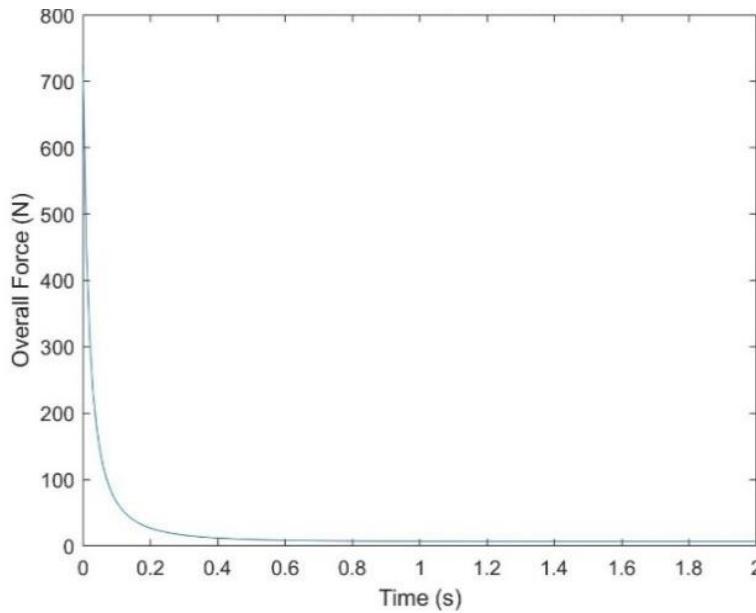
Figure 70: Force on nose cone bulkhead force vs. time
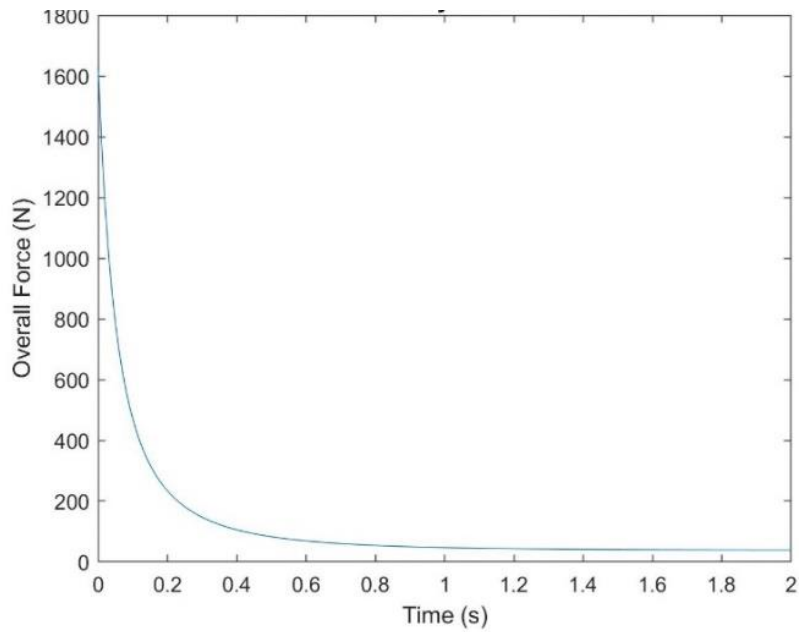
Figure 71: Force on main body bulkhead vs. time
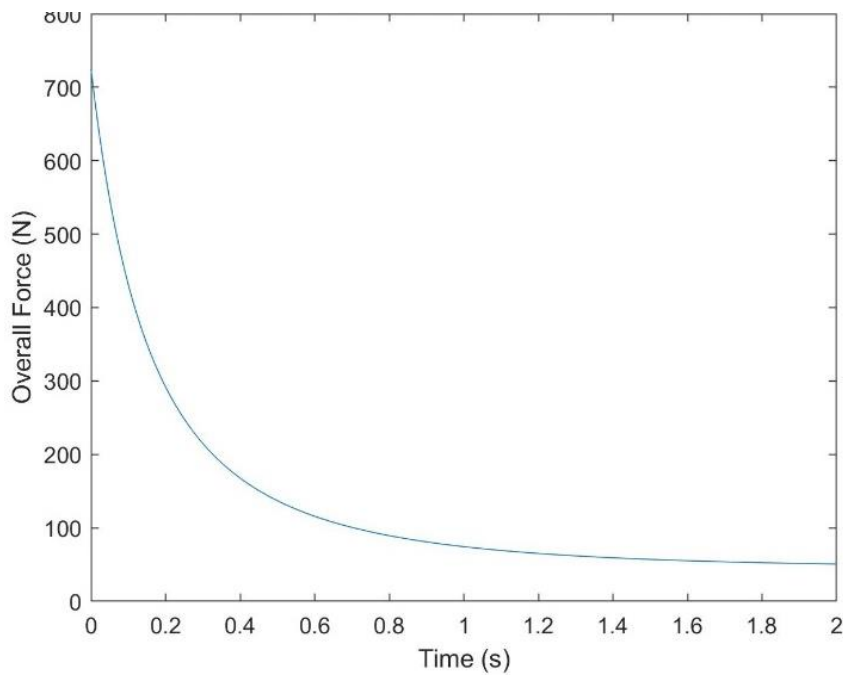
Figure 72. Force on drogue parachute bulkhead vs. time

From the MATLAB simulations, the maximum force on each bulkhead will correspond to the initial value when the fully opened parachute is assumed to be travelling at the maximum velocity. The forces displayed are overestimates of the actual forces experienced by the couplings, since the initial force used in the code assumes a freefall velocity after 5 s. However, during launch, the

drogue parachute was designed to deploy at apogee, where the velocity is at its minimum. The maximum forces, as displayed by the plots, for each of the bulkheads is displayed in Table 12.

Table 12: Calculated Forces on Bulkheads

Component	Calculated Force
Nose cone Bulkhead	700 N
Main Body Bulkhead	1600 N
Lower Body Bulkhead	700 N

These forces generated by the MATLAB code were then used in ANSYS Transient Structural simulations to find the stresses on each of the bulkheads. The transient structural analysis involves a force as a function over time and determined the response of an object under the time dependent load. Since the nose cone and lower body bulkheads were estimated to have the same force applied, they are assumed to have similar stresses on their bulkheads. Figure 73 and Figure 74 below show the distribution of stress across the bulkheads at time equal to zero.

The yield strength of the bulkheads, made from plywood, is approximately 20 Mpa (given by ANSYS), which is higher than all stresses generated by ANSYS. These simulations allowed the MQP team to have confidence that no bulkheads would break during the main flight and descent of the rocket.

Table 13: Stresses on Bulkheads

Component	Calculated von Mises
Nose cone and Lower Body Bulkheads	5.4 Mpa
Main Body Bulkheads	12.39 Mpa
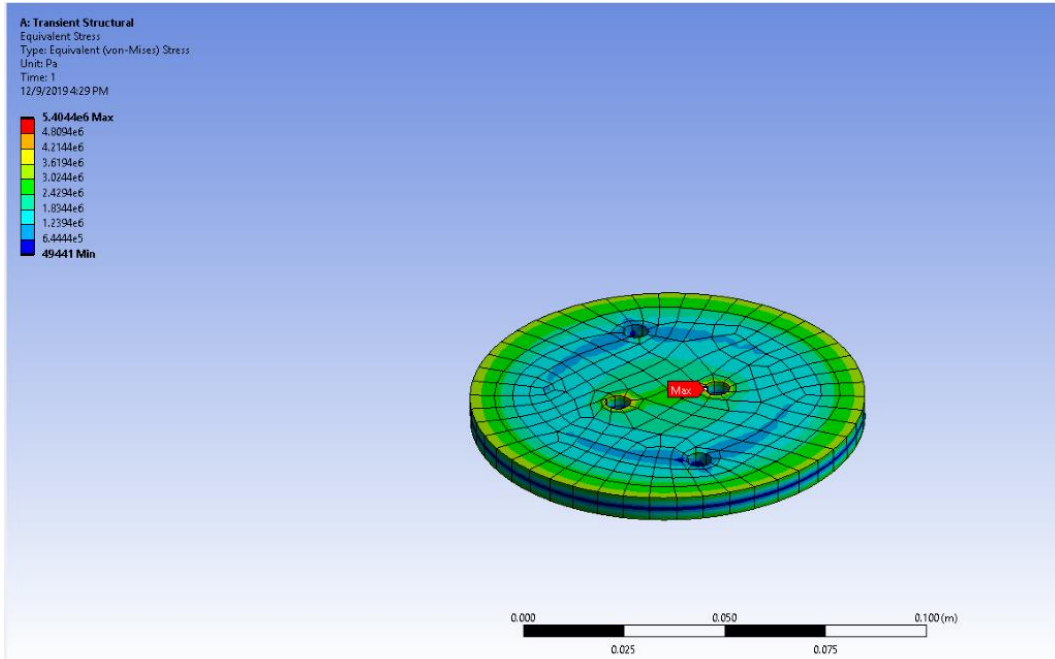
Figure 73. Von-Mises stress on nose cone and lower body bulkhead
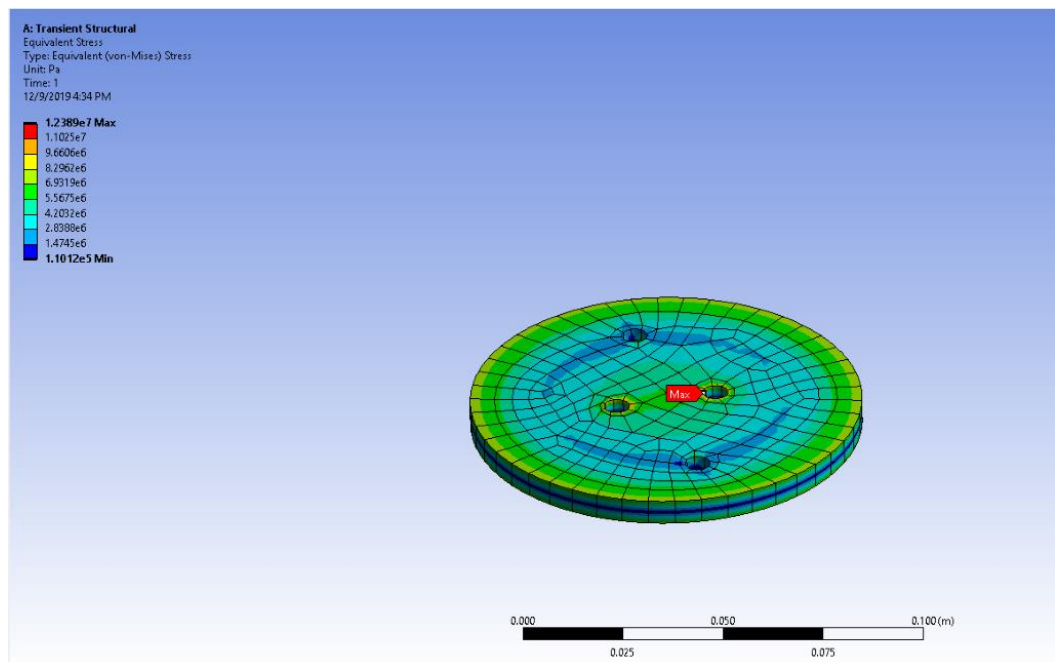
Figure 74. Von-Mises stress on main body bulkhead

The maximum stresses generated by the SOLIDWORKS simulations are shown in Table 13.

2.2.4   Parachute Sizing Model (ARS Analysis Task 4)

Selecting an adequate parachute size in order to recover the HPMR was an extremely important task. The ARS subteam decided to design a parachute recovery system with three separate parachutes. This design was chosen because there needed to be sufficient drag to recover the rocket effectively at a desired descent velocity of approximately 4.5 – 6 m/s. In the approach we selected, a drogue parachute is deployed from the lower airframe section of our model rocket. Drogue parachutes are typically smaller than the main parachutes, designed to control the descent of the model rocket, and "stabilize the rocket so that the main parachute can open without failing" [15]. Once the drogue parachute deploys, two main parachutes, one for the nose cone and one for the airframe of the rocket, deploy. The nose cone parachute is attached to a bulkhead on the inside of the nose cone, which is shown in Figure 75 as the green label in the figure. In Figure 75, the main parachute can be seen attached to a u-bolt on the electronics bay, and finally in Figure 75, the drogue parachute can be seen attached to a u-bolt in the lower airframe. The locations and size of these parachutes were critical in the design phase of the recovery system. The mass of the rocket section each parachute would recover was directly related to how large the inflated diameter needed to be. Furthermore, if the parachutes used for the recovery were too small, the model rocket would descend with a velocity too large, increasing the likelihood of damage to the rocket once it strikes the ground.

Figure 75. Main body of high-powered model rocket showing location of parachutes

The team needed to create a simplified model to estimate shape and dimensions of the drogue and main parachutes to insure an acceptable landing velocity. Using MATLAB software, the team was able to calculate the required inflated diameter sizes for three parachutes needed for the safe recovery of the rocket. Required inputs for this analysis were the rocket mass and airframe geometry at different stages of separation during launch. The code for this calculation can be seen in Appendix C and calculated the required inflated diameters of three parachutes: a drogue parachute, nose cone parachute, and main body parachute. To calculate the required diameter of the inflated parachute, the drag force must be related to the area and velocity [75]. The force of wind resistance is given by

$$F_D = \frac{1}{2}\rho C_d A V^2$$
2-4

The team then substituted the above equation into Newtons Second Law. This results in

$$mg = \frac{1}{2}\rho C_d A V^2$$
2-5

Next, the area of the inflated parachute was solved for.

$$A = \frac{mg}{\frac{1}{2}\rho C_d V^2}$$
2-6

Furthermore, it is known that the equation for the cross-sectional area of a parachute is

$$A = \frac{\pi D^2}{4}$$
2-7

The inflated diameter of the parachutes needed to recover the HPMR were then found by substituting 2-6 into 2-7and solving for the inflated diameter. in the diameter is then given by

$$D = \sqrt{\frac{8m_s g}{\pi C_d \rho V^2}}$$

2-8

With respect to the geometry, the parachute is assumed to be a perfect hemisphere when inflated [104]. The team assumed a coefficient of drag of 0.75 [76] for this calculation. In Eq. 2-8, m_s is the mass of the system, g is the gravity of Earth, C_d is the drag coefficient of a standard parachute, ρ is the density of air, and V is the descent velocity of the model rocket.

Prior to executing this code, the following assumptions were made:

- C_d for a standard, hemispherical parachute is between 0.75 - 0.8[104] [77]

- For a drogue parachute, the initial descent velocity is 15 m/s

- For a main parachute, the desired recovery velocity is 5 m/s

Table 14 summarizes results generated from the MATLAB parachute sizing code.

Table 14: Properties of the Drogue, Nose cone, and Main Parachutes

Parachute Component	Mass of the System	Required Inflated Diameter
Drogue Parachute	4.70 kg	0.76 m = (29.7 in)
Nose cone Parachute	0.79 kg	1.03 m = (40.5 in)
Main Parachute	2.55 kg	1.9 = (72.9 in)

From the data in Table 14, both the drogue and nose cone parachutes can have a significantly smaller inflated diameter than the main parachute. When analyzing the calculations for this analysis, the ARS team needed the drogue parachute to deploy and cause the HPMR to descent at an initial rate 15 m/s. The drogue parachute's function was to slow the HPMR's initial descent

108

after reaching apogee, allowing time for the nosecone and main parachutes to deploy. Furthermore, since the drogue parachute was slowing down the HPMR's entire mass, the drogue parachute needed to slow the rocket's descent velocity in order to ensure that the nosecone and main parachutes would not be destroyed once they were deployed. Therefore, as can be seen in Table 14, the drogue parachute's desired size was calculated to be 29.7 in order to slow down the model rocket upon deployment and have an initial descent of 15 m/s. However, the ARS subteam decided on a 36 in drogue parachute. The subteam could have purchased a parachute that was closer to 29.7 in, but the team agreed through further analysis that a 36 in drogue parachute would still allow the rocket to descend at have an adequate initial descent velocity close to 15 m/s, specifically 12.37 m/s. Furthermore, though 40.5 in was a desired parachute size for the inflated diameter of the nose cone parachute, the ARS subteam concurred that a 36 in parachute would suffice for this application for the same reasons as the drogue parachute. When it came to the calculation of the size of the main parachute, ARS subteam calculated a 72 in inflated diameter, and was able to use that sized parachute as we had one in stock. The main parachute allowed for the HPMR to be recovered at the desired velocity of 5 m/s. The drogue parachute and the main parachute were connected to the upper and lower airframe of the HPMR through a u-bolt on the main bulkheads.

2.2.5   Autorotation Blade Model (ARS Analysis Task 5)

Once the autorotation recovery system was designed, an aerodynamic and kinematic analysis was performed to determine whether it provided a sufficient force to slow the descent of the HPMR. The ARS subteam used a MATLAB and Fluent model to evaluate whether commercially available RC helicopter rotor blades were sufficient to use for the autorotation system.

2.2.5.1 MATLAB model

The model used aerodynamic and kinematic equations to describe the motion of the rocket during descent, which is comprised of the altitude and velocity from apogee to landing. After the rocket reaches apogee, it would freefall for about 3s before the parachute fully deployed from motor ejection charge. About 10s later, the autorotation recovery system was deployed. This time was selected to give the parachute ample time to stabilize and orient the rocket vertically. In order to model the descent of the HPMR, the velocity and height of the rocket were calculated for three segments: freefall, drogue parachute descent, and the parachute with autorotation descent. Also, free body diagrams (FBD) of the blade and cross-section of the blade were created to standardize a coordinate system and to better understand the relationship between the aerodynamic forces and air velocities. These FDBs are provided in Figure 76 and Figure 77.
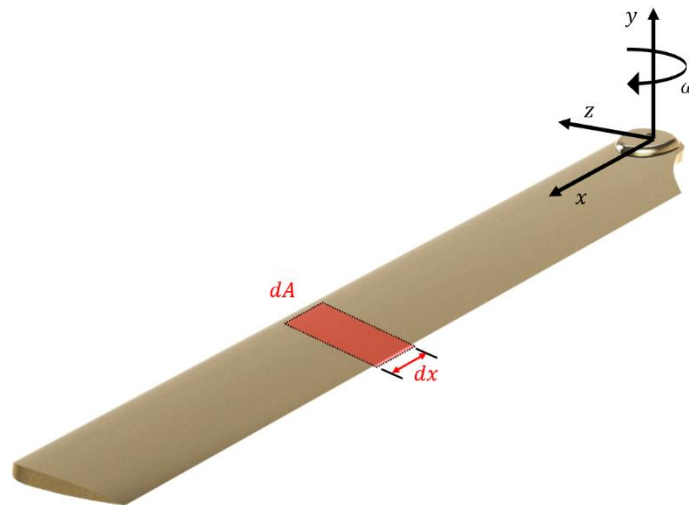
Figure 76: Diagram of the coordinate system of the rotor blade
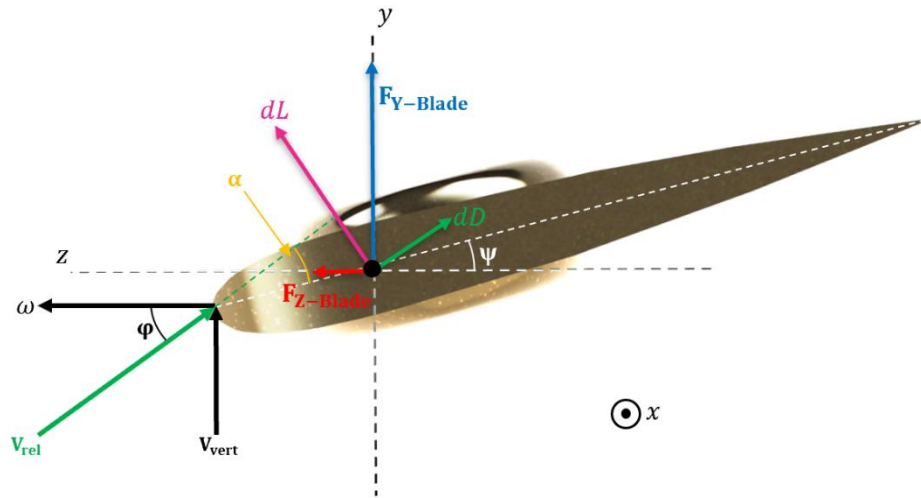
Figure 77: Free-body diagram on the cross-section of a rotor blade

The freefall descent calculation involved using the basic kinematic equations of motion for velocity and height, Eqs. 2-9 and 2-10. The initial conditions at apogee were assumed to be 0 m/s and at an altitude of 640 m. Since the rocket is in freefall, the only force acting on the rocket is gravity. Drag on the rocket was ignored. Therefore, the rocket was accelerating downward at 9.81 m/s^2. These values were used in the equations of motion to determine the distance traveled during freefall and velocity before parachute deployment.

$$V = V_0 + a_y t \qquad\qquad\qquad \text{2-9}$$

$$h = h_0 + V_o\, t + \frac{1}{2} a_y\, t^2 \qquad\qquad\qquad \text{2-10}$$

The values of the height and velocity at the end of freefall were the initial conditions used in the equations of motion for the when the drogue parachute was deployed. When the parachute was deployed, the drag force caused a decrease in the downward acceleration. The new acceleration,

111

calculated in Eq. 2-11, results from summing the forces in the vertical direction. We ignored any rotation of the rocket or parachute about the X and Z axes, which would have caused the drag force to have multiple components.

$$a = \frac{F_{Drogue}}{m} - g \qquad \text{2-11}$$

The drag force due to the parachute is calculated using Eq. 2-4, from Section 2.2.4, using the descent velocity of the HPMR. Since the descent velocity is time dependent, the model needed to account for time varying velocity. The velocity and height of the rocket were calculated for a 10 s recovery period with a parachute using Eqs. 2-9 through 2-11 with a time step of 0.1 s. The height and velocity at the end of this period are then used as the initial conditions for the start of the autorotation system at the time of deployment. When the autorotation system is deployed, the aerodynamic forces were analyzed to determine their effects on the rotation of the rotor blades and descent of the rocket.

During the descent of the autorotation system, the rotor blades experience different wind velocities that affect the lift and drag of the rotor blades. The wind-induced lift and drag forces are given by Eqs. 2-12 and 2-13.

$$L = \frac{1}{2}\rho A C_l V^2 \qquad \text{2-12}$$
$$D = \frac{1}{2}\rho A C_d V^2 \qquad \text{2-13}$$

The two wind velocity components acting on the autorotation system includes the upward wind velocity due to the descent of the rocket and the wind velocity caused by the rotation of the rotor blades. The upward wind velocity is equal but opposite of the descent velocity of the rocket.

Since the descent velocity varies with time, the model also needed to account for a time varying velocity. The relative wind velocity caused by the rotation of blades varied along the span of the rotor blades due to the angular velocity of the blades. As a result, the linear velocity of the oncoming wind from the rotation of the blades is a function of the angular velocity times the distance from the root of the rotor blade (the origin of the coordinate system) to some point x along its span. The coordinate system of the rotor blade is demonstrated in Figure 76. Since relative rotational wind velocity varies along the span of the blade, the model took this into account when calculating the relative wind velocity for the lift and drag forces. In order to analyze the effects of these two velocity components on the forces of the autorotation system, they were combined to find the resultant relative wind velocity, shown in Figure 77.

The descent velocity was assumed to be perfectly vertical along the y-axis while the wind velocity from the rotation of the rotor blades was assumed to be perfectly horizontal along the z-axis, so the Pythagorean Theorem was used to obtain the relative wind velocity in Eq. 2-14. The angle of the relative wind velocity (φ), measured with respect to the magnitudes of the descent and relative rotational velocity, so it was determined from geometry as seen in Eq. 2-15.

$$V_{rel} = \sqrt{(\omega x)^2 + (V_y)^2} \qquad \text{2-14}$$

$$\varphi = arctan\left(\frac{V_y}{\omega x}\right) \qquad \text{2-15}$$

The relative wind velocity and angle was calculated along the entire span of the rotor blade since they are functions of the spanwise coordinate, x. These values were calculated every differential section, dx, of 0.01 m across the entire rotor blade. To calculate the lift and drag forces on the rotor blades the lift and drag coefficients need to be determined. These coefficients are

113

functions of the velocity and AOA, so the AOA needed to be calculated. The angle of the relative wind velocity is equal to the sum of the AOA (α) and pitch angle (Ψ), as seen in Figure 15. Therefore, the AOA was calculated using Eq. 2-16.

$$\alpha = \varphi - \Psi \qquad\qquad \text{2-16}$$

Once the AOA and relative wind velocities were determined, the lift and drag coefficients were calculated using quadratic equations created using a MATLAB built function, called *fit*, and data from XFLR5 for the selected rotor blade airfoil. When calculating the lift and drag coefficient data for the rotor blade airfoil, XFLR5 requires that a Reynolds number and range of the AOAs be input into the program. The equation to calculate the Reynolds number is provided by Eq. 2-17 below. In the equation, chord length (C) and the air dynamic viscosity (μ) are required to find the Reynolds number. The air dynamic viscosity was determined to be $1.789 \cdot 10^{-5}$ Ns/m for sea level conditions [78].

$$Re = \frac{\rho V_{rel} C}{\mu} \qquad\qquad \text{2-17}$$

The Reynolds number equation is a function of the relative wind velocity, therefore it changed with both time and along the span of the rotor blade. The model needed to account for the changing Reynolds numbers when calculating the lift and drag coefficients. In order to do this, the model incorporated three ranges of Reynolds numbers: high, medium, and low. These ranges were determined using estimates of different Reynolds number under for various descent conditions. If the HPMR had a relative velocity of about 1 m/s, the case where the autorotation is deployed around apogee, then the Reynolds number would be about 3,800. For a case where the autorotation system is deployed after three second of free fall, the Reynolds number is about 100,000. Using

these two estimates, the ranges of the Reynolds numbers were created: 1,000-10,000 with increments of 1,000; 10,000-100,000 with increments of 10,000, and 100,000-1,000,000 with increments of 100,000. These ranges were assumed to provide enough data for the model because a 1,000,000 Reynolds number equates to a relative wind velocity of about 265 m/s or a Mach number of 0.77, which the tip of the of the rotor blade will not exceed. Next, the lift and drag coefficients for these Reynolds number ranges at AOAs from -5 to 25 deg were calculated in XFLR5. The data sets from these simulations were input into the MATLAB model where the coefficients were selected based on the calculated the Reynolds number for each differential section of the rotor blade. This data was used to create a curve fit function that calculate the lift and drag coefficients for AOA at the differential section of the rotor blade.

Additionally, the differential section of the rotor blade was tested to determine if it was stalled. It will experience stall conditions if the AOA is greater than the critical AOA for its Reynolds number. The critical AOA is the maximum AOA of the lift coefficient curve versus AOA. To calculate the critical AOA, the lift coefficient curve fit function was differentiated, set equal to zero, and solved for the AOA. If the AOA of the differential section of the rotor blade was higher than the critical AOA, then the autorotation model creates curve fit functions created from stall lift and drag coefficient data. The AOA of the differential section of the rotor blade is then input in the curve fit function to calculate the lift and drag coefficient.

Using these coefficients, the lift and drag forces are calculated along a spanwise element of the rotor blade using Eqs. 2-18 and 2-19, which are very similar to Eqs. 2-12 and 2-13. The main differences are that these equations find the lift and drag for a differential section of the rotor blade. The differential lift and drag forces are calculated across the entire span of the blade. In order to calculate these forces, the density of air was assumed to be a constant 1.225 kg/m^3, (corresponding

to a temperature and pressure of 15°C and 0.1013 MPa respectively).The value of the area (dA) is the chord length times the differential length of the rotor blade (dx) as seen in Eq. 2-20. After the lift and drag forces were calculated, the rotation of the rotor blades and descent of rocket needed to be analyzed.

$$dL = \frac{1}{2}\rho(dA)C_l V_{rel}^2 \qquad \text{2-18}$$

$$dD = \frac{1}{2}\rho(dA)C_d V_{rel}^2 \qquad \text{2-19}$$

$$dA = C \cdot dx \qquad \text{2-20}$$

To analyze the descent of the rocket, its acceleration was calculated by summing the forces acting on it in the vertical direction. Eq. 2-21 represents the net acceleration of the rocket. Within this equation, the variable n is the number of blades on the autorotation system and $F_{y-Blade}$ is the total vertical force along the y-axis produced by one rotor blade. The value for $F_{y-Blade}$ is calculated in Eq. 2-22 by summing the vertical components of the lift and drag forces across the span of rotor blade.

$$a_y = \frac{F_{Drogue}}{m} + \frac{nF_{y-Blade}}{m} - g \qquad \text{2-21}$$

$$F_{y-Blade} = \sum_{X=0}^{b} dL\cos(\alpha) + dD\sin(\alpha)\,dx \qquad \text{2-22}$$

Once the acceleration is calculated, Eqs. 2-9 and 2-10 are used to compute the velocity and height of the rocket. Next, the rotation of the blades is analyzed. Since there was no motor or other device rotating the rotor blades, only the horizontal component of the aerodynamic forces along the z-axis causes them to rotate. These horizontal components are used to calculate the torque on the blades, which in turn is used to find their angular velocity. The torque is calculated through

Eq. 2-23, which sums all the torques along the span of the rotor blades. The torque along the span of the blade is the distance x from the root of the point force times the aerodynamic force, which is Eq. 2-24. The torque is then used to find the angular acceleration ($\dot{\omega}$) of the rotor blades through Eq. 2-25 and the moment of inertia (I) of the autorotation system.

The moment of inertia of the autorotation system was calculated using the SOLIDWORKS model shown in Figure 57 and Figure 58. The model incorporated the nose cone, bulkheads, rotors, and other hardware. The lower half of the rocket was not taken into account when calculating the moment of inertia because the bearings within the autorotation system, demonstrated in Figure 59, were assumed to prevent it from rotating during descent. The SOLIDWORKS mass properties function was used to calculate the moment of inertia. The angular velocity is calculated using Eq. 2-26 and the angular acceleration.

$$\tau = n \sum_{X=0}^{b} x dF_{z-Blades} \qquad \text{2-23}$$

$$dF_{z-Blade} = dL\sin(\alpha) - dD\cos(\alpha) \qquad \text{2-24}$$

$$\tau = I\dot{\omega} \qquad \text{2-25}$$

$$\omega = \omega_o - \dot{\omega}\,dt \qquad \text{2-26}$$

Since the model is time dependent, a small-time span of 0.1 s is used in the descent velocity, height, and angular velocity calculations. The aerodynamic and motion analysis is iterated until the height of the rocket equaled zero. After each iteration, the calculated descent velocity, height, and angular velocity is used as the initial conditions for the next iteration. A MATLAB Code, provided in Appendix D, was used to perform the iterative process of the autorotation blade

analysis. A flow chart for the iteration process can be seen in Figure 78 and the nomenclature used within these equations is provided in Table 15.
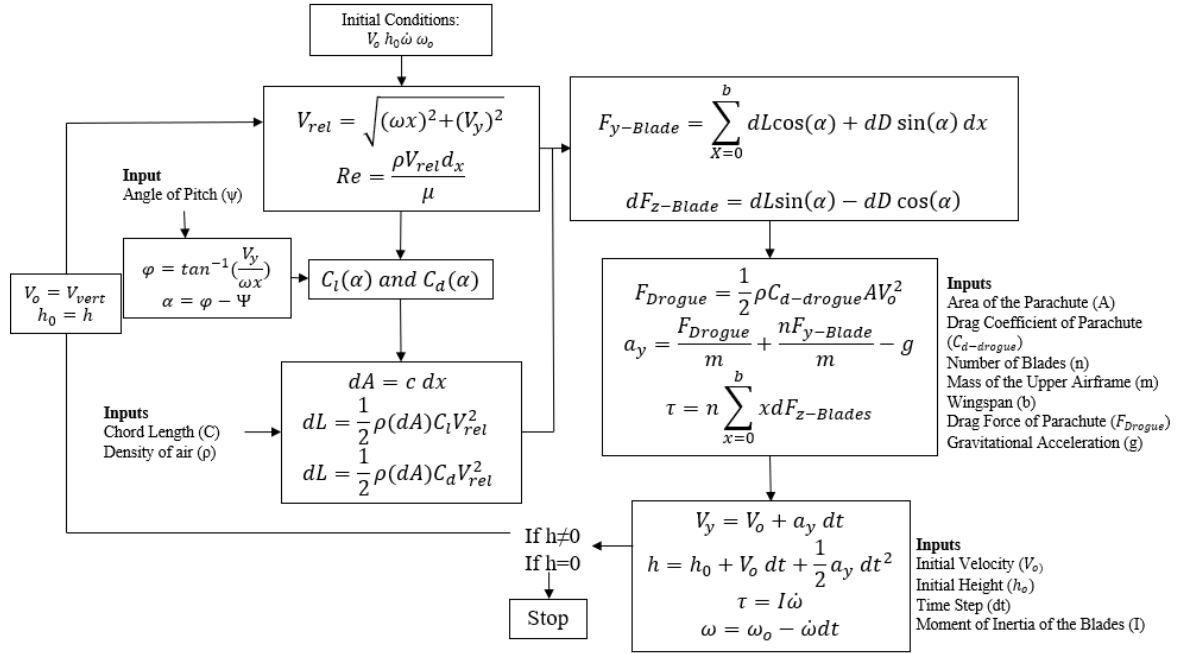
Figure 78: Flow chart for autorotation blade model

Table 15: Nomenclature and Units for the Autorotation Blade Model

Variable	Parameter	Units
V	Velocity	m/s
V_o	Initial Velocity	m/s
a	Acceleration	m/s^2
h	Height of the Rocket	M
h_0	Initial Height of the Rocket	M
F_{Drogue}	Drag Force of the Drogue Parachute	N
m	Mass of Rocket	Kg

g	Gravitational Constant	m/s^2
x	Distance from the root of the rotor blade to a point along the blade	M
ω	Angular Velocity of rotor blades	Rad/s
V_{rel}	Relative Wind Velocity	m/s
φ	Angle of Relative Wind Velocity d	Rad
ρ	Density of Air	Kg/m^3
dA	Differential Area of the Blade	m^2
C	Chord length	M
dx	Deferential Length of the Blade	M
C_l	Lift Coefficient	-
C_d	Drag Coefficient	-
$F_{y-Blade}$	Total Vertical Aerodynamic Force on the Blade	N
τ	Torque of the Blades	N m
b	Blade Span	M
$dF_{x-Blade}$	Deferential Horizontal Aerodynamic Force Along the Blade	N
n	Number of Blades	-
α_τ	Angular Acceleration	Rad/s^2
I	Moment of Inertia	kg m^2
ω_o	Initial Angular Velocity	Rad s^2
dt	Time Step	S

The purpose of the autorotation model was to estimate the aerodynamic forces of the recovery system in order to determine its effects on the descent velocity of the rocket. Once the autorotation model was completed, it was used to investigate four different cases. These cases

included recovery with no drogue parachute, and a 1, 2, and 3-foot diameter drogue parachute. All other conditions were assumed to be unchanged throughout each analysis and are provided in Table 16.

Table 16: Parameter values assumed for each autorotation analysis case

Variable	Value
Pitch angle	5 deg
Initial height	731.5 m
Initial velocity	0 m/s
Initial acceleration	-9.8 m/s^2
Moment of inertia	0.0944 kg/m^3
Airfoil	NACA 0012
Free fall time	3 s
Drogue parachute time	10 s
Coefficient of drag for parachute	0.75
Initial angular acceleration of rotor blades	0 rads/s^2
Initial angular velocity of rotor blades	0 rads/s

The first case evaluated whether the autorotation system, by itself, was able to slow the HPMR enough to an acceptable landing velocity. The autorotation system landed at 6.86 m/s after 100 seconds. The descent data is provided within Figure 79 and Figure 80. This analysis was to test the autorotation system alone. It is not an accurate representation of the descent of the HPMR with only the autorotation system because the model assumes that the autorotation system was oriented perpendicularly to the downward descent velocity. In reality, the autorotation system would have to correctly orient itself upon deployment.
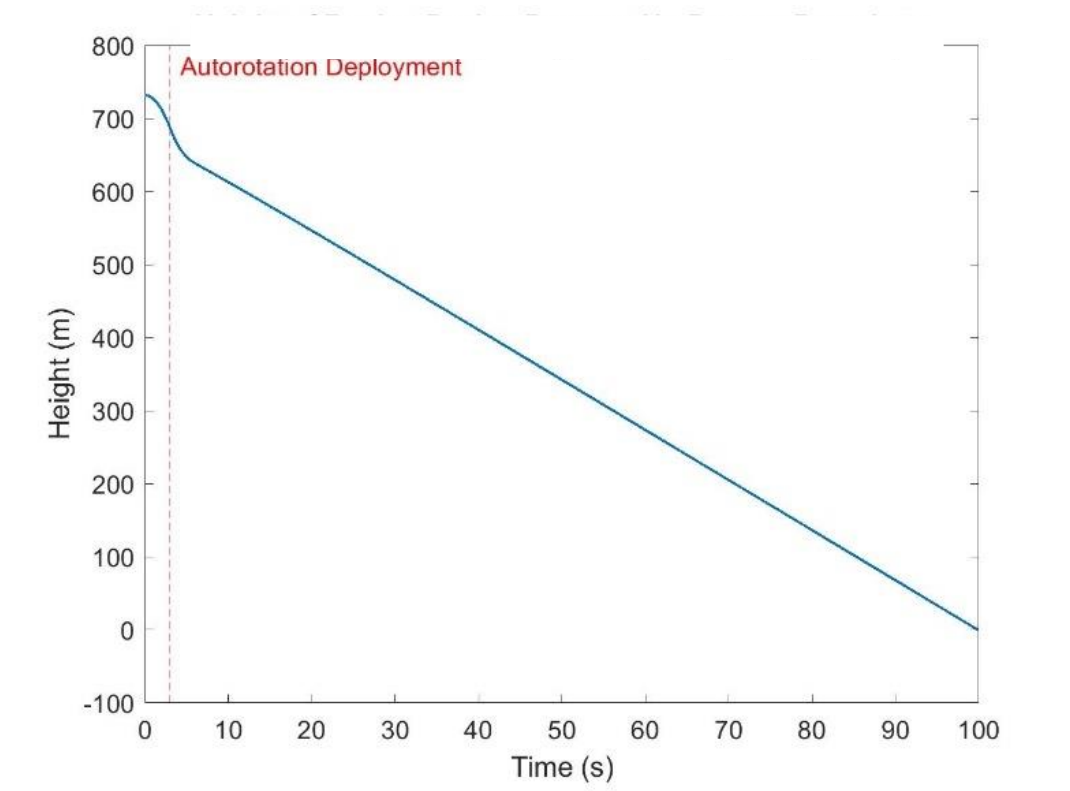
Figure 79: Height of the HPMR without a drogue parachute
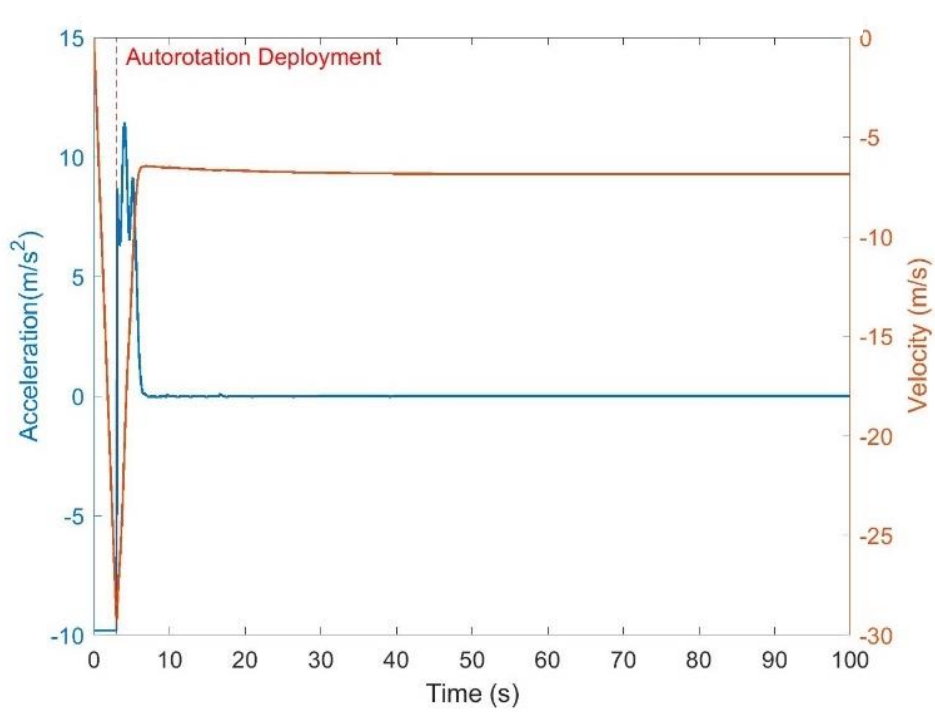
Figure 80: Acceleration and velocity during descent without a drogue parachute

When the autorotation recovery system was deployed it created an initial positive acceleration of 8.4 m/s^2, then it rapidly decreased and increased multiple times. The rapid change in the vertical acceleration was caused by the increasing angular acceleration of the rotor blades. When the autorotation system was deployed, it was assumed that the rotor blades fully deployed with no initial angular velocity and acceleration. The aerodynamic forces acting on the rotor blades upon deployment caused the HPMR to initially experience a positive vertical acceleration of 8.4 m/s^2. As the rocket descended, the rotor blades began to rotate, which changed the lift and drag forces acting on the rotor blades. As the aerodynamic forces changed, the vertical acceleration of the rocket changed, too.

This rapid change in the vertical acceleration created two minimum and three maximum points. After the initial positive acceleration, the acceleration curve immediately started to decrease due to the decrease in the AOA. As the rotor blades of the autorotation system increases in angular velocity, the relative rotational wind velocity increases, which causes the AOA to decrease. This relationship was expected from Eq. 2-15. Therefore, as the blades begin to spin, the AOAs decrease from their initial high stall angle of 85 deg. Also, the initial AOA of 85 deg was greater than the critical AOA, so the blades experienced stall conditions. As discussed previously in this section, the critical AOA is the angle where the coefficient of lift versus angle reaches a maximum. If the airfoil experiences any angles greater than the critical AOA, then the airfoil becomes experiences stalled conditions. When the model determines the airfoil of the rotor blade is stalled, then the stalled lift and drag coefficients, seen in Figure 81, were used to calculate the lift and drag. Under the stalled conditions, there is a significant decrease in the lift force and increase in the drag force. When a NACA 0012 is stalled and AOA decreases, the lift coefficient

increases while the drag coefficient decreases, which is demonstrated by the lift and drag coefficient curves in Figure 81.
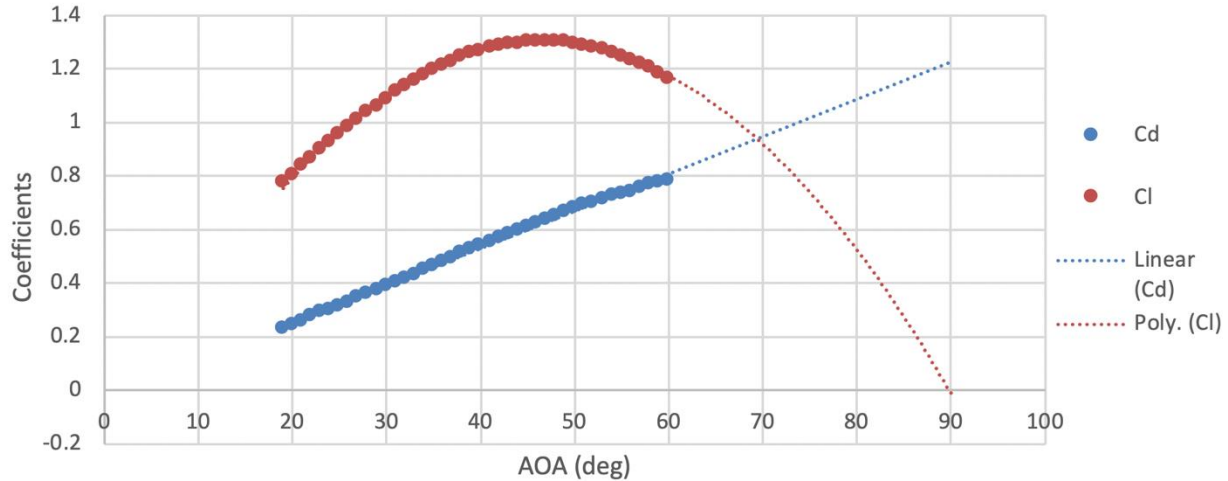
Figure 81: Lift and drag coefficient curve fit functions for a NACA 0012

As the rotor blades continued to increase in angular velocity, the AOA decreased across its span. These changes caused the lift force to increase and drag force to decrease. Eventually, when the blade experienced AOAs that were about 68 deg or less, the total force along the y-axis started to increase, which caused the acceleration to increase as well. At about 3.5 s, the rotor blade experienced various AOAs along its span that were 68 deg or lower, therefore the acceleration increased causing one minimum point as demonstrated in Figure 80. The AOAs continued to decrease with time while remaining under stall conditions. Eventually, the AOAs reach the maximum lift coefficient at about 47 deg, which is shown in Figure 80. At this point, the decreasing AOA caused the lift coefficients to decrease. When the lift coefficients along the span of the blade start to decrease, the lift force decreases causing a decrease in the acceleration, which created a maximum point at 4.1 s. The curve fit functions for the stall lift and drag coefficients of the NACA 0012 created the first maximum and minimum points within the acceleration plot. The second

123

maximum and third minimum points were caused by the transition from stalled to idea airflow. Ideal airfoil is the condition where the airfoil does not experience turbulent airflow. This transition occurred when values of the AOA along the span of the rotor blade decreased below the critical AOA, which was 12.7 deg. When the blade transitioned into an ideal airflow, the lift coefficient increased, therefore causing an increase in the total vertical force and acceleration. Similar to the first minimum point, this increase in acceleration led to a minimum point at 4.7 s. After the third minimum point, the AOA continued to decrease. Eventually, the majority of the blade experiences AOAs less than the critical AOA, so lift coefficient began to decrease. When the lift force of the blades decreased, it created the third maximum point at 5.2 s. These points all occurred within 1.7 s of each other, which meant that the rotor blades had a high angular acceleration that caused the rotational wind velocity to rapidly increase and decrease the AOA.

Case 2 was performed on the autorotation recovery system with a 1 ft drogue parachute attached to it. The graphs of the descent characteristics are shown in Figure 82 and Figure 83. The landing velocity of the HPMR was 6.65 m/s and it had a descent time of 66.1 s. Both graphs display the parachute and autorotation deployment. The landing velocity for Case 2 was 0.2 m/s higher than for Case 1, so the 1 ft parachute did not help decrease the landing velocity.

When the parachute was deployed in the model, it decreased the acceleration to about zero. Even though the parachute decreased the acceleration, the acceleration was still in the negative y-direction, therefore the velocity continued to increase in the negative y-direction. When the autorotation system was deployed, it provided an initial acceleration of 21.24 m/s in the positive y-direction. This positive acceleration decreased the descent velocity. Similar to the results from Case 1, the acceleration of autorotation system with a 1 ft drogue parachute had three maximum and two minimum points due to the increasing and decreasing lift coefficient. These minimum
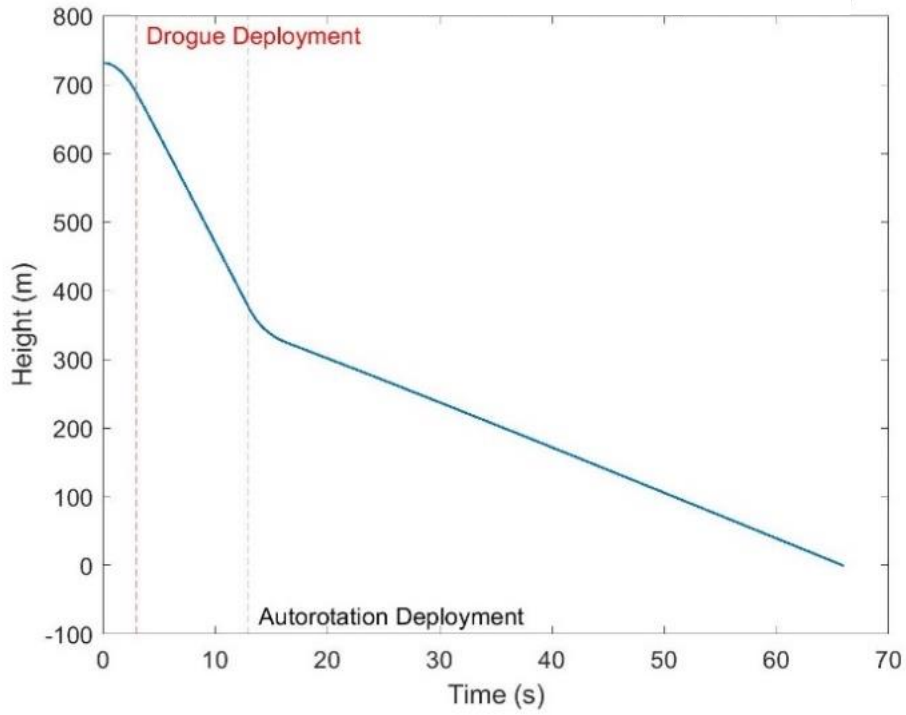
Figure 82: Height of the HPMR with a 1 ft drogue parachute
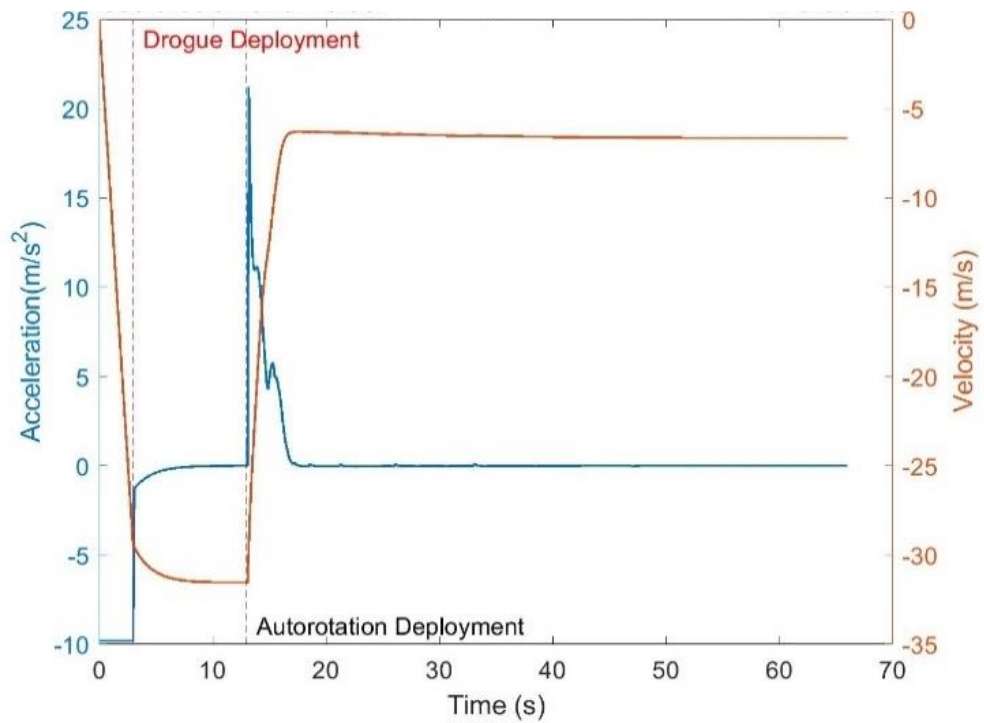
Figure 83: Acceleration and velocity of the HPMR with a 1 ft drogue parachute

points occurred at 13.7 and 14.9 s. The three maximums occurred at 13.2, 14, and 15.3 s. These points were all within 2.1 s, which were slightly greater than Case 1 due to a slightly lower angular acceleration.

The analysis for Case 3 involved determining the effects of using a 2 ft drogue parachute with the autorotation recovery system. Surprisingly, the landing velocity was significantly higher than first and second analysis with a velocity of 9.55 m/s. The total descent time was 66.8 s. The reason this combination of recovery systems produced a higher landing velocity was that the drogue parachute provided an initial positive acceleration along the y-axis, which decreased the descent velocity of the rocket, unlike the 1 ft parachute in the second analysis. When the autorotation system was deployed, the lower descent velocity was unable to produce a high lift and drag force to create a large positive acceleration along the y-axis nor did it provide a large horizontal force to accelerate the rotation of the rotor blades. This caused a slower rotational velocity and lower rotational wind velocity, which meant the AOAs remained higher. The higher AOAs caused the rotor blades to be stalled for the entire descent. Therefore, the acceleration graph in Figure 85 only has one maximum and minimum point unlike the acceleration for Case 1 and second Case 2.
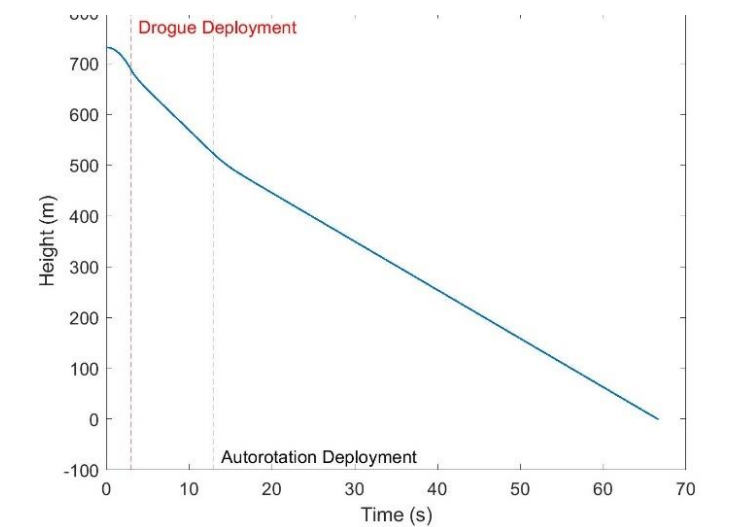
Figure 84: Height of the HPMR with a 2 ft drogue parachute
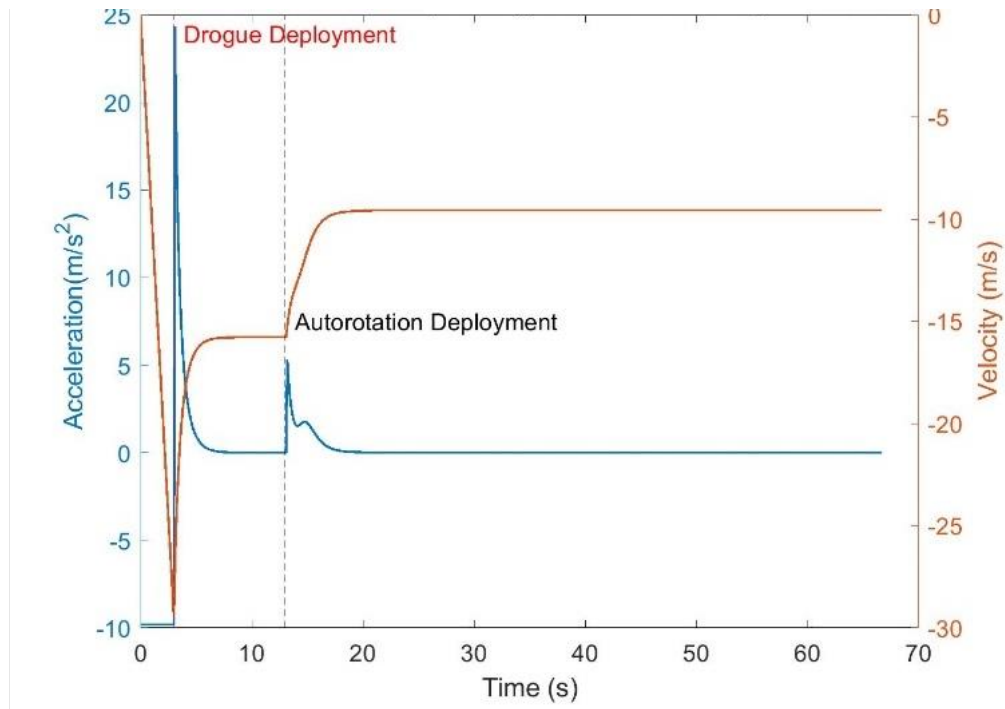
Figure 85: Acceleration and velocity of the HPMR with a 2 ft drogue parachute

The analysis for Case 4 assumed a 3 ft parachute with the autorotation system to determine its effects on the descent height, velocity and acceleration. The graphs of these values are provided below in Figure 86 and Figure 87. The final descent velocity was 7.91 m/s with descent time of 85 s. The decrease in descent velocity from the previous analysis was caused by the larger vertical force supplied by the larger parachute. The three-foot diameter parachute provides an initial positive acceleration of 67 m/s^2 and by the time the autorotation system was deployed the descent velocity was 10.2 m/s. Similar to the third analysis, the slower descent velocity caused the autorotation system to provide significantly less aerodynamic forces to decelerate the HPMR when compared to the first analysis. The autorotation system only decreased the HPMR by 2.3 m/s after deployment, which is small compared to the deceleration from the parachute. At this diameter, the

drogue parachute becomes the main recovery method, which defeats the purpose of designing the autorotation system.
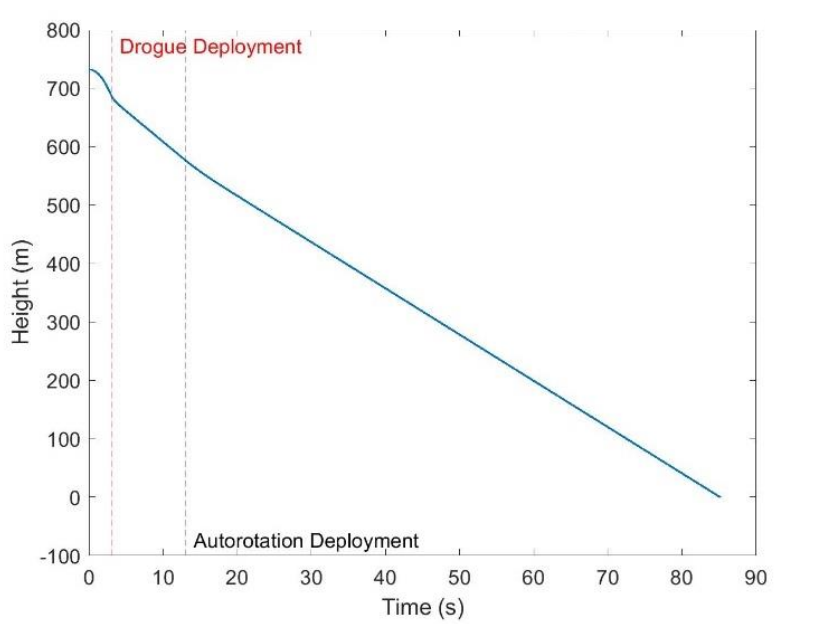
Figure 86: Height of the HPMR with a 3 ft drogue parachute
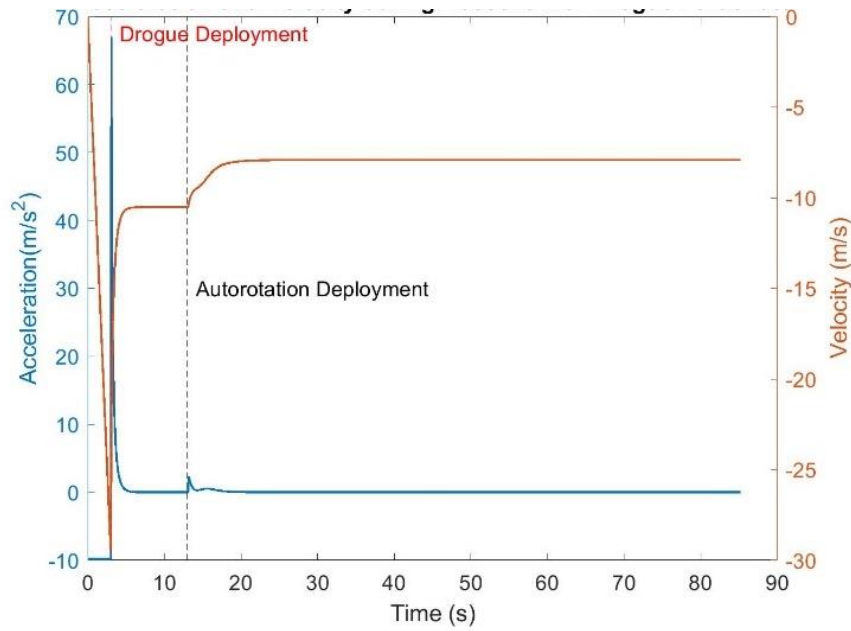
Figure 87: Acceleration and velocity of the HPMR with a 3 ft drogue parachute

The use of a drogue parachute was important to orient the HPMR before deploying the autorotation system, but it has the negative impact of increasing the landing velocity of the rocket. The second analysis with the 1 ft drogue parachute provided the lowest descent velocity when a drogue parachute was used. The velocity was still higher than the desired landing velocity of 5 m/s. If a 1 ft drogue parachute was used with the autorotation system, the rocket may be damaged by the high landing velocity. The results of all four cases are summarized in Table 17:

Table 17: Results of the four autorotation models

Case:	Recovery Method	Landing Velocity (m/s)	Result
1	Autorotation system	6.86	Landing velocity slightly higher than 5 m/s and may cause damage upon landing
2	Autorotation system with a 1 ft drogue parachute	6.55	Landing velocity slightly higher than 5 m/s and may cause damage upon landing
3	Autorotation system with a 2 ft drogue parachute	9.55	Landing velocity too high and will damage rocket
4	Autorotation system with a 3 ft drogue parachute	7.91	Landing velocity too high and will damage rocket. Additionally, the larger parachute defeats the purpose of the autorotation system

2.2.5.2 Fluent Model

In order to try to verify locations of stall zones across the blade, a Fluent simulation was performed. The analysis needs to account for the rotational velocity of the blades, and therefore the variance of AOA across the blade span. The analysis performed considers the rotational velocity of the blade due to spinning, however, the analysis presented in this section does not include a user-defined function (UDF) to account for the changing AOA across the span of the blade. Figure 88 shows velocity components and the resultant velocity along the span of the rotor. The figure also illustrates how the varies along the span.
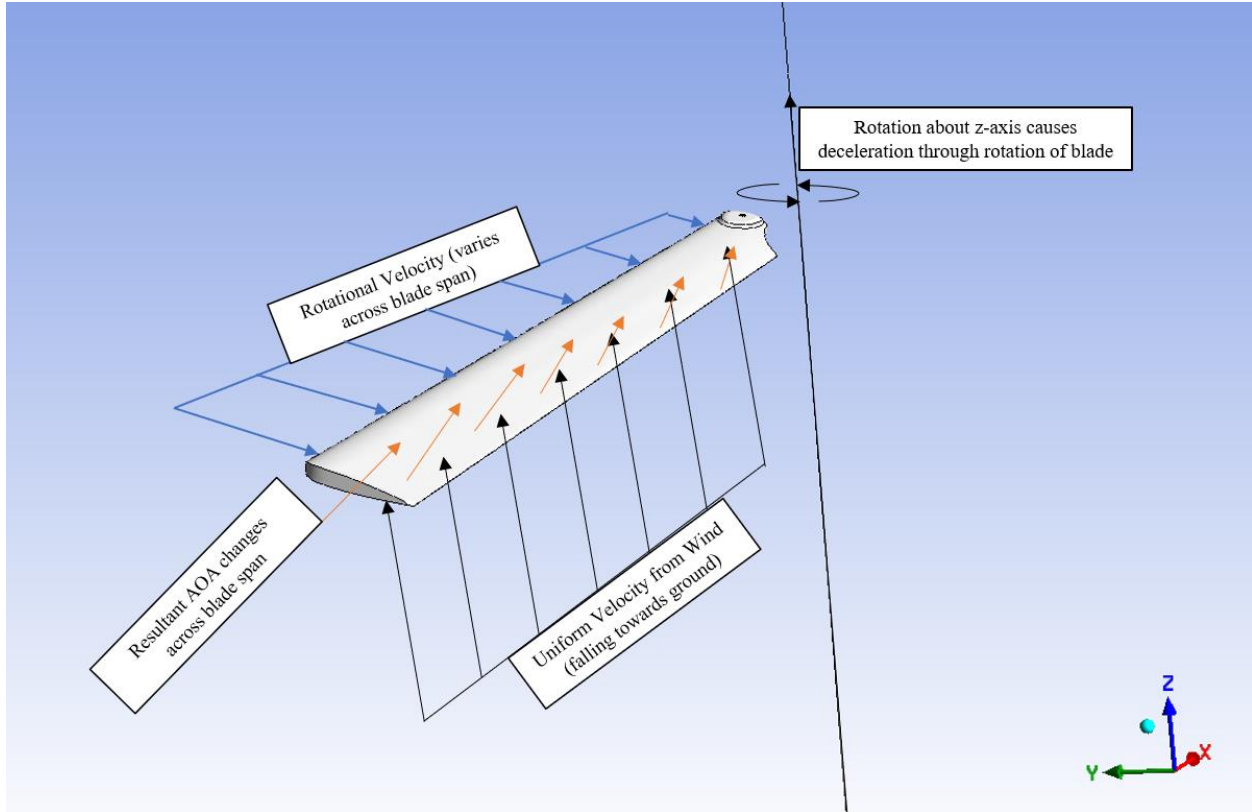
Figure 88: Forces acting upon blade

A NACA 0012 airfoil was modeled as the rotor blade used within this simulation. The simulation itself was based upon a Cornell University tutorial [79] originally intended for the blade of a wind-turbine, the find the forces acting upon it as it spun due to wind. The orientation of the blade is shown in Figure 89 and Figure 90.

After being oriented, meshing was completed in Fluent, and created the domain around the blade that contains moving air. The physics was then set up in order to run the simulation. Figure 91 shows the domains and boundaries used in the simulation.
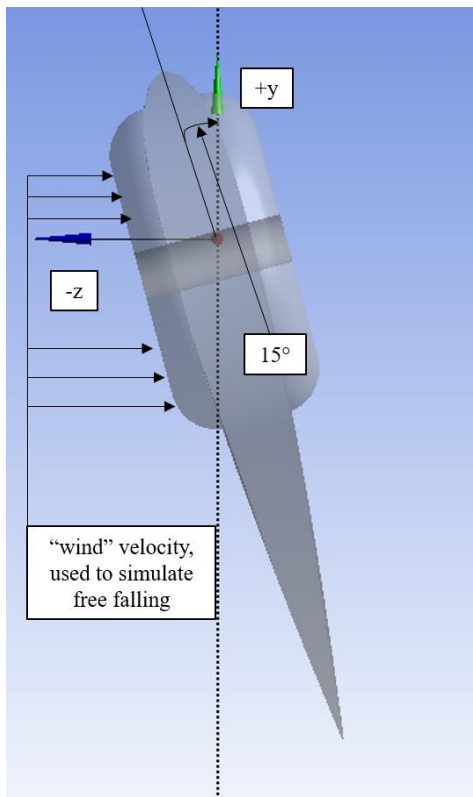
Figure 89: Orientation of blade
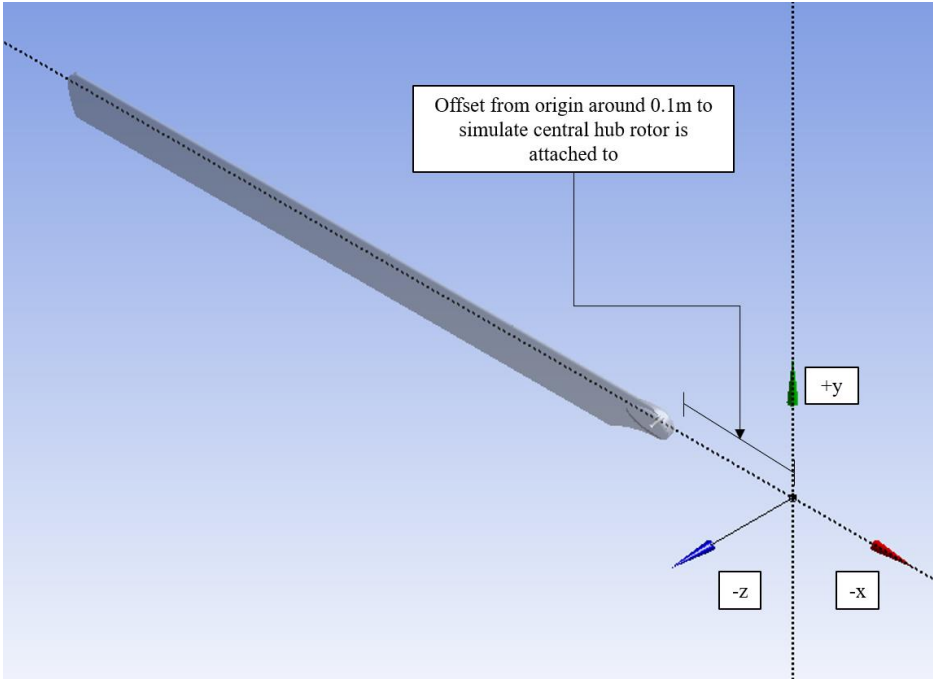
Figure 90: Isometric view of blade orientation
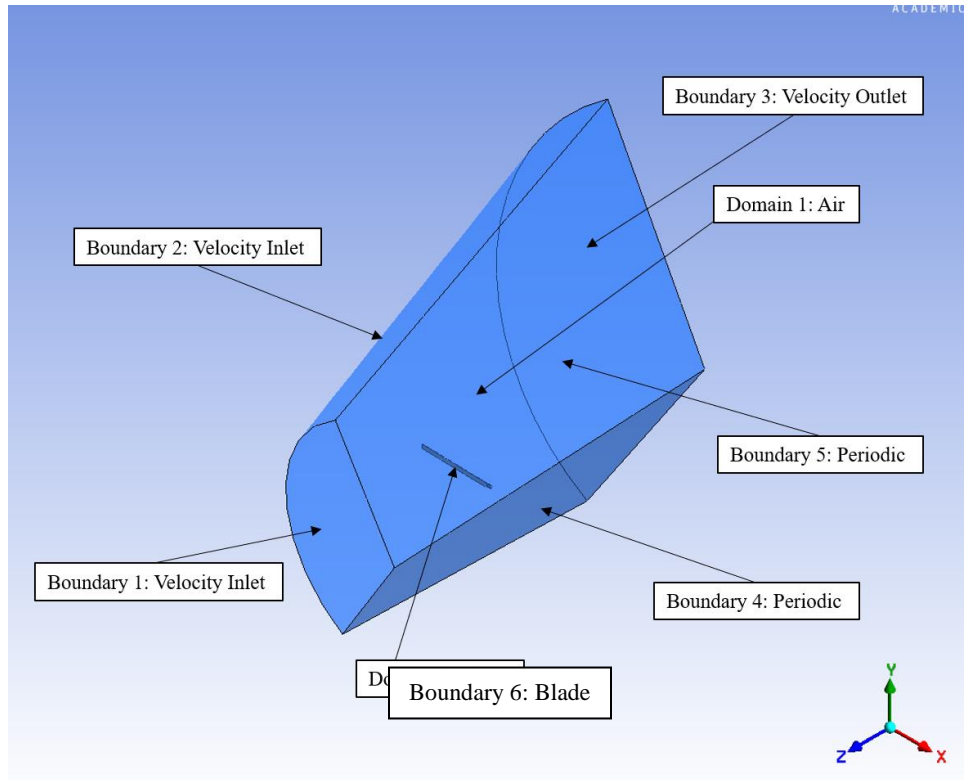
Figure 91: Domain and boundaries for fluent analysis of blade

Table 18: Domains, materials, and material values chosen in the geometry of Fluent Blade Model

Domain	Material Chosen in COMSOL and Applied to Domain	Material Value	Description
1	Air	$\rho = 1.225\dfrac{kg}{m^3}$ $\mu = 1.7894\text{e-}05\dfrac{kg}{ms}$	Air is used as the fluid that is acting on the blade during the simulation. Sea-level conditions were assumed.
2	ABS PC	$\rho = 1070\dfrac{kg}{m^3}$	The ABS PC was used to model the blade as a 3-D prototyped blade. The density is the standard given by SOLIDWORKS.

Table 19: Boundary conditions applied to domains and boundary lines in the model

Boundary lines in COMSOL	Domains corresponding to boundary lines	Boundary Conditions		Description
		Boundary Condition and Constitutive Relation (if applicable)	Equation and value	
1	Domain 1	Mass Flow Rate	$\dot{m} = \int \rho \vec{v} \cdot \overrightarrow{dA}$ $\rho = 1.225 \frac{kg}{m^3}$	Computes inlet mass flow rate
2	Domain 1	Mass Flow Rate	$\dot{m} = \int \rho \vec{v} \cdot \overrightarrow{dA}$ $\rho = 1.225 \frac{kg}{m^3}$	Computes inlet mass flow rate
3	Domain 1	Mass Flow Rate	$\dot{m} = \int \rho \vec{v} \cdot \overrightarrow{dA}$ $\rho = 1.225 \frac{kg}{m^3}$	Computes outlet mass flow rate
4 and 5	Domain 1	Periodic Boundary	-	Rotationally bound Periodic Boundary. No pressure drop within boundaries, signifies an axis of rotation. This was used to display the central hub of the auto-rotation design.
6	Domain 2	Pressure Outlet	$\frac{\partial p}{\partial r} = \frac{\rho v_\theta^2}{r}$ $\rho = 1.225 \frac{kg}{m^3}$	Measures Pressure across blade

Table 20 Initial values of the model

	Domains Initial Value is Applied to	Value	Description
Initial Values	Domain 1	$V_z = 12$ m/s	Sets a wind speed of 12 m/s in the z direction heading from boundary 1 towards boundary 3.
Initial Values	Domain 2	Rotation about z –axis = 2.22 rad/s	Simulates the blade rotating around the z-axis at 2.22 rad/s
Initial Values	Domain 2	$\alpha = 15°$	AOA for blade is set at 15° counterclockwise from the y-axis.

To complete the simulation, a mesh node was sized to be around 0.1m, and after the simulation performed over 10,000 iterations, it was completed. The pressure on the bottom face (where the wind is contacting the blade) and the pressure on the top face was found using a pressure counter tool. Figure 92 and Figure 93 show the results. For reference, a pressure value of zero indicates a location where no force from the wind is felt on the blade, so a positive value represents a higher pressure and a negative value would indicate a lower pressure.
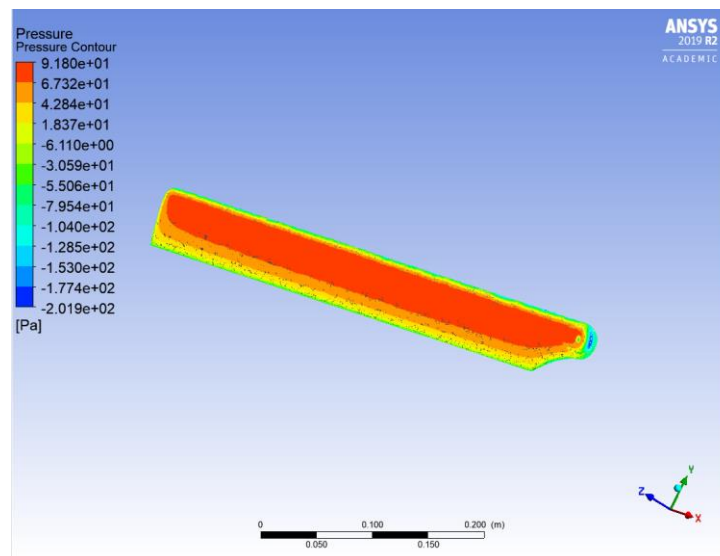
Figure 92: Bottom of blade pressure contours
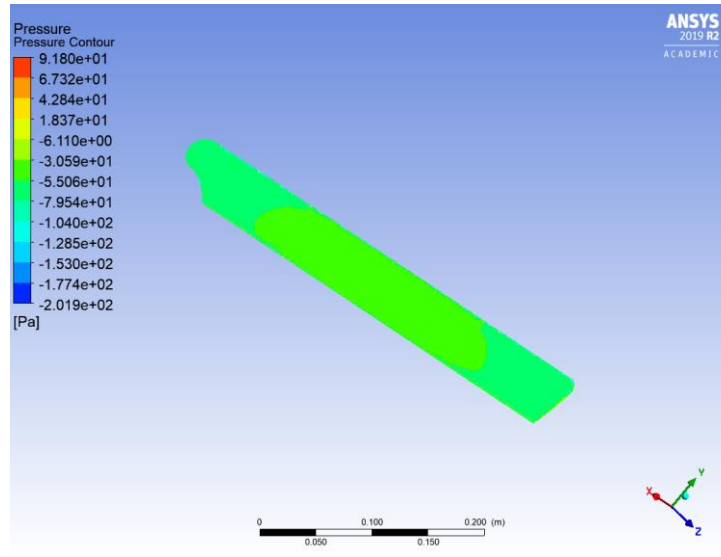
Figure 93: Top of blade pressure contours

As can be seen in Figures 83 and 84, the assumed AOA is reflected in the pressure distribution of the bottom of the blade, with the pressure being the highest where the wind initially contacts the blade, and decreased as it flows around the blade. The top of the blade shows two different pressure zones. A very low-pressure zone on the blade would indicate a stall zone. From the simulation, it is inconclusive if, using the parameters listed, there are any stall zones along the span of the blade. A stall condition would be seen if the coefficient of lift suddenly started to decrease after achieving its maximum. In terms of our simulation, this would show a lower pressure across the span of the blade near a similar location where the maximum pressure is applied. However, if a more realistic simulation is performed that also accounts for the changing AOA across the blade span, it should be possible to identify regions of stall.

3 Propulsion, Thermal, and Separation Systems – Design and Analysis

The literature review completed by the PTSS subteam provided a foundation for analyzing the propulsion and stage separation assemblies of the HPMR. In this section, the I216 rocket motor is analyzed using COMSOL and Cantera in order to predict temperature distribution throughout the casing and motor performance parameters such as thrust and specific impulse. Additionally, the design of a spring-loaded stage separation is presented for implementation in the innovative rocket.

3.1. Methodology

Two independent propulsion systems were designed for this project: a high risk, innovative system and a low risk, baseline system. The innovative design consisted of a two-stage motor with stage separation between the first and second stages. This method also included designing an onboard ignition system capable of igniting the second stage motor mid-flight as well as the design of a spring-loaded separation system to deploy the parachute out of the nose of the rocket. Due to the complexities involved with the design and test of a multi-stage launch vehicle, the PTSS subteam also pursued a baseline propulsion system so that it launched within our time schedule. The baseline system consisted of a single stage motor, a single ignition system and a black powder separation system to deploy the parachute. In order to further analyze the feasibility of both methods, the PTSS subteam conducted a motor performance analysis of composite propellant motors using Cantera modelling software. Additionally, the PTSS subteam conducted a temperature distribution analysis using COMSOL Multiphysics® modelling software [80]. This level of advanced analysis for a model rocket propulsion system contributed to the academic merit of investigating two propulsion systems

136

3.1.1 Propulsion

With the end goal of producing enough thrust to achieve the altitude goal of 1500 ft while also maintaining a thrust-to-weight ratio of approximately 5:1 (to ensure a safe speed when the rocket leaves the launch rail), the propulsion system can be configured in different ways. Work on this project included an investigation of motor staging with two different rocket motors instead of using a single motor. Staging motors increases the complexity of the propulsion system due to additional ignition and stage separation systems. Although the two-stage propulsion system was not flight tested, we researched and analyzed the concept of motor staging and compared it to the baseline approach of launching a single stage model rocket.

3.1.1.1 Engine Systems

For our innovative design, the PTSS subteam decided to use a two-stage propulsion system based on the benefits staging provides in attaining high altitudes. Although the team did not fly a rocket with multiple stages due to complexities in design and a limited time schedule, the PTSS subteam pursued this concept in depth as if the team was going to fly it. When selecting the motors for each stage, the PTSS subteam took into consideration many different factors, the first being the manufacturer. The PTSS subteam primarily looked at Aerotech and Cesaroni motors because both are nationally recognized manufacturers of high-powered rocket motors and our team already had familiarity in purchasing from them for previous projects. Ideally, the PTSS subteam wanted to select a motor manufactured by Cesaroni because they required less assembly of the propellant kit in comparison to Aerotech motors. An MQP team from 2018-2019 encountered a launch failure when testing their high-powered rocket. This was due to a malfunction in a motor that was improperly assembled [18]. For this reason, we wanted to select a motor that required a minimal amount of assembly if possible. The next factor was whether to use a single-use or reloadable

rocket motor. A reloadable rocket motor means that the aluminum motor casing can be reused. However, the propellant kits containing the propellant grain must be purchased for each launch. Figure 94 below shows a 38 mm reloadable aluminum casing.

Figure 94: Reloadable 38 mm aluminum motor casing

A typical single-use motor would look very similar to the motor shown in Figure 18. Although reloadable motors are initially more expensive than single-use motors, if multiple launches are planned, reloadable rockets are more economical over time. For this reason, the PTSS subteam wanted both stages to be reloadable. The next consideration was the total impulse limit. Since the highest level of certification by any member on our team was a Level 1 certification, the National Association of Rocketry restricts the total impulse of all motors in a rocket to be less than 640 N-s. Additionally, one of the requirements is that the motor used to get the rocket off the launch rail must provide a thrust to weight ratio of approximately 5:1. When calculating the thrust to weight ratio for motor selection, the PTSS subteam approximated the weight of the rocket, based on previous experience of some team members, to be 15 lbs. Given this constraint, the PTSS subteam needed to select a first stage motor that had a large enough thrust in order to achieve a thrust to

weight ratio of 5:1. After taking into consideration these different factors, the PTSS subteam compiled a table of motors to select from. This table can be found in Appendix E.

The Aerotech and Cesaroni websites provided motor performance parameters that the PTSS subteam included in the table to help select the motor for each stage.

The PTSS subteam decided to select the Cesaroni H400 because it provided an average thrust of 400 N and yielded a thrust to weight ratio of approximately 6:1. The total impulse of this motor was 255 N-s. When selecting the second stage motor, the only additional constraint was that the combined total impulse for the first and second stage had to be less than 640 N-s. Furthermore, the PTSS subteam still wanted to maintain a thrust to weight ratio of approximately 5:1 after stage separation. The PTSS subteam approximated a 3 lb decrease in weight after stage separation. This weight loss came from structural mass of the first stage and the mass of the booster motor. Given these two factors in consideration, the PTSS subteam chose the Cesaroni I212 as the second stage motor because it had a total impulse of 364 N-s and an average thrust of 212 N which corresponds to a thrust to weight ratio of 3.97:1 for a 12 lb. rocket. The combination of these motors provides a total impulse of 619 N-s which is approaching the threshold for allowable total impulse with a Level 1 certification.

The thrust curves for the Cesaroni H400 and I212 motors is provided in Figure 95 and Figure 96, respectively. These plots were generated in MATLAB.

As already mentioned, due to the complexities of staging, specifically concerning the stage separation and second stage ignition systems, the PTSS subteam decided to pursue a baseline propulsion system that would be ready for flight during our given time schedule. This baseline propulsion system consists of a single stage motor. In determining motor selection, the only factors considered were that the PTSS subteam not exceed the maximum total impulse limit (640 N-s)
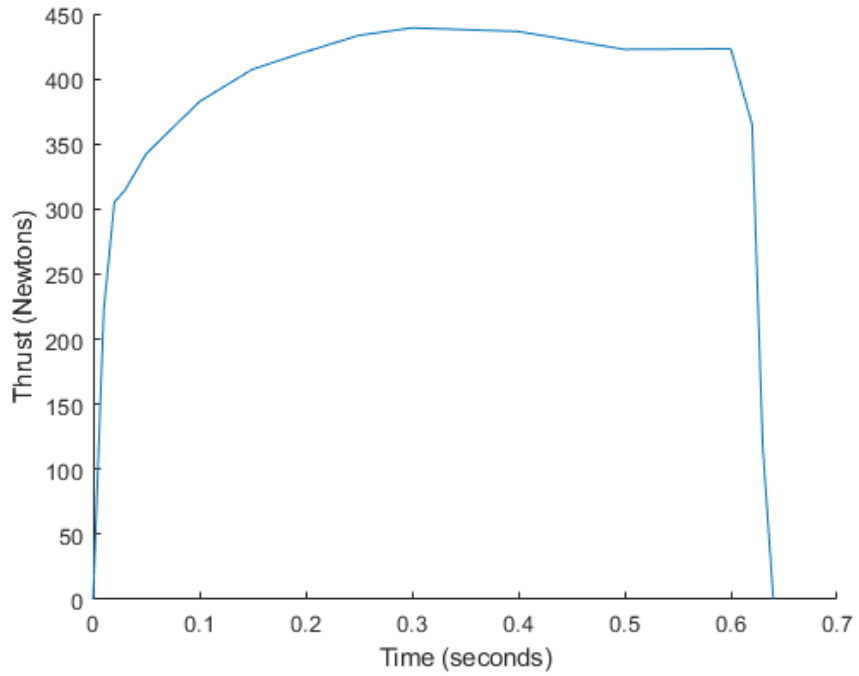
Figure 95. Thrust curve for H400N motor
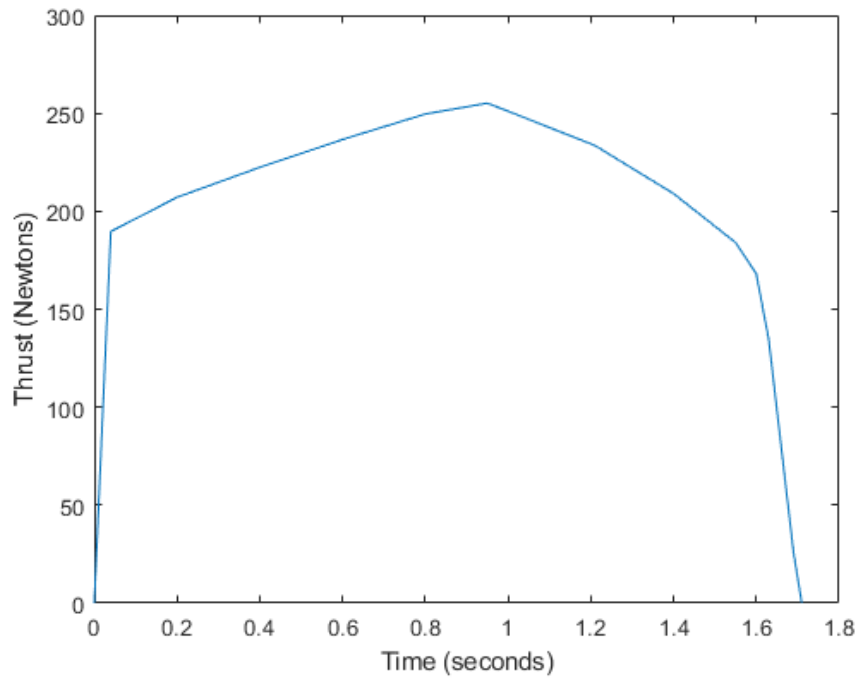
Figure 96. Thrust curve for I212 motor

and that the motor be reloadable. The PTSS subteam compiled a list of possible motors that can be found in Appendix E.

After evaluating the list, the PTSS subteam selected the Cesaroni I216 because it provided a total impulse of 636 N-s and it was a reloadable motor. This motor provides an average thrust of 216 N.

It is important to note that many rocket motors are manufactured with a delay charge already in them. However, one of the benefits associated with reloadable motors is that the delay charge is a separate component assembled into the motor by the user. Thus, if the user does not want a delay charge, one can simply "plug" the motor by not inserting the delay charge when assembling the propellant kit. For this reason, the PTSS subteam did not choose only motors that were manufactured without a delay charge.

3.1.1.2 Ignition/Mounting Systems

The commercial motor kits for our baseline and innovative designs all include commercial e-match igniters. Our plan was to use these igniters for ignition of the first stage motor and then for the stage separation of the second stage in the innovative design. The igniters included in these kits operate on the same basis of those described within Section 1.1.2.2 and come with an igniter wire that is pre-dipped in a pyrogen. For the Cesaroni I216 igniter, the pyrogenic tip consists of Barium chromate, Magnesium powder, and Viton fluoroelastomer. These all have varying composition percentages with the Magnesium powder having the highest content. Additionally, the other motors that will be used in the innovative design also include the same igniter for launch.

For stage separation, the PTSS subteam used a firewire igniter which is also an e-match igniter that is provided by Apogee Components. This igniter incorporates boron to initiate the burning of the igniter. On board electronics were used to ignite this component as the motors used in both the

baseline and innovative designs utilized composite propellants. An important factor that affected the choice of this igniter was that it requires a low current to be lit, which is beneficial in requiring less power from the onboard electronics.

For launch all first stage ignition systems were connected to a launch controller that provided the necessary power for a successful launch. The launch controller included a 12 V battery as was recommended to be used in the Handbook of Model Rocketry to get the igniter wire to burn bright red. This voltage battery also allows for a more efficient power supply as it only delivers about a fourth of the current to create the same ignition temperature as a 6-volt battery [35].

3.1.1.3 *Temperature Distribution Model*

In order to model the temperature distribution across the I216 motor, the PTSS subteam utilized COMSOL. Our subteam created a 2D asymmetric model of the cylindrical combustion chamber and propellant grain. The aluminum casing that the motor is encased in was also taken into consideration when creating the model. After creating the model our subteam combined heat transfer in a solid and fluid domain in a time-dependent, conjugate heat transfer analysis which provided a realistic model of the temperature distribution across the rocket motor.

For the solid region, as pictured in Figure 97, the analysis evaluated conditions across three domains, which all spanned a length of 0.186 mm. The first domain is the aluminum motor casing, which spanned a width of 0.005 mm. The second domain is the solid ammonium perchlorate with a width of 0.006 mm, and third is a domain containing the volumetric heat source, which spanned 0.002 mm. In conducting the analysis each domain had varying conditions and inputs that are summarized in Table 21 below.
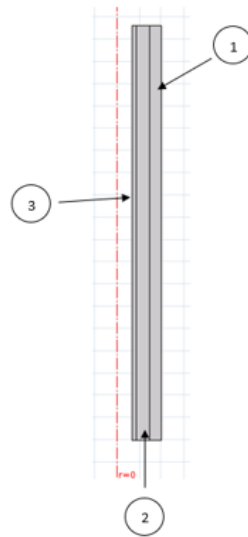
Figure 97: Graphic of solid domain boundaries

Table 21: Boundary Condition Material and Option Inputs

Boundary	Material	Condition	Option	Input
1	Aluminum Casing	Heat Flux	Convective Heat Coefficient	$h = 25$ W/(m^2·K) $T_{ext} = 293.15$ K
2	Solid Ammonium Perchlorate	Initial Value	Temperature	293.15 K
3	Fluid	Volumetric Heat Source	General Source	6.665×10^9 W/m^3
3	Fluid	Temperature	N/A	2547.7 K

In determining the inputs for the varying conditions of the domains, the general source value for the volumetric heat source was calculated. Cantera was used in this instance to obtain the necessary value of the heat of reaction regarding the fuel assumed in the motor, which was aluminum. More information on the chemical reaction that was analyzed can be found in the

following section. This heat of reaction value was then used to evaluate the enthalpy released

during combustion within the motor using Eq. 3-1:

$$Q = \frac{\dot{m}_{fuel}h_{RP}}{V} \qquad \text{3-1}$$

where h_{RP} is equal to the heat of the reaction per kmol of fuel, V is the volume of the fluid domain,

and $\dot{m}_{fuel}$ is the mass flow rate of fuel. Regarding the mass flow rate of the fuel, this was calculated

through by using the total mass flow rate of the motor and subtracting the mass flow rate of the

oxidizer, which was ammonium perchlorate in this case. The values for the following parameters

are listed in Table 22: Heat of Reaction Equation Variablesbelow:

Table 22: Heat of Reaction Equation Variables

Variable	Value
h_{RP}	741,870 (J/kg)
V	2.337x10^{-3} (m^3)
$\dot{m}_{fuel}$	0.021 (kg/s)
$\dot{m}_{oxidezer}$	.0706 (kg/s)
$\dot{m}_{total}$	.0916 (kg/s)

Additionally, we assumed ambient conditions outside of the motor to be a temperature of

293.15 K and pressure of 1 atm. We also applied a material to each of the domains as listed in

Table 23. The table lists the thermal conductivity, heat capacity, density, ratio of specific heats,

and dynamic viscosity for all materials considered in our model.

As COMSOL did not contain physical properties for the ammonium perchlorate, the PTSS

subteam referred to the 2019 MQP [18] for the thermal conductivity, density, and heat capacity of

the material. Additionally, physical properties from the motor performance analysis completed in

Cantera were used to define the fluid domain. These properties included the initial temperature,

heat capacity at a constant temperature, and specific heat ratio.

Table 23: Physical Properties of COMSOL Model Domains

Material	Domain Applied	Thermal Conductivity (W/m·K)	Density (kg/m³)	Heat Capacity at Constant Pressure (J/kg·K)	Dynamic Viscosity (Pa·s)	Ratio of Specific Heats
Aluminum Casing	1	238	2700	900	-	-
Ammonium Perchlorate	2	.5301	1949	1084	-	-
Volumetric Heat Source	3	.03	29.1863	1554.9	3.78	1.2401
Fluid	4	.03	29.1863	1554.9	3.78	1.2401

The analysis for the fluid domain, as pictured in Figure 98, was defined by four different

boundary conditions. All the conditions and inputs are summarized in Table 24.
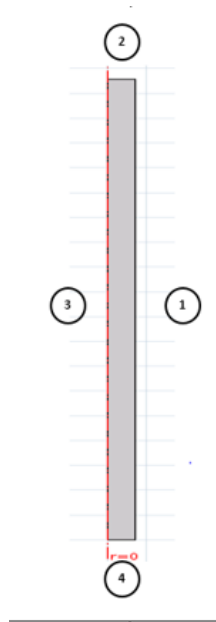
Figure 98: Graphic of fluid domain boundaries

Table 24: Table of Fluid Domain Boundary Conditions and Inputs

Boundary	Condition	Option	Input
1	Inlet	Velocity	21.7 m/s
2	Wall	No Slip	u = 0
3	Symmetry	N/A	N/A
4	Outlet	Pressure	2.24 MPa

For boundary condition 1, we identified an inlet velocity. In selecting a velocity boundary condition for the inlet, COMSOL specifies velocity as, $\boldsymbol{u} = -\boldsymbol{n}U_o$ where $\boldsymbol{n}$ is the boundary normal, oriented outward from the domain and U_o is the normal inflow speed. Additionally, in choosing the **velocity** option, COMSOL sets the velocity vector to $\boldsymbol{u} = \boldsymbol{u_o}$ where $\boldsymbol{u_o}$ is user defined. In our model this value was defined as 21.7 m/s. Through modifying the mass flow rate equation to solve for velocity, we were able to solve for the fluid velocity at the inlet. The value was calculated using Eq. 3-2.

$$u = \frac{\dot{m}}{(\rho_{NH_4ClO_4})(A_{is})} \qquad\qquad 3\text{-}2$$

where $\dot{m}$ is the mass flow rate of the motor, $\rho_{NH_4ClO_4}$ is the density of ammonium perchlorate, and A_{is} is the inner surface area of the fluid domain.

Boundary condition 2 represents a wall for which a "no slip" condition was set. Under this option, it is assumed that a boundary layer forms between the fluid flow and the wall itself. Within this boundary layer, the fluid velocity relative to the wall is zero. Since we have a stationary wall in our model, the velocity can be described as $u = 0$ where u is the velocity vector.

For boundary condition 3, the boundary represented a symmetrical axis, upon which there is no diffusion of shear stresses. The symmetry boundary condition is defined by the requirement that there be no fluid penetration and a vanishing shear stress. These lead to both a Dirichlet and Neumann condition that are shown in Eqs. 3-3 and 3-4, corresponding to compressible and

incompressible flows respectively. These equations are written in this report using the exact scalar, vector, and tensor notation used in the COMSOL documentation. For this study, the flow in the combustion chamber was assumed compressible/weakly-compressible and therefore used the condition given by Eq. 3-3.

$$\mathbf{u} \cdot \mathbf{n} = 0, \quad \left(-p\boldsymbol{I} + (\mu(\nabla\mathbf{u} + (\nabla\mathbf{u})^T) - \frac{2}{3}\mu(\nabla \cdot \boldsymbol{u})\boldsymbol{I})\right)\boldsymbol{n} = 0 \tag{3-3}$$

$$\mathbf{u} \cdot \mathbf{n} = 0, \quad (-p\boldsymbol{I} + \mu(\nabla\mathbf{u} + (\nabla\mathbf{u})^T))\mathbf{n} = 0 \tag{3-4}$$

where u is the velocity vector, n is the normal vector, I is the identity matrix, T is the transpose, and μ is the fluid dynamic viscosity. When analyzing a model with 2D axial symmetry, COMSOL does not require a boundary condition to be selected along the axis where r = 0. An Axial Symmetry node gets automatically applied by COMSOL to dictate that u_r = 0 and that "no stresses in the z direction" are conditions implemented on the boundaries selected.

Lastly, for boundary condition 4, we identified a pressure (normal stress) outlet condition where there is a fluid net outflow from the overall fluid domain. For a compressible/weakly-compressible flow, COMSOL defines this condition using Eq. 3-5.

$$\left[-p\boldsymbol{I} + \mu(\nabla\boldsymbol{\mu} + (\nabla\boldsymbol{\mu})^T) - \frac{2}{3}\mu(\nabla \cdot \boldsymbol{u})\boldsymbol{I}\right]\boldsymbol{n} = -p_0\boldsymbol{n} \tag{3-5}$$

where p is the pressure, μ is the fluid's dynamic viscosity, T is the fluid transpose, u is the fluid velocity, I is the identity matrix, n is the unit vector normal to the boundary and p_0 is the relative pressure to the motor at the outlet as specified by the user. The outlet pressure was taken to be the chemical equilibrium mixture pressure calculated in Cantera (as described in Section 0) which is representative of the chamber pressure for our model.

3.1.1.4 Motor Performance Analysis

The National Association of Rocketry publishes motor performance parameters based on tests conducted in their own lab. Some of these parameters include average thrust and specific impulse [34]. However, in order to validate and compare to the NAR findings, the PTSS subteam conducted a motor performance analysis using Cantera. Cantera is an open-source software capable of conducting chemical kinetic, thermodynamic, and transport calculations for many different applications. It is written in C++ and can be executed through C++, Python, MATLAB or Fortran. There are unique Cantera commands corresponding to each of these applications. The PTSS subteam used the MATLAB interface for this project. Cantera was created by Professor David Goodwin at the California Institute of Technology and is capable of solving chemical equilibrium problems using its own built in chemical equilibrium solver [81]. The solver uses an element potential method that reduces each element in the reaction down to a nonlinear algebraic equation [44].

The goal of this analysis was to determine the composition of the reaction products, identifying the dominant product species, the adiabatic chemical equilibrium temperature, and other thermodynamic properties such as the specific heat ratio. These analysis products were used to calculate the motor thrust and specific impulse.

In order to get the desired outputs from this analysis, we decided to perform a chemical equilibrium analysis in Cantera. Before beginning the analysis, the PTSS subteam made the following assumptions. We assumed that the mole fractions for the reactant species in the motor were 0.8 ammonium perchlorate (AP) and 0.2 aluminum. The chemical reaction equation is shown in Eq. 3-6

$$8NH_4ClO_4 + 0.2Al \rightarrow aO_2 + bH_2O + cN_2 + dHCl + eAl + f(trace\ species) \qquad \text{3-6}$$
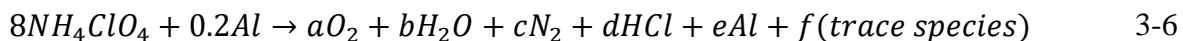
where a, b, c, d, e, and f are the unknown product mole numbers to be calculated. Composite model rocket motors typically consist of fuel, an oxidizer (typically ammonium perchlorate) and an inert binder substance [32]. However, the manufacturer of the I216 motor does not specify the exact ratios. The assumption of mole fractions consisting of 0.8 AP and 0.2 aluminum was made because the oxidizer is typically the dominant reactant species in model rocket motors, constituting approximately 80% of the reactants [32]. The next assumption we made was that chemical equilibrium occurs in the chamber of the motor before being accelerated through the nozzle. Cantera also requires users to hold specific preset parameters constant when using the chemical equilibrium solver. We chose to hold the internal energy and volume of the reaction constant during equilibrium because although there is heat loss through the motor casing, we considered this heat loss to be negligible for the purpose of the chemical equilibrium analysis. Additionally, although the chamber volume is increasing as propellant burns, we considered the volume to be fixed at 416.22 cm^2 (volume after all propellant has burned) during the equilibrium process. Table 25 is a summary of all assumptions made during this analysis:

Table 25. Summary of assumptions made for motor performance analysis in Cantera

Assumption
Reactants are ammonium perchlorate and aluminum
Chemical equilibrium occurs in motor chamber
Constant specific internal energy and volume during chemical equilibrium process
Complete combustion

After all necessary assumptions were made, the PTSS subteam then provided Cantera with the required inputs to complete the chemical equilibrium calculation. The inputs included an initial temperature equal to 293.15 K and a chamber pressure equal to 101,325 Pa. These conditions were then put into a MATLAB script which utilized Cantera's chemical equilibrium solver to solve for

chemical equilibrium. The script the PTSS subteam wrote in MATLAB for this analysis can be found in Appendix F.

3.1.1.5 One-Dimensional Isentropic Nozzle Flow Analysis

In tandem with the CFD model of the motor nozzle in COMSOL, the PTSS subteam also performed an analytical calculation of the thrust and specific impulse assuming 1D, isentropic flow in the nozzle. In order to find an analytical solution to the nozzle flow problem, we assumed the flow to be one-dimensional flow and isentropic. This assumption implies that there is no heat flux through the motor casing. Despite knowing this to be false, as is evident from the results from the temperature distribution model, solving this one-dimensional isentropic flow problem still served as a baseline calculation for our other analysis tasks.

For the upstream conditions, the PTSS subteam used the thermodynamic properties obtained from the chemical equilibrium problem solved by Cantera. Limited data was provided by the motor manufacturer regarding the nozzle geometry and expansion ratio of the I216 motor. Therefore, we approximated the expansion ratio to be five based on similar model rocket motors which did have available motor geometry data [82]. Table 26 summarizes the conditions used:

Table 26: Conditions used for one-dimensional isentropic nozzle flow solution

Property	Value	Unit
Chamber Temperature, T_1	2547.7	K
Chamber Pressure, p_1	2.24	MPa
Chamber Density, ρ	2.87	Kg/m^3
Mass Basis of Specific Heat at Constant Pressure, C_p	1414.4	J/kg-K
Mass Basis of Specific Heat at Constant Pressure, C_v	1109.0	J/kg-K
Mean Molecular Weight, M_m	27.22	Kg/kmol
Specific Heat Ratio, k_m	1.28	-
Expansion Ratio, $\frac{A_e}{A_t}$	5.00	-

Using the values in Table 26, the PTSS subteam used the isentropic flow equations (Eq. 3-7 through Eq. 3-11) to relate the area ratio, Mach No., and ratio of specific heats to temperature, pressure and density in the nozzle flow:

$$\frac{A}{A_t} = \left(\frac{k_m + 1}{2}\right)^{\frac{-k_m+1}{2(k_m-1)}} \frac{\left(1 + \frac{k_m - 1}{2}M^2\right)^{\frac{k_m+1}{2(k_m-1)}}}{M} \tag{3-7}$$

$$M = \sqrt{\frac{2}{k_m - 1}(\frac{T_o}{T} - 1)} \tag{3-8}$$

$$\frac{T_o}{T} = 1 + \frac{k_m - 1}{2}M^2 \tag{3-9}$$

$$\frac{p_o}{p} = \left(1 + \frac{k_m - 1}{2}M^2\right)^{\frac{k_m}{k_m-1}} \tag{3-10}$$

$$\frac{p_o}{p} = (\frac{\rho_o}{\rho})^{k_m} \tag{3-11}$$

In these equations, A is the nozzle exit area, A_t is the area at the throat, k_m is the specific heat ratio, M is the mach number, T_o is the chamber temperature, T is temperature, p_o is the chamber pressure and p is the exit pressure.

The exit velocity u_e was calculated using Eq. 3-12:

$$u_e = \sqrt{\frac{2k_m}{k_m - 1}RT_o(1 - \left(\frac{p}{p_o}\right)^{\frac{k_m-1}{k_m}})} \tag{3-12}$$

In this equation, R is the universal gas constant. Using the exit velocity, the mass flow rate, $\dot{m}$, was calculated using Eq. 3-13:

$$\dot{m} = \rho u_e A_e \qquad \text{3-13}$$

where ρ is the exit density and A_e is the exit area of the nozzle. This value was then used in calculating the thrust from the motor T:

$$T = \dot{m} u_e + (p - p_a) A_e \qquad \text{3-14}$$

where p_a is the ambient pressure taken to be 101,325 Pa. Similarly, Eq.3-14 was used to calculate the specific impulse, I_{sp}:

$$I_{sp} = \frac{u_e}{g} + \frac{p_o}{p} \frac{A_e}{A_t} \frac{c^*}{g} \qquad \text{3-15}$$

where g is gravity and c^* is the characteristic velocity that can be defined by Eq. 3-16:

$$c^* = \frac{\sqrt{\frac{k_m R T_o}{M_m}}}{k_m \sqrt{\frac{2}{(k_m + 1)^{\frac{k_m+1}{(k_m-1)}}}}} \qquad \text{3-16}$$

where M_m is the mean molecular weight provide by the chemical equilibrium calculation in Cantera. The MATLAB file we used to evaluate the isentropic flow properties can be found in Appendix F.

3.1.2　Separation

　Multiple methods of initiating stage separation were found in the literature review including black powder and carbon dioxide. Based upon the requirements for a "baseline" and "innovative" rocket separation system, the PTSS subteam decided to use three different separation methods. The baseline rocket incorporated one motor ejection charge, as well as two black powder charges. Black powder charges were chosen for use in the baseline design because they are the most widely used form of separation in model rocketry and the least complex. For the innovative rocket, only two separation events were needed. The first was an ejection charge from the motor that was used to separate the first booster stage of the rocket. The second was needed to separate the nose cone from the main body of the rocket. Expanding upon the 2007 MQP project [6], a spring separation system was designed and implemented to eject the nose cone.

3.1.2.1　*Black Powder Charges*

　For the baseline rocket system, the PTSS subteam used four separate black powder charges for redundancy and to ensure the rocket properly deployed its parachutes. Two charges were used to separate the lower airframe from the upper airframe and two charges were used to eject the nose cone. These events were designed to take place at apogee (approximately 1000 ft) and at 700 ft respectively. Since the upper and lower airframes had different internal volumes, the PTSS subteam used Eq. 3-17 through 3-18 to calculate the required black powder for each section independently:

$$V = \frac{\pi D^2 L}{4} \qquad\qquad \text{3-17}$$

$$n = \frac{pV}{R_s T} \qquad\qquad \text{3-18}$$

153

The volume of each rocket body tube was found from the diameter D of the section in meters, and the length L, by substituting them into Eq. 3-17. After the internal volume V is found, it can be substituted into Eq. 3-18, to find n, the number of moles of black powder required for separation. The internal pressure of the rocket body tube is represented by p in Pascals. The temperature T is set to 1738.7 deg Kelvin, the combustion temperature for black powder [83]. The universal gas constant R of 8.314 J/mol-K was divided by the molar mass of the black powder combustion products of 162.1406 g/mol to obtain the specific gas constant R_s of 0.051276 J/g-K [84]. This changed the final output n to be in grams instead of moles. Each input was converted to metric units before being using in the equation, such as the rocket dimensions listed in Section 2.1.1.

Multiple model rocketry sources document the required pressure to eject the nose cone of a three to four-in diameter rocket as approximately 10 to 15 psig [48] [47]. The PTSS subteam measured the force to separate the nose cone from the rocket as 8 N, or approximately 0.6 psig. A detailed discussion of this is given in Section 3.1.2.2. The PTSS subteam decided to use the pressure of 15 psig to calculate the maximum amount of black powder to use, to make sure all parts of the rocket fully separated. The gauge pressure had to be converted to absolute pressure before it was used in the equations above. Adding the atmospheric pressure of 14.18 psia at 1000 feet to the 15psig needed for the rocket, produced a pressure of 29.18 psia [78]. Similarly, the pressure at 700 ft was found to be 29.33 psia [78]. Holding R_s, and T constant, Eq. 3-18 reduces to the following equation:

$$n = 0.01121pV \qquad\qquad 3\text{-}19$$

Using an inner diameter of 3.876 in, and a length of 10 in, the volume of the lower body section was found to be 299.703 cm^3. The maximum black powder used at apogee was then calculated to be 4.3626 g using Eq. 3-19. Although the total length of this section was 28 in, the internal volume to be pressurized was shortened due to the rocket motor being inserted on one end, and the electronics bay inserted on the other. Using the same diameter of 3.876 in and a length of 20 in for the upper body tube, the PTSS subteam calculated the maximum black powder for separation at 700 ft to be 8.77 g. The length of the upper airframe was originally 28 in as well, however the insertion of the nose cone and the electronics bay shortened the internal length to be pressurized. A safety factor was unnecessary in this situation, as more black powder could damage components inside the rocket, and each separation event had at least one backup charge.

For each separation event, the PTSS subteam programmed the on-board raven altimeter to ignite the first charge, wait two seconds, and then ignite the second charge. The motor's built in ejection charge was used as a third form of redundancy for the first separation event. The PTSS subteam also drilled 3 s out of the rocket motor's delay charge (see Section 1.1.2.1 for a discussion of delay charge), using a plastic bit specific to the motor that was used. This was done so the motor ejection charge fired a few seconds after the second black powder charge, but before the nose cone separation event.

The PTSS subteam also assessed the need for ventilation holes, which are sometimes used to prevent a buildup of pressure from popping the nose cone out of the rocket. Due to the diameter of the rocket being small, and the relatively low target altitude, vent holes were not needed. If the rocket were to exceed its' apogee, and reach 2000 ft, the maximum pressure difference would be about 0.991 psig [85]. This is much lower than the minimum required pressure of 10 psig for separation and would not affect the position of the nose cone.

3.1.2.2 Nosecone Separation System Model (PTSS Analysis Task 3)

The PTSS subteam decided to use a spring separation system for the nose cone separation. This design consisted of a series of layered rings as shown in Figure 99.
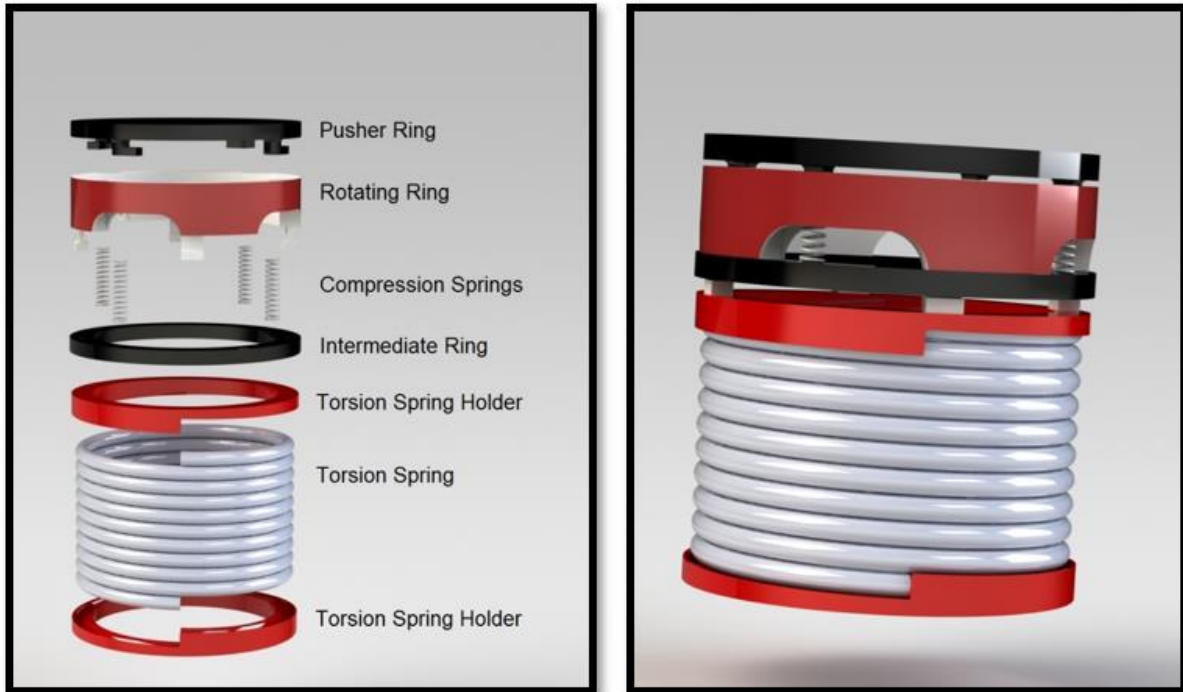
Figure 99: Exploded view (left) and normal view (right) of the separation system

In order to eject the nosecone, a force needs to be applied to the bottom face of the nosecone to break the shear pins. The general idea for generating this force was to use compression springs to push the nosecone from below. In addition, a series of rotating rings were used to physically block the springs from uncompressing until the rocket reaches apogee. A motor would then rotate the rings so the compression springs would 'unlock' and push the nosecone forward. This method was chosen because the center of the rocket needed space for the autorotation system, hence why rings were chosen as opposed to solid cylinders. We also had to make sure the motor that would rotate the rings was not in the way of the autorotation device, therefore we decided to have the

motor mounted vertically against the inner side of the rocket body. In order to translate the rotational motion of the motor to the rings, an internal gear was designed. Although, due to manufacturing and servo size limitations, the internal gear design was then replaced with the torsional spring design.

The length and spring constant for the compression springs were chosen based on the force to eject the nose cone. This ejection force is dependent on the friction force between the lip of the nose cone that will rub against the inner wall of the rocket body and the force required to shear the shear pins. The force to push out the nose cone solely due to friction was experimentally determined in the MQP lab in Higgins Laboratories. The rocket was assumed to be pointing towards the ground during separation, so the experiment was set up with the rocket facing the ground as shown in Figure 100.

Figure 100: Rocket orientation during nose cone separation test without shear pins

A Dr. Meter ES-PS01 hanging scale was attached to the back end of the rocket and the nose cone was pulled out manually. The nose cone was pulled out impulsively to best simulate the impulsive force that the spring separation system would exert on the nose cone. A camera was

pointed at the scale and took a video of the force readings during the experiment. The maximum force was then manually picked out from the video which was played back in slow motion. This was done three times which resulted in an average of 7.9 N. This force was then added to the force required to shear the shear pins.

$$F_{eject} = n_{shear}F_{shear} + F_{nosecone}$$ 3-20

In this equation, F_{eject} is the total force to eject the nose cone, n_{shear} is the number of shear pins, F_{shear} is the force to shear one shear pin and $F_{nosecone}$ is the frictional force to pull out the nose cone without shear pins. This total ejection force using one shear pin was calculated to be 103.2 N (95.3 N of this was due to the shear pin itself) which is the minimum force required to eject the nose cone. An autorotation device needs to fit in between the spring separation mechanism in the body of the rocket, which limited the width of the separation system. The allotted space is shown in Figure 101.
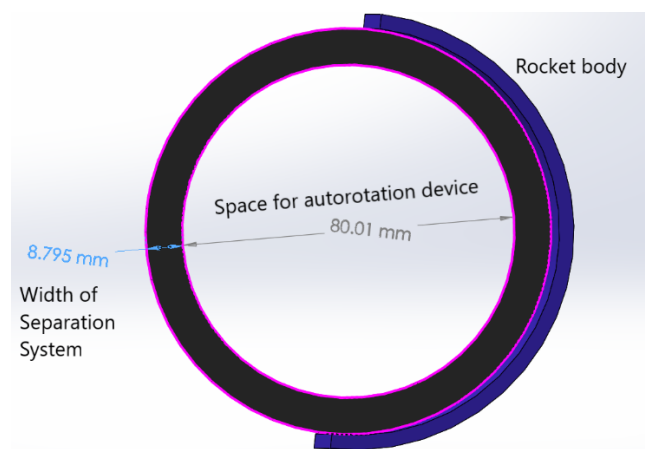
Figure 101: Cross-sectional view of rocket showing allotted space for separation system

Since only the width of the separation system was limited (space along the axis of the rocket was not limited), the spring lengths were not constrained. The necessary spring constant was found using Hooke's Law,

$$F_{eject} = kx.$$

3-21

In this equation, F_{eject} is the ejection force found previously, k is the spring constant, and x is the length of compression of the springs. While the compression length was not limited, we did not want it to be too long since bending long springs with high forces can cause them to buckle. Due to the small radius that was allotted for the spring separation system and the large force required to eject the nose cone, we decided to use four springs equally spaced around the inner diameter of the rocket.

Several design iterations were made before arriving at the final torsional spring design. The first few iterations used a gearing and servo mechanism instead of a torsional spring to produce the necessary torque to rotate the rotating ring. The two main iterations of this gearing system are shown below in Figure 102 and Figure 103. For the first iteration, a small servo would be attached to the pinion gear which would cause the rings to rotate. This gear would be turned on when the rocket was at apogee. We decided to only print a small portion of the internal gear so that once the rings rotated enough to unlock the compression springs, the system wouldn't keep rotating and jam pieces together. Although, there was not a cheap enough option for a servo that was the same width as the pinion gear and produced enough torque. In order to compensate, the final iteration of the gearing design was developed to have four pinion gears, so each servo could have less torque.

Figure 102: First iteration of gearing design
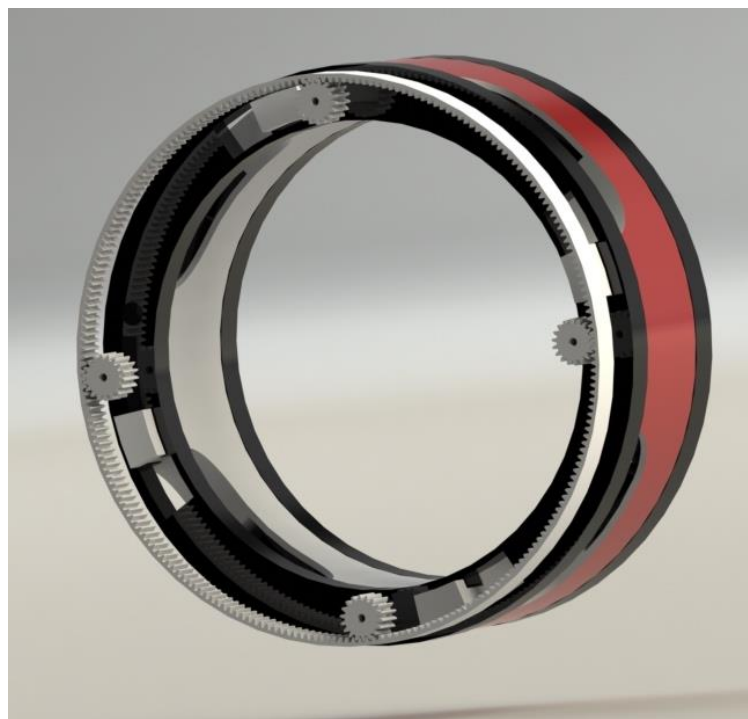
Figure 103: Final iteration of gearing design with full internal gear

There were several options for gear-driven systems in order to translate the torque from the shaft of the servo to the rotating ring, but the PTSS subteam used an internal gear setup. Since the

design must fit on a relatively small scale (within a width of 0.75 in due to space needed for the autorotation system), a setup with the simplest geometry was desired. The internal gear setup as shown in Figure 103 has both the pinion and internal gear in the same plane, whereas perpendicular gear setups would require bevel or miter gears that have a more complex tooth geometry. This simple geometry also reduced the possibility of errors during 3D printing. The 3D printed parts for the final iteration of the gearing system are shown below in Figure 104.

Figure 104: 3D printed parts for the gearing arrangement

The torque required by the servo in order to ensure that the turning ring rotates enough to unlock the spring separation mechanism is dependent on the frictional force between the rotating

rings. This is because the friction force is the only force opposing the rotation of the rotating ring. The frictional force, $F_{friction}$, is dependent on the coefficient of friction of PLS (the material of the rings in contact) and the normal force, which is the force of the springs pushing the two rings together. This resultant frictional force points in the direction of rotation. Since the internal gear is fixed to the rotating ring, this friction force is also the force that is experienced at the point of contact between the gear teeth. The friction equation below also includes a safety factor, SF. The F_{eject} term is the total ejection force that was calculated in the previous equation and acts as the normal force in the friction equation below.

$$F_{friction} = F_{eject}\mu(SF) \qquad\qquad 3\text{-}22$$

This force multiplied by the distance between the center of the pinion gear and point of contact on the tooth results in the torque induced due to friction. In this equation, r_{pitch} refers to the pitch radius of the pinion gear, or the distance between the gear center and tooth contact point. Figure 105 shows how the torque is applied to the internal gear.
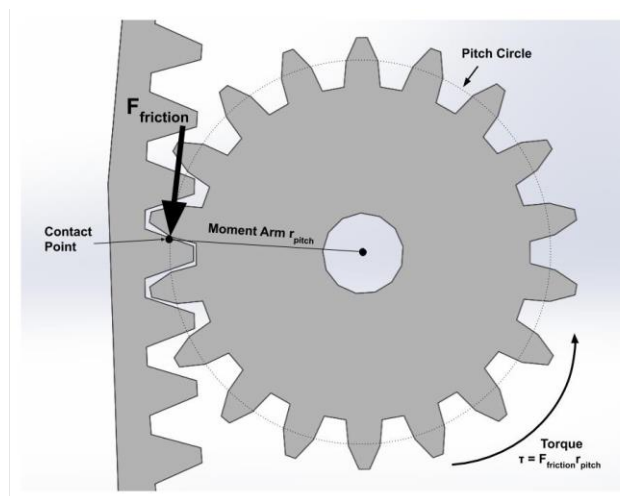
Figure 105: Diagram of torque calculation for internal gear setup

The equation for torque can be seen below.

$$\tau = F_{friction} r_{pitch}$$

This torque is the minimum torque that the servo needs to overcome in order to spin the rotating ring. Figure 106 is a graphic representation of how the required torque was found.
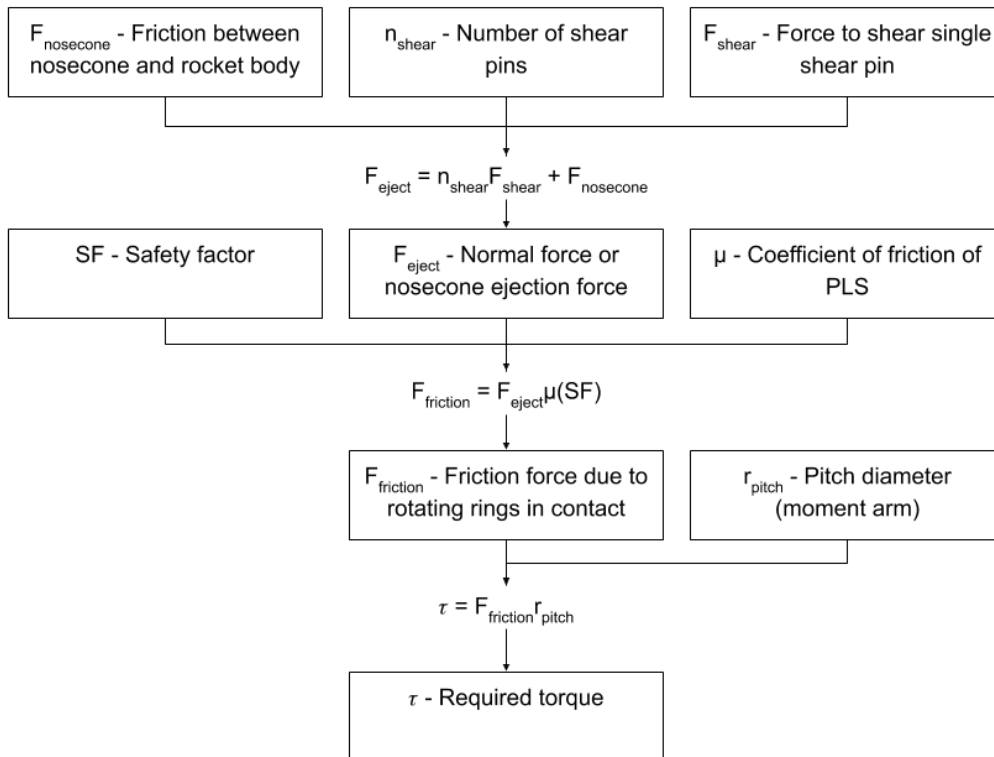
Figure 106: Visual representation of the process for finding the required torque

The required torque was calculated for various numbers of shear pins and safety factors and is shown in Table 27 and Figure 107. The frictional force between the nose cone and rocket body is variable but small compared to the shear pin force so this frictional force was assumed constant.

Table 27: Required Torque based on number of shear pins and safety factor

Number of Shear Pins	Required Torque (N-mm)		
	SF=1	SF=1.5	SF=2
0	6.4	9.6	12.8
1	82.7	123.9	165.2
2	158.8	238.2	317.6
3	235	352.5	470
4	311.2	466.8	622.4
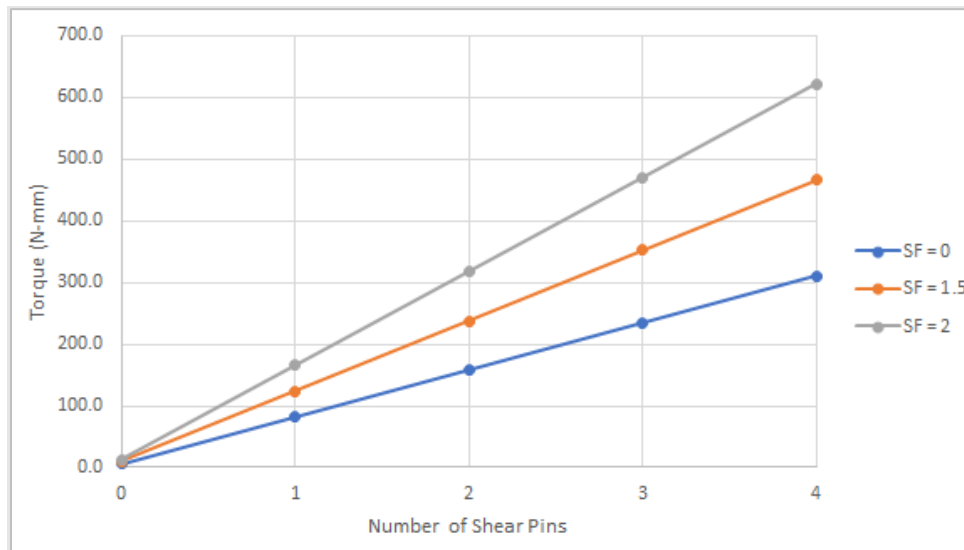
Figure 107: Required servo torque versus number of shear pins for various safety factors

As can be seen, the torque increases linearly with number of shear pins, with the safety factor also having a significant impact. For servo selection for the gearing iterations, we decided to use the torque needed from one shear pin and a safety factor of 1.5 which resulted in a required torque

of 123.86 N-mm. Commercially available motors that fit within the size constraints did not produce this amount of torque, so we decided to have four servos (and consequently four pinion gears) meshing with the same internal gear. While having multiple driving gears connected to the same gear can cause increased wear on the gear teeth, we decided this was reasonable since the angle that the ring needed to rotate (16-18 deg) was small. Although, any practical use would require at least two shear pins, which is why the final torsion spring design was selected.

The final torsion spring design with the pin pulling mechanism is shown below in Figure 108 and Figure 109.
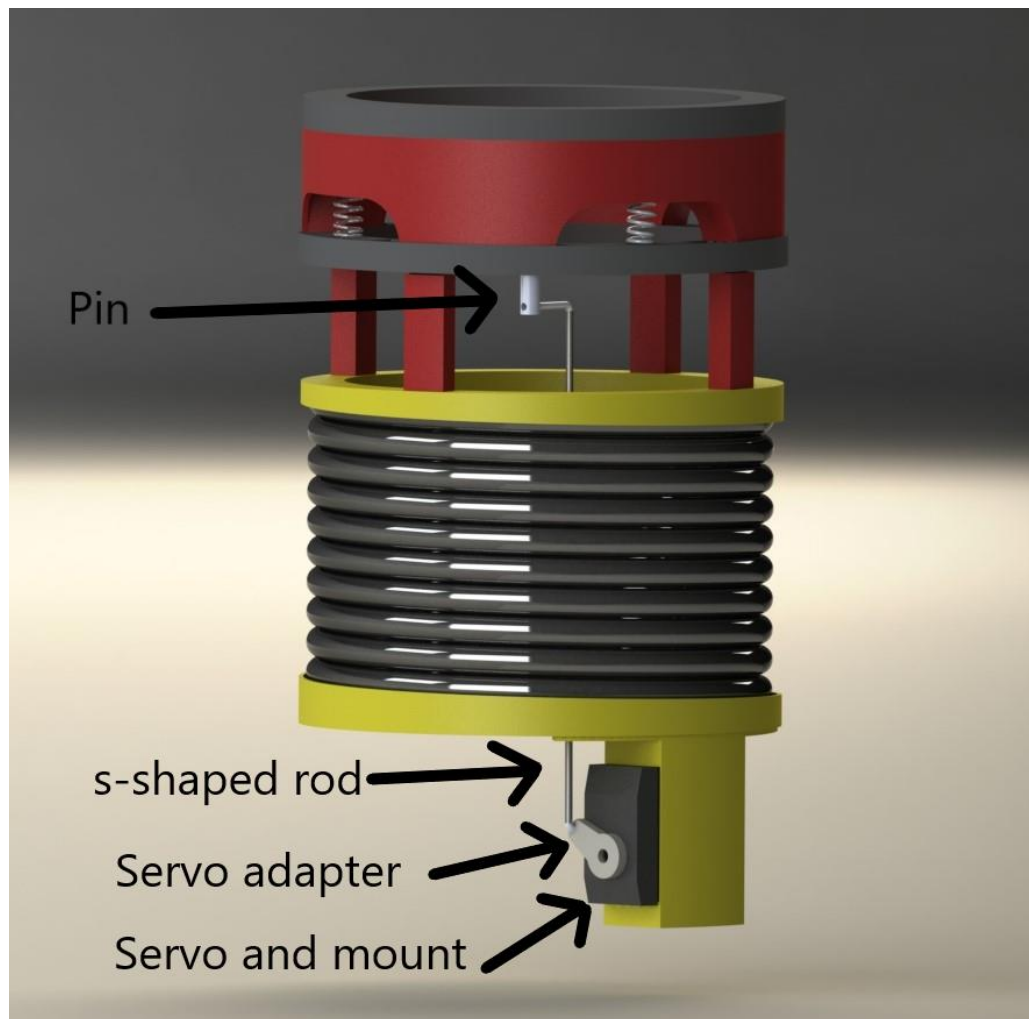
Figure 108: Final torsion spring design with pin pulling mechanism
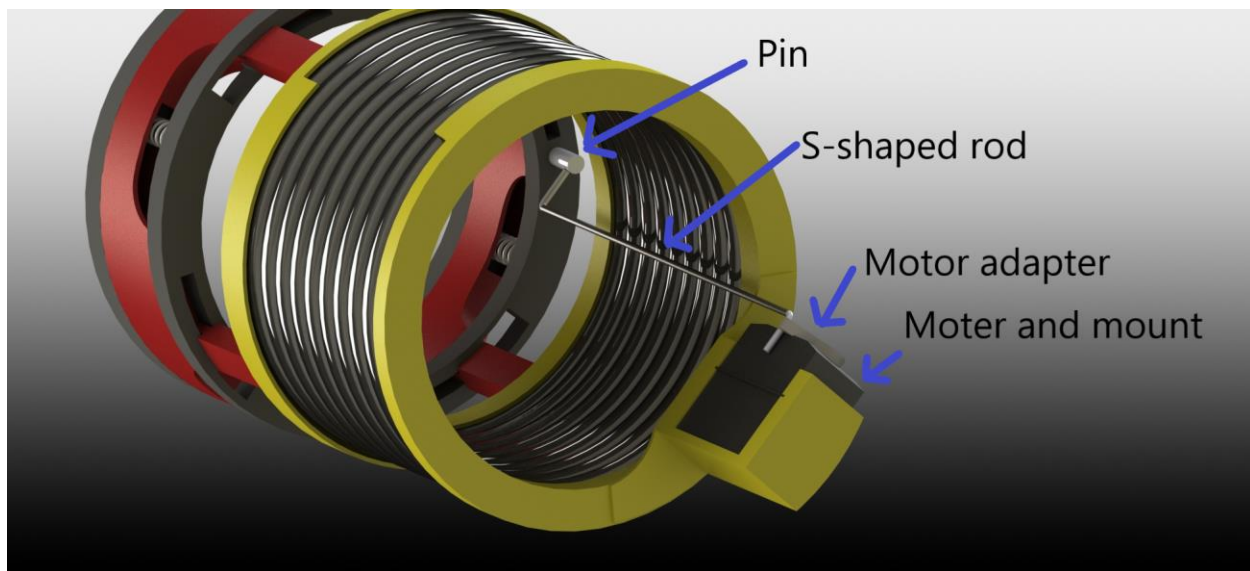
Figure 109: Inside view of pin pulling mechanism

In this design, a torsion spring is attached to the rotating ring. After the compression springs are fully compressed, the rotating ring and torsion spring are rotated to lock them in place. To prevent the torsion spring from returning to its' equilibrium position, a pin is inserted between the layer one ring, and the rotating ring. This pin is the silver cylinder connected to the long thin s-shaped rod in Figure 109. A thin metal rod connects the pin to the lever arm of the servo motor. The rod is positioned against the inside of the torsion spring, to avoid contact with the auto rotation system. When the nose cone needs to be ejected, the flight computer sends a signal to the servo motor. This turns the lever arm of the servo motor and pulls the pin toward the bottom of the rocket. Once the pin is release, the torsion spring returns to its' equilibrium position, releasing the compression springs, which extend and push against the bulkhead of the nose cone.

The torsion spring used in this design can produce a torque of 1470.71 N-mm at 17 deg of twist (the required angle the rotating ring must rotate to release the compression springs). This spring was quoted from Acxess Spring in California and produced more than enough torque for

two or more shear pins. This means that in order to release the system, a pin must be pulled longitudinally in the direction of the rocket body, which was not geometrically constrained. The torsion spring dimensions were calculated using Acxess Spring's torsion spring calculator [86]. The outer diameter, inner diameter, and required torque were the inputs, and the number of coils were the output. The material was chosen to be music wire ASTM A228 to lessen the torque, since it had already passed to the required torque for multiple shear pins. The 3D printed parts for the final torsional spring arrangement are shown below in Figure 110.
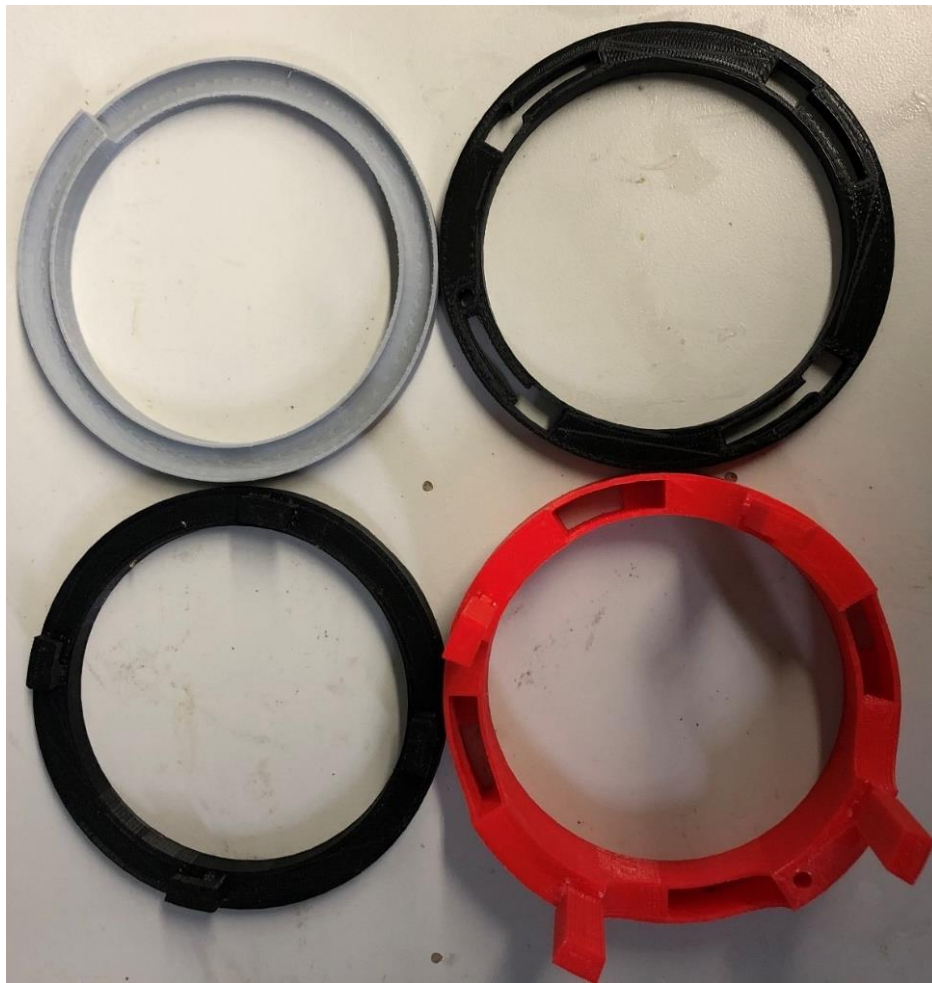
Figure 110: 3D printed parts for the torsional spring arrangement

These parts are like the parts for the gearing arrangement where adjustments were made to the rotating ring to accommodate the torsion spring holder. Figure 111 shows these parts put together without the springs.

Figure 111: Assembled torsional spring separation system

The system is shown upside down where the torsional spring would fit into the grey torsional spring holder on top. The rotating pieces fit together and were able to rotate with little resistance. The torsional spring itself was not purchased because we decided it was not worth the cost (quoted at $259.38 for one spring from Acxess Spring). While the full system was not assembled, both the portion shown in Figure 111 and the pin pulling mechanism were assembled, showing proof of concept of the design. A placeholder part was printed with the same

dimensions as the torsional spring in order to visualize the entire system and is shown below in

Figure 112 and Figure 113.

Figure 112: Torsion spring placeholder
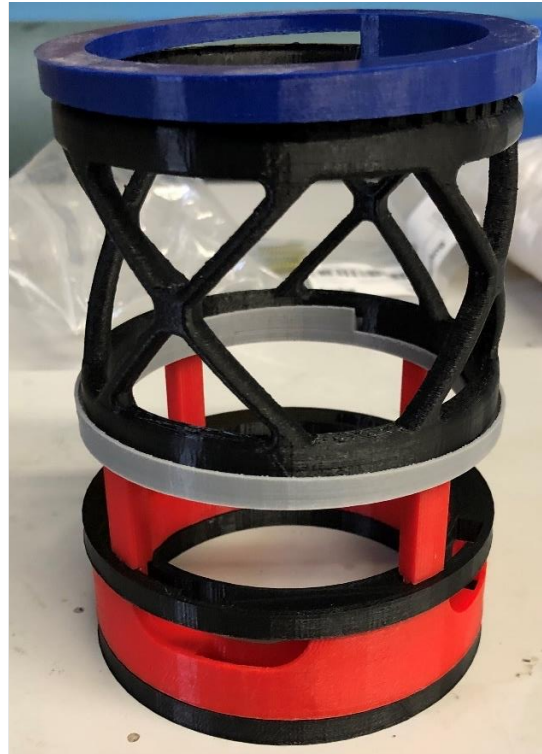
Figure 113: Final assembled separation system with torsional spring placeholder

Springs were epoxied to the intermediate ring, fed through the rotating ring, and epoxied to the bottom of the pusher ring on the L-shaped pieces. The rotating ring would fit into the L-shaped piece of the pusher ring, holding the springs in a compressed position and preventing the pusher ring from moving upwards. This rotating ring fits through spaces in the intermediate ring and is epoxied to the torsion spring holder. The rotating ring also has T-shaped pieces that fit into the intermediate ring to restrict it to purely rotational motion. The torsion spring is twisted and kept in this torqued position by a pin that goes through the intermediate and rotating ring. When the pin is pulled, the torsion spring untwists, causing the rotating ring to rotate with it, which moves it out of the way of the L-shaped pieces on the pusher ring.

3.2. Analysis

The PTSS subteam analyzed the temperature distribution throughout the motor casing, validated motor performance properties for the I216 motor, and investigated the implementation of a spring-loaded stage separation system. The results of these analysis tasks are presented in this section. For the temperature distribution model, the temperature gradient in the I216 motor is presented. For the motor performance analysis, the overall chemical equilibrium equation and reaction properties for the combustion reaction in the I216 motor are presented. Additionally, the results from designing and manufacturing a spring-loaded separation system are discussed.

3.2.1 Temperature Distribution (PTSS Analysis Task 1)

This section presents the results of the temperature distribution analysis conducted using COMSOL. Table 28 summarizes the boundary conditions that were defined for this analysis.

Table 28: COMSOL Boundary Conditions for the thermal model

Boundary	Material	Condition	Condition Equation	Option	Input
1	Aluminum Casing	Heat Flux	$q_0 = h(T_{ext} - T)$	Convective Heat Coefficient	h = 25 W/(m²·K) T_{ext} = 293.15 K
2	Solid Ammonium Perchlorate	Initial Value	$T = user\ defined$	Temperature	293.15 K
3	Fluid	Volumetric Heat Source	$Q = Q_0$ where Q_0 is user defined	General Source	6.665x10⁹ W/m³
3	Fluid	Temperature	$T = T_0$ where T_0 is user defined	N/A	2547.7 K

COMSOL used these specified boundaries and values too compute the temperature across the model of the motor that we were conducting the analysis on. Figure 114 provides a visual representation the temperature distribution at 2.9 seconds or the estimated burn time of the I216 motor.
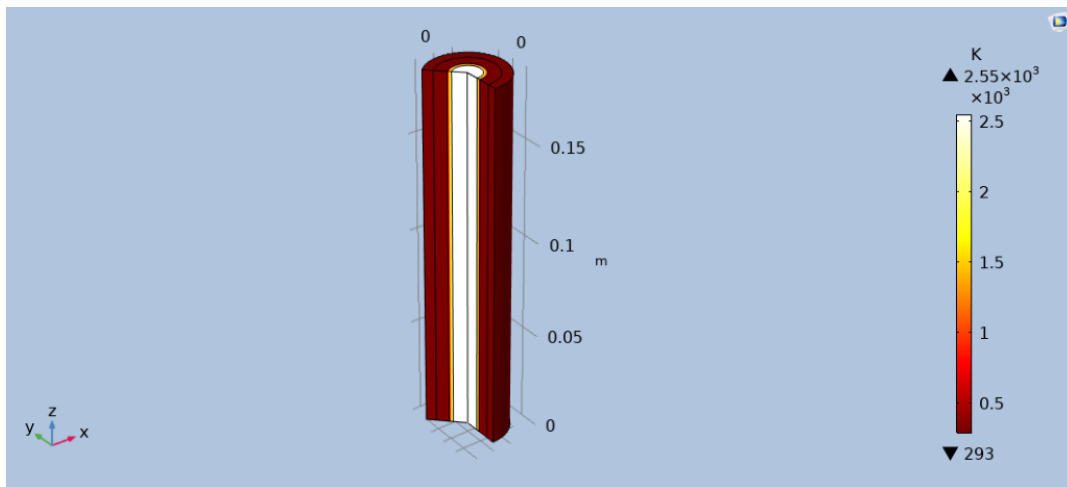
Figure 114: Temperature distribution in motor at t = 2.9s

In addition, Figure 115 shows a line plot of the radial temperature distribution across the motor at a height of 0.186 m, which is the top surface of the motor, and at 2.9 seconds after launch.
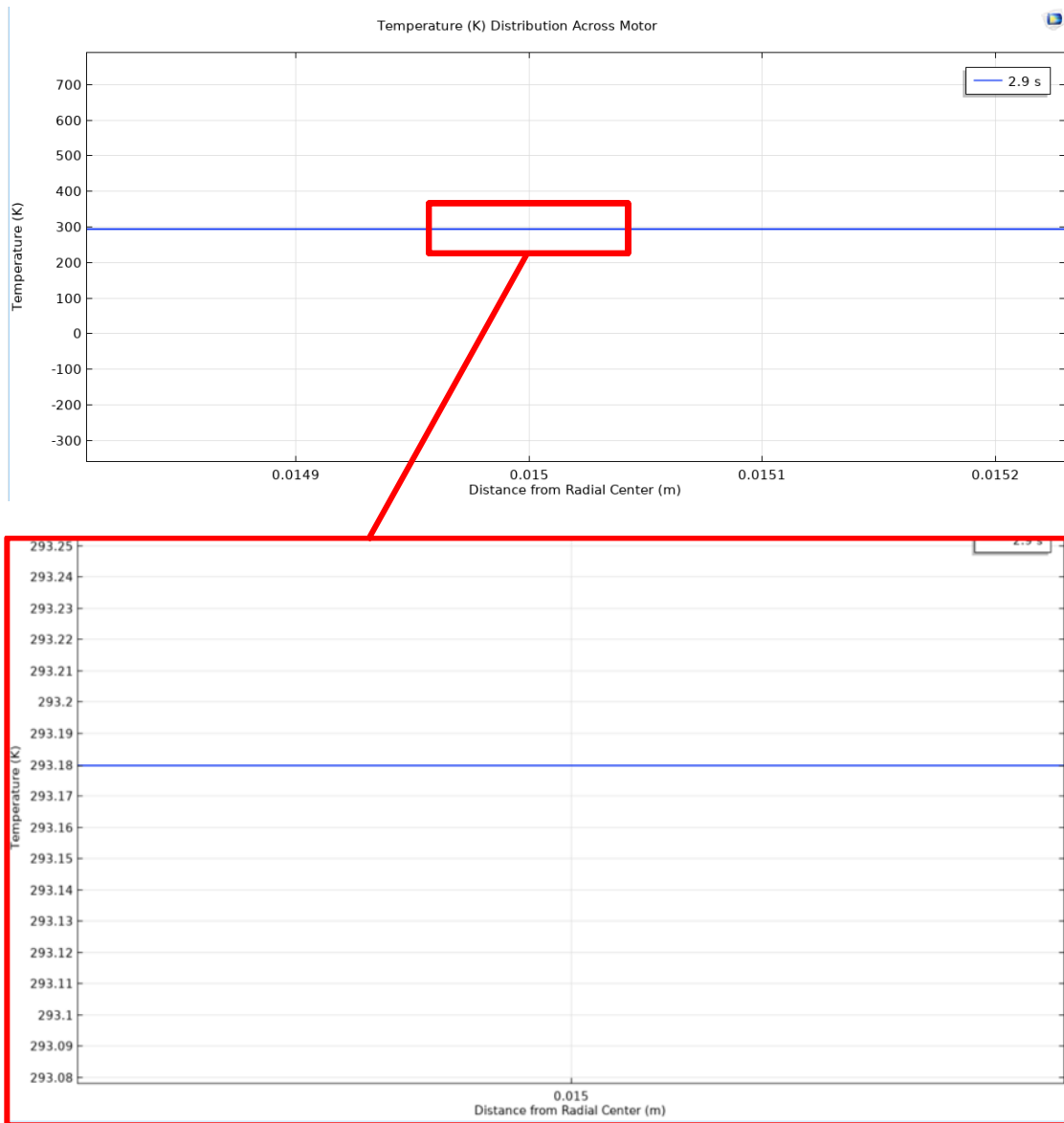
Figure 115. Final temperature at distance of 0.015 m

Using COMSOL's ability to zoom into specific data points, the exact final temperature of the aluminum casing (the area where the distance from the radial center is 0.015 m) can be seen. From analyzing the resulting data sets the final temperature of aluminum casing at 2.9 seconds was

293.18 K. While this is only 0.03 K greater than the initial temperature that was set for the outermost boundary, this does signify that there was heat transfer through the motor casing.

In addition to the temperature distribution calculation, as a sanity check to ensure our model was working properly, we also looked at the velocity magnitude within the fluid domain that was specified for the analysis. Table 29 below lists the fluid domain boundary conditions applied in our model. This simulation was run as a time-dependent study, so the boundary conditions are slightly modified to establish initial values. The condition listed in Table 29 for the outlet boundary includes a hydrostatic stress reference pressure that is added to the pressure specified for the outlet boundary condition given by Eq. 3-5. When a user modeling a compressible flow selects the option *Compensate for hydrostatic pressure,* according to the user's guide*, "*the hydrostatic pressure is automatically added to the pressure entered in p user input." The parameter *K* represents the viscous stress tensor, i.e. the second and third terms in the square brackets in Eq. 3-5. As noted earlier, these equations are written in this report using the exact scalar, vector, and tensor notation used in the COMSOL documentation.

Table 29: COMSOL boundary conditions and Inputs for the fluid domain model

Boundary	Condition	Condition Equation	Option	Input
1	Inlet	$u = -U_0 n$ where U_0 is user defined	Velocity	$U_0 = 21.7$ m/s
2	Wall	$\mathbf{u} = 0$	No Slip	N/A
3	Symmetry	N/A	N/A	N/A
4	Outlet	$[-pI + K]n = -(p_o + p_{hydro})n$	Pressure	$p_o = 2.24$ MPa

These conditions were all preset options that COMSOL provided for the user to choose from. Figure 106 provides a visualization of where the boundaries are defined.

With these boundary layers and conditions established, COMSOL then produced a 2D axisymmetric graphic representation of the velocity magnitude. As seen in Figure 117, the area pertaining to the no slip wall condition towards the top of the motor corresponds to a velocity of 0 m/s as expected. Whereas at the outlet of the model, the velocity magnitude is at its greatest value of 2220 m/s.
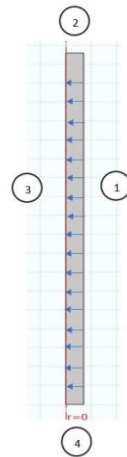
Figure 116: Location of boundaries in the fluid domain
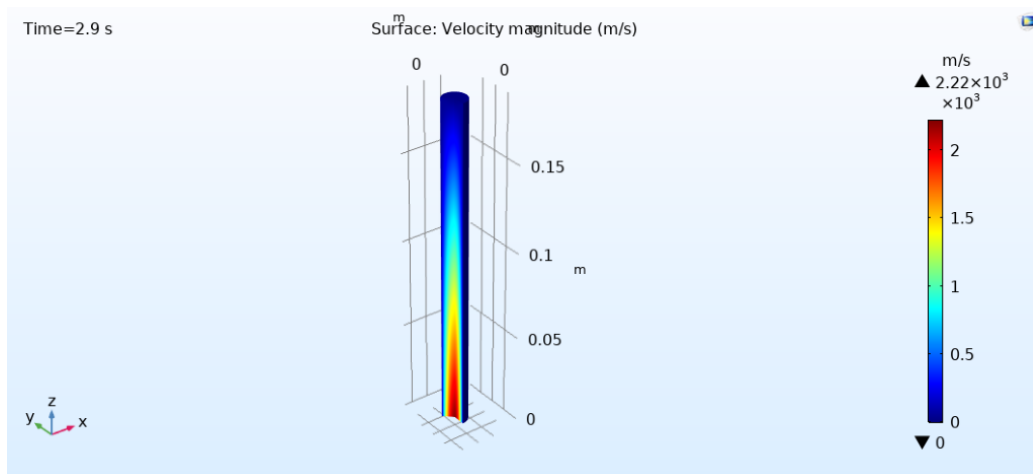
Figure 117: 2D axisymmetric velocity magnitude graphic

3.2.2 Motor Performance Model (PTSS Analysis Task 2)

This section presents results of using Cantera to simulate the chemical equilibrium problem for ammonium perchlorate and aluminum. Table 30 summarizes the assumed conditions for this calculation:

Table 30: Assumptions used in chemical equilibrium analysis in Cantera

Conditions
Reactants are ammonium perchlorate and aluminum
Chemical equilibrium occurs in motor chamber
Constant specific internal energy and volume during chemical equilibrium process
Complete combustion
Initial temperature = 293 K
Initial pressure = 101,325 Pa
Fixed internal volume = 416.22 cm^2

Cantera assumed decomposition of the reactants and formation of all possible products. There were a total of 41 combustion product species, however the five dominant species are listed by name and the remaining species are listed as trace species in the overall chemical equation. The overall reaction (in terms of each species respective mole number) is:

$$0.8NH_4ClO_4 + 0.2A \rightarrow 0.21673O_2 + 0.2825H_2O + 0.088376N_2 + 0.15951HCl + 0.20179Al + trace\ species \qquad \text{3-24}$$
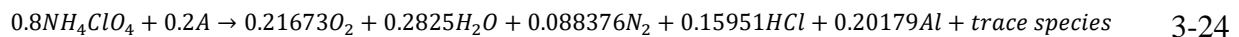
In addition, thermodynamic properties of the reaction were found and are listed in Table 31. Table 32 summarizes properties of the flow in the motor nozzle that were calculated using isentropic flow relations. This calculation assumed a gas mixture with properties listed in Table 31, and a chamber pressure and temperature of 2.24 MPa and 2547.70 K respectively.

Motor performance data published by the manufacturer shows that the thrust is 216.0 N and the specific impulse is 207.58 s for the I216 motor [87].We expected the analytical solution to

result in a higher specific impulse compared to the listed value from the manufacturer. We expected this in part because the isentropic flow calculation neglects many losses in a real flow (viscous effects, divergence loss, etc.) and also because the chamber temperature used for the initial condition was taken as the chemical equilibrium temperature in Cantera and did not account for any heat losses. There would be a heat flux through the motor casing hence lowering the chamber temperature and ultimately lowering the specific impulse as well.
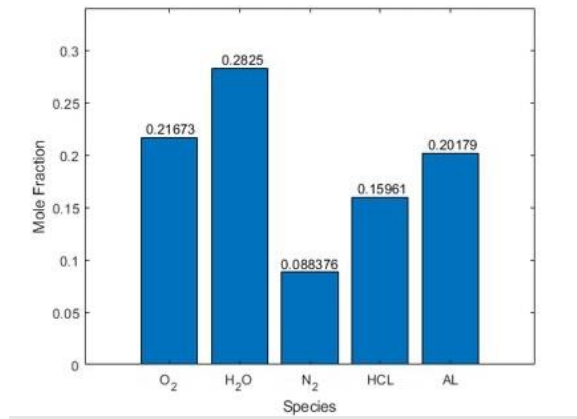
Figure 118: Mole fractions for the primary product species for the equilibrium chemical reaction

Table 31: Thermodynamic properties for product mixture obtained from chemical equilibrium solution

Property	Value	Unit
Chemical Equilibrium Temperature	2547.70	K
Pressure	2.24	MPa
Density	2.87	Kg/m^3
Mass Specific Heat at Constant Pressure	1414.40	J/kg-K
Mass Specific Volume at Constant Pressure	1108.96	J/kg-K
Mean Molecular Weight	27.22	Kg/kmol
Specific Heat Ratio	1.28	-

Table 32: Properties of the flow in the motor nozzle (analytical solutions)

Property	Value	Unit
Expansion Ratio, $\frac{A_e}{A_t}$	5.00	-
Exit Mach, M_e	2.92	-
Exit Temperature, T_e	1169.71	K
Exit Pressure, p_e	60,810.85	Pa
Exit Density, ρ_e	0.17	kg/m3
Exit Velocity, U_e	2676.50	m/s
Characteristic Velocity, c^*	1330.89	m/s
Thrust, T	237.02	N
Specific Impulse, I_{sp}	272.83	s

4 Flight Dynamic Analysis – Design and Analysis

The goal of Flight Dynamics Analysis team was to run various analysis of the vehicle while in flight. Some of the analysis includes evaluation of aerodynamic loads, rocket performance, and spin stabilization. Each task was done using various software tools such as MATLAB and ANSYS Fluent. MATLAB was used to solve the necessary equations which evaluated the aerodynamic forces and performances of the rocket. The MATLAB analysis required inputs such as rocket geometry, inertia properties, center of pressure and center of mass of the rocket. Similarly, Fluent required inputs like rocket geometry along with boundary conditions, fluid properties and mesh characteristics. Fluent was mainly used to run simulation at different conditions which would provide the team with necessary outputs. Using Fluent, the FDA subteam was able to estimate the aerodynamic forces and moments on the vehicle at various trim conditions. The analysis product from Fluent includes plots of forces, pressure contours and moments acting on vehicle of various design. The FDA subteam was also responsible for designing components such as the fins, e-bay sled and helping other sub-team with the integration of avionics such as accelerometer, altimeter and gyros.

4.1. Baseline Fin Design and Production

The fins for the rocket were chosen to be a trapezoid shape as shown in Figure 119. The trapezoid shape was selected because it is easier to add an airfoil profile to the shape which makes the manufacturing process convenient. One method for sizing rocket fins uses the diameter of the rocket to determine the root chord, span, and tip chord of the fins. These initial dimensions of the fins were based on the method for fin sizing described in reference [82]. Here, the root chord and the span of the fins were twice the diameter of the rocket. The tip chord of the fins had the same size as the rocket's diameter. These fin dimensions, based on the diameter of the rocket, provided

us with fins that were too large and proved to be unstable after analysis in OpenRocket. As mentioned in Section 1.1.3.1, the stability margin for an ideal rocket is between 1.5-2.5. The fin design based on the diameter of the rocket had stability of 5.0, which would make the rocket overstable. To get the stability within the range, a new fin size had to be designed. Figure 120 shows the dimensions of the fin with which the desired stability was achieved.
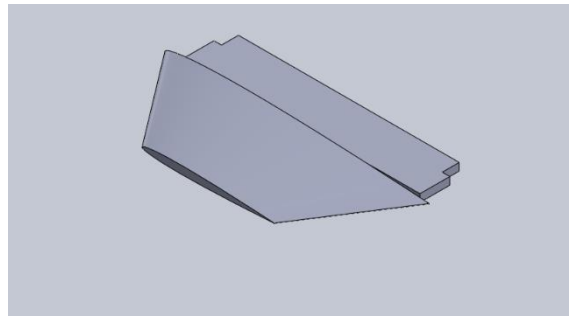
Figure 119: SOLIDWORKS model of baseline fin.
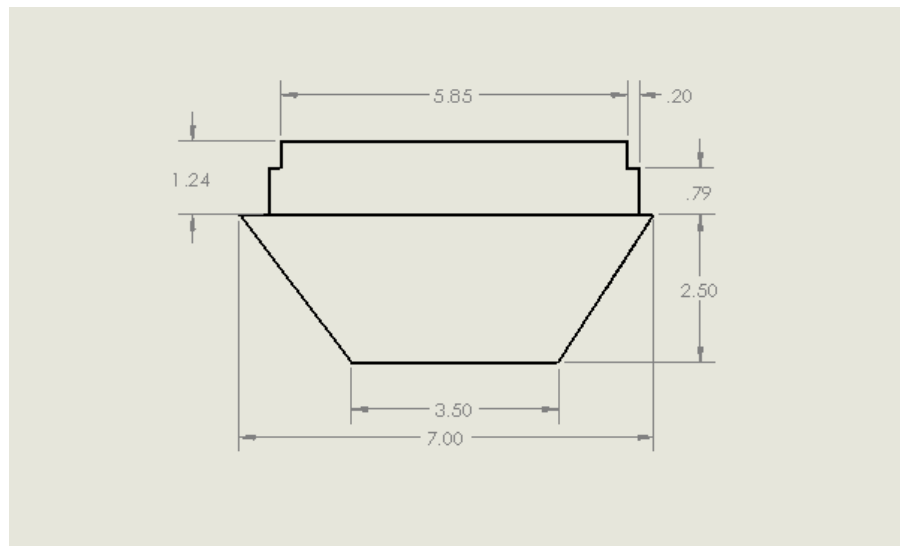
Figure 120: Fin and fin tab with dimensions

An airfoil profile was added to the fin to make it aerodynamically efficient. The airfoil selected was a symmetrical NACA 0006 which has a thickness of 6% with respect to its chord. This airfoil

was selected because it has low drag coefficient at 0 deg angle of attack compared to other airfoils such as NACA 0008 and NACA 0012. The drag coefficient of the airfoil can be found from Airfoil Tools site or from running a simulation assuming specific flight conditions using Fluent. For our case, the drag coefficient was analyzed in Fluent as a 3D fin rather than a 2D airfoil. The fin was analyzed at velocity of 103 m/. The model used to analyze the fin was a turbulent flow k-epsilon (k-ε) model. The drag coefficient of the fin was determined to be 0.005. Figure 121 shows the convergence history for the drag coefficient solution.
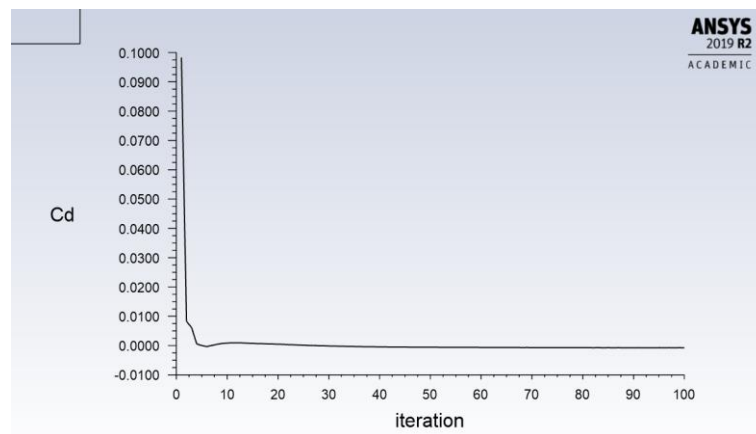
Figure 121: Convergence history for fin drag coefficient calculation using ANSYS Fluent
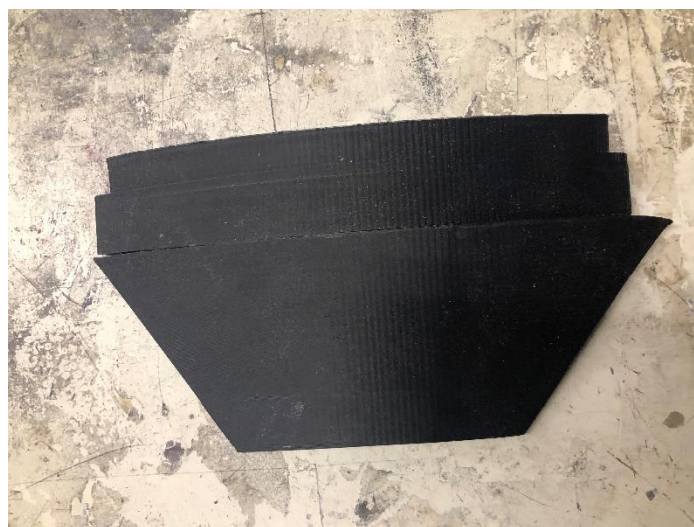
Figure 122: 3D printed fin

4.2. Avionics and the E-Bay

4.2.1 Avionics Selection

Since the innovative rocket did not require additional sensors or different electrical components, the components in the e-bays of both the baseline and innovative rockets were the same. A Raven 3.0 altimeter (Featherweight Altimeters) acted as the microprocessor, IMU and altimeter. The Raven therefore served as the onboard flight computer, using its built-in microcontroller to trigger flight events including the deployment of a parachute in the baseline rocket and the release of the recovery system in the innovative rocket. The Raven is equipped with a 400 Hz axial accelerometer and 200 Hz lateral accelerometer, both capable of detecting acceleration of +/- 105 gees of acceleration. The Raven also has a 20 Hz barometer with data values accurate to 0.3% which was used to determine altitude [88]. These frequencies refer to the measurement bandwidth, or how frequently data is collected. For example, 20 Hz for the barometer implies that the barometer takes pressure data 20 times per second, or collects a data point every 0.05 s. The accelerometer and barometer send information to the Raven's microcontroller which was programmed to trigger flight events with four outputs that could relay a maximum current level of 25 A. The Raven's microcontroller was programmed with the Featherweight Interface Program (Featherweight Altimeter) to execute these events. The outputs placed one significant constraint on the flight event profile; there cannot be more than four individual events that need to be triggered for a single flight. The Raven is powered using a lithium-polymer (LiPo) battery, which could power the Raven during the flight and sending the appropriate power to trigger flight events [88]. Additionally, a data collection board (RD- KL25-AGMP01) (NXP/Freescale, Eindhoven Netherlands) was used to collect data for analysis after launch. This collection board is equipped with a six-axis e-compass (FXOS8700CQ) (NXP/Freescale, Eindhoven Netherlands), a

three-axis digital angular rate gyroscope (FXAS21002C) (NXP/Freescale, Eindhoven Netherlands), a precision altimeter and temperature sensor (MPL3115A2) (NXP/Freescale, Eindhoven Netherlands), and a microcontroller capable of saving data to a micro SD card so that data can be downloaded through a USB port after flight.

Figure 123. RD-KL25-AGMP01 evaluation board [89]. © 2015, NXP

This collection board has a built-in battery that powers the sensors and data logger during flight [90]. An arming switch was installed on the outside of the rocket body to turn on the Raven and data collection board immediately before launch. This switch ensured that power is not used until needed, resulting in a smaller flight battery requirement. Additionally, activating the sensors just before launch ensures critical flight data is recorded. The sensors only have a limited memory capacity of 480 s of high rate recording and 35 mins of low rate recording for the Raven and 160

KB for the data collection board. If the sensors were turned on during pre-launch preparations it would be possible for too much of the limited memory space to be used on useless data.

The Raven provided acceleration and barometric data, while the data collection board provided acceleration, barometric, and gyroscopic data. The Raven and data collection board were selected over other sensors because they both have independent microcontrollers. This allows the Raven and data collection board to be independent of each other. Additionally, this setup does not need an external microcontroller like an Arduino, saving space and reducing complexity. Finally, these components were selected because they both have their own batteries and support internal data collection. Specifications for the Raven 3.0 Altimeter and the data collection board can be found in Table 33 and Table 34.

Table 33. Specifications for the Raven 3.0 Altimeter (Anon, 2015)

Raven 3.0 Altimeter Specifications	
Axial Accel Range	70 Gs
Axial Accel Frequency	400 Hz
Axial Accel Resolution	0.09 Gs
Lateral Accel Range	70 Gs
Lateral Accel Frequency	400 Hz
Lateral Accel Resolution	0.09 Gs
Download Interface	USB Mini
Baro Range (kft)	100
Baro Resolution	0.00004 atm
Pyro Outputs	4
Single-Battery Max Output (Amps)	9 and 40
2-Battery Max Output (Amps)	9 and 40
Other Recorded Measurements	Temperature 4 Continuity Voltages All Event Logic Battery Voltage
High-Rate Recording Time	480 seconds
Low-Rate Recording Time	35 minutes
Size	0.8" x 1.8" x 0.5"
Mass	6.6 grams

Table 34. Collection Board Technical Specifications (Freescale Semiconductor, 2015)

RD – KL25 – AGMP01 Collection Board Specifications	
RD-KL25-AGMP01	Data Collection Reference Design with 10-axis sensing via the FXAS21002C, FXOS8700CQ, and MPL3115A2
FXOS8700CQ	6-Axis Sensor with Integrated Linear Accelerometer and Magnetometer
FXAS21002C	3-Axis Digital Angular Rate Gyroscope
MPL3115A2	20 to 110 kPa, Absolute Digital Pressure Sensor
MC32BC3770CSR2	2.0 A Switch-Mode Charger with Intelligent Power-Path for 1-Cell Li-Ion Battery
Kinetis KL25Z	Kinetis KL25, 48 MHz Cortex-M0+ Based Microcontroller with USB
Kinetis K20	Kinetis K20, Cortex-M4 up to 160KB flash

In the event of a crash, having two independent systems that can provide flight data ensured a backup for the acceleration and barometric data. A drawback to this selection was price, but the budget allowed for the two systems, providing some redundancy. Flight sensor data from the HPMR test flight are presented in Section 5.3. The data was used in subsequent analysis of the model rocket, including comparing the real flight performance and dynamic results to flight simulations. Specifically, the barometric data from both sensors was used to determine the maximum height the rocket achieved in a given test flight. The accelerometer data from both sensors determined the acceleration during launch. Additionally, the accelerometer data was useful in comparing the descent velocity of the model rocket under the parachute to the estimates from the baseline rocket recovery system model. The measurements by the gyroscope on the data collection board are especially critical to analyzing flight performance. The measurements will be used by future teams to better understand how the fin design may affect the spin of the rocket during launch and throughout flight.

4.2.2 Avionics Testing

To ensure the Raven would trigger the series of events for releasing the apogee and main parachutes, a flight simulation was performed. The Raven is preprogrammed with a feature that enables the user to perform a realistic flight simulation. This is useful for verifying the deployment settings and checking the connections to the terminal blocks that are installed on the tops and bottoms of the e-bay. The Raven's deployment settings are shown in Figure 124:

Figure 124: Raven deployment settings

The "Apogee Pyro Channel" controls the event that triggers the primary charge for the apogee parachute with the 3rd channel as a backup for this parachute on a slight time delay. Channels require all conditions to be met at a given time before an electrical signal is sent to the charge. Both the apogee and the 3rd channel require a negative velocity (< 0 ft/s) to send the signal. The condition is directly dependent on measurements from the accelerometer. The "Main Pyro Channel" controls the event that triggers the primary charge for the main parachute with the 4th channel as a backup for this parachute on a slight time delay. Both channels require the height above the ground to be less than 704 ft. The pressure must also be increasing, as this indicates that the rocket is falling. These conditions are met by measurements from both the accelerometer and barometer. Each of these channels were tested for continuity and firing an electrical signal during flight simulation. For the continuity test, a channel was wired into a terminal block installed on the e-bay and a length of wire was used to connect the positive and negative sides of the terminal block. The Raven was then turned on and indicated through a series of audible beeps a particular channel and if it detected continuity on that channel. This continuity test was conducted for each of the channels on the Raven as well as all four terminal blocks on the e-bay. Next, for the electrical test, the length of wire connecting the positive and negative sides of the terminal blocks were replaced with a resistor and an LED. The Raven then underwent a flight simulation with one channel connected to a terminal block and LED. If the LED lit at the correct time based on the simulated flight, the test was successful. This process was repeated for each channel until every channel triggered the electrical signal at the expected time during the simulated flight.

4.3.   Aerodynamic Load Analysis

4.3.1   Aerodynamic Loads – Simple Model (FDA Analysis Task 1)

To understand interactions between the rocket and its environment, a series of analytical calculations based on the rocket's geometry and flight conditions were completed. The aerodynamic parameters of interest, which can be used to calculate loads and moments, were the drag coefficient, normal aerodynamic force coefficient, and aerodynamic moment coefficients. Once these were found, their respective forces could be plotted parametrically as functions of angle of attack and velocity to characterize a range of flight conditions. These plots could be compared to the same respective plots generated as part of FDA Analysis Task 2, helping to determine the accuracy of the analytic method. If the results of FDA Analysis Tasks 1 and 2 were comparable (on the same order of magnitude), the analytic method could be deemed valid. The model presented in this section is based primarily on the model described in the literature [91]. The assumptions made by the analytic aerodynamic load calculations apply to this rocket and were [91]:

- Calculations initially assume the rocket's angle of attack is approximately 0 deg. Later calculations analyze the angle of attack over a small range of values, from 0 to 10 deg.

- The flow of air over the rocket could be considered "steady flow" since the properties of air during flight do not vary significantly with respect to the expected maximum altitude

- The rocket does not physically deform during flight and could be considered a rigid body

- The nose tip of the rocket is conical and thus a sharp point

This analytic method, described in this section, was chosen for calculating aerodynamic loads because of its ability to estimate the complex aerodynamic coefficients using simple, analytical expressions derived from semi-empirical and analytic methods.

The rocket's geometry was divided into the body, base, tail, and fin components whose aerodynamic loads were calculated individually then recombined to obtain the total coefficient value. For this analysis task, the "body" includes to nose cone, upper frame, and lower frame. Base, tail, and fins correspond to the aft end of the rocket near the fins and are collectively referred to as the "tail." A graphical representation of the drag components and how they relate to the different parts of the rocket are shown in Figure 125.
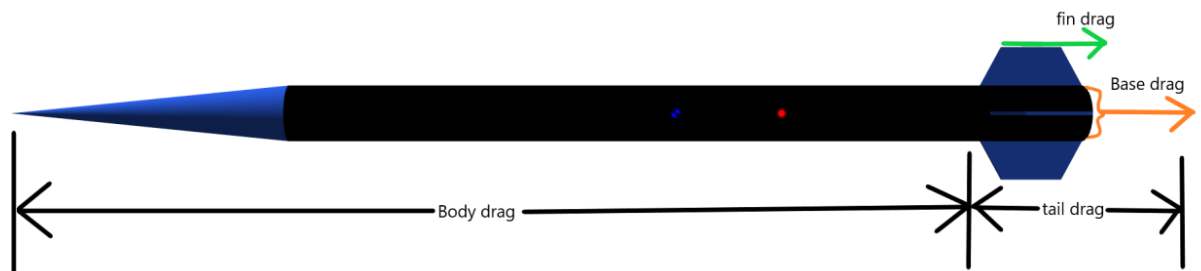
Figure 125: General location of where drag components are on the rocket.

Effects of body and tail interference were also estimated, accounting for drag effects occurring near the surface of the rocket where the fins are affixed to the body [91]. Figure 125 illustrates how the various components are broken down for drag estimation; the relevant geometric notation and values are presented in Appendix H.

Figure 126 shows the direction and orientation of the aerodynamic forces used in the calculations.
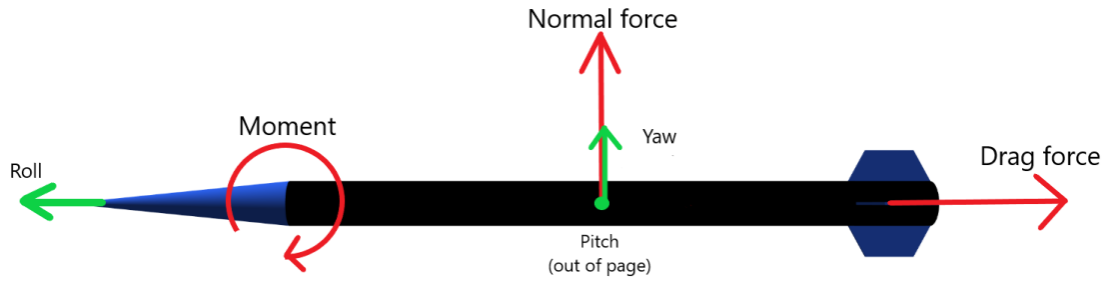
Figure 126: Orientation of aerodynamic loads and principle Euler directions.

Figure 127 below shows a top-down flowchart for calculating the total drag coefficient, discussed below. Every equation in the flowchart is a numbered equation in the text and can also be found in Appendix G located in Section 7.7. The equations labelled "A" and "B" on the right side of the flowchart correspond to the "A" and "B" blocks on the left side of the flowchart, respectively. The individual terms for the equation in the first "A" block are defined in all other "A" blocks that follow. The same is true for the "B" blocks.

The equation for Total Drag Coefficient, C_D, represented by

$$C_D = C_{D_{T_T}} + C_{D_{T_B}}$$

4-1

divides the rocket into "tail" and "body" components.

The equation for the tail drag component, $C_{D_{T_T}}$, is given by

$$C_{D_{T_T}} = C_{D_{f_T}} + C_{D_{L_T}} + C_{D_{B_T}} + C_{D_{TT}}$$

4-2

189

Drag on tail (fins)

$$C_{D_{T_T}} = C_{D_{f_T}} + C_{D_{L_T}} + C_{D_{B_T}} + C_{D_{TT}}$$ A

Total Drag

$$C_D = C_{D_{T_T}} + C_{D_{T_B}}$$

Drag on body

$$C_{D_{T_B}} = C_{D_P} + C_{D_{BB}}$$ B

Fin skin friction drag

A $$C_{D_{f_T}} = 2NC_{f_c}\left(\frac{A_T}{A_r}\right)$$

N: Number of fins
A_T: Planform area of one exposed fin
A_r: Reference area

$$C_{f_c} = C_f(1 - 0.12M^2)$$
M: Mach number

$$C_f = \frac{1.328}{\sqrt{R_e}}$$
R_e: Reynold's number

Fin leading edge drag

A $$C_{D_{L_T}} = 2N\left(\frac{Sr_L}{A_r}\right)\cos^2\Gamma_L\,(\Delta C_D)$$

N: number of fins
S: fin semi span
r_L: fin leading edge radius
A_r: reference area
Γ_L: leading edge sweep angle

$$\Delta C_D = (1 - M^2)^{-0.417} - 1$$
M: Mach number

190

Figure 127: Total drag coefficient top-down flowchart displaying how formulas relate to one another, used for calculations

is the sum of the tail skin friction drag coefficient, $C_{D_{f_T}}$, tail leading edge drag coefficient, $C_{D_{L_T}}$, tail trailing edge drag coefficient, $C_{D_{B_T}}$, and tail thickness drag coefficient, $C_{D_{TT}}$. The relations used to calculate these terms are given by Equations 4-3 through 4-6:

$$C_{D_{f_T}} = 2NC_{f_c}\left(\frac{A_T}{A_r}\right) \qquad \text{4-3}$$

$$C_{D_{L_T}} = 2N\left(\frac{Sr_L}{A_r}\right)\cos^2\Gamma_L(\Delta C_D) \qquad \text{4-4}$$

$$C_{D_{B_T}} = \frac{0.135N\left(\frac{A_{B_f}}{A_r}\right)}{\sqrt[3]{C_{f_B}}\sqrt{K-M^2\cos^2\Gamma_c}} \qquad \text{4-5}$$

$$C_{D_{TT}} = 4NC_{f_c}\left(\frac{A_T}{A_T}\right)\left[\left(\frac{t_r}{c_r}\right)\cos^2\Gamma_c + \frac{30\left(\frac{t_r}{c_r}\right)^4\cos^2\Gamma_c}{\left(\sqrt{K-M^2\cos^2\Gamma_c}\right)^3}\right] \qquad \text{4-6}$$

and can be substituted into Eq. 4-2 to find the tail drag component.

The body component of drag, $C_{D_{T_B}}$, can be broken into two components: body pressure drag, C_{D_P}, and body base drag, $C_{D_{BB}}$, shown in Equations 4-7 through 4-9:

$$C_{D_{T_B}} = C_{D_P} + C_{D_{BB}} \qquad \text{4-7}$$

$$C_{D_P} = \frac{6A_{W_B}C_{f_c}}{f_B^3 A_r (K-M^2)^{0.6}} \qquad \text{4-8}$$

$$C_{D_{BB}} = \frac{0.29\left(\frac{A_B}{A_r}\right)}{\sqrt{C_{f_c}\left(\frac{A_W}{A_B}\right)(K-M^2)}} \qquad \text{4-9}$$

The body components of drag can be substituted into Eq. 4-7. The tail and body components from Eq. 4-2 and 4-7 can be substituted into Eq. 4-1 to find the total drag coefficient.

192

The flowchart in Figure 128 below visually represents how the normal force coefficient derivative, C_{N_a}, was found using the formulas described in this section.
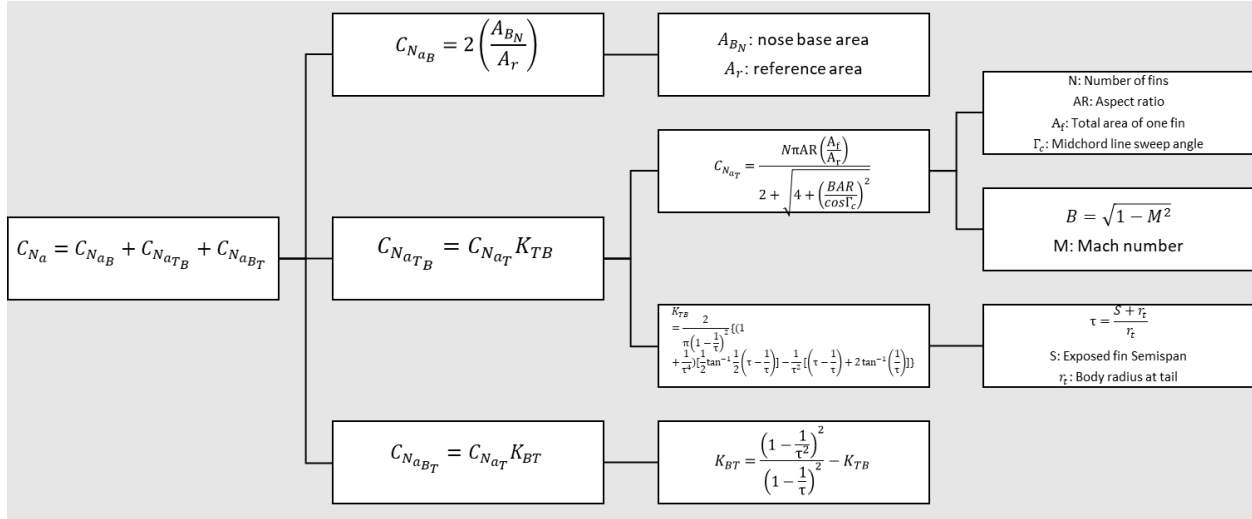
Figure 128: Normal force coefficient derivative top-down flowchart for calculations

The normal force coefficient derivative, C_{N_a},

$$C_{N_a} = C_{N_{a_B}} + C_{N_{a_{T(B)}}} + C_{N_{a_{B(T)}}},$$

4-10

is the sum of the body normal force coefficient derivative, $C_{N_{a_B}}$, the tail interference factor, $C_{N_{a_{T(B)}}}$, and body interference factor, $C_{N_{a_{B(T)}}}$.

The components of the normal force coefficient derivative are broken down as follows.

$$C_{N_{a_B}} = 2\frac{A_{BN}}{A_r},$$

4-11

$$C_{N_{a_{T(B)}}} = C_{N_{a_T}} K_{T(B)}$$

4-12

$$C_{N_{a_{B(T)}}} = C_{N_{a_T}} K_{B(T)}$$

4-13

such that each term is:

$$C_{N_{a_T}} = \frac{N\pi(AR)\left(\frac{A_f}{A_r}\right)}{2 + \sqrt{4 + \left(\frac{\beta(AR)}{\cos \Gamma_c}\right)^2}}$$

$$K_{T(B)} = \frac{2}{\pi\left(1 - \frac{1}{\tau}\right)^2}\left\{\left(1 + \frac{1}{\tau^4}\right)\left[\frac{1}{2}\tan^{-1}\frac{1}{2}\left(\tau - \frac{1}{\tau}\right)\right] - \frac{1}{\tau^2}\left[\left(\tau - \frac{1}{\tau}\right) + 2\tan^{-1}\left(\frac{1}{\tau}\right)\right]\right\}$$

$$K_{B(T)} = \frac{\left(1 - \frac{1}{\tau^2}\right)^2}{\left(1 - \frac{1}{\tau}\right)^2} - K_{T(B)}$$

Figure 129 shows a flowchart visually representing how the pitch moment coefficient, C_m, was calculated using the equations presented in this section.
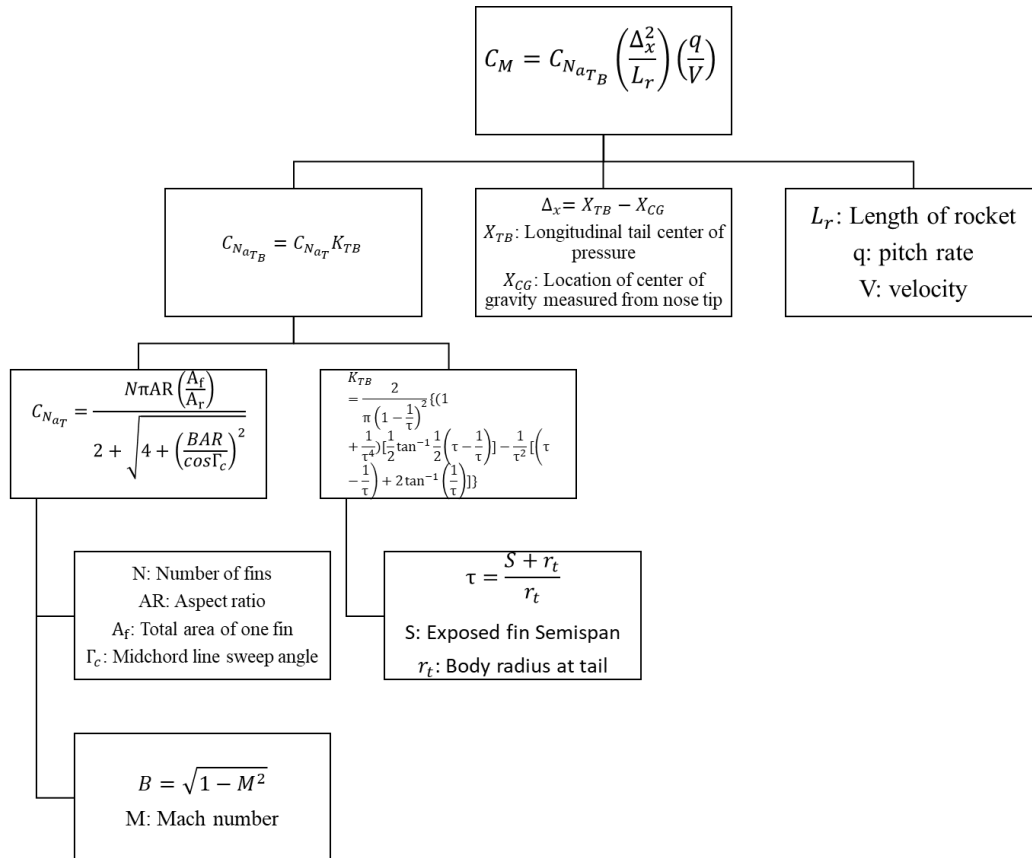
Figure 129: Pitch moment coefficient top-down flowchart for calculations

The moment coefficient, C_m, is given by:

$$C_m = C_{N_{a_{T(B)}}} \frac{(\Delta x)^2}{L_r} \left(\frac{q}{V}\right)$$

<div align="right">4-17</div>

where the normal force coefficient derivative for the tail with respect to the body, $C_{N_{a_{T(B)}}}$ was previously calculated.

Once drag, normal force, and moment coefficients were calculated, each coefficient and its respective force were plotted as functions of velocity or angle of attack. The assumptions made for calculating the aerodynamic loads on the rocket, described at the beginning of this section, are only valid given a small angle of attack. No specific range of angle of attack was specified as "small" during literature review. Regardless, due to the range of angle of attack FDA Analysis Task 2 uses for simulation, from 0 - 90 deg, we deemed it advantageous to include a larger range of angle of attack for this analysis task, where applicable. Comparison of the theoretical and simulation parametric plots should provide some insight into whether specific assumptions hold over a particular range of values. For example, over what range of angle of attack does the simpler, analytic method used in this section hold and at what value of AOA does it breaks down?

The goal of FDA Analysis Task 1 was to determine the drag coefficient, pitching moment coefficient, and lift coefficient derivative using the analytic model described in this section. These aerodynamic loads were found for flight velocities ranging from 0 to 137.16 m/s, the latter being the maximum velocity read by the rocket's sensors during flight. The calculations assume air density and viscosity at sea level.

The results for Analysis Task 1—the aerodynamic loads on a high-powered model rocket versus airspeed—are shown in Figure 130 through Figure 134 below. The geometric properties of the rocket used for these calculations can be found in Appendix H and a nomenclature table to

better understand the calculations can be found in Appendix G. For the locations on the rocket at which the aerodynamic loads occur, i.e. tail vs. body, refer to Figure 130.
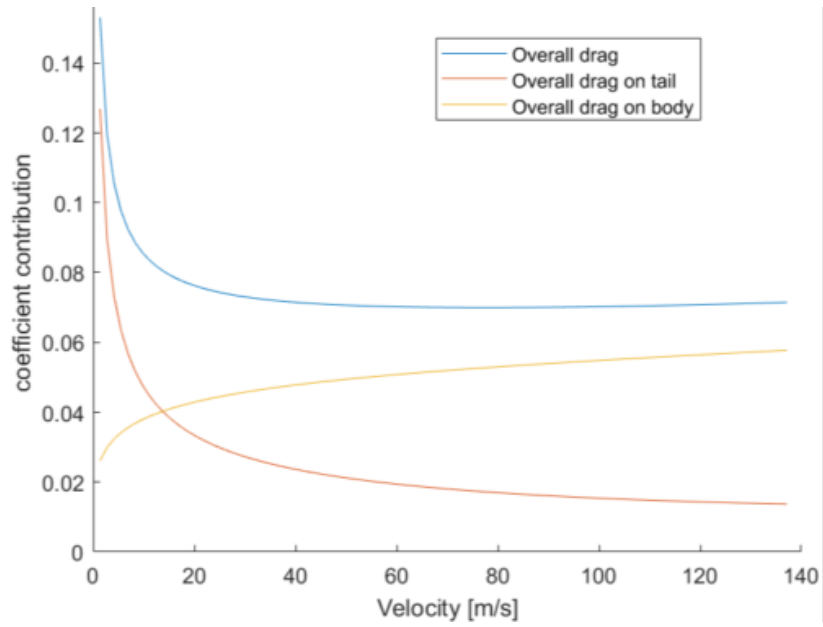
Figure 130: Drag coefficient as a function of velocity.
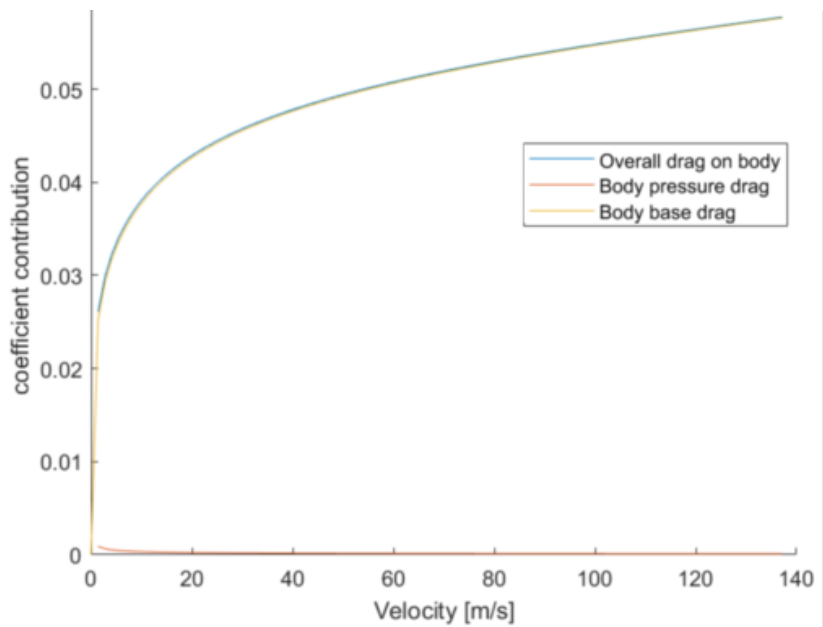
Figure 131: Body drag as a function of velocity.
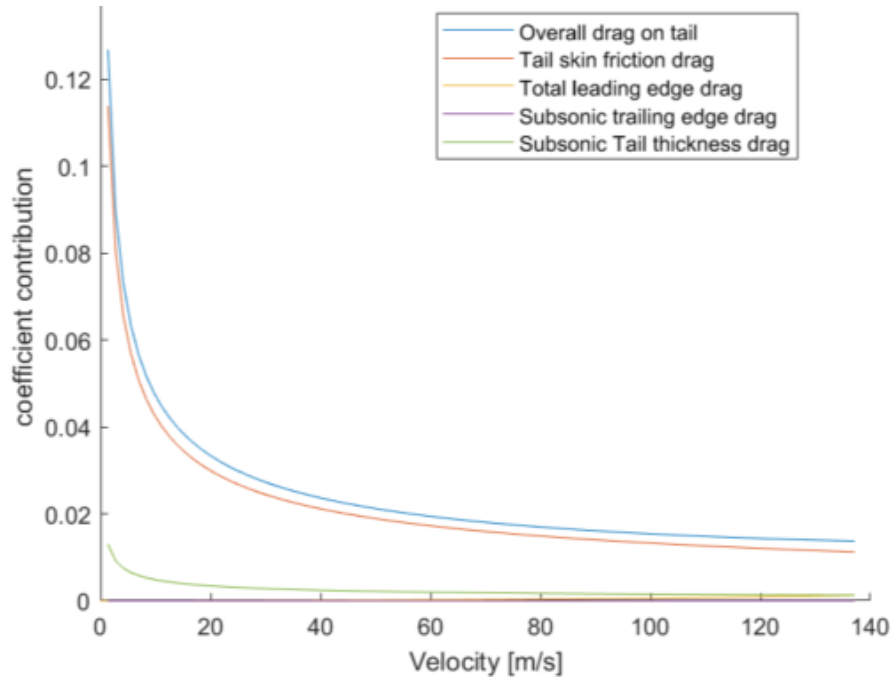
Figure 132: Tail drag as a function of velocity.

The behavior of the drag coefficient as a function of velocity, shown in Figure 130, can be best understood by plotting the individual terms of the total drag coefficient. The overall drag curve shows that at a specific velocity, the rocket experiences a minimum drag. This is a result of the drag on the body increasing faster than the drag on the tail decreases.

The behavior of tail drag may be nonintuitive. One possible explanation for its decrease with velocity is that the drag on the tail is analogous to lift-induced drag [92]. Lift-induced drag (D_i) decreases with flight speed (V) and is also a function of lift (L), air density (ρ), and wingspan (b) shown in Eq. 4-18 from Ref [93]:

$$D_i = \frac{L^2}{0.5\rho V^2 \pi b^2}$$

4-18

Figure 131 shows a breakdown of the components of drag on the body. The body base drag, which increases with velocity, dominates the pressure drag, which decreases with velocity.

197

Figure 132 shows how the rocket's tail is affected by drag over a range of velocities. The drag components of the tail—skin friction, leading and trailing edge drag, and tail thickness drag—are shown. The plot shows that all tail drag terms decrease as velocity increases. The skin friction drag created by the fins is much larger than the leading and trailing edge drag, and tail thickness drag. This supports the selection of the NACA 0006 airfoil because of the airfoil's relatively low drag coefficient. Since the NACA 0006 airfoil has a very small leading-edge radius, i.e. slender and streamlined, and because it tapers to a point at its trailing edge, the leading and trailing edge drag contributions being smaller than that of skin friction is expected. Because the fins were modeled as flat plates in this section, the small contribution of tail thickness drag is also expected.
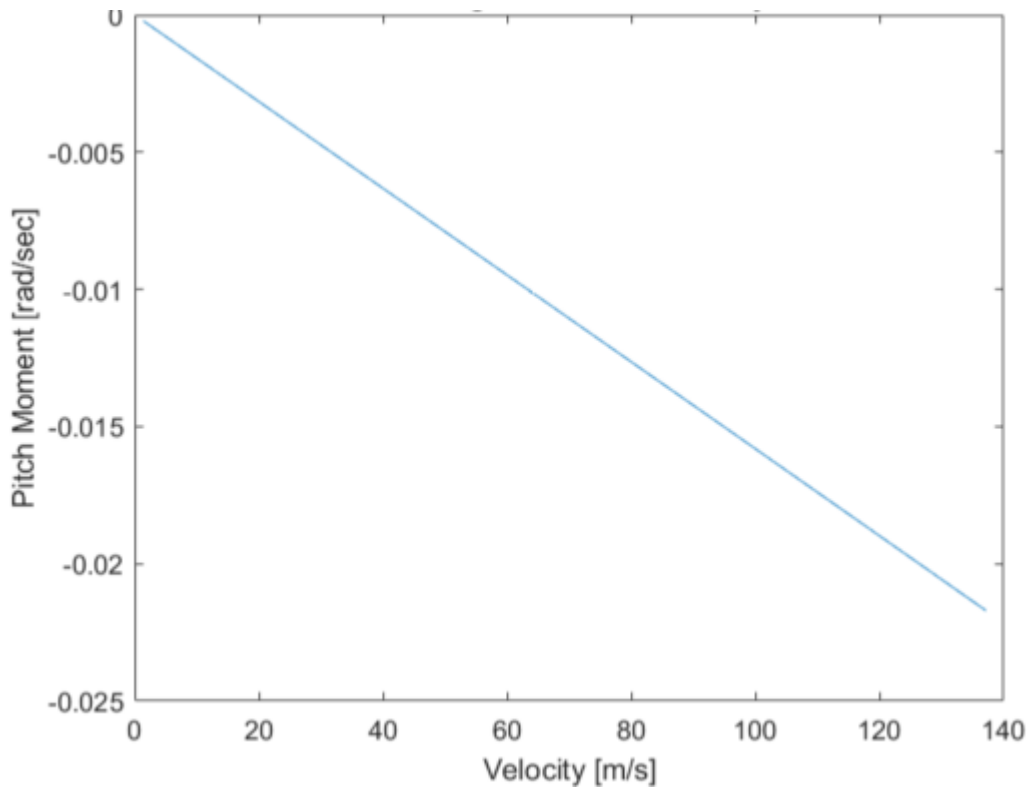
Figure 133: Pitching moment as a function of velocity.

Pitching moment, the force that describes a rocket's tendency to point along its velocity vector, can be seen across the same range of flight velocities in Figure 133. The plot shows that, given a constant pitch rate, the pitching moment is linear with respect to velocity. This is true for any constant pitch rate for low flight velocities. When the pitching moment was plotted up to 340 m/s (approaching Mach 1), the magnitude of pitch moment began to increase faster and no longer at a linear rate.
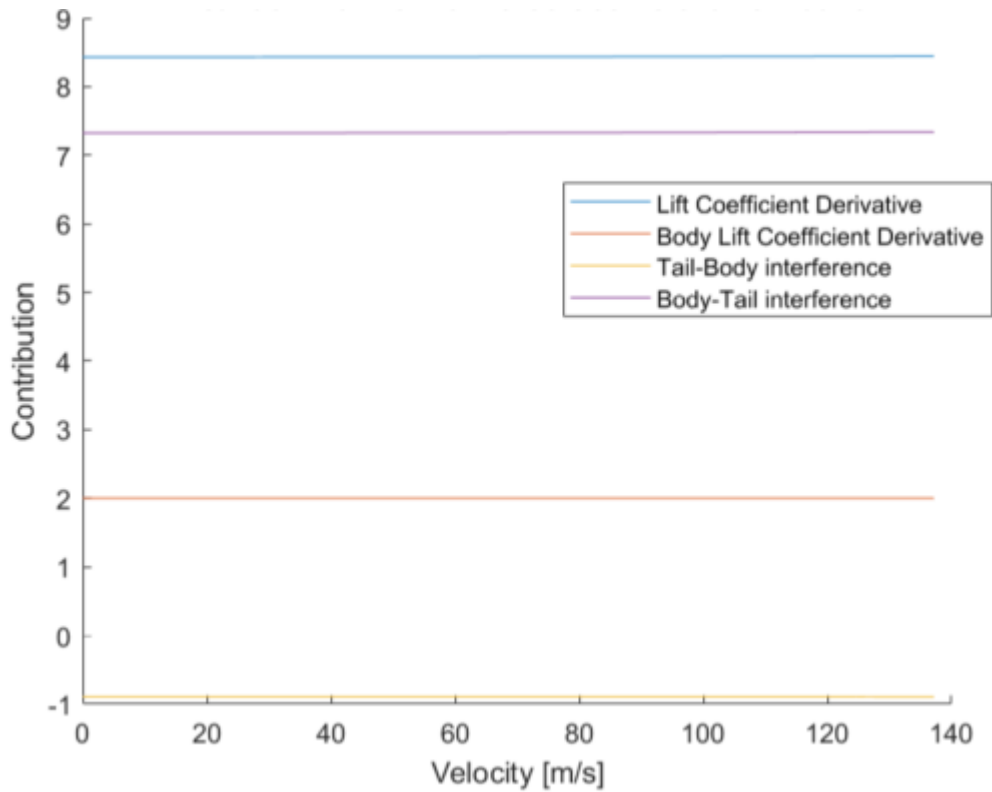
Figure 134: Normal Force coefficient derivative as a function of velocity

The normal force coefficient derivative describes how a rocket reacts to short-term disturbances to trim conditions (which include a constant velocity and angle of attack). It is a linear function of airspeed for Mach numbers much less than 1, so only the actual flight velocities were considered/plotted. The normal force coefficient derivative and the terms it is comprised of can be

seen in Figure 134. Body-tail interference accounts for drag created by the tail with respect to the rocket body. Tail-body interference accounts for drag created by the body with respect to the rocket tail [91]. The total lift coefficient derivative is comprised mostly of the body-tail interference. The difference in magnitude between body-tail and tail-body interference approximates non-idealities in the flow over the region around the fins. Since the body is a much larger object within the flow compared to the tail, the inequality between the two may be because turbulence-like effects are greater coming from the rocket body over the fins versus the effects coming from the fins influencing the body.

4.3.2 Aerodynamic Loads - Simulation (FDA Analysis Task 2)

To estimate the aerodynamic loads exerted on the baseline and innovative rocket we built a simulation of the airflow around the rocket in Fluent. The flow chart in Figure 135 outlines the general process for setting up an external flow simulation.
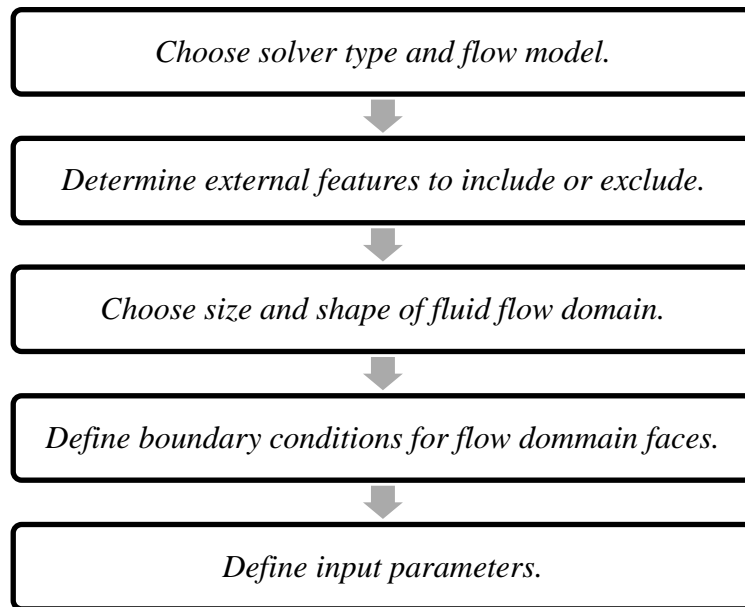
Figure 135: Top-level process for setting up external flow simulations in ANSYS Fluent.

Since the rocket was originally expected to reach a maximum velocity of 103.02 m/s (Mach 0.3) during its first test flight, the flow around it would primarily be in the incompressible regime [94]. Therefore Fluent's pressure-based solver was chosen for this simulation. Reynolds Number was then calculated to determine the appropriate flow model. The Reynolds number is defined as:

$$Re = \frac{\rho V L}{\mu}.$$

<div align="right">4-19</div>

The Reynolds number was calculated with respect to the diameter (L) of the rocket for flight through the air. Here the values of density (ρ) and viscosity (μ) used are for air at 101.32 kPa and the temperature is 20°C. Although the rocket's altitude varies during flight, the maximum expected altitude of 1900 m is negligible compared to the upper boundary of the troposphere (20 km). Therefore it was reasonable to assume altitude to be at sea level. For the majority of velocities (V), between 0 and 103.02 m/s, the Reynolds number calculated was on the order of 10^5. Flows with Reynolds numbers between 10^4 and 10^6 are classified as moderately turbulent and therefore require a viscous model for simulation [94]. Since the viscous k-ω model is well suited for aerodynamic studies, as discussed in Section 1.1.3.5, this was the specific model chosen for predicting what aerodynamic loads acted on the rocket.

Figure 136: Comparison of the modeled nose cone (top) and the real nose cone (bottom)

For both the baseline and innovative rocket models, all external features, besides the fins, were excluded for simplicity. Minor physical features have minimal impact on results, they can drastically increase a simulation's run time. The fins were included because the comparison between the baseline and innovative rockets explored the effect of fin design on aerodynamic loading. Figure 136 also shows that the nose cone of the model used in Fluent does not exhibit the long elliptical profile of the real nose cone. The nose cone was modeled as a right cone for, again, simplicity. Modeling the elliptical cone would be more complex and contribute very little to the simulation results.
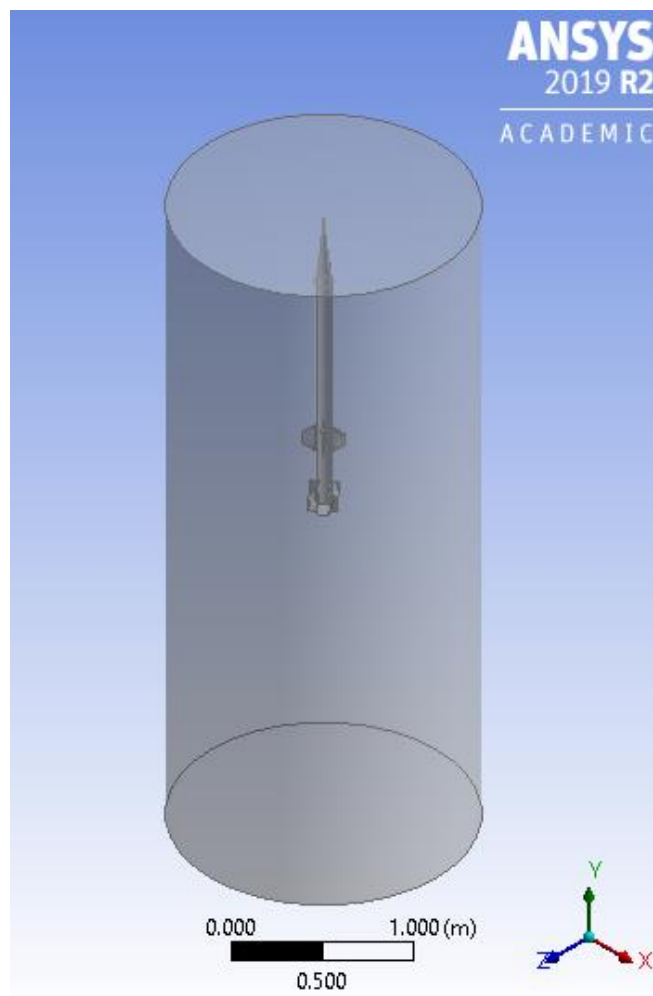
Figure 137: Rocket model nested within the fluid flow domain.

Since Fluent's pressure-based solver was not designed to simulate flows with infinite bounds, external flow studies require the user to model "virtual test sections" around the object of interest. The size and shape of the fluid flow domain define the boundaries necessary for Fluent to perform calculations. The flow domain shown in Figure 137 was sized based on where flow disturbances would most likely occur near the rocket. After running several test simulations we determined that significant disturbances developed within a radius of 17.78 cm from the rocket's cylindrical face and 21.3 m below the rocket. Despite the symmetry of the rocket about the longitudinal Y-axis, a complete cylinder was chosen for the fluid flow domain's shape. When the body of interest is symmetrical about the flow velocity vector, simulations can be simplified by analyzing a periodically repeated segment. In this case, however, the angle of attack of the flow velocity vector changes relative to the rocket, invalidating the symmetry simplification. Therefore the flow domain had to envelop the entire rocket.

Properly assigning boundary conditions to each face of the flow region also required several attempts. Initially, the inlet and outlet were defined as the top and bottom faces of the cylinder respectively. Meanwhile, the sides of the cylinder and the surface of the rocket were defined as stationary walls. Since it is time-consuming to reorient a model in Fluent, the required changes in the angle of attack were acheived by turning the inlet air velocity vector relative to the stationary vertical axis. Figure 138 depicts how the turned inlet flow interacted with the wall of the cylinder in the initial trials. When defined as a wall, the side of the flow domain acted similarly to the wall of a pipe and reoriented the flow parallel to the rocket. In addition to inaccurately representing flow in infinite space, this boundary condition introduced undesired wall disturbances that interfered with the visualization of flow features related to the rocket's geometry. As shown in Figure 138 (b), redefining the side of the flow domain as part of the inlet produced the desired

initial flow field. The orientation of the incoming path line remained constant across the height of the flow domain allowing the rocket to encounter a uniform stream of air as it would in reality.
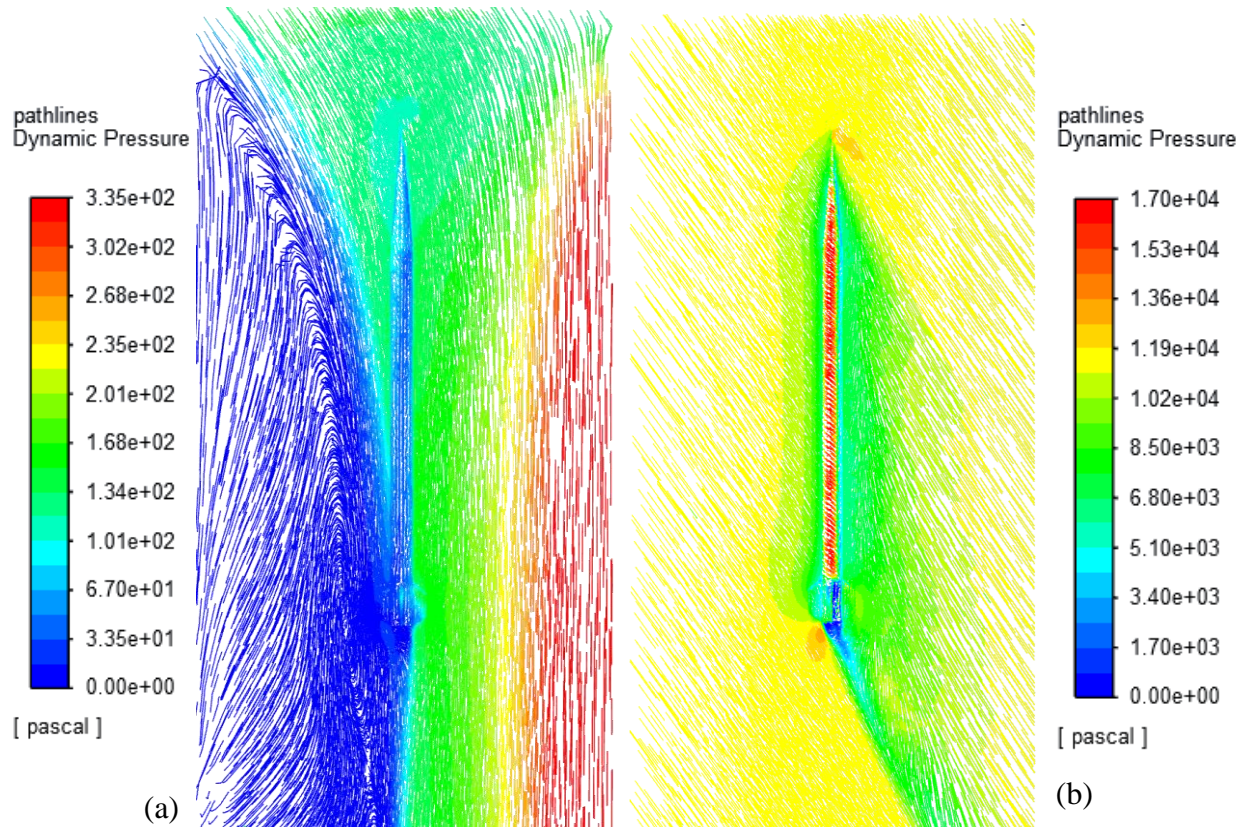
Figure 138: Comparison of flow when sides of flow region are defined as (a) walls or (b) inlets.

Figure 139 and Table 35 through Table 37 specify the boundary types and associated boundary conditions used for both the baseline and innovative rocket simuations.

Figure 139 visualizes the two domains and four boundaries utilized by the Fluent simulations designed to calculate the aerodynamic loads acting on the two version of the rocket. Domain 1 define the fluid flow domain that surrounds the rocket (Domain 2). The materials assigned to each

domain can be found below in Table 35. The region outside of boundaries 1, 2, and 3 was not part

of the simulation and therefore has no fluid properties or material associated with it.
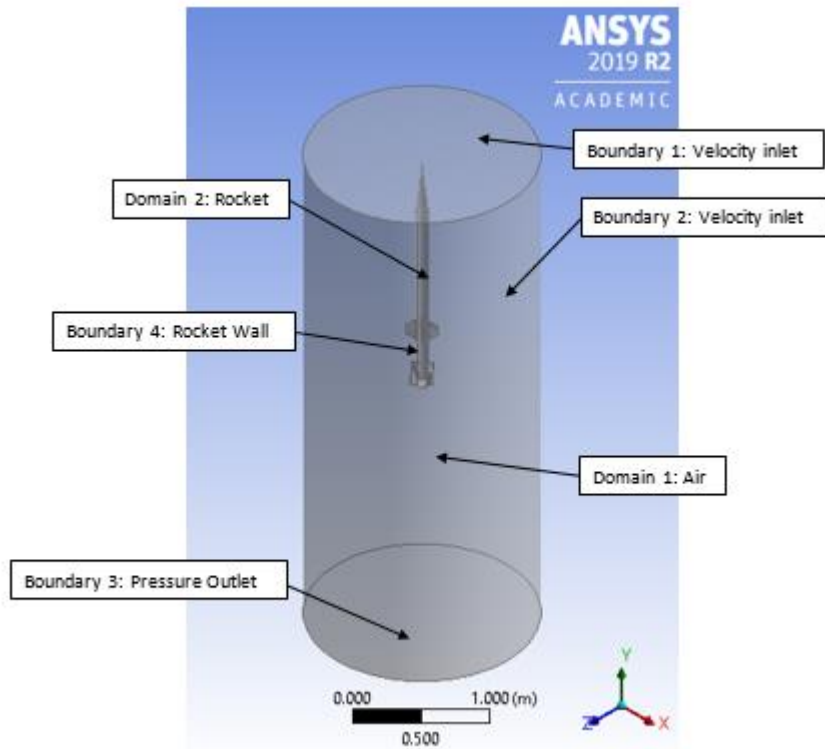
Figure 139: 3D ANSYS Fluent model geometry showing labeled domains and boundaries.

Table 36 specifies the type of boundary, fluid flow equations, and scalar properties associated

with each of the four boundary faces of the Fluent model geometry. Table 37 specifies the initial

values defined at the inlet.

Table 35. Domains, materials, and material values chosen in the geometry of Fluent model

Domain	Material Chosen in ANSYS Fluent and Applied to Domain	Material Value	Description
1	Air	$\rho = 1.225 \frac{kg}{m^3}$ $\mu = 1.7894\text{e-}05\frac{kg}{ms}$	For flight simulations at sea level, density and viscosity of air at sea level were chosen.
2	Aluminum	$\rho = 2719 \frac{kg}{m^3}$ $K_s = 0$	Aluminum was selected for the surface of the rocket and $K_s = 0$ is roughness height corresponding to smooth walls.

Table 36. Boundary conditions applied to domains and boundary line in the model

Boundary Faces in Fluent	Domains corresponding to boundary line	Boundary Conditions		Description
		Boundary Condition and Constitutive Relation (if applicable)	Equation and value	
1	Domain 1	Inlet Velocity	$V = 0 \text{ to } 137.15\frac{m}{s}$ $\alpha = 0 \text{ to } 90°$ $\rho = 1.225\frac{kg}{m^3}$	Define velocity magnitude and direction (relative to origin) and air density at inlet
2	Domain 1	Inlet Velocity	$V = 0 \text{ to } 137.15\frac{m}{s}$ $\alpha = 0 \text{ to } 90°$ $\rho = 1.225\frac{kg}{m^3}$	Define velocity magnitude and direction (relative to origin) and air density at inlet
3	Domain 1	Conservation of energy	$\frac{\partial p}{\partial r} = \frac{\rho v_\theta^2}{r}$ $\rho = 1.225\frac{kg}{m^3}$ $p_{gauge} = 0 \text{ Pa}$	Computes pressure gradient given expected outlet static pressure
4	Domain 1, Domain 2	Wall shear stress	$\tau_w = \mu\frac{\partial v}{\partial n}$ $\mu = 1.7894\text{e-}05\frac{kg}{ms}$	Predicts shear stress on the fluid at the wall using the properties of the flow adjacent to the wall/fluid boundary

Table 37. Initial inlet values of the model

	Domains Initial Value is Applied to	Value	Description
Initial Values	Domain 1	$V = 0$ to $137.15 \frac{m}{s}$ at intervals of 15.24 m/s	Simulates all possible flight velocity magnitudes
Initial Values	Domain 1	$\alpha = 0\ to\ 90°$ at intervals of $10°$	Simulates all possible angles of attack

Since turbulence was considered in this simulation, the choice of wall material for Boundary 4 had the potential to contribute to the end results. In reality, the rocket's outer surface consists of several varieties of polymers and composites. However, Fluent only allows the user to describe solid surfaces as homogeneous materials. Since the outer layers of the rocket's surface were designed to be smooth, aluminum was selected as an analogous material for the simulation. As discussed previously, the air surrounding the rocket was assumed to be constant at 101.32 kPa and 20°C at sea level. Finally, the range for the inlet velocity magnitude was based on expected values. As previously discussed, the maximum velocity estimated using OpenRocket was 103.02 m/s (338 ft/s). However, during the flight test the rocket reached a maximum velocity of 135.63 m/s (445 ft/s). Therefore, simulation cases were run for velocities from 0 to 137.16 m/s (450 ft/s) to accommodate velocity intervals of 15.24 m/s (50 ft/s). Note that the velocity interval in meters is not a whole number because it was subject to init coversion. Flunet simulations for Analysis Task 2 were originaly run using the United States customary unit system. The AOA range was selected based on precaution. Since flight conditions are not completely certain until launch, it was decided that an AOA range from 0 to 90 deg would address all possible anomalies.

It is understood that in reality the rocket would rotate relative to the stationary velocity and gravity vectors as shown in Figure 140. However, it would have been time consuming to reorient of the rocket before running each case. Therefore, to simulate the effect of the rocket rotating in free space, the velocity vector was rotated relative to the rocket and the body-fixed force vectors as shown in Figure 141.
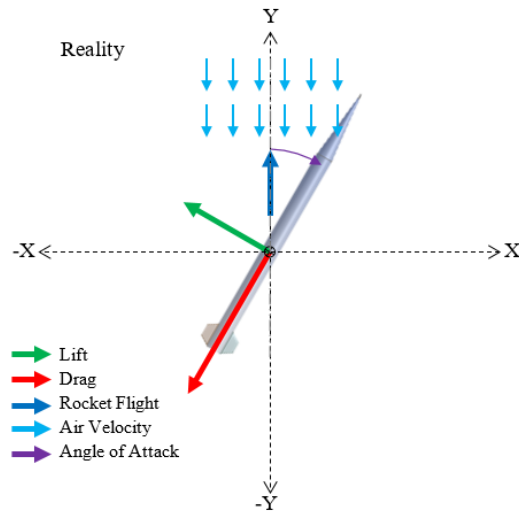
Figure 140: Illustration of vectors and angle definitions relative to the stationary velocity vector
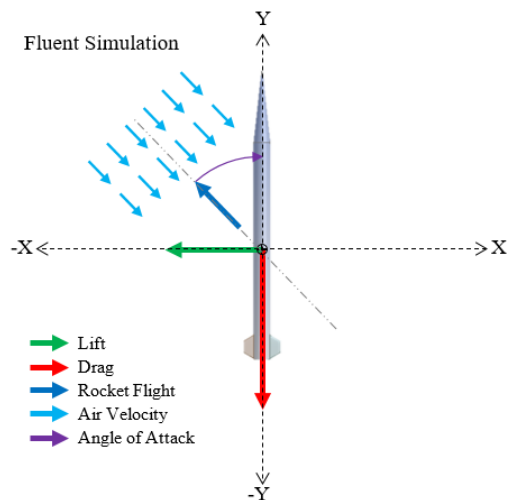
Figure 141: Illustration of vectors and angle definitions relative to the stationary rocket and body fixed forces.

The velocity vector components, V_x and V_y, used for initialising each case of the simulation were found from the equations

$$V_x = Vcos(\alpha) \qquad\qquad 4\text{-}20$$

$$V_y = Vsin(\alpha) \qquad\qquad 4\text{-}21$$

Where V is the maginitude of the air velocity and α is the angle of attack as defined in Figure 141. Figure 141 also shows that the lift and drag vectors were defined as body-fixed. This was done in order to further simplify the process of setting up idividual cases. If not defined in this way, the lift and drag vectors would have required adjusting for every change in angle of attack.

Setting up the simulation in this way also resulted in an unusual situation where a portion of the fluid flow would exit through the right side of the Boundary 2 inlet. This penomena is defined by the Fluent User Guide as "Reversed Flow" [61]. When ANSYS detects reversed flow at an inlet boundary, the program compensates by ingnoring the properies defined at that inlet. Instead, ANSYS automaticaly changes the properties of that inlet to those of the adjacent fluid domain elements [61].

After setting up the simulation according to the specifications detailed above, a total of 100 cases were run to build the database of aerodynamic loads found in Appendix J. Each case was initialized from the inlet face using the inlet velocity magnitude and AOA expressed as cartesian components of the velocity direction vector. The most common trend seen across plots for both the baseline and innovative rockets was the quadratic relationship between velocity and most aerodynamic loads. Figure 142 shows the baseline plot of velocity versus lift for all angles of attack.
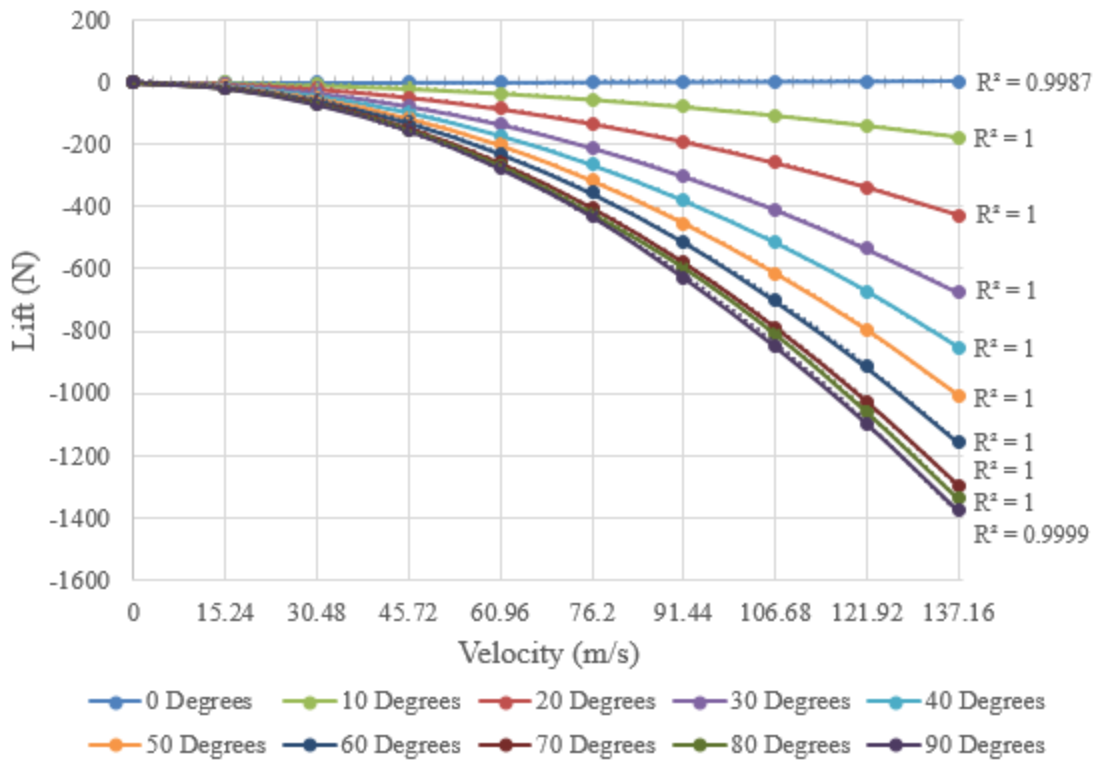
Figure 142: Plot of lift as a function of velocity for the baseline rocket showing the variance of each curve to a quadratic trend line.

Quadratic trend lines were fit to each curve and, as the variances (R^2) indicate, all fit the positive quadratic model with little to no error. Meanwhile, plots for the drag, and moments M_x, M_y, and M_z do not exhibit correlations as clean as the lift-velocity relationship. The relationship is either oscillatory or breaks down at higher angles of attack. For the innovative rocket, all loads reliably followed the quadratic rule. The only exception existed in higher angle cases for M_x. The conformity to quadratic relationships is consistent with the involvement of the dynamic pressure (Q) in calculating aerodynamic forces and moments. Dynamic pressure, given by:

$$Q = \frac{1}{2}\rho V^2 \, ,$$

4-22

is directly proportional to the square of the airspeed (V) [94]. Deviation from the dependency on V^2 is most likely due to the limitation of flow over the top of the two fins perpendicular to the oncoming stream of air as the angle of attack gets larger. Boundary layer separation would cause pressure to suddenly drop on one side of the fin and disrupt the forces these fins contribute the system.

When the aerodynamic loads were plotted against the AOA, only the lift conformed to a general trend for either version of the rocket. While the lifting force increased reliably with AOA, the behavior of the other loads was not consistent for angles of attack ranging from 0 to 90 deg.
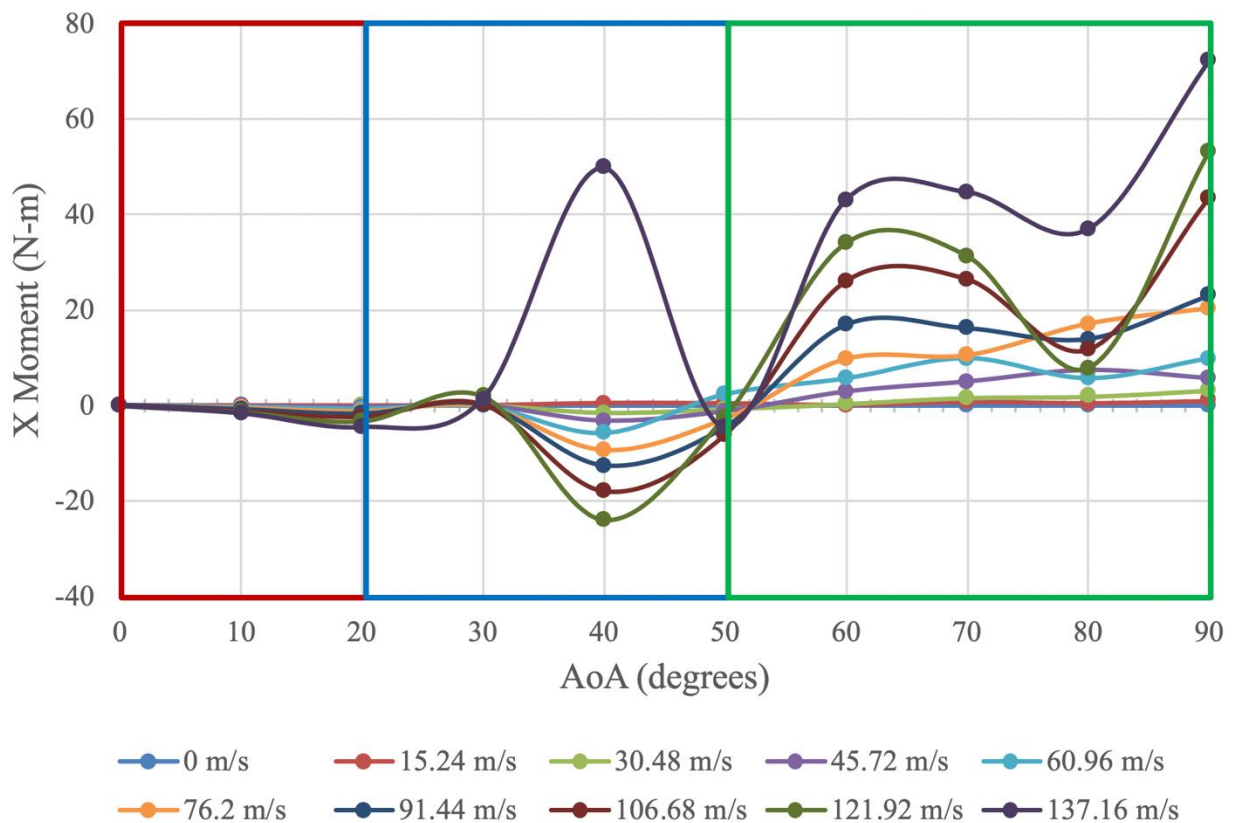
Figure 143. Plot of Mx as a function of AOA for the baseline rocket. Boxed regions show distinct response to changes in the angle of attack.

For the baseline rocket, AOA-dependent behavior would distinctly transition at 20 degrees and at 50 degrees. Figure 143 shows a good example of this inconsistent behavior in a plot of AOA vs. M_x. However, any AOA above 20 deg would be unlikely to occur for a stable rocket flying in typical conditions. Therefore, the 0 to 20 deg range on each plot was of the most interest within this analysis task. For this range of angles, lift, M_x and M_z showed reliable linear increases in magnitude. Drag and M_y remained relatively constant from 0 to 10 deg AOA. Beyond 10 deg, drag decreases slightly while M_y increases slightly. Again, the irregularities for higher-angle cases are most likely due to boundary layer separation on the fins perpendicular to the flow of oncoming air. For the innovative rocket, there was only a consistent relationship with AOA for lift and M_x. In both cases, lift and M_x increase in magnitude with AOA. Although trends seen for drag, M_y, and M_z were still irregular, they were more stable than they were for the baseline rocket. For these loads, the change in behavior only occurred once at or near an AOA of 50 deg.

Comparing the performance of the baseline and innovative rockets, it appears that cambered fins had a significant effect on all aerodynamic loads. Most notable was the increase in the moment about the Y-axis. For all angles and velocities, the innovative rocket experienced a greater M_y when fin camber was applied. C_{my} for the baseline and innovative rockets are plotted together in Figure 144 and Figure 145 to illustrate this change.

This increase in Y moment is a direct result of the cambered fins. Cambered fins produce a force perpendicular to the chord of the fin, even at zero AOA. This force induces a spinning moment on the rocket about its Y-axis. As the angle of attack increases, the spinning moment increases, keeping it greater than the moment induced by the symmetrical fin of the baseline rocket at nonzero AOA.
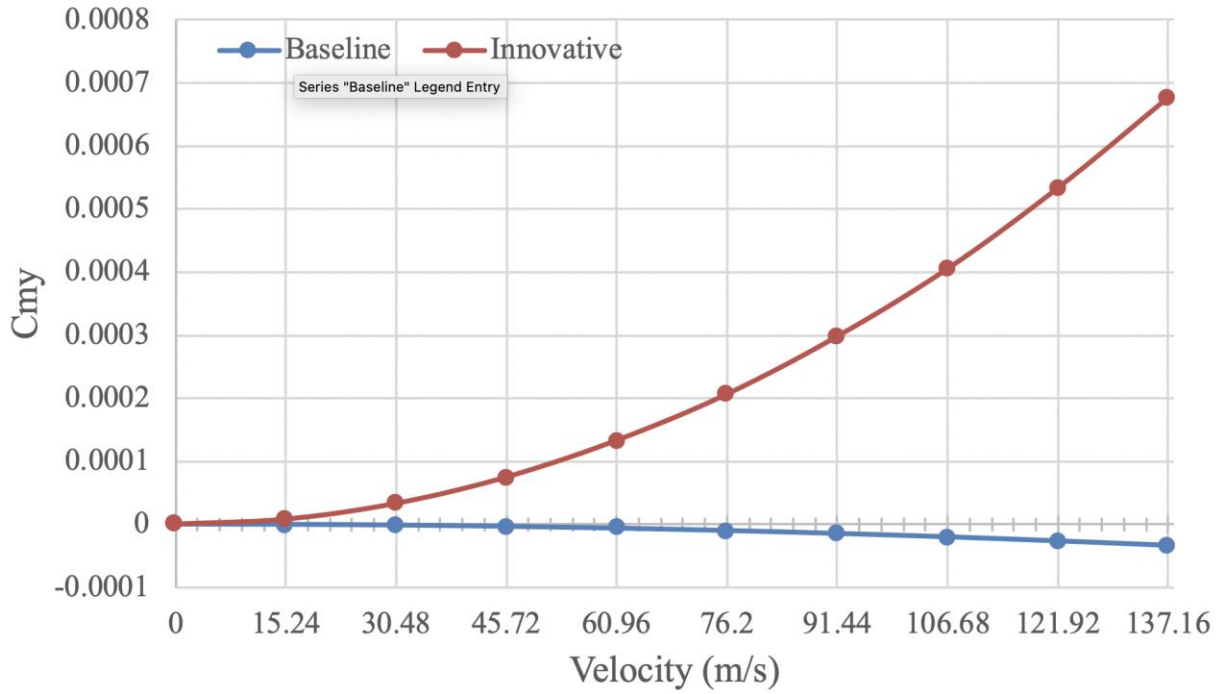
Figure 144: Plot of C_{my} vs. velocity comparing the innovative (with cambered fins) and baseline
(without cambered fins) rockets.
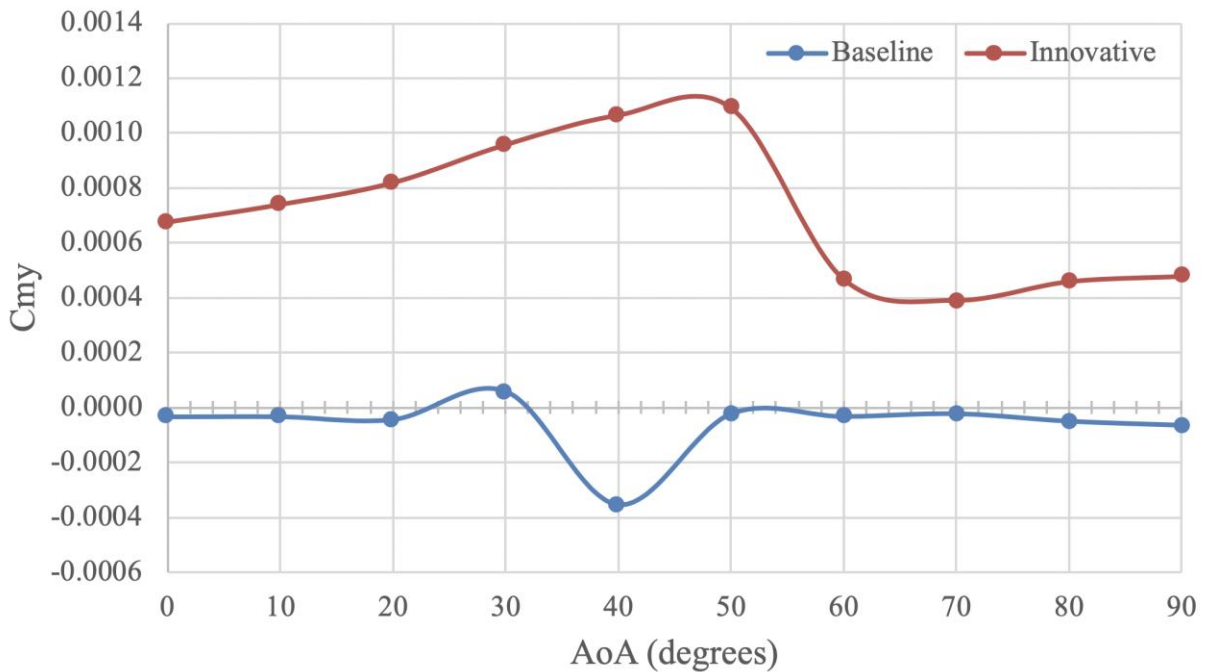
Figure 145: Plot of C_{my} vs. AOA comparing the innovative (with cambered fins) and baseline
(without cambered fins) rockets.

Additionally, dynamic pressure contours were created for each velocity and AOA case considered. These provided a visual of how the air moved and dynamic pressure changed around the rocket. The dynamic pressure is defined as the increase in the surrounding air's pressure due to motion compared to its pressure when static. Therefore, a value of zero implies that the surrounding air is static. In both the baseline and innovative cases, the highest pressures, shown in warmer colors, occurred where oncoming air struck the rocket at or close to perpendicular. For zero degrees AOA, this meant the nose tip and leading edges of the fins experienced the highest air pressures. As the airflow turned, pressure grew on the rocket's fuselage, as illustrated by Figure 146 (a) and (b).
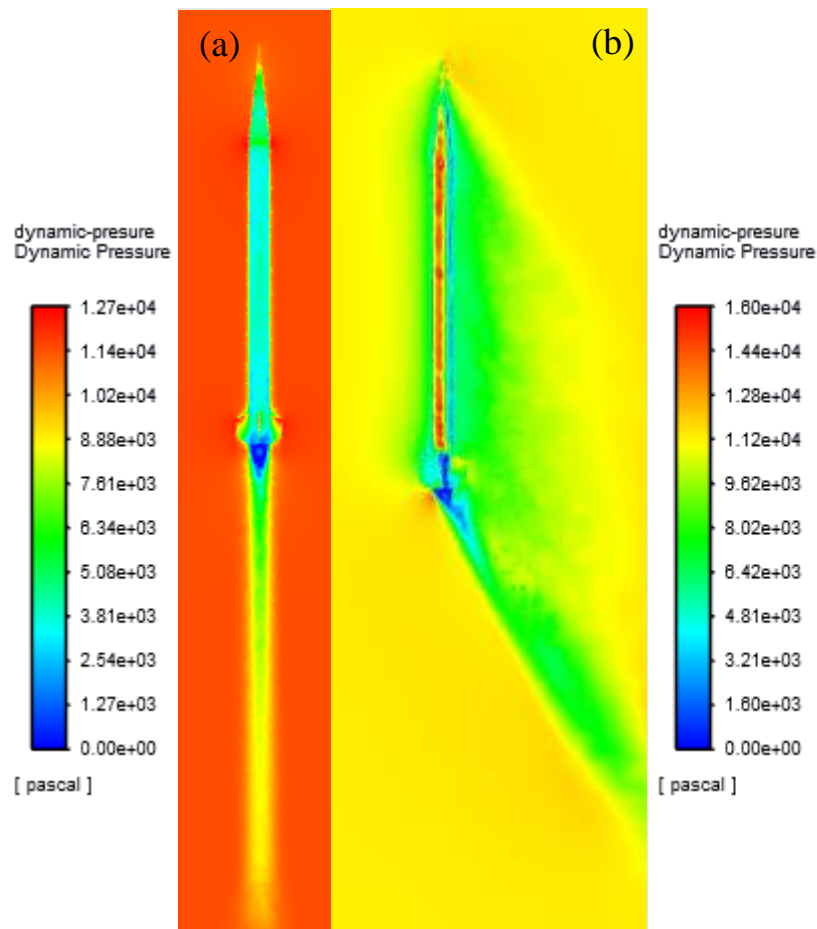
Figure 146: The dynamic pressure contour around the baseline rocket at 137.16 m/s and an angle of attack of 0 deg. (a) and of 40 deg. (b).

These contours also show how lower pressures, coded in cooler colors, occur primarily in the wake of the rocket. As in the examples above, all cases show wakes in which pressure is lower than the surrounding airflow. The lowest pressure in each wake occurs at the very base of the rocket. The catalog of dynamic pressure contours in Appendix J shows the full extent of these trends for all velocities and angles of attack considered.

4.3.3   Fin Design for Vehicle Spin Stabilization (FDA Analysis Task 3)

The goal of FDA Analysis Task 3 was to evaluate the effectiveness of different fin designs to provide spin stabilization during flight. The three fin designs chosen were:

1. Fins with symmetric airfoil at non-zero angle of attack.

2. Fins with cambered airfoil.

3. Fins with a moveable control surface.

Each fin was designed in SOLIDWORKS and implemented on the baseline rocket. Figure 147 through Figure 149 show the three SOLIDWORKS models used for simulation for each case.

Using ANSYS Fluent, Cases 1, 2 and 3 were simulated using the k-ω turbulence model. This model was chosen for its improved accuracy of wall boundary conditions compared to the standard k-ε turbulence model. The simulations of each case were set up similarly, with Figure 150 and Table 38 through

Table 40 specifying the boundary types and associated boundary conditions used for this section.
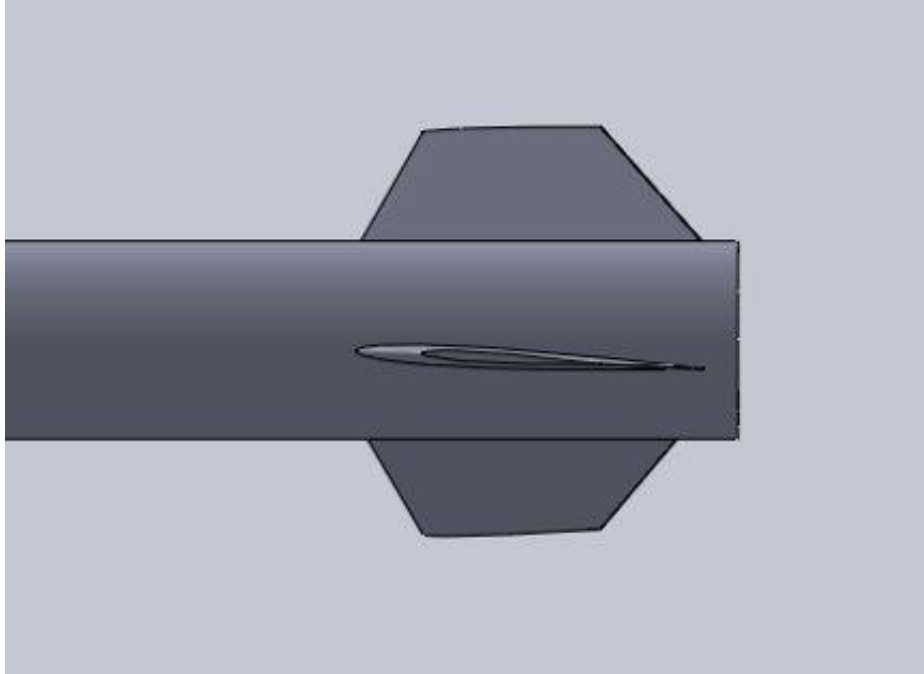
Figure 147: Case 1, Symmetrical fins with an angle of attack
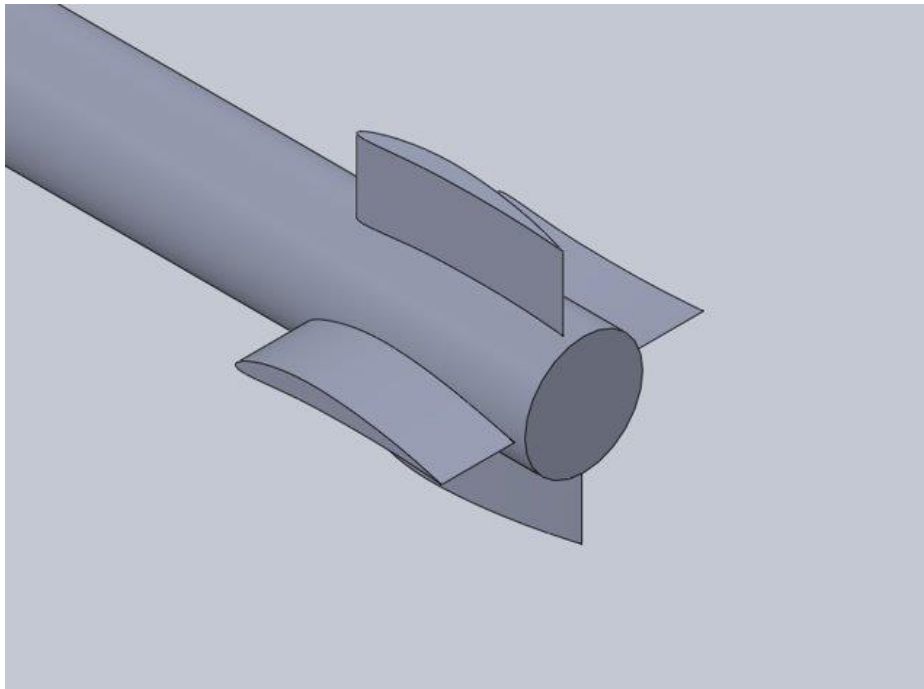
Figure 148: Case 2, Cambered airfoil at zero angle of attack
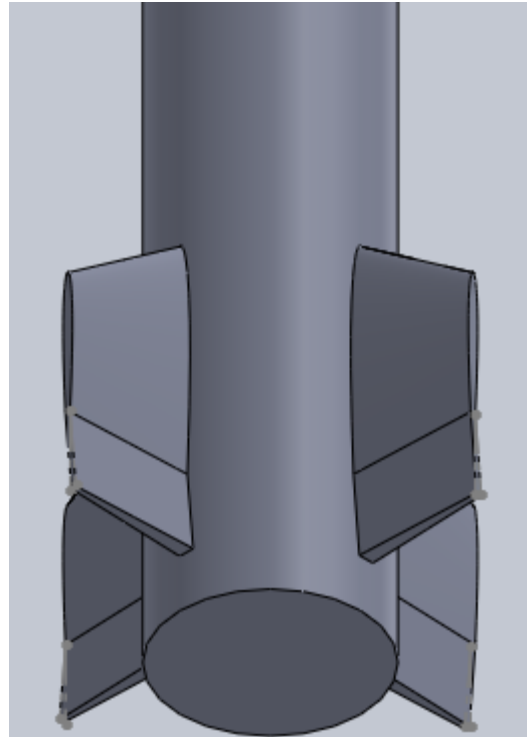
Figure 149: Case 3, Symmetrical airfoil with an extended control surface known as a "Rolleron"
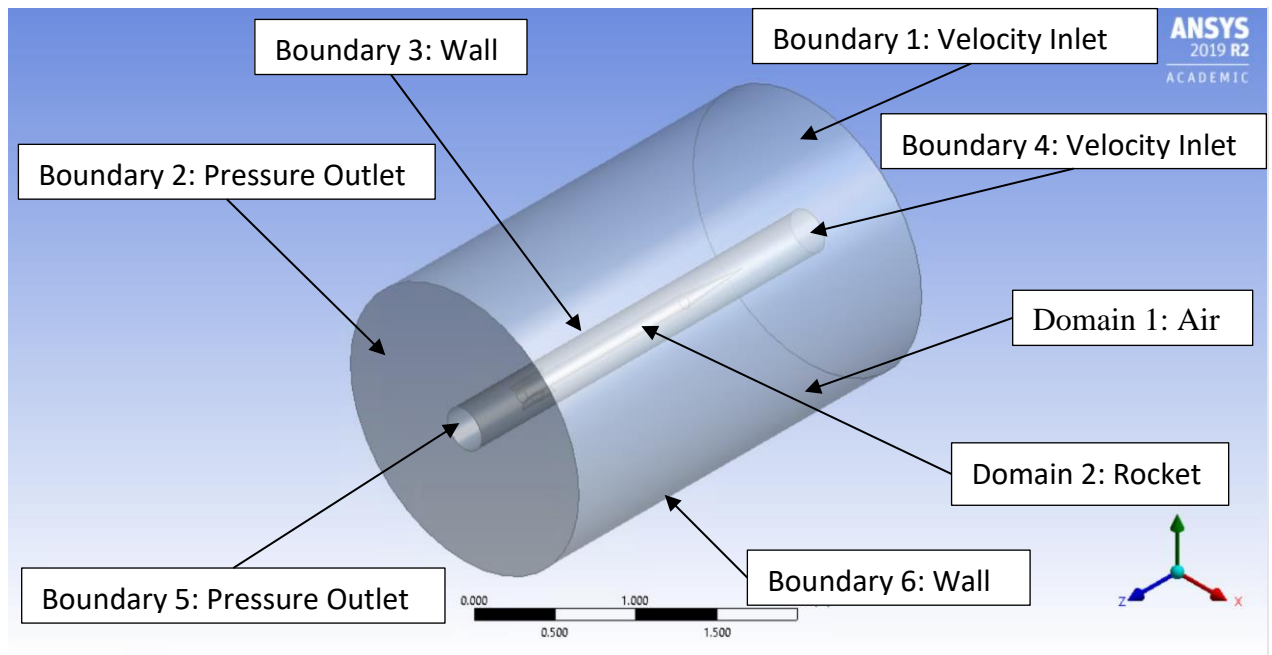
Figure 150: 3D ANSYS Fluent model geometry showing labeled domains and boundaries.

Table 38. Domains, materials, and material values chosen in the Fluent model geometry

Domain	Material Chosen in ANSYS Fluent and Applied to Domain	Material Value	Description
1	Air	$\rho = 1.225\,\dfrac{kg}{m^3}$ $\mu = 1.7894\text{e-}05\dfrac{kg}{ms}$	For flight simulations at sea level, density and viscosity of air at sea level were chosen.
2	Aluminum	$\rho = 2719\,\dfrac{kg}{m^3}$ $K_s = 0$	Aluminum was selected for the surface of the rocket and $K_s = 0$ is roughness height corresponding to smooth walls.

Table 39. Boundary conditions applied to domains and boundary line in the Fluent model

Boundary lines in Fluent	Domains corresponding to boundary lines	Boundary Conditions		Description
		Boundary Condition and Constitutive Relation (if applicable)	Equation and value	
1	Domain 1	Mass flow rate	$\dot{m} = \int \rho \vec{v} \cdot \overrightarrow{dA}$ $\rho = 1.225\,\dfrac{kg}{m^3}$	Computes inlet mass flow rate
2	Domain 1	Conservation of energy	$\dfrac{\partial p}{\partial r} = \dfrac{\rho v_\theta^2}{r}$ $\rho = 1.225\,\dfrac{kg}{m^3}$ $p_{gauge} = 0\ \text{Pa}$	Computes pressure gradient given initial static pressure
3	Domain 1, Domain 2	Wall shear stress	$\tau_w = \mu \dfrac{\partial v}{\partial n}$ $\mu = 1.7894\text{e-}05\dfrac{kg}{ms}$	Predicts shear stress on the fluid at the wall using the properties of the flow adjacent to the wall/fluid boundary
4	Domain 2	Mass flow rate	$\dot{m} = \int \rho \vec{v} \cdot \overrightarrow{dA}$ $\rho = 1.225\,\dfrac{kg}{m^3}$	Computes inlet mass flow rate
5	Domain 2	Conservation of energy	$\dfrac{\partial p}{\partial r} = \dfrac{\rho v_\theta^2}{r}$ $\rho = 1.225\,\dfrac{kg}{m^3}$	Computes pressure gradient given initial static pressure

6	Domain 2, Domain 0 where Domain 0 is outside of the air boundary and has no influence on the simulation for this case	Wall shear stress	$\tau_w = \mu \dfrac{\partial v}{\partial n}$ $\mu = 1.7894\text{e-}05 \dfrac{kg}{ms}$	Predicts shear stress on the fluid at the wall using the properties of the flow adjacent to the wall/fluid boundary

Table 40. Initial inlet values of this model

	Domains Initial Value is Applied to	**Value**	**Description**
Initial Values	Domain 1 and Domain 2	$V = 0$ to $140 \dfrac{m}{s}$ at intervals of 10 m/s	Simulates all possible flight velocity magnitudes

The Analysis Task 3 Fluent simulations consist of two domains. Domain 1 is the outer cylinder, which is of relatively no interest in simulation results. Domain 2 is the inner cylinder containing the rocket and is the region of most interest during simulations. The simulation was modeled as two concentric cylinders in order to increase the refinement of the mesh closer to the rocket, increasing the accuracy of simulation results, while keeping the mesh element size of the outer cylinder relatively large because no aerodynamic affects occur at that distance from the rocket. The surface of the rocket was modeled as Aluminum because of its similar smoothness to the rocket's finished surface and because of the limitations Fluent imposes with surface material selection.

The faces of the inner and outer cylinder perpendicular to the Z-axis in Figure 150 define boundaries for inlet velocity (Boundaries 1 and 4) and pressure outlet (Boundaries 2 and 5). The components of the velocity inlet enter the domains perpendicularly through boundary 1 and 4 and flow exits the domains at boundary 2 and 5. The curved surface of the inner and outer cylinder, boundary 3 and 6, represent walls with no-slip condition. The boundary condition of these two

surfaces were treated as walls instead of velocity inlets because of a combination of inexperience with Fluent and the fact that the presence of the walls ended up having no effect on simulation results. The simulation results for this section were unaffected because the velocity inlet was only simulated at zero angle of attack. Compared to the effects seen by FDA Analysis Task 2 in Figure 138, where the wall boundaries deflected the flow back towards the rocket during simulations that involved a nonzero angle of attack, the flow for this task was only considered at a zero angle of attack. Because the flow was simulated at zero angle of attack for all cases of this task, flow was not deflected by the walls and simply flowed past them.

Boundary 6 could have been modeled as velocity inlets with a tangential flow and no stress, however it was concluded that the results produced by the simulation were accurate without altering the boundary.

Table 41: Model conditions for the various cases of FDA Analysis Task 3 described in this section

Parameter	Case 1	Case 2	Case 3
Fin Type	Symmetrical	Cambered airfoil	"Rolleron"
Airfoil	NACA 0006	NACA 6409	NACA 0006
Number of fins	3 and 4	4	4
Velocity (m/s)	0-140	0-140	0-140
Gravity (m/s^2)	9.8 (x-direction)	9.8 (-direction)	9.8 (y-direction)
Fin AOA	1, 3 and 5 degrees	0 Degrees	0 Degrees
Aileron AOA	-	-	3, 5, and 10 Degrees
Fluid	Air	Air	Air
Solid	Aluminum	Aluminum	Aluminum
Walls	Stationary	Stationary	Stationary
Models	Viscous (k-ω)	SST (k-ω)	Viscous (k-ω)
Turbulent Intensity	1%	1%	1%
Turbulent viscosity	10	10	10

Table 41 lists the viscous model conditions for each case. For the first case, the fins on the baseline rocket were canted at different angles of attack. The rocket was then analyzed in Fluent

to determine the moment induced by the canted fins. The angles chosen for analysis were 1, 3 and 5 deg. For each angle of attack, the impact of having three or four fins was also assessed. Figure 151 shows SOLIDWORKS models of the rocket with three and four fins at an AOA of 5 deg.
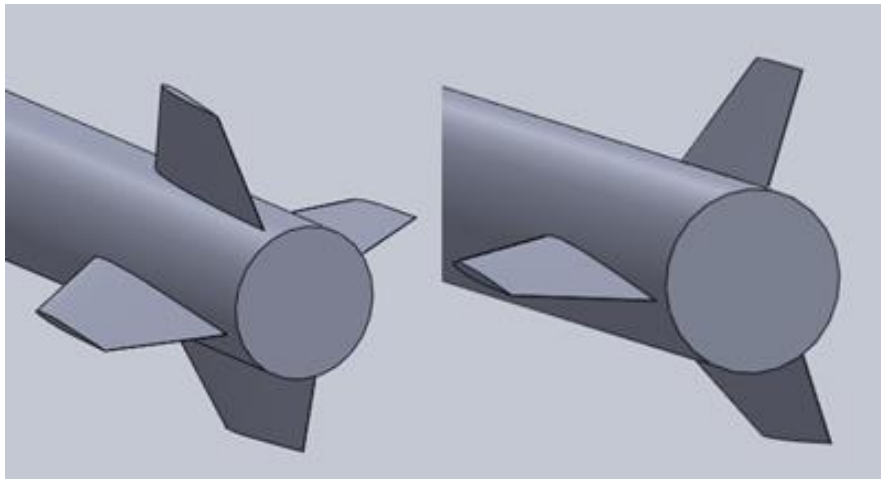
Figure 151. 4 fins (left) and 3 fins (right) canted at 5 deg angle of attack

All the cases were analyzed at sea level air density and airspeeds ranging from 0 to 140 m/s. As shown in Figure 152, the rocket models were enclosed inside a cylindrical tube, which was defined as the fluid domain. The top face of the cylinder was defined as the inlet where the air flow enters while the cylindrical portion acted as the walls. The standard k-ω turbulence model was used for the simulation of these cases. This model operates better in boundary layer cases, which provides more accurate results compared to other models. The moment of interest for this analysis task was the spinning moment about the rocket's longitudinal axis. In this case, the longitudinal axis of the rocket is oriented in the negative x-direction as shown in Figure 152. The moment center where the moment acts is the distance from the top face of the cylinder to the point of center of gravity of the rocket which is at 1.25 m.
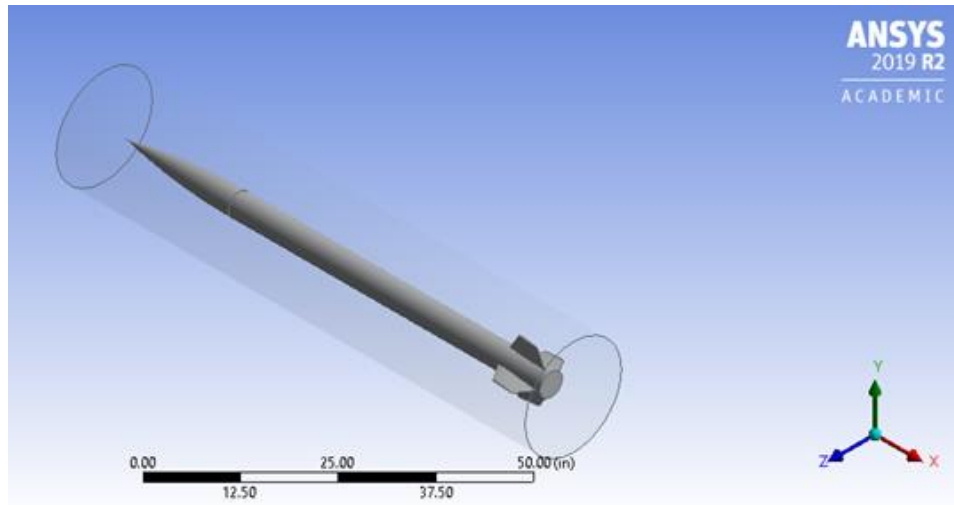
Figure 152. Enclosed flow region used for fluent simulations

Fluent provided information on aerodynamic forces such as lift, drag, and pitching moment. Since FDA Task 3 was focused on the spinning moment of the rocket, the results for lift and drag were not included in this analysis. The moment coefficient was plotted at different airspeeds for all cases. To determine the moment coefficient, Fluent calculates the moment and divides it by the dynamic pressure (q), the reference area (A_{ref}) selected by the user and the diameter of the rocket (d) as shown in Eq. 4-23

$$C_m = \frac{M}{qA_{ref}d},$$ 4-23

For Case 1, the moment on the rocket behaves differently at various velocities. As shown in Figure 153 the case at 3 deg AOA with three fins produces a greater moment than the case at 5 deg AOA with 4 fins at 140 m/s. However, at airspeed of 120 m/s, the 5 deg AOA case with 4 fins produces a greater moment than the 3 deg AOA case with three fins. At 140 m/s, canting three fins at 5 deg produced a greater moment compared to other angles of attack with 4 fins. The velocity at which the rocket leaves the launch rail is 24.69 m/s. Figure 153 shows the moment does

not exceed 0.65 N-m for any of the cases. The maximum moment at this velocity is given by 3 fins at 3 deg AOA which is exactly 0.65 N-m. Using the right-hand rule, the negative sign convention shows the moment is in a clockwise direction. The results from this example shows how many fins and at what angle they should be oriented in order to get a particular moment on the rocket.
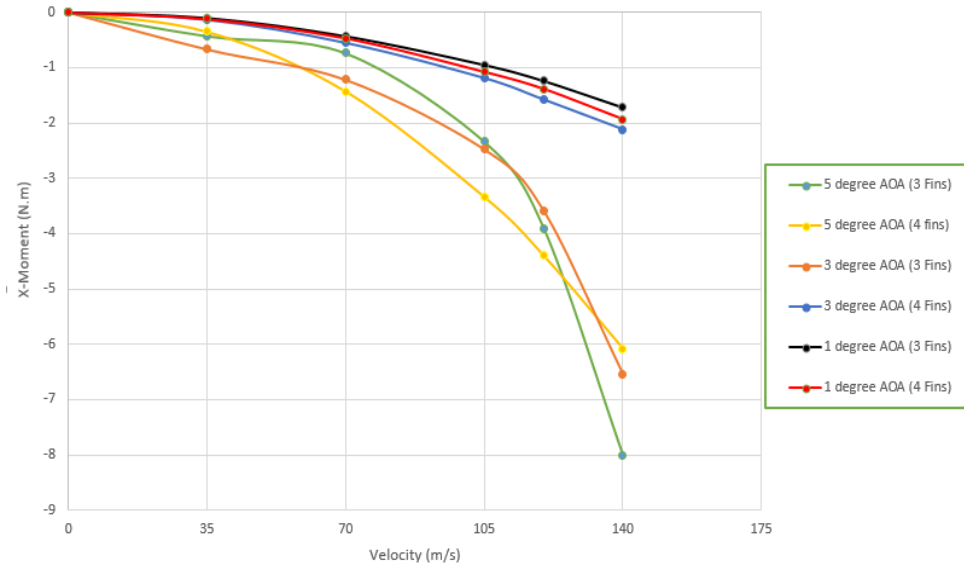
Figure 153. Moment vs. Velocity plot for 3 and 4-fin rockets with different fin cants

Fluent was also able to provide dynamic pressure contours for each case. The contour provides information about pressure on the top, bottom and leading edge of the fins. As shown in Figure 154, the pressure on the top fin has slightly warmer color compared to the bottom part of the fin. This shows that there is higher dynamic pressure on the top part of the fin than on the bottom. This results in a lift force acting on each fin, which is what induces the x-moment.
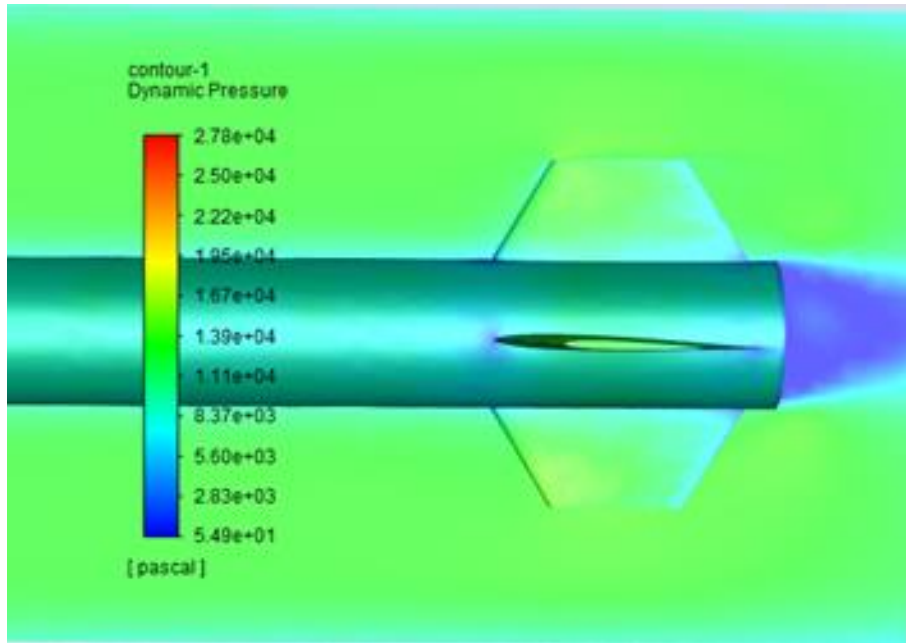
Figure 154. Dynamic pressure contour for fins at 1 deg AOA

Case 2, which uses cambered-airfoil fins, also provided both a moment versus velocity plot and a dynamic pressure contour. The dynamic pressure contour, shown in Figure 155, illustrates how pressure is distributed around the rocket for a flight velocity of 137 m/s and AOA of 0 deg. A magnified picture of the rocket fins is also included in Figure 156.

The contours show a maximum value at the leading edge of the fins. Because of the airfoil's camber, there should be a higher pressure on the upper surface of the fins, where the velocity of the air is highest. This is shown in the contour above as a warmer color. For the lower surface of the fin, where air is moving slower, the contour shows that surface in a cooler color.

Compared to the dynamic pressure contour from Case 1, the dynamic pressure on the fins of Case 2 show that the pressure distribution is more evenly distributed along the entire surface of the fins, rather than just at the tip of the fin.
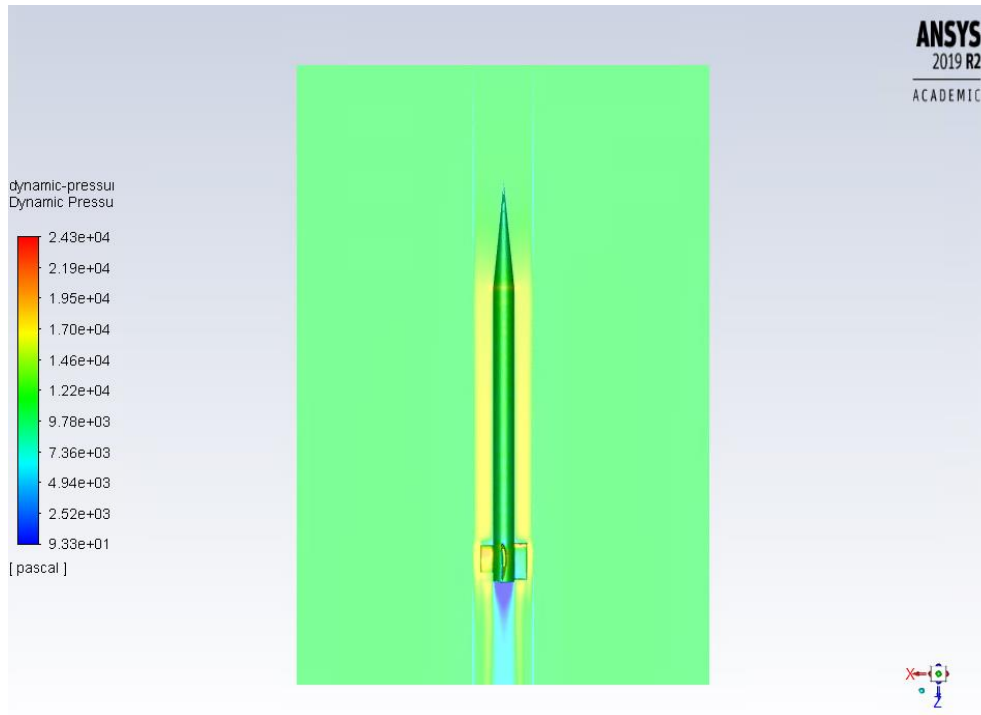
Figure 155: Dynamic pressure contour of baseline rocket with cambered-airfoil fins.
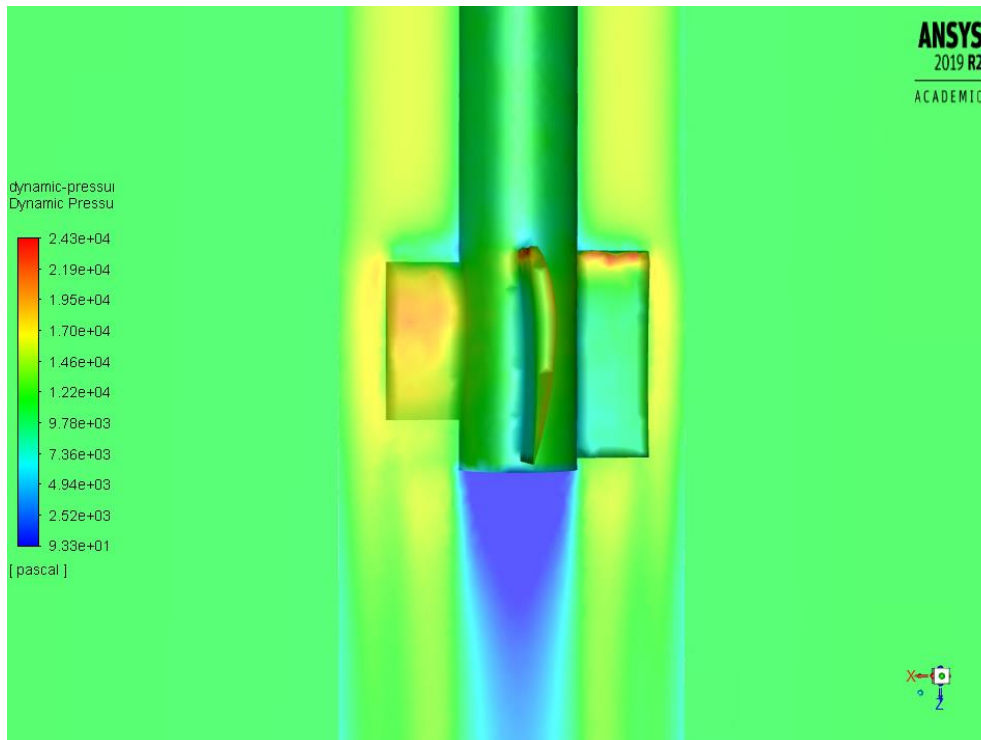
Figure 156: Close-up of cambered fins of Case 3 for FDA Analysis Task 3

The difference in dynamic pressure between the two sides of each fin generates a net moment about the z-axis. The moment generated by these fins is plotted as a function of velocity in Figure 157. The cambered airfoil moment plot is comparable to the 5 deg AOA, 3-finned orientation of Case 1. The moment curves are relatively similar, with both cases generating about 8 Nm of torque at 140 m/s. Although the coordinate axes used for simulations differed between cases, the moment generated and plotted use the same axis; the axis that points along the body from nose cone, through the rocket's long axis. From comparing Figure 153 and Figure 157, the cambered airfoil provides a larger moment than all of Case 1's simulations for a rocket with 4 fins, showing that the cambered airfoil design is more effective at generating a moment than a symmetrical airfoil 4-fin configuration at an angle of attack.
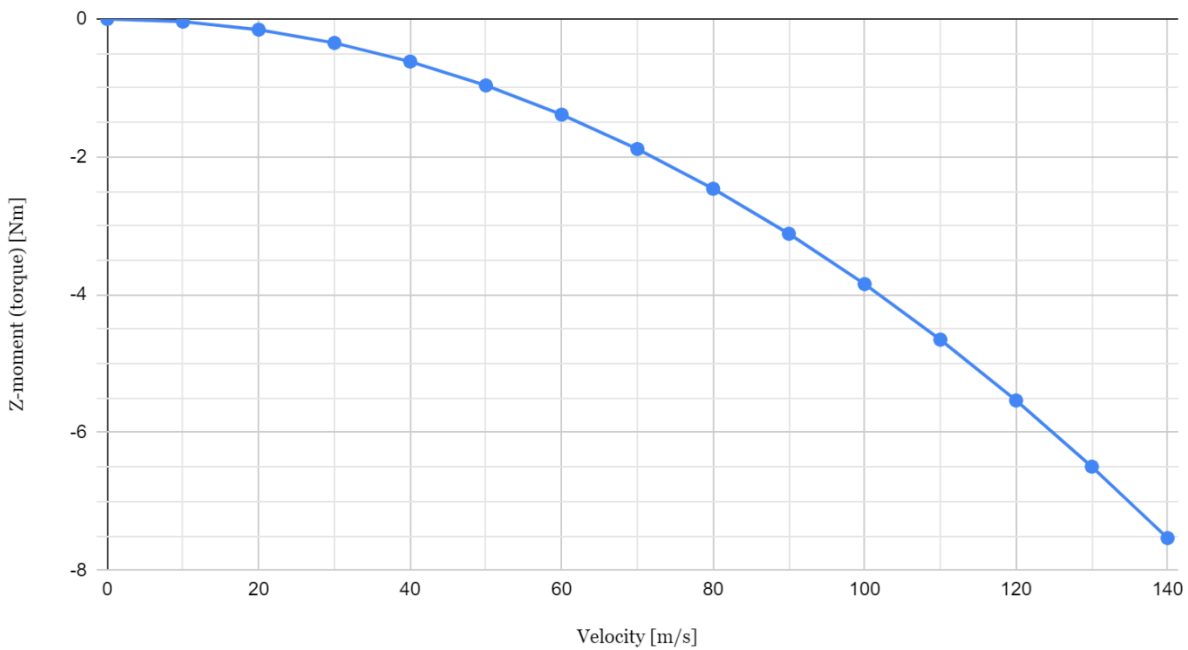
Figure 157: Net torque generated by cambered airfoil fins as a function of velocity

For Case 3, a control surface at the bottom of a symmetrical NACA 0006 airfoil was deflected at angles of 3, 5, and 10 degrees. These three control surface deflection angles were modeled on

the baseline rocket using SOLIDWORKS as seen in Figure 158. This control surface extends 1.5 in. from the bottom of the tab to the hinge. The block to the right of the control surface was added to fix an issue of meshing. The fin and control surface without the block perfectly fit against the side of the rocket in SOLIDWORKS but when imported to ANSYS there was a small separation between the control tab and the body of the rocket. This separation caused the meshing process in ANSYS to fail. The addition of this block fixed this issue. Fluent was able to handle the hinge, straight edges, and sharp corners easily. The element size of the mesh was adjusted to be smaller. Initially, the element size was too large and ANSYS saw the entire fin as a surface with no width coming out of the rocket.
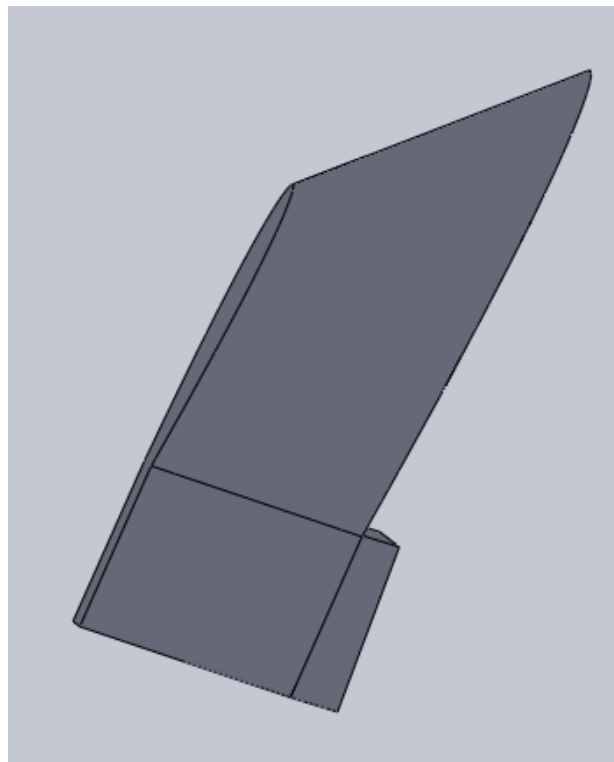
Figure 158: NACA 0006 fin with control tab

The entire rocket body and the four fins were imported into ANSYS Fluent for analysis at a velocity of 81 ft/s, the approximate velocity at which the rocket left the 12 ft launch rail according

to OpenRocket flight simulation and at 450 ft/s, the estimated maximum velocity that the rocket achieves. Dynamic pressure contours for each of these three control surface cases can be found in Figure 159 below. These dynamic pressure contours illustrate the pressure differential on each fin. On the left side of the rocket, the control surface is deflected out of the page. On the right side of the rocket, the control surface is deflected into the page. The difference in the dynamic pressure contours on the right and left fin reflect a higher pressure on the right fin's control surface and a lower pressure on the left fin's control surface. This pressure differential is apparent across all velocities but is more pronounced at higher velocities.
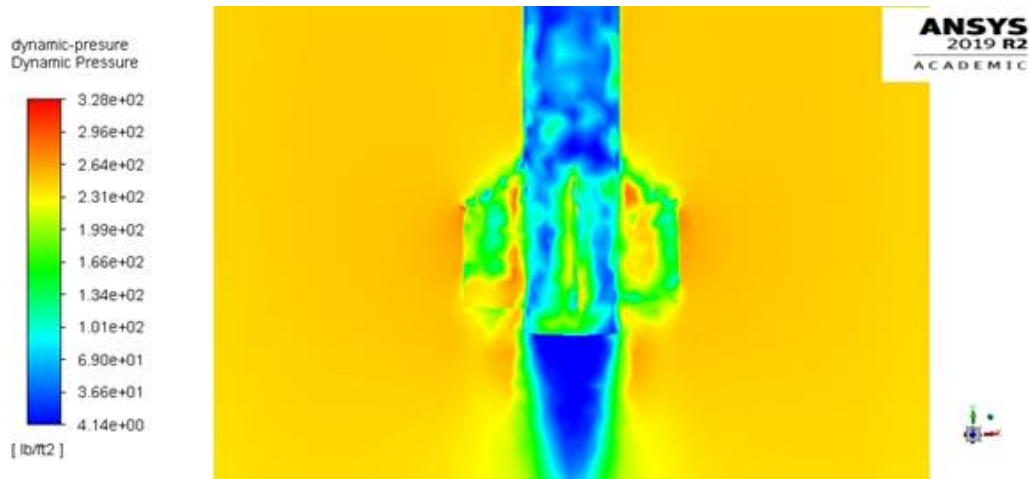
Figure 159: Dynamic pressure contour for case 3 at 450 ft/s

Additionally, the moment and moment coefficient about the y-axis were calculated for the three deflection angles. These values can be found in Table 42.

Table 42. Comparison of aerodynamic moments due to control surface tilted at various
angles

	3 Degree Control Surface	5 Degree Control Surface	10 Degree Control Surface
Aerodynamic Moments at 81 ft/s			
Moment (lbf/ft)	-0.06611	-0.09826	-0.12638
Moment Coefficient	-1.37858e-05	-2.17858e-05	-2.63584e-05
Aerodynamic Moments at 450 ft/s			
Moment (lbf/ft)	-1.46463	-2.96274	-4.02768
Moment Coefficient	-.000073432	-.00040546	-0.00084001

These aerodynamic moments decrease as the control surface angle decreases as well as when the flight velocity decreases. It is also important to note that the trend across control surface angles is not linear, as the moment at 450 ft/s between 5 and 10 deg is much closer than the moment between 3 and 5 deg. This is possibly due to errors in the type of model Fluent is using or is a result of the 10 deg control surface being too extreme of an angle, causing disruption to the flow. Attempted solutions to achieve more precise and accurate moments were to recreate the rocket body and fins in SOLIDWORKS. Making the element size smaller for a more detailed ANSYS analysis as well as running the mesh command with the defeaturing tool on. These attempts resulted in small changes to the moments (1-3%) but no noteworthy trends.

A comparison of the moments produced by Case 1, 2, and 3 at launch rail velocity and maximum velocity can be found in Section 5.3.3.

4.4.   Vehicle Dynamics and Performance Model (FDA Analysis Task 4)

The purpose of FDA Analysis Task 4 was to create and run a model to estimate the baseline rocket's trajectory as functions of time from launch to impact. Originally, the model was to use

rocket geometry, inertia properties, center of mass and center of pressure locations, thrust curve data, drag and moment models from FDA Analysis Tasks 1 and 2, the wind profile across a given topography, and the average wind speed across the rocket's altitude range. Two coupled systems of nonlinear ordinary differential equations were formulated: one system represented the Newton's Second Law equations of motion describing vehicle trajectory, while the other, Euler's Equations for rigid body dynamics, described attitude. This model followed that presented by Box et al. but was simplified by making various assumptions mentioned in Section 1.1.3.6. Briefly, these assumptions are: zero angle of attack; zero body lift; constant heading angle; and negligible gravity force gradients. Thus, the model of the rocket's flight which is presented here treats the rocket as a point mass traveling in a single plane due to external forces acting on it rather than a rigid body which also experiences external moments. A detailed flowchart describing the original plan for the rigid-body model can be found in Appendix L, although it was eventually unused in favor of the point-mass model.

Under the point-mass assumptions listed above, the rocket states which must be solved for over time in order to produce a planar trajectory are horizontal position; vertical position; airspeed; mass; and a flight path angle defined as the angle of the velocity vector from the vertical. Respectively, these are referred to as: $x, z, V, M,$ and θ. The analysis required us to first define a set of coupled, nonlinear differential equations describing the time derivatives of each of these states, then these equations can be solved simultaneously at regular intervals across a time step of integration.

Equations describing these state time derivatives during the rocket's ascent are found below. $t_{burnout}$ is the time at which the rocket motor has consumed all of its fuel; A_{RB} is the rocket's frontal cross-sectional area; g represents acceleration due to gravity; C_D is the drag coefficient for

a given airspeed at zero angle of attack, found using spline interpolation of the results of Analysis

Task 2. I_{sp} is the motor's specific impulse, while T is the thrust provided at a given time, spline-

interpolated from the manufacturer's thrust curve. ρ is standard atmospheric density.

$$\frac{dx}{dt} = V\sin\theta \ , \tag{4-24}$$

$$\frac{dz}{dt} = V\cos\theta \ , \tag{4-25}$$

$$\frac{dV}{dt} = \frac{1}{M}\left(T - \frac{1}{2}\rho V^2 A_{RB} C_D - Mg\cos\theta\right), \tag{4-26}$$

$$\frac{dM}{dt} = \frac{-T}{gI_{sp}} \ while \ t < t_{burnout} \ , \tag{4-27}$$

$$\frac{dM}{dt} = 0 \ while \ t > t_{burnout} \ , \tag{4-28}$$

$$\frac{d\theta}{dt} = g\frac{\sin\theta}{V} \ , \tag{4-29}$$

Similar equations describe the time derivatives of these same states as the rocket descends

from apogee. Throughout descent, parachutes are deployed, and the rocket motor never burns.

These relations are given by Equations 4-30 through 4-32; some are identical to those describing

their respective state during ascent. Nomenclature remains the same, except that A_P represents

current deployed parachute area and $C_{D,P}$ represents the parachute drag coefficient. All the

assumptions previously made still hold.

$$\frac{dV}{dt} = \frac{1}{M}\left(-\frac{1}{2}\rho V^2 A_P C_{D,P} - Mg\cos\theta\right), \tag{4-30}$$

$$\frac{dM}{dt} = 0 \ , \tag{4-31}$$

$$\frac{d\theta}{dt} = g\,\frac{sin\theta}{V}\,, \hspace{5cm} \text{4-32}$$

These equations of motion were implemented into a series of MATLAB scripts using the built-in ODE45 ordinary differential equations solver. These scripts themselves can be found in Appendix M; a summary of their purposes can be found in Table 43.

Table 43: Summary of rocket simulation MATLAB scripts

Script Title	Description
flight.m	Defines differential equations modeling ascent to apogee
descent.m	Models parachute descent from apogee
standard_atmosphere.m	Calculates standard atmospheric density at a given altitude
terminate1.m	Ends ascent solution at apogee
terminate2.m	Ends descent solution upon landing
trajectory_solver.m	Stores constants, initializes solution to both sets of differential equations and calls ODE45, defines timespan and time step of integration, outputs trajectory as well as time profiles of each state

Within this solution, the state of the rocket at apogee, representing the "final" solution to the ascent equations, is passed as the initial state for the descent equations. Deployment of the first 36 in diameter motor bay parachute occurs at apogee; deployment of the nose cone and main body parachutes of 36 in and 54 in diameter, respectively occurs at a descending altitude of 700 ft. Drag from any combination of parachutes is assumed to act opposite to the velocity vector at any point when deployed.

A sample set of results produced by the flight simulator that is, a two-dimensional plot of trajectory as well as time profiles of each state can be found in Figure 160 through Figure 165.
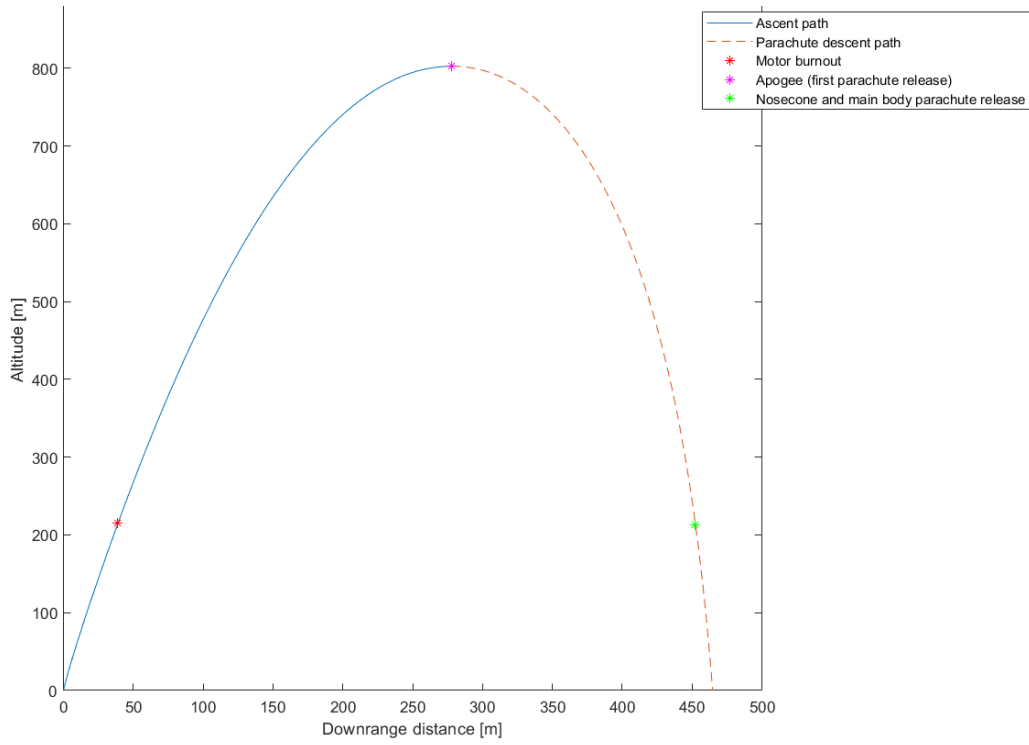
Figure 160: Two-dimensional simulated rocket trajectory for a launch angle of 3 deg clockwise from vertical.
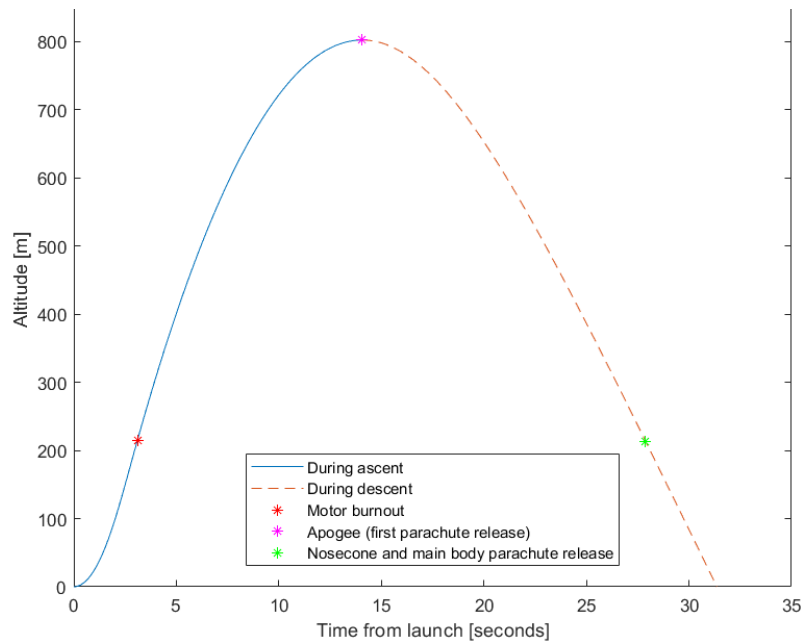
Figure 161: Altitude plotted over time for simulated launch at a launch angle of 3 deg
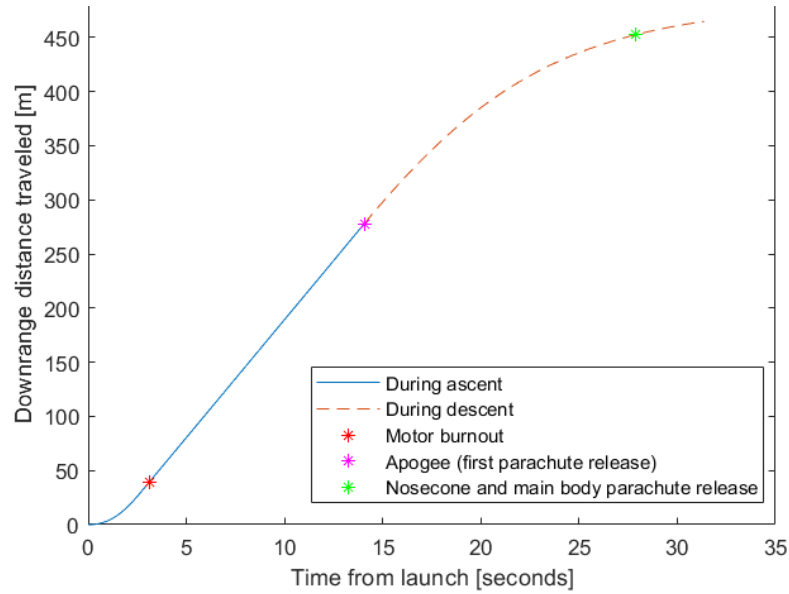
Figure 162: Downrange distance from launch point plotted over time for simulated launch at a launch angle of 3 deg
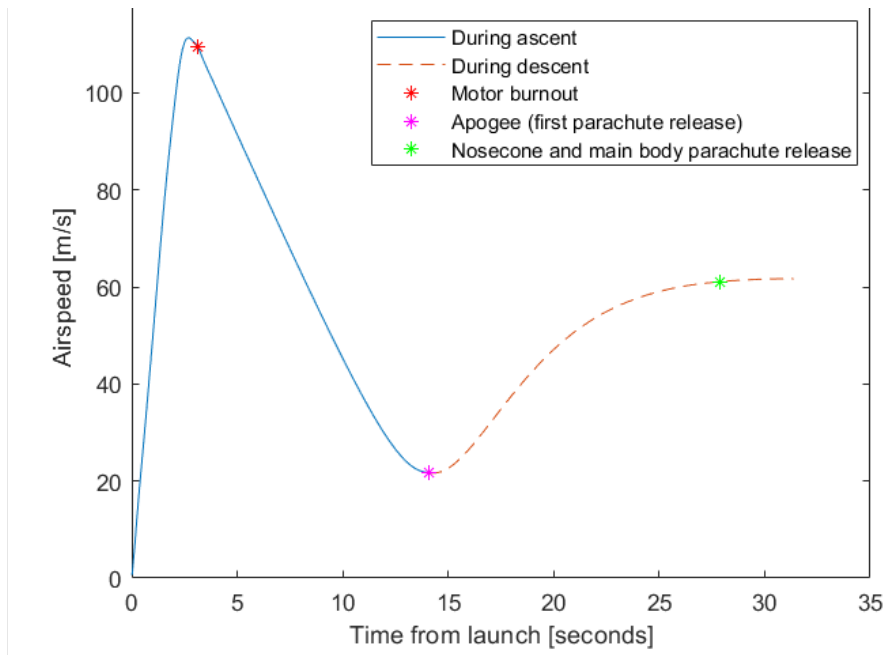
Figure 163: Rocket airspeed plotted over time for simulated launch at a launch angle of 3 deg
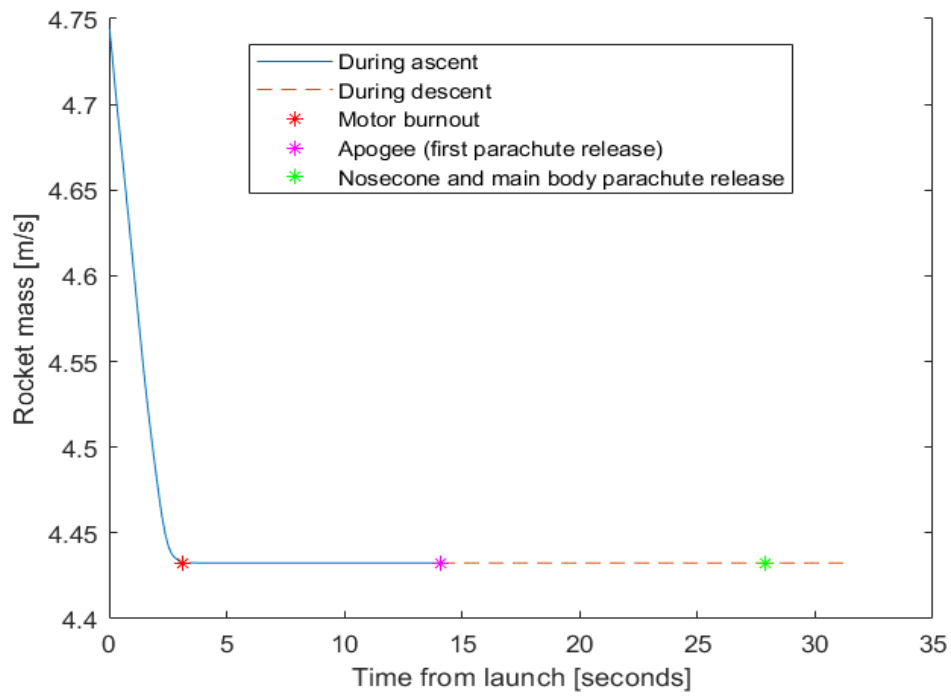
Figure 164: Rocket mass plotted over time for simulated launch at a launch angle of 3 deg
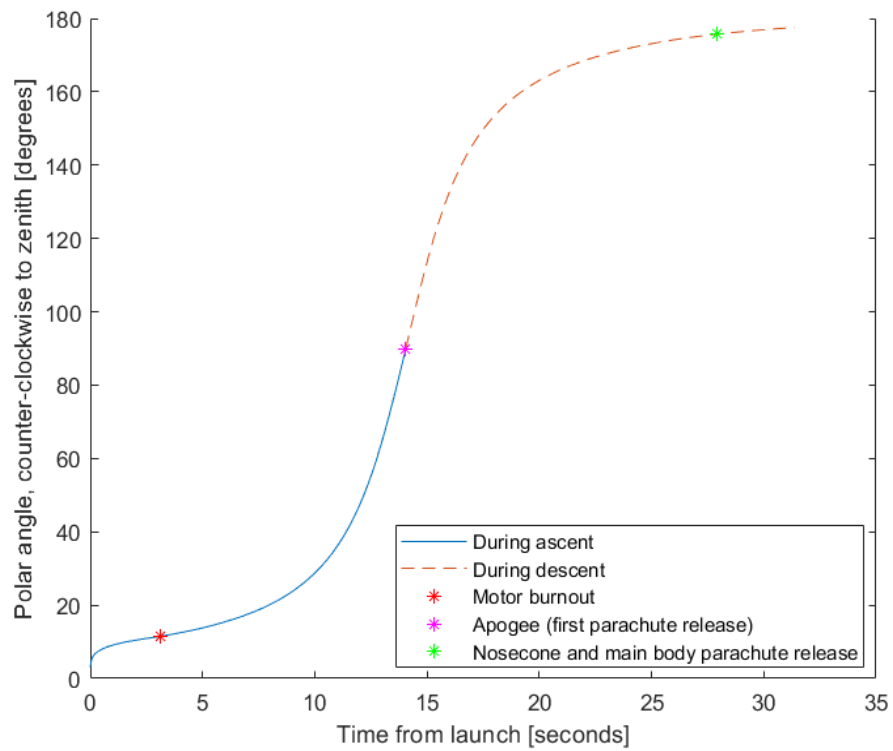
Figure 165: Flight Path angle vs. time for simulated launch at a launch angle of 3 deg

Flight events of interest are marked in each plot, and their effects on the various rocket states can be seen clearly. Motor burnout, which occurs 3.1 s after launch, causes immediate deceleration in both the vertical and horizontal directions; rocket mass suddenly becomes constant, and the polar flight angle begins to change more rapidly as the rocket's main axis tips towards horizontal, which it reaches at apogee. The release of the first parachute at apogee causes immediate horizontal deceleration as drag opposing the rocket's velocity (which is completely horizontal at apogee) suddenly increases. The total airspeed, meanwhile, increases from apogee as the rocket begins falling towards the ground, and approaches a terminal velocity with the apogee parachute deployed. The polar angle continues to increase quickly during the first moments of this fall, then begins to approach 180 deg (at which point the rocket would be pointing directly towards the ground) as the nose cone and main body parachutes are deployed at an altitude of 700 ft. This final event causes one last deceleration as the rocket reaches the ground and lands.

The simulation's calculated apogee altitude for this case differs slightly from the measured height to which the baseline rocket climbed on its launch day. Non-idealities make this discrepancy reasonable. Assuming a zero angle of attack at all times throughout the simulator's model effectively minimizes drag; any spin induced on the rocket by aerodynamic loads on the fins and/or body would reduce the rocket's upwards momentum so that kinetic energy could exist in the spinning motion.

4.5. Baseline Rocket Launch Results

A launch of the baseline rocket was performed on November 16, 2019 in Amesbury, Massachusetts, authorized by the Central Massachusetts Spacemodeling Society. The temperature was approximately 35ºF, the sky was sunny, and winds came at 10 to 15 miles per hour from the

North West. Results of this launch pertinent to the FDA subteam's work are presented in this section; basic characteristics of the rocket flown are presented in Table 44 below.

Table 44: Baseline rocket characteristics.

Rocket Characteristic	Description
Length	74 in
Mass with motor	135 oz
Motor used	I216
Maximum altitude reached	Approximately 2700 ft

No gyroscopic data was recorded during flight due to software compatibility issues with the data collection board. Proper drivers were not shipped with the board, meaning that the board could not be properly calibrated or tested even once drivers were received from the manufacturer.

Table 45 lists the launch success criteria for the FDA subteam, which summarizes the baseline rocket launch's results. Figure 166 shows an altitude plot extracted from data collected by the Raven altimeter, averaging measurements based on readings of barometric pressure and acceleration. The maximum acceleration experienced during this launch was approximately 70 m/s^2; the maximum velocity reached was approximately 450 m/s. There are two inconsistent jumps in data that occur on the altitude plot. The first occurs at approximately 17 s and is a result of a black powder discharge ejecting the first parachute, resulting in some sensor noise. The second inconsistency is a result of the same disturbance to the accelerometer and barometric readings and occurs at approximately 63 s. Here, an additional black powder discharge ejected the second parachute.

No gyroscopic data was recorded during flight due to software compatibility issues with the data collection board. Proper drivers were not shipped with the board, meaning that the board could not be properly calibrated or tested even once drivers were received from the manufacturer.

Table 45: FDA subteam launch success criteria

Test Objective	Pass/Fail	Success Criteria	Verification
Stabilized Flight	Pass	Rocket Orientation remains vertical; nose cone points upwards throughout flight, within several degrees of zenith	Rocket does not visibly "turn over" and enter non-vertical flight
	Fail	Weather cocking perturbs flight in excess of several degrees; rocket trajectory otherwise deviates from upwards	
Record Flight Data(Raven Altimeter)	Pass	Raven altimeter is activated successfully by external switch and records flight data to internal memory until being deactivated after landing	Raven data log contains stream of altitude, accelerometer data
	Fail	Raven does not activate, or otherwise fails to store flight data	
Record Flight Data (collection board gyroscopes)	Pass	Data collection board achieves the same success as the Raven, recording gyroscopic flight data	Collection board data log contains stream of orientation data from activation to recovery
	Fail	Sensors do not activate, or board otherwise fails to store flight data	
Detect Launch	Pass	Raven altimeter detects launch; event is visible in post flight data log	Raven data log shows launch event at particular flight time, marked by increase in
	Fail	Raven does not detect launch; data is missing the event	
Detect Apogee	Pass	Raven detects apogee; event is visible in data log	Raven data log shows apogee event at particular flight time, marked by decrease in acceleration
	Fail	Raven fails to detect apogee; data log is missing the event	
Signal for Separation Charges Sent	Pass	Raven recognizes flight events and sends signals to individual separation charges with proper time delays, deploying recovery system successfully	Raven data log shows deployment of signal for each individual separation charge; visual verification during flight that separation occurs and parachutes deploy
	Fail	Raven does not recognize flight events or otherwise fails to send separation charge signals; separation events do not occur during flight and parachutes are not deployed	
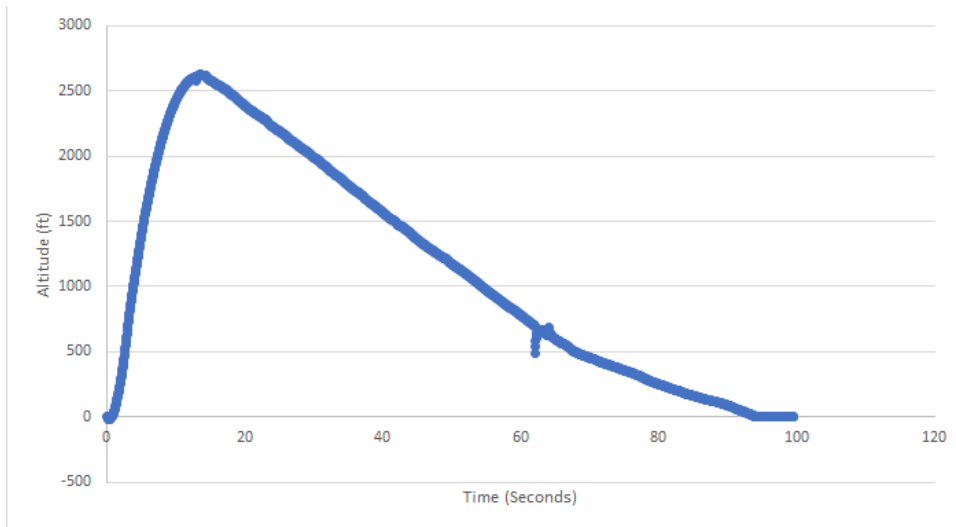
Figure 166: Plot of altitude versus time as measured on the baseline rocket launch from altimeter measurements.

Figure 167 shows the altimeter's recorded velocity and acceleration data. Sudden spikes in accelerometer noise occurred at launch and at each black powder charge event as discussed above; these were the root cause of noise spikes in altitude readings.
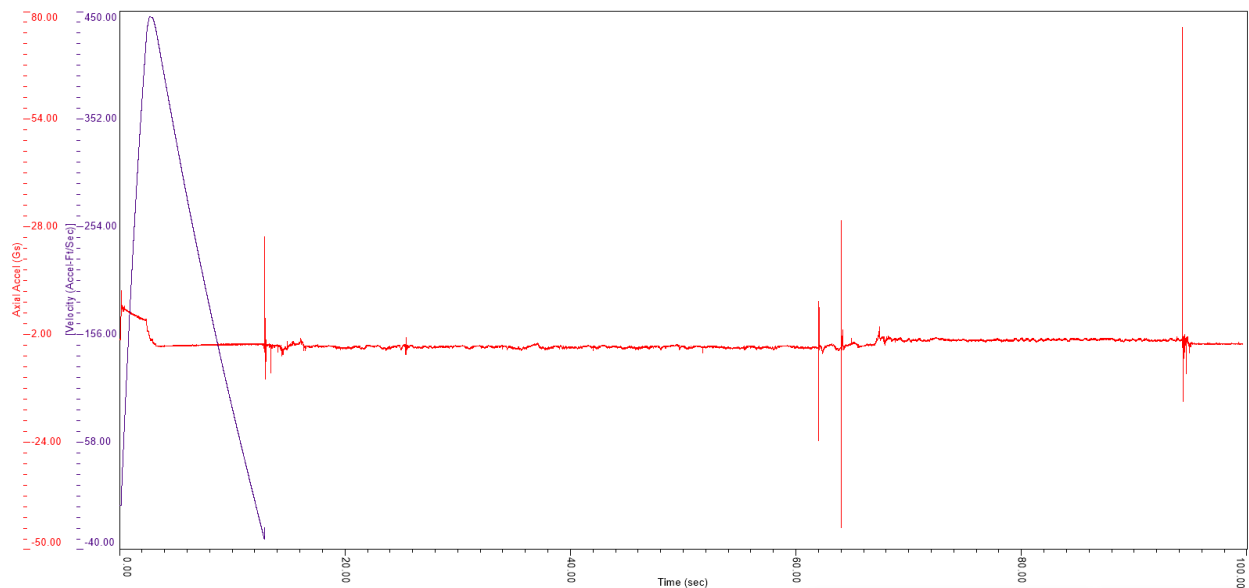
Figure 167: Acceleration (red) and velocity (purple) data collected by altimeter during flight.

5   Summary, Conclusions, Recommendations, Broader Impacts

In terms of the planning and administration of the design and construction of a HPMR, our team developed a few recommendations to ensure that future teams continue to be successful. To start, it is very important to set a launch date early in the project. Announcing a launch date early in the project allows for a hard deadline to be declared. This means that programs and tools such as a Gantt chart can be used to track progress and developments of the HPMR towards its end date. This also allows for supplies to be ordered in advance, and analysis tasks to be completed before the construction of the HPMR. Finally, we recommend that all materials ordered from external vendors be inspected as soon as they arrive to make sure they are accurate and in good condition. When our team received the first nose cone, it was a component that was not manufactured to our standards and was not in great condition from the manufacturer. We had to order a new nose cone from another manufacturer since we were not confident in the nose cone's performance during launch.

5.1.   Airframe and Recovery Systems

Conclusions and recommendations from the Airframe and Recovery System subteam tasks are summarized in Sections 5.1.1 through 5.1.5. Various conclusions were made through the design and analysis of these two HPMR's. ARS Analysis Tasks 1-4 confirmed the HMPR could be safely launched and recovered due to the structural integrity of the airframe, the safe descent velocity calculations during recovery, as well as the stress analysis on the rocket fins and u-bolt bulkheads.

5.1.1   Airframe Stress Distribution (ARS Analysis Task 1)

The analysis of the structural integrity of the airframe Blue Tube 2.0 material proved to be adequate. One concern was that the Blue Tube 2.0 would not withstand the impulsive ignition of the black powder charges. Therefore, the goal of ARS Analysis Task 1 was to determine whether the airframe would deform or yield under the conditions of the black powder ignition. In the ARS Analysis Task 1 in ANSYS, results show that the maximum stress on the Blue Tube 2.0, which is rated to withstand a pressure of 15 psig, was 4.517 MPa on the upper airframe and 4.44 MPa on the lower airframe. This demonstrates a safety factor of 26.5 and 27 respectively with regards to the properties of Blue Tube 2.0 provided by the manufacturer.

Our analysis of the structural integrity of the airframe proved to be successful. There were no damages to the airframe due to the pressure from the ignition of the black powder charges during the flight test (see Section 4.5 for the results of the baseline rocket launch). This proved that our analysis using ANSYS was successful as the results from the ANSYS simulation demonstrated that our airframe could withhold the pressure from black powder ignition.

For future rocketry projects, the ARS subteam recommends in depth analysis on the airframe of the model rocket. Whether the material is Blue Tube 2.0 or another commonly used material for model rocketry, it is extremely important to have a thorough stress analysis on the internal compartments of the airframe from the impulse of the ignition of the motor. If the ignition of the motor, or other separation charges, created a pressure that is too large for the airframe of the rocket to handle due, the airframe could yield and deform. This would prove disastrous for the model rocket and any test flights that may take place.

5.1.2 Fin Analysis (ARS Analysis Task 2)

The fin analysis task was successful in ensuring the fins would not be damaged during flight. ARS Analysis Task 2 helped the team understand what landing velocity was realistic so that the rocket would not break when it hit the ground. A recommendation is that a device, such as the "fin guillotine" (see Figure 33), be used to cut the slots for the fins that will eventually be epoxied to the airframe. A device like this will ensure the slots cut in the airframe be as accurate as possible, more so than when cutting them with a Dremel or saw.

5.1.3 Stresses on U-Bolt Bulkhead Coupling (ARS Analysis Task 3)

The analysis task determining whether the stresses on the u-bolt bulkheads generated by the parachutes deploying was successful. The simulations performed using MATLAB, to find the forces generated by parachutes, and ANSYS, to create a stress distribution across the bulkhead, suggested that the bulkheads would not fail during the rocket's flight. The main recommendations for constructing the bulkheads would be to use a precise machine to cut the parts, and then to ensure the connections on the bulkhead are tight and sturdy. By creating a stable bulkhead structure, the possibilities of failure can be decreased.

5.1.4 Parachute Sizing Model (ARS Analysis Task 4)

The main goal of ARS Analysis Task 4 was to calculate the needed parachute size of the drogue, nosecone, and main parachutes. The main conclusion from ARS Analysis Task 4, for the traditional recovery system, was that the calculation of the required size for three parachutes (two being 36 in and one being 72 in) would be adequate during recovery for our HPMR. The results of ARS Analysis Task 4 indicated a required inflated main parachute diameter of 72 in., and then a 36 inch drogue and 36 inch nosecone parachute. Using the three parachutes for the test flight (see Section 4.5), the rocket was recovered safely with a descent velocity of approximately 5 m/s

as measured by the calculations in MATLAB and discussed in Section 2.2.4. This validated our parachute sizing model and confirmed the results were accurate. The ARS subteam was able to conclude from these results that our parachute sizing model and inflated diameter equations and calculations were completed correctly.

The same methodology can be used in future recovery analyses to determine the size of drogue, nosecone, and main parachutes. The ARS subteam recommends using MATLAB to complete these calculations, while also using software such as OpenRocket to gain an accurate mass estimate of each subsystem of the model rocket. Our team used OpenRocket to calculate the mass of the entire HPMR, the nosecone, and the upper and lower airframes of the model. It is recommended that each of these sections have their mass accounted for individually, that way the parachute sizing model can be done correctly based on the mass of the system that the parachute will be recovering.

5.1.5 Autorotation Blade Model (ARS Analysis Task 5)

Using the results from the four cases from the autorotation MATLAB model, the ARS subteam concluded that successful recovery using an autorotation system could not be accomplished with commercially available supplies. An autorotational recovery system is not ideal for a model rocket this size. While the concept was sufficient enough for our analysis, and our MATLAB code was accurate and executed properly, the model rocket could not decelerate at an adequate rate only using the aerodynamic forces from the COTS rotor blades and the rocket. If more time were allowed for this project, ARS would have looked at the possibility of designing our own rotor blades to more effectively slow the rockets descent.

If an autorotation recovery system were used on a future model rocket, we recommend that the rotor blades be designed using a desired airfoil and with a blade twist. Designing a rotor blade

could provide greater aerodynamic forces to slow the descent velocity of the model rocket. The designed rotor blade could be analyzed using the MATLAB model developed by the ARS subteam, but we also recommend performing physical tests. These tests may include wind tunnel or drop tests. Performing physical tests would provide a more accurate representation of the performance of the designed rotor blades on an autorotation recovery system.

When it comes to the actual design and construction of an HPMR, many recommendations have been generated as a result of our analysis. Based on our findings, specifically the design of both the traditional and innovative recovery systems, we recommend that detailed solid models of the rocket be generated. For example, CAD models designed in SOLIDWORKS proved to help our team determine the spacing, tolerances, and overall configuration of the entire recovery system and the model rocket. It is extremely important that these models are as accurate and realistic as possible. With the generation of an accurate CAD model, spacing and allotment inside the airframe of the model rocket can be used to determine the orientation and configurations for each subsystem of the model rocket.

Even though we were not able to successfully design the innovative autorotation system to provide a slow enough descent velocity, we conclude this project was a success. Our first version of the HPMR with the traditional parachute recovery system was both launched and recovered safely. While the HPMR with the innovative recovery system was not able to be launched, we were satisfied with the construction and design of this rocket. We took great care in designing each component of the HPMR with the innovative recovery system and were extremely satisfied with the launch of the first HPMR.

5.2.   Propulsion, Thermal, and Separation Systems

Conclusions from the Propulsion, Thermal, and Separation System subteam tasks are summarized below.

5.2.1   Motor Performance Model (PTSS Analysis Task 1)

The PTSS subteam investigated the combustion reaction that occurs in the model rocket motor using the software Cantera. We conducted a chemical equilibrium analysis that modeled the decomposition of ammonium perchlorate and aluminum into unknown product species. The goal of PTSS Analysis Task 1 was to calculate performance parameters for the I216 Cesaroni motor, such as thrust and specific impulse, to then compare this predicted performance data with the manufacturer data.

Our attempt to predict the motor performance proved to be successful. We calculated the specific impulse to be 273 s (207 s per manufacturer) and calculated the thrust to be 237 N (216 N per manufacturer) [87]. Despite our calculations being higher in comparison to the manufacturer, this result was expected. The analysis in Cantera assumed there was no heat loss throughout the motor casing and the isentropic flow assumed to calculate the specific impulse and thrust neglected many losses in a real flow such as viscous effects and divergence losses.

For future work, we suggest including heat loss during the chemical equilibrium analysis in Cantera. Despite the heat loss in the motor being small (as is evident by our temperature distribution analysis in COMSOL), this extra heat loss term would better represent the energy exchange that occurs in the motor, which could affect the final temperature and hence performance. In addition, we suggest using the chemical reaction properties from Cantera as chamber conditions for a nozzle flow analysis using CFD. The use of CFD software would accurately model the

viscous effects of the flow in the nozzle and provide a more precise prediction for the specific impulse and thrust of the motor.

5.2.2 Temperature Distribution (PTSS Analysis Task 2)

To estimate the temperature distribution across the rocket motor, we utilized COMSOL to complete the analysis. By conducting a heat transfer and laminar flow study we estimated what the final temperature of the motor casing would be after the stated burnout time of I216 motor. The primary goal was to see if there was a significant flux of heat (indicated by a large temperature gradient) radially outward through the motor casing, to be able to see if there would be any risk of structural failure due to excessive heating.

Our model in the end was successful in running and showing sensible results. Again, the final calculated temperature of the aluminum casing came out to 293.13 K. Although only being a slight increase in temperature from the initial temperature that was set, it shows that heat transfer did occur.

In the future we suggest looking into how to analyze the exhaust gas flow of the rocket motor more accurately. While our model was sufficient enough to evaluate the heat transfer across the motor, the flow in the fluid domain of the motor can be modeled with better accuracy by looking further into how COMSOL's laminar flow module works. Alongside, looking into how to better use the laminar flow module, looking at the other fluid flow modules may also be useful to explore alternatives of modeling the flow through the motor. Additionally, if possible, our team recommends trying to more accurately identify the composition of the commercial model rocket motor to be able to more accurately model the equilibrium reaction. Our team assumed that the motor was 100% solid ammonium perchlorate, but from reading literature on model rocket motors,

that was not found to be the case. Knowing the actual composition, and finding the corresponding thermochemical data, will assist in ensuring that the resulting data is sensible and accurate.

5.2.3 Nosecone Separation System Model (PTSS Analysis Task 3)

Through multiple design iterations, the PTSS subteam created an innovative spring-based separation system for a model rocket. This system utilized four compression springs to eject the nose cone of the rocket, along with a servo motor, pin, and torsional spring to simultaneously release the compression springs. The PTSS subteam created a SOLIDWORKS model, which was used to 3D print each of the necessary components. A representative physical model was assembled.

For future work involving separation systems, the PTSS subteam recommends that a larger diameter rocket be used. Due to sizing constraints, the PTSS subteam calculated the maximum force of the proposed spring system would only be enough to shear one shear pin. This was based on the diameter of springs available, which fit within the allotted space. Increasing the diameter of the rocket would allow for larger springs, as well as stronger motors or other release mechanisms.

5.2.4 Motor Staging

The innovative rocket design included the use of a two-stage propulsion system. This design requires two motors, additional black powder charges for stage separation, an onboard ignition system for the second stage and an additional set of fins. Although the innovative rocket was never launched, it was assembled along with the two-stage propulsion system.

If this innovative rocket were to be launched, the PTSS subteam recommends ensuring that the upper stage is made as light as possible due to the requirement of minimum thrust-to-weight ratio imposed by the National Association of Rocketry. Having a second stage already increases the mass simply due to the need of a second stage and motor. Therefore, making sure the upper

stage of the rocket is lightweight will help maximize the altitude. In addition, we recommend the use of multiple redundancies for the onboard ignition system. It is extremely important that the second stage ignites midflight, otherwise, the rocket could fail to reach its target altitude. Overall, the implementation of a multi-stage model rocket complicates the design but also enables a user to maximize the altitude for a given certification from the NAR.

5.3. Flight Dynamic Analysis

Conclusions from the Flight Dynamics Analysis subteam tasks are summarized here.

5.3.1 Aerodynamic Loads – Simple Model (FDA Analysis Task 1)

The results of the analytic methods used to calculate aerodynamic loads in FDA Analysis Task 1 can be expanded on with the following recommendations in mind. Given sensor data such as yaw, pitch, and roll rate values from test flights, future teams would be able to create plots of the moments the rocket experiences during flight as a function of flight velocity in the yaw, pitch, and roll directions. Similarly, in order to plot the moment, instead of assuming the pitch rate of the rocket is some constant value, the accuracy of the plots would be improved with sensor data implemented in the code.

With a better understanding of how stability derivatives, like those used to analyze the stability of planes, describe the stability of a rocket, there is room to expand the usefulness of results. For example, comparing the lift coefficient stability derivative calculated in this analysis task to that of other model rockets, high-powered model rockets, and missiles could be useful when assessing the rocket's stability compared to similar flight vehicles.

5.3.2 Aerodynamic Loads – Simulation (FDA Analysis Task 2)

In general, the trends illustrated by the plots of aerodynamic loads and dynamic pressure contours from FDA Analysis Task 2 appear to be valid. The majority of loads exhibited quadratic relationships with velocity, reflecting their theoretical link to dynamic pressure. The pressure contours also behaved as expected, since they showed high pressure where the airflow hit the rocket and low pressure where the rocket itself blocked the flow. Additionally, at 0 deg AOA, flow in rocket's wake looked relatively smooth, but as the AOA increases, the flow in the wake appeared more turbulent.

Some unusual behavior was also noted. Examining the data gathered from the baseline rocket cases showed that despite the symmetric fins, the baseline rocket experienced lift forces up to 2.31 N at 0 deg. Additionally, the moments about the x and z-axes should have been 0, or at least of the same magnitude, but they were not. Even with the rocket's rotational symmetry around the y-axis, unique, non-zero x and z-moments (up to 0.08 and 1.27 N-m respectively) existed at 0 deg AOA. Since these loads were relatively small compared to loads experienced at larger angles of attack, the FDA subteam considered them negligible.

Although the discrepancies were small, there are several possible reasons for their existence. The first is the turbulence model selection. A k-ω model was chosen for its superior handling of aerodynamic problems. After further research into the k-ω model, it was found that solutions generated by the standard version, used for this project's simulations, can be highly sensitive depending on the free stream turbulent kinetic energy (k) and specific dissipation rate (ω). This means that the values of k and ω are directly linked to the accuracy of the solution. It was unclear from the literature exactly how k and ω affect the solution, but it was specified that the effects make the standard k-ω model a poor choice for use in ANSYS Fluent [61]. Therefore, the FDA

subteam recommends that more research be done into the other types of k-ω models available. The Shear Stress Transport (SST) version, in particular, showed some promise since it is calibrated to compensate for the standard model's sensitivity to k and ω. This means the SST k-ω model is more likely to accurately evaluate equations associated with turbulence that effect aerodynamic loads [61].

It is also likely that inexperience played a role in the inaccuracy of the simulation. Due to the limited time frame of the project, less emphasis was put on mastering the software before beginning the analysis process. Having never used ANSYS Fluent before, the FDA subteam did not have much knowledge of successful simulation methods. Some background research was done on this subject, but no general method was found that could be applied to all problems. If more time were available to learn the intricacies of ANSYS Fluent, a method might have been developed for correcting the lift and moment errors.

The data in Appendix K only provides steady-state estimates of the loads the baseline and innovative rockets could have experienced during flight. While this is very important information, Fluent has the capability to facilitate more interesting analysis. Future MQPs involved with high-powered model rocketry might consider using Fluent's transient solver to estimate how aerodynamic loads change over time. They could also attempt to write user defined functions for simulating the effect of wind on aerodynamic loads. The results of these analyses could then be used to predict the kind of disturbances the rocket would encounter during its flight.

5.3.3   Fin Design for Vehicle Spin Stabilization (FDA Analysis Task 3)

A comparison of the moments for 81 ft/s and 450 ft/s for Case 1, 2, and 3 can be seen in Table 46. These two velocities are (1) the velocity at which the rocket leaves a 12-foot launch rail

according to OpenRocket and (2) the maximum velocity our rocket achieves, according to both OpenRocket and confirmed by flight data offloaded from the Raven 3.0 Altimeter.

Table 46: Comparison of Moments

Moments at 81 ft/s (lb-ft)		Moments at 450 ft/s (lb-ft)	
Case 1:		Case 1:	
1 degree 3 fins	0.03319	1 degree 3 fins	1.2540
1 degree 4 fins	0.03467	1 degree 4 fins	1.4014
3 degrees 3 fins	0.4794	3 degrees 3 fins	4.794
3 degrees 4 fins	0.03688	3 degrees 4 fins	1.5489
5 degrees 3 fins	0.33190	5 degrees 3 fins	5.9
5 degrees 4 fins	0.2581	5 degrees 4 fins	4.499
Case 2: Cambered Fin	0.1844	Case 2: Cambered Fin	5.5317
Case 3:		Case 3:	
3 degree control surface	0.06611	3 degree control surface	1.46463
5 degree control surface	0.09826	5 degree control surface	2.96274
10 degree control surface	0.12638	10 degree control surface	4.02768

At 81 ft/s, Case 1, a symmetrical airfoil at an angle of attack of 3 degrees with 3 fins produced the highest moment while leaving the launch rail. At 450 ft/s, Case 2, a cambered fin produced the highest moment at the maximum flight velocity. The moment causes a spin which results in stabilization of the rocket, similar to an arrow spinning through the air. While the rocket is spinning it is more resistant to changes in flight path when affected by wind disturbances or

251

external forces, resulting in a straighter and more accurate flight path. However, spinning the rocket as fast as possible is not the perfect solution. There is an ideal spin rate, as overspinning the rocket could result in an over stabilized rocket, which if disturbed tends to point into the direction of an external force such as a gust of wind. This ideal spin rate was not calculated due to time constraints. Based on the comparisons between cases as well as the different configurations of Case 1, an optimal fin orientation may exist that produces a high moment while minimizing drag. For example, more fins do not always produce a higher moment, which could be due to the drag caused by additional of fins. Also, the optimal fin orientation is dependent on the angle of attack of the symmetrical fins. Finally, a high moment at the end of the launch rail may not be ideal, as the moment could cause friction and shear forces on the launch rail buttons, possibly resulting in a bad launch. More analysis can be done to determine the optimal design configuration to induce spin stabilization on a high-powered model rocket. Future teams could expand on this analysis by implementing these fin designs into rockets that are test flown. Future teams can also use Fluent's transient solver to simulate the rocket's spin as a function of time.

5.3.4 Vehicle Dynamics and Performance Model (FDA Analysis Task 4)

Several expansions upon FDA Analysis Task 4 may be considered to make it a more robust, complete description of the rocket during flight. Using similar equations of motion and maintaining the zero angle of attack assumption, i.e., continuing to treat the rocket as a point mass, a second azimuthal angle could be used to describe the rocket's motion in three dimensions. This would require describing the rocket's position in spherical coordinates, and may thereby require moving between a spherical and Cartesian coordinate system at different points throughout the solution. With this expansion, lift generated by the rocket body, which in the current solution would act perpendicular to the plane in which the rocket travels—could be imparted on the point

mass, although this remains negligible if not zero when considering a zero angle of attack according to the aerodynamic load results of FDA Analysis Task 2. Moreover, a wind gust term could be added as a directional force acting on the point mass, either in the two-dimensional case considered here, or in the three-dimensional case being described. This could be implemented realistically using an algorithm which generates an altitude-dependent, statistically random wind speed at each time step. Gawronski's "Modeling Wind-Gust Disturbances for the Analysis of Antenna Pointing Accuracy" [95] contains useful analysis and algorithms for this purpose.

A considerably more complicated case, which was originally planned for this solution, involves eliminating the zero angle of attack assumption, treating the rocket as a rigid body, and coupling a set of ordinary differential equations to find its orientation at regular time steps with those that are used to find its motion through space. A biaxial table lookup could use results such as those of FDA Analysis Task 2 to find aerodynamic force and moment coefficients as they relate to both airspeed and angle of attack. Box et al. have created a remarkably complete model for this simulator, which includes their own stochastic method of imparting wind on the rocket.

The only failed FDA baseline launch success criteria should be mentioned when drawing conclusions and making recommendations. The FDA subteam recommends more thorough product research in order to avoid software issues which prevented us from collecting gyroscopic data; reaching out to the manufacturer about drivers beforehand could have helped us choose a more reliable data collection board. Using an altimeter with gyroscopes would have reduced the complexity of the e-bay's layout and made the offloading and reading of data much more straightforward. We did not encounter any such options while selecting avionics, but also did not seek one out, opting to use the Raven 3.0 altimeter primarily because one was already in our possession and did not need to be purchased.

Many FDA baseline successful launch criteria were met but had room for improvement. A visibly stable flight was achieved with the baseline rocket's trapezoidal fins, but this fin shape was selected as a precaution against fin tip damage upon landing. The rocket may be more likely to land on the corner of a clipped delta fin, but these fins were described in the literature as the most aerodynamically efficient option which typically produces less drag than other common shapes, including trapezoidal [96]. This shape should be considered if a future team seeks to achieve the highest altitude possible for a given motor.

5.4.   Overall Project Broader Impacts

The HPMR program set out to design, analyze, assemble, and test a high-powered rocket. During this process, the team encountered different social, economic, and societal impacts.

From a social perspective, actively vs. passively controlled rockets are social consideration. Many military and commercial rockets are actively guided but regulated by the government to ensure safety among society. For example, the military uses actively guided missiles in combat applications, which are only appropriate in that context. These are weapons that can cause extreme devastation. Although actively guided rockets that do not carry any explosives can provide an interesting challenge for hobbyist, this is a major social consideration and any guided hobby rocket is not legal.

Expanding on the social perspective, the model rocketry community is accessible to all people from many different backgrounds. Not only does it attract academic groups like this one, but also model enthusiasts that may not know much about aerospace engineering. Model rocket excites young kids too. Rocket launches often have parents and kids working and learning together how to build model rockets. Some Boy Scouts around the country have even had the opportunity to earn a rocketry badge. Model rocketry clubs often have groups of friends and is great networking

254

opportunity. Online resources have a plethora of information for beginners, enthusiasts, and experts. Although the cost of rockets varies with the size of the rocket, there is virtually a rocket for any budget.

From an economical perspective, the HPMR team set out to create a reusable system, which could be launched any number of times. This is a similar philosophy, albeit on a much smaller scale, to that of a company such as SpaceX, which reuses portions of its rockets for various missions to the International Space Station, Geostationary Orbit and others. These reusable missions require the support of large teams of engineers and technicians, building the economy in the aerospace industry with the number of jobs it provides. Relaunching rockets is beneficial to the economy, as the cost per launch can be lowered if a rocket is reused.

Model rocketry drives its own industry as well. Companies including Apogee Components Inc., Giant Leap Rocketry, Always Ready Rocketry and others would not exist without this niche market. Passion from the model rocketry community drives the innovation and success for companies like the ones mentioned.

Model rocketry can have some environmental impacts. The main impacts are caused by the chemicals used to launch the rocket. To prevent the contamination of fields where rockets are typically launch, launching authorities like CMASS place fireproof blankets under launchpads. This prevents crops from being burnt and chemicals from seeping into the soil. Ammonium perchlorate (one of the main reactants in the rocket motor) is toxic to humans, but because they are in small quantity and done outdoors, it poses little harm to humans at or near a launch site.

6 References

[1]   M. Newton, "Rocketry Basics," January 2012. [Online]. Available: https://www.nar.org/wp-
        content/uploads/2014/03/NAR-Rocketry-Basics.pdf.

[2]   D. Cavender, "NASA High Powered Video Series Counterpart Documents," National Aeronautics and
        Space Administration, [Online]. Available:
        https://www.nasa.gov/sites/default/files/atoms/files/sl_video_instruction_book.pdf.

[3]   T. Milligan , "Parts of a Rocket," Apogee Components, 20 September 2016. [Online]. Available:
        https://www.apogeerockets.com/education/downloads/Newsletter426.pdf. [Accessed 2019].

[4]   T. Benson , "Model Rocket Satey," 2014. [Online]. Available: https://www.grc.nasa.gov/WWW/K-
        12/rocket/rktsafe.html .

[5]   ""1.1" (29) Phenolic Tube 36"","" 2019. [Online]. Available:
        https://www.rocketarium.com/Build/Airframes/Phenolic/11?cPath=19_185&

[6]   N. Belham, R. Caron, S. Dempsey and R. Niles, "WPI AIAA Research Rocket for the Investigation and
        Observation of Recovery and Staging (WARRIORS II)," WPI Major Qualifying Project (MQP) Report
        JB3-RCK2, Advisor: J. Blandino, 2007.

[7]   "Battle of the Rockets," [Online]. Available: http://www.rocketbattle.org.

[8]   C. Cooper, D. Dings, P. Dohn, J. Fennick, K. Foster, E. George, N. LaPierre and T. Moquin, "Design and
        Integration of a High-Powered Model Rocket-I," WPI Major Qualifying Project (MQP) Report NAG-
        1901, Advisor: N. Gatsonis, 2019.

[9]   R. DeHate, C. Valledor and A. Wimmer, "MIT Rocket Team Critical Design Review," 25 Jan 2012.
        [Online]. Available: http://web.mit.edu/rocketteam/www/usli/2011-
        12/MIT%20RT%20CDR%202012.pdf.

[10]   M. Momenee, "Constructions Ideas for Electronic's Bays," Apogee Components, 7 June 2011. [Online].
        Available: https://www.apogeerockets.com/education/downloads/Newsletter288.pdf. [Accessed 2019].

[11]   J. Barrowman, "Calculating the center of pressure of a model rocket," [Online]. Available:

         http://www.rockets4schools.org/images/Calculating.pdf.

[12]   A. Milligan, "Drag of Nose Cones," Apogee Components, 27 August 2013. [Online]. Available:

         https://www.apogeerockets.com/education/downloads/Newsletter346.pdf. [Accessed 2019].

[13]   T. Milligan, "The Different Rocket Recovery Techniques," Apogee Components, 11 July 2017. [Online].

         Available: https://www.apogeerockets.com/education/downloads/Newsletter447.pdf. [Accessed 2019].

[14]   C. Dunn, "NASA Conducts First Ares I Rocket Cluster Parachute Test," National Aeronautics and Space

         Administration , 2019. [Online]. Available:

         https://www.nasa.gov/mission_pages/constellation/ares/cluster_chute2.html.

[15]   N.A., "Drogue Parachutes," Apogee rockets, 2019. [Online]. Available:

         https://www.apogeerockets.com/Building-Supplies/Parachutes/Drogue-Parachutes.

[16]   B. Boen , "NASA to Test World's Largest Rocket Parachutes for Ares I," National Aeronautics and Space

         Administration, 09. [Online]. Available:

         https://www.nasa.gov/mission_pages/constellation/ares/cluster_chute.html.

[17]   J. Manfredo, "Properly Sizing Parachutes for Your Rockets," Apogee Components, 7 October 2005.

         [Online]. Available: https://apogeerockets.com/education/downloads/Newsletter149.pdf. [Accessed

         2019].

[18]   C. Murphy, J. Furter, J. Tavares, M. Handy, N. Songer, N. Lucena Farias, S. Halfrey and V. Legere,

         "Design and Integration of a High-Powered Model Rocket – III," WPI Major Qualifying Project (MQP)

         Report JB3-1901, Advisor: J. Blandino, 2019.

[19]   N.A., "Autorotation," SKYbrary Aviation Safety, 2017. [Online]. Available:

         https://www.skybrary.aero/index.php/Autorotation.

[20]   Federal Aviation Administration, "Aerodynamic of Fligth," in *Helicopter Flying Handbook*, Oklahoma,

         OK, Department of Tranportation, 2012.

[21]   N. Hall, "Inclination Effects on Lift," National Aeronautics and Space Adminstration, 2018. [Online].

         Available: https://www.grc.nasa.gov/www/k-12/airplane/incline.html.

[22]   N. Hall, "Inclination Effects on Drag," National Aeronautics and Space Administration, 2015. [Online].

         Available: https://www.grc.nasa.gov/WWW/K-12/airplane/inclind.html.

[23]   "Helicopter Rockets," Apogee Components, 2019. [Online]. Available:

         https://www.apogeerockets.com/Rocket-Kits/Helicopter-Rockets. [Accessed September 2019].

[24]   "Helicopter Rockets," Estes, 2019. [Online]. Available:

         https://estesrockets.com/?s=heli&search_id=default&post_type=product. [Accessed October 2019].

[25]   "Flip Flyer," Estes, 2019. [Online]. Available: https://estesrockets.com/product/002416-flip-flyer/.

         [Accessed October 2019].

[26]   J. Dennehy, K. Maurer, J. Le, A. Valenti and S. Zaccarine, "Project Hummingbird: Recovery of a Rocket

         Using Autorotation," ERAU Directed Research project report, Faculty Mentor: E. Perrell, submitted 2018

[27]   Northwestern University, "Propulsion," Northwestern University, 2016. [Online]. Available:

         http://www.qrg.northwestern.edu/projects/vss/docs/propulsion/3-how-is-rocket-propulsion-different-from

         jet.html. [Accessed 3 December 2019].

[28]   G. Sutton and O. Biblarz, Rocket Propulsion Elements, Hoboken: John Wiley & Sons, Inc, 2017.

[29]   "Rocket Motor Basics," Apogee Components, 2019. [Online]. Available:

         https://www.apogeerockets.com/Rocket-Motor-Basics-Quick-Start-Guide. [Accessed 3 September 2019].

[30]   T. Benson, "Model Solid Rocket Engine," National Aeronautics and Space Administration, 2014.

         [Online]. Available: https://www.grc.nasa.gov/WWW/K-12/rocket/rktengine.html. [Accessed 2

         September 2019].

[31]   D. Leihmier, "Lehmier Launch System," University of Akron, Honors Research Projects, 2017. [Online].

         Available: https://ideaexchange.uakron.edu/cgi/viewcontent.cgi. [Accessed 5 September 2019].

[32]   R. Braeunig, "Rocket Propellants," Rocket and Space Technology, 2008. [Online]. Available:

         http://www.braeunig.us/space/propel.htm. [Accessed 3 September 2019].

[33]   "Standard Motor Codes," National Association of Rocketry, 2019. [Online]. Available:

         https://www.nar.org/standards-and-testing-committee/standard-motor-codes/. [Accessed 2 September

         2019].

[34]   "NAR Motor Testing," National Association of Rocketry, 2019. [Online]. Available:

https://www.nar.org/nar-motor-testing/. [Accessed 3 September 2019].

[35]   G. Stine and B. Stine, Handbook of Model Rocketry, Wiley, 2004.

[36]   T. V. Milligan, "Why Do Spinning Rockets Fly Straighter?," *Apogee Components Peak of Flight

Newsletter,* Vols. February 10, 2009, no. 228, pp. 1-3, 2009.

[37]   G. Jacobs, "Amatuer Rocket Motor Ignition and Igniters," Jacobs' Rocketry, 2018. [Online]. Available:

http://www.jacobsrocketry.com/aer/ignition_and_igniters.htm. [Accessed 23 September 2019].

[38]   T. Milligan Van, Rocketry Reservoir: Stockpile of Resources for ROcketry Educators, Apogee

Components.

[39]   "Threaded CO2 cartridges versus non-threaded CO2 cartridges," Genuine Innovations, 2017. [Online].

Available: https://www.genuineinnovations.com/blogs/learn-about-our-tech/threaded-co2-cartridges-

versus-non-threaded-co2-cartridges-for-bikes. [Accessed 23 September 2019].

[40]   T. Milligan, "How 2-Stage Rockets Work," Apogee Components, 2019. [Online]. Available:

https://www.apogeerockets.com/Tech/How_2-Stage_Rockets_Work. [Accessed 8 September 2019].

[41]   T. Milligan, "How to Multi-Stage Rockets Part 2," Apogee Components, 2003. [Online]. Available:

https://www.apogeerockets.com/education/downloads/Newsletter99.pdf. [Accessed 8 September 2019].

[42]   T. Milligan, "Electronic Staging of Composite Propellant Rocket Motors," Apogee Components, 2002.

[Online]. Available: https://www.apogeerockets.com/education/downloads/Newsletter91.pdf. [Accessed 8

September 2019].

[43]   S. Youngblood, M. Hargether, M. Grubelich and V. Saul, "JANNAF 46th Combustion Propulsion

Systems Hazards Joint Subcommittee Meeting," December 2014. [Online]. Available:

https://www.researchgate.net/publication/307888140_Computational_Modeling_of_a_Liquid_Nitrous_O

xide_and_Ethanol_Fueled_Rocket_Engine. [Accessed 3 December 2019].

[44]   Cantera Developers, "Cantera Matlab Tutorial," Cantera, 2019. [Online]. Available: https://cantera.org/.

[Accessed 22 October 2019].

[45]   "An E-Match That Doesn't Require an Explosive Permit," Apogee Components, 2019. [Online].

         Available: https://www.apogeerockets.com/Rocket-Motors/Motor-Starters/Firewire-Initiator-6-pk.

         [Accessed 12 September 2019].

[46]   "Ejection Canister Caps," Apogee Components, 2019. [Online]. Available:

         https://www.apogeerockets.com/Ejection_Systems/Ejection_Canisters/Ejection_Canister_Caps_2_pk.

         [Accessed 12 September 2019].

[47]   V. Knowles, "Ejection Charge Sizing," Vern's Rocketry, 2007. [Online]. Available:

         http://www.vernk.com/EjectionChargeSizing.htm. [Accessed February 2020].

[48]   "Ejection Charge Calculator," Rimworld, 2019. [Online]. Available:

         http://www.rimworld.com/nassarocketry/tools/chargecalc/index.html. [Accessed 30 September 2019].

[49]   "Tinder Rocketry's-Peregrine exhaustless CO2 ejection system," Apogee Components, 2016. [Online].

         Available: https://www.apogeerockets.com/downloads/PDFs/Tinder_Peregrine.pdf. [Accessed 29

         September 2019].

[50]   "Rocket Stability," NASA, [Online]. Available: https://www.grc.nasa.gov/WWW/k-

         12/rocket/rktstab.html. [Accessed 1 October 2019].

[51]   "What is an Over-Stable Rocket," Apogee Rockets, [Online]. Available:

         https://www.apogeerockets.com/education/downloads/Newsletter05.pdf. . [Accessed 30 September 2019]

[52]   T. Sarradet, "The Model Rocket," [Online]. [Accessed 20 September 2019].

[53]   D. Wyatt, "An Actively Stabilized Model Rocket," University of Cambridge Directed Research project

         report for Fourth-year Undergraduate Project in Group C, submitted 2006/2007.

[54]   C. Gasmire, "Model Rocket Spin Stabilization Explained," The Model Rocket, 2019. [Online]. Available:

         https://themodelrocket.com/model-rocket-spin-stabilization-explained/. [Accessed 12 December 2019].

[55]   B. Evans, "First Minotaur V Rocket Boosts NASA's LADEE Spacecraft on Mission to the Moon,"

         AmericaSpace, 7 September 2013. [Online]. Available: https://www.americaspace.com/2013/09/07/first-

         minotaur-v-rocket-boosts-nasas-ladee-spacecraft-on-mission-to-the-moon/. [Accessed 6 October 2019].

[56]   J. Henry J. Cornille, "A Method of Accurately Reducing the Spin Rate of a Rotating Spacecraft," NASA, Washington, 1962.

[57]   T. Benson, "Rocket Roll Motion," NASA, 12 June 2014. [Online]. Available: https://www.grc.nasa.gov/www/k-12/rocket/roll.html. [Accessed 7 October 2019].

[58]   M. Belliss, T. Braun, P. Brayshaw, G. Matook, K. Moore, A. Otterman, A. Sanchez-Torres and D. Stechmann, "WPI AIAA Research Rocket for the Investigation and Observation of Recovery and Staging (WARRIORS I)," WPI Major Qualifying Project (MQP) Report JB3-RCK1, Advisor: J. Blandino, 2006.

[59]   J. Buhler, T. Coverstone, M. Cummings, S. Fleming, T. Huleatt, T. McDonald, P. Renaud and M. Yocom, "WPI AIAA Research Rocket for the Investigation and Observation of Recovery and Staging (WARRIORS III)," WPI Major Qualifying Project (MQP) Report JB3-RCK3, Advisor: J. Blandino, 2008.

[60]   A. Alvarez, G. Gerhardt, E. Kelly, J. O'Neill and J. Whitehouse, Design and Integration of a High-Powered Model Rocket-II, WPI Major Qualifying Project (MQP) Report MAD-1901, Advisor: M. Demetriou, 2019.

[61]   ANSYS, Inc., "Fluent User's Guide," ANSYS, Inc., 2019. [Online]. Available: https://ansyshelp.ansys.com/account/secured?returnurl=/Views/Secured/corp/v194/flu_ug/flu_ug.html. [Accessed 12 December 2019].

[62]   ANSYS, Inc., "Fluent Theory Guide," ANSYS, Inc., 2019. [Online]. Available: https://ansyshelp.ansys.com/account/secured?returnurl=/Views/Secured/corp/v194/flu_th/flu_th.html. [Accessed 12 December 2019].

[63]   S. Box, C. Bishop and H. Hunt, "Stochastic Six-Degree-of-Freedom Flight Simulator for Passively Controlled High-Power Rockets.," *Journal of Aerospace Engineering,* vol. 24, pp. 31-45, 2011.

[64]   "High Powered Rocketry Safety Code," National Association of Rocketry, 2012. [Online]. Available: https://www.nar.org/safety-information/high-power-rocket-safety-code/. [Accessed 1 October 2019].

[65]   "Align RC Heli-Blades," AMain Hobbies, 2019. [Online]. Available: https://www.amainhobbies.com/align-rc-heli-blades/c816?fb=147&lg=fb. [Accessed 5 December 2019].

[66] "SAB Blades," BK Hobbies, 2019. [Online]. Available: https://www.bkhobbies.com/SAB-Blades-s/1861.htm. [Accessed November 2019].

[67] "Switch Blades," BK Hobbies, 2019. [Online]. Available: https://www.bkhobbies.com/Switch-Rotorblades-s/1832.htm. [Accessed November 2019].

[68] "About Us," Switch Blades, 2019. [Online]. Available: http://www.switchrotorblades.com/about-page/. [Accessed November 2019].

[69] D. Lednicer, "The Incomplete Guide to Airfoil Usage," University of Illinois at Ubrana-Champaign, 15 Sept 2010. [Online]. Available: https://m-selig.ae.illinois.edu/ads/aircraft.html.

[70] W. J. Bousman, Airfoil Dynamic Stall and Rotorcraft Maneuverability, 2000.

[71] "Airfoil Tools," [Online]. Available: https://airfoiltools.com/. [Accessed February 2020].

[72] Espe, "Vulcanized Fibre Specifications," Espe Manufcaturing Co, 2019. [Online]. Available: https://www.espemfg.com/pdfs/vulcfibreprop.pdf.

[73] Matweb, "Plywood," n.d.. [Online]. Available: http://www.matweb.com/search/datasheet_print.aspx?matguid=bd6620450973496ea2578c283e9fb807.

[74] Ultimaker, "PLA and ABS Strength Data," [Online]. Available: https://ultimaker.com/download/67934/TDS%20PLA%20v3.011.pdf.

[75] R. Culp, "Parachute Descent Calculations," 2008. [Online]. Available: http://www.rocketmime.com/rockets/descent.html.

[76] T. Benson, "Velocity During Recovery," National Aeronautics and Space Administration, [Online]. Available: https://www.grc.nasa.gov/WWW/k-12/VirtualAero/BottleRocket/airplane/rktvrecv.html .

[77] T. W. Wacke, "Parachute Recovery Systems Design Manual," *U.S. Naval Weapons Center, U.S. Navy,* p. 82, 1991.

[78] E. Toolbox, "U.S. Standard Atmosphere," 2003. [Online]. Available: https://www.engineeringtoolbox.com/standard-atmosphere-d_604.html. [Accessed 25 November 2019].

[79]   "Confluence Cornell," [Online]. Available:

https://confluence.cornell.edu/display/SIMULATION/Wind+Turbine+Blade+FSI+%28Part+1%29+-

+Geometry. [Accessed March 2020].

[80]   COMSOL, "Understand, predict, and optimize physics-based designs and processes with COMSOL

Multiphysics® Software," 2019. [Online]. Available: https://www.comsol.com/comsol-multiphysics.

[Accessed 9 September 2019].

[81]   Cantera Developers, "About Cantera," Cantera, 2019. [Online]. Available:

https://cantera.github.io/docs/sphinx/html/about.html. [Accessed 3 December 2019].

[82]   R. Nakka, "NAKKA Rocketry," 2018. [Online]. Available: http://www.nakka-rocketry.net/paradigm.htm

[Accessed 25 November 2019].

[83]   Anonymous, "Material Safety Data Sheet," 17 March 2009. [Online]. Available:

https://www.epa.gov/sites/production/files/2015-05/documents/9530608.pdf. [Accessed February 2020].

[84]   E. Vitz, "Forensics: Gunpowder Stoichiometry," Chemistry LibreTexts, 7 February 2020. [Online].

Available:

https://chem.libretexts.org/Bookshelves/General_Chemistry/Book%3A_ChemPRIME_(Moore_et_al.)/03

Using_Chemical_Equations_in_Calculations/3.02%3A_The_Limiting_Reagent/Forensics%3A_Gunpowd

er_Stoichiometry. [Accessed February 2020].

[85]   T. Milligan, "Pressure Relief Holes," *Apogee Peak of Flight Newsletter,* no. 68, p. 1, 2009.

[86]   Acxess Spring, "Spring Calculator and Instant Quote," Axcess Spring, 2020. [Online]. Available:

https://www.acxesspring.com/spring-calculator.html. [Accessed 2 February 2020].

[87]   Anonymous, "CSRocketry," Chris' Supplies, 2019. [Online]. Available:

https://www.csrocketry.com/rocket-motors/cesaroni/motors/pro-38/5g-reloads/cesaroni-i216-14a-classic-

rocket-motor.html. Accessed 11/25/19. [Accessed 25 November 2019].

[88]   F. Altimeters, "Raven Altimeter," 2019. [Online]. Available: https://www.featherweightaltimeters.com/.

[89]   NXP, "Reference Design KL25-AGMP01 User Guide," September 2015. [Online]. Available:

https://www.nxp.com/files-static/sensors/doc/user_guide/RD-KL25-AGMP01-UG.pdf.

[90]   Freescale Semiconductor, "Reference Design KL25-AGMP01 User Guide," September 2015. [Online].

         Available: https://www.nxp.com/files-static/sensors/doc/user_guide/RD-KL25-AGMP01-UG.pdf.

         [Accessed 2019].

[91]   J. Barrowman, "The practical calculation of the aerodynamic characteristics of slender finned vehicles,"

         The Catholic University of America, Washington, 1967.

[92]   N.A., "Induced Drag," SKYbrary Aviation Safety, 29 July 2017. [Online]. Available:

         https://www.skybrary.aero/index.php/Induced_Drag.

[93]   J. Anderson, Introduction to Flight, McGraw-Hill, 2005.

[94]   F. M. White, Fluid Dynamics, New York: McGraw-Hill Education, 2001.

[95]   W. Gawronski, "Modeling Wind-Gust Disturbances for the Analysis of Antenna Pointing Accuracy,"

         IEEE Antennas and Propagation Magazine, vol. 46, no. 1, 2004.

[96]   T. Van Milligan, "What is the best fin shape for a model rocket?," *Peak of Flight,* no. 422, 2017.

[97]   Anon, Reference Design KL25-AGMP01 User Guide, 2015.

[98]   A. Harish, "What Is the Meaning of the Von Mises Stress and the Yield Criterion?," 10 March 2020.

         [Online]. Available: https://www.simscale.com/blog/2017/04/von-mises-stress/.

7 Appendices

7.1. Appendix A: Gantt Chart

On the next 2 pages is the Gantt Chart the team used to manage the timeline of the project.

7.2. Appendix B: Forces on Bulkhead MATLAB Code

```matlab
clear; clc;

%Nosecone Parachute

%Density of Air
rho = 1.225;

%Coefficient of Drag from Parachute
C_d = 0.75;

%Area of Parachute in m^2
A = 0.6567;

%Acceleration due to Gravity
g = 9.8;

%Mass of Maximum Load in kg
m = 0.69;

%Force of Gravity
F_g = m * g;

%Time Step
t_step = 0:0.01:2;

%Initial Velocity of body when Parachute opens
v_i = g * 5;

%Code for Equation of Motion
for i = 1:201

    dt       = 0.01;
    F_d(i)   = 0.5*rho*C_d*A*v_i(i).^2;
    a(i)     = (F_d(i) - F_g)./m;
    v_f(i)   = v_i(i) - a(i) * dt;
    v_i(i+1) = v_f(i);

end

%Plot of Outputs
figure
plot(t_step,F_d)
title('Force on Nosecone Bulkhead vs. Time');
xlabel('Time (s)')
ylabel('Overall Force (N)')
```
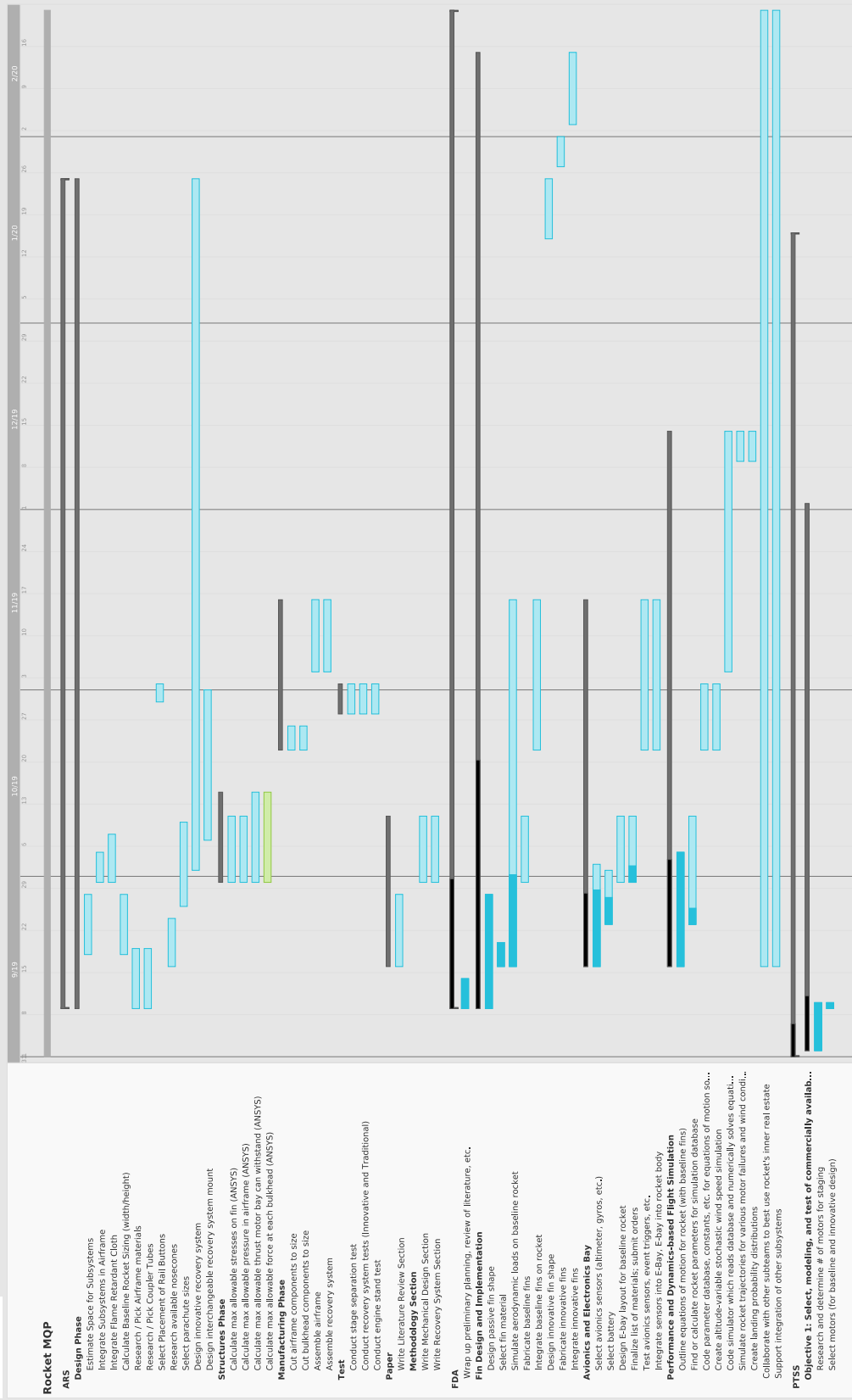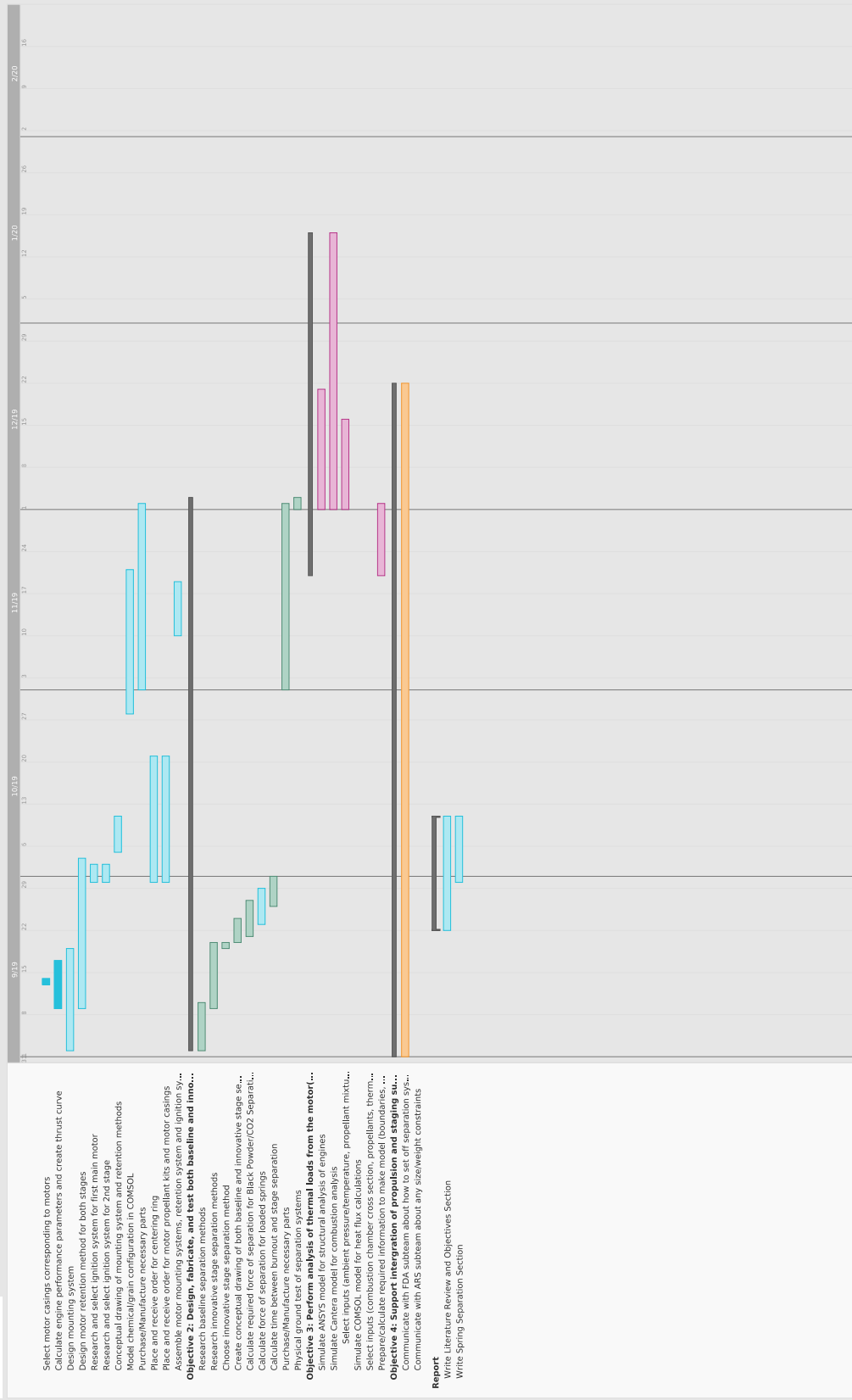
teamgantt
Created with Free Edition

Rocket MQP

ARS
Design Phase
Estimate Space for Subsystems
Integrate Subsystems in Airframe
Integrate Flame Retardant Cloth
Calculate Baseline Rocket Sizing (width/height)
Research / Pick Airframe materials
Research / Pick Coupler Tubes
Select Placement of Rail Buttons
Research available nosecones
Select parachute sizes
Design innovative recovery system
Design interchangeable recovery system mount
Structures Phase
Calculate max allowable stresses on fin (ANSYS)
Calculate max allowable pressure in airframe (ANSYS)
Calculate max allowable thrust motor bay can withstand (ANSYS)
Calculate max allowable force at each bulkhead (ANSYS)
Manufacturing Phase
Cut airframe components to size
Cut bulkhead components to size
Assemble airframe
Assemble recovery system
Test
Conduct stage separation test
Conduct recovery system tests (Innovative and Traditional)
Conduct engine stand test
Paper
Write Literature Review Section
Methodology Section
Write Mechanical Design Section
Write Recovery System Section

FDA
Wrap up preliminary planning, review of literature, etc.
Fin Design and Implementation
Design passive fin shape
Select fin material
Simulate aerodynamic loads on baseline rocket
Fabricate baseline fins
Integrate baseline fins on rocket
Design innovative fin shape
Fabricate innovative fins
Integrate innovative fins
Avionics and Electronics Bay
Select avionics sensors (altimeter, gyros, etc.)
Select battery
Design E-bay layout for baseline rocket
Finalize list of materials; submit orders
Test avionics sensors, event triggers, etc.
Integrate sensors into E-Bay, E-bay into rocket body
Performance and Dynamics-based Flight Simulation
Outline equations of motion for rocket (with baseline fins)
Find or calculate rocket parameters for simulation database
Code parameter database, constants, etc. for equations of motion so...
Create altitude-variable stochastic wind speed simulation
Code simulator which reads database and numerically solves equati...
Simulate rocket trajectories for various motor failures and wind condi...
Create landing probability distributions
Collaborate with other subteams to best use rocket's inner real estate
Support integration of other subsystems

PTSS
Objective 1: Select, modeling, and test of commercially availab...
Research and determine # of motors for staging
Select motors (for baseline and innovative design)

7.3. Appendix C: Parachute Sizing MATLAB Code

```matlab
rho = 1.225; %kg/m^3?

g = 9.81; %m/s^2?

C_d = 0.75;?

v = 5; %safe decent velocity m/s?

Vdrogue = 15 % decent velocity of drogue parachute?

 ?

%%drogue parachute diameter?

mdrogue = 4.7062; % mass of entire rocket in kg?

DrogueDiameter = sqrt((8*mdrogue*g)/(pi*C_d*rho*Vdrogue^2))?

 ?

%%nose cone parachute diameter?

mnose cone = 0.79; % mass of nose cone section in kg?

NoseconeDiameter = sqrt((8*mnose cone*g)/(pi*C_d*rho*v^2))?

 ?

%%main parachute ?

mmain = 3.91223 % mass of the upper and lower airframe in kg ?

Maindiameter = sqrt((8*mmain*g)/(pi*C_d*rho*v^2))
```

7.4. Appendix D: MATLAB Code for Autorotation Model

Autorotation Model without Drogue Parachute

```matlab
n=3; %number of blades
b=0.603; %in meters
c=0.055; %chord length in meters
h=2400*0.3048; %height at apogee in meters????
g=-9.81; %in m/s^2
rho=1.225; %density of air in kg/m^3
mu=1.789*10^-5; %N-s/m^2
angle_pitch=deg2rad(5); %rads
I=distdim(distdim(convmass(322.45,'lbm','kg')/144,'ft','m'),'ft','m'); %moment of
inertia of the system; converts lbs in^2 to kg m^2
m=convmass(7.5,'lbm','kg');

Cl_data_high=readmatrix("NACA_0012_Cl_high");
Cd_data_high=readmatrix("NACA_0012_Cd_high");
Cl_data_med
=readmatrix("NACA_0012_Cl_med");
Cd_data_med=readmatrix("NACA_0012_Cd_med");
Cl_data_low=readmatrix("NACA_0012_Cl_low");
Cd_data_low=readmatrix("NACA_0012_Cd_low");
Cl_stall=readmatrix("NACA_0012_Cl_stall");
Cd_stall=readmatrix("NACA_0012_Cd_stall");

%Deployment times
time_freefall=3; %seconds
dt=0.1; %seconds

% Descent of rocket after apogee (no autorotation)
% Initial Conditions
Vo=0;
Ho=h;

V_freefall=Vo+g*time_freefall;
H_freefall=Ho+Vo*time_freefall+0.5*g*time_freefall^2;

% Decent with autorotation
% Initial Conditions
Vo=V_freefall;
Ho=H_freefall;
Height=H_freefall;
V_y=Vo;
Wo=0;
W_vel=0;
i=1; %used as a counter for the while statement

%stores data
F_auto=zeros();
V_auto=zeros();
Height_auto=zeros();
AOA=zeros();
accel_auto=zeros();
Rotational_speed=zeros();
Torque=zeros();
Re=zeros();

while Height>0
dx=0.01;
d=1;
```

269

```matlab
dThor=zeros(numel(0.1:dx:b),1);
dFx=zeros();
for x=0:dx:b

    if W_vel == 0
    angle_induced_wind=90/180*pi;
    else
    angle_induced_wind=abs(atan(V_y/(W_vel*x))); %the absolute value was added because
a negative normal angle is positive for AOA
    end
    V_rel=sqrt((W_vel*x)^2+(V_y)^2);
    AOA(d,i)=angle_induced_wind-angle_pitch; %in radians
    Re(d,i)=rho*abs(V_rel)*c/mu;% unit less

    %This creates the functions for lift and drag coeff. based on imported
    %data
    if Re(d,i)>=100000
    Re_look_up=round(Re(d,i),-5); %rounds the Reynolds number to a value used to
calculate Cl & Cd within files
    Column=find(Cl_data_high(1,:)==Re_look_up); %Finds the column that contains the Cd
& Cl values
    Cd_values=Cd_data_high(2:32,Column);
    Cl_values=Cl_data_high(2:32,Column);
    AOAs=(-5:25)';
    aoa_crit_test=5:0.01:20;
    elseif Re(d,i)>=15000 && Re(d,i)< 100000 %if the Reynolds number is between 10000
and 1000000 then these values are used
    Re_look_up=round(Re(d,i),-4); %rounds the Reynolds number to a value used to
calculate Cl & Cd within files
    Column=find(Cl_data_med(1,:)==Re_look_up); %Finds the column that contains the Cd
& Cl values
    Cd_values=Cd_data_med(2:32,Column);
    Cl_values=Cl_data_med(2:32,Column);
    AOAs=(-5:25)';
    aoa_crit_test=5:0.01:15; %test values to find the critical AOA
    elseif Re(d,i)<15000  %if the Reynolds number is below 10000 then these values are
used
    Cd_values=Cd_data_low(1:56,1);
    Cl_values=Cl_data_low(1:56,1);
    AOAs=(-5:50)';
    aoa_crit_test=40:0.01:50; %test values to find the critical AOA
    end

    Cl_function=fit(AOAs, Cl_values, 'smoothingspline'); %Creates a function of Cl for
an input AOA
    Cd_function=fit(AOAs, Cd_values, 'smoothingspline');%Creates a function of Cd for
an input AOA

    %tests the AOA for stall
    Dif=1;
    f=1;
    while Dif>0
        Dif=round(differentiate(Cl_function,aoa_crit_test(f)),3);
        if Dif==0
            critical_AOA=aoa_crit_test(f);
        end
        f=f+1;
    end

    if AOA(d,i)>(critical_AOA*pi/180) %keep it in radians
        Cl_function=fit((19:60)', Cl_stall(1:42,1), 'poly2'); %Creates a function of
Cl for an imput AOA
```

```matlab
        Cd_function=fit((19:60)', Cd_stall(1:42,1), 'poly1');%Creates a function of Cd
for an input AOA
    end

    AOA_deg=rad2deg(AOA(d,i)); %the Cl and Cd functions are determined by AOAs in
degrees
    Cl=Cl_function(AOA_deg); %Cl value used for analysis
    Cd=Cd_function(AOA_deg); %Cd value used for analysis

    dA=dx*c;% differential area of the blade
    dL=0.5*rho*dA*Cl*V_rel^2;
    dD=0.5*rho*dA*Cd*V_rel^2;

    %Horizonal forces
    dThor(d)=x*(-dD*cos(AOA(d,i))+dL*sin(AOA(d,i)));

    %Vertical forces
    dFx(d)=(dL*cos(AOA(d,i))+dD*sin(AOA(d,i)));
    d=d+1;
end
T=3*sum(dThor);
Fy_blade=sum(dFx);
accel_y=n*Fy_blade/m+g; %g is negative so it's added to the force equation


V_y=Vo+accel_y*dt;
Height=Ho+V_y*dt+0.5*accel_y*dt^2;

Vo=V_y;
Ho=Height;

ang_accel=T/I; % calculates the angular acceleration using torque and moment of
inertia
W_vel=Wo+ang_accel*dt;

Wo=W_vel; %set the calculated angular velocity of blades as the initial angular
velocity for the next iteration

F_auto(i)=Fy_blade;
V_auto(i)=V_y; %collects decent velocity data
Height_auto(i)=Height;
accel_auto(i)=accel_y;
Rotational_speed(i)=W_vel;
Torque(i)=T;
i=i+1;
end

%% Autorotation descent
figure(1)
yyaxis left
plot((0:1:i-2)*dt,accel_auto(1,:), 'LineWidth', 1);
xlabel('Time (s)'); ylabel('Acceleration(m/s^2)'); title('Acceleration and Velocity
during descent');

%figure(3)
yyaxis right
plot((0:1:i-2)*dt,V_auto, 'LineWidth',1);
ylabel('Velocity (m/s)')

figure (2)
%yyaxis left
plot((0:1:i-2)*dt,Height_auto,'LineWidth',1);
```

```matlab
ylabel('Height (m)'); xlabel('Time (s)'); title('Height of Rocket During Descent');
```

```matlab
%% Whole descent
%free fall
T_ff=0:dt:time_freefall;
accel_ff=g*ones(1,numel(T_ff));
V_o=0;
V_ff=V_o+g.*T_ff;
H_ff=h+V_o.*T_ff+1/2.*accel_ff.*T_ff.^2;

%Entire descent motion
T_descent=(0:(time_freefall/dt+i-1))*dt;
accel_descent=[accel_ff accel_auto];
V_decent=[V_ff,V_auto];
Height_descent=[H_ff,Height_auto];

figure(1)
yyaxis left
plot(T_descent,accel_descent, 'LineWidth', 1);
xlabel('Time (s)'); ylabel('Acceleration(m/s^2)'); title('Acceleration and Velocity
During Descent No Drogue Parachute');

yyaxis right
plot(T_descent,V_decent, 'LineWidth',1);
ylabel('Velocity (m/s)');
xline(time_freefall,'--r','Autorotation
Deployment','LabelVerticalAlignment','top','LabelOrientation','horizontal');

figure (2)
plot(T_descent,Height_descent,'LineWidth',1);
ylabel('Height (m)'); xlabel('Time (s)'); title('Height of Rocket During Descent No
Drogue Parachute');
xline(time_freefall,'--r','Autorotation
Deployment','LabelVerticalAlignment','top','LabelOrientation','horizontal');
```

Autorotation Model with Drogue Parachute

```matlab
n=3; %number of blades
b=0.603; %in meters
c=0.055; %chord length in meters
h=2400*0.3048; %height at apogee in meters????
g=-9.81; %in m/s^2
rho=1.225; %density of air in kg/m^3
mu=1.789*10^-5; %N-s/m^2
angle_pitch=deg2rad(5); %rad1`
I=distdim(distdim(convmass(322.45,'lbm','kg')/144,'ft','m'),'ft','m'); %moment of
inertia of the system
m=convmass(7.5,'lbm','kg');

Cl_data_high=readmatrix("NACA_0012_Cl_high");
Cd_data_high=readmatrix("NACA_0012_Cd_high");
Cl_data_med=readmatrix("NACA_0012_Cl_med");
Cd_data_med=readmatrix("NACA_0012_Cd_med");
Cl_data_low=readmatrix("NACA_0012_Cl_low");
Cd_data_low=readmatrix("NACA_0012_Cd_low");
Cl_stall=readmatrix("NACA_0012_Cl_stall");
Cd_stall=readmatrix("NACA_0012_Cd_stall");

%Deployment times
```

```matlab
time_freefall=3; %seconds
time_drogue=10;
dt=0.1; %seconds

% Descent of rocket after apogee (no autorotation)
% Initial Conditions
Vo=0;
Ho=h;


V_ff=Vo+g*time_freefall;
H_ff=Ho+Vo*time_freefall+0.5*g*time_freefall^2;

% Descent with drogue chute
% Initial Conditions
C_d = 0.75; % drag coefficient of parachute
Diameter=distdim(2,'ft','m');
A = pi*Diameter^2/4;%Area of Parachute in m^2
Vo=V_ff;
Ho=H_ff;

%data storage
accel_d=zeros();
V_d=zeros();
H_d=zeros();
d=1;
for i = 0:dt:time_drogue
    F_drogue= 0.5*rho*C_d*A*Vo^2;
    accel_d(d)=F_drogue/m+g; %g is negative so its added to the force equation
    V_d(d)=Vo+accel_d(d)*dt;
    H_d(d)=Ho+Vo*dt+0.5*accel_d(d)*dt^2;

    Vo=V_d(d);
    Ho=H_d(d);
    d=d+1;
end

% Descent with autorotation and drogue chute
% Initial Conditions; need to subtract 1 since 1 is added at the end of
% the for loop
Vo=V_d(d-1);
Ho=H_d(d-1);
Height=H_d(d-1);
V_y=Vo;
Wo=0;
W_vel=0;
i=1; %used as a counter for the while statement

%stores data
F_auto=zeros();
V_auto=zeros();
Height_auto=zeros();
AOA=zeros();
accel_auto=zeros();
Rotational_speed=zeros();
Torque=zeros();
Re=zeros();

while Height>0
dx=0.01;
d=1;
dThor=zeros(numel(0.1:dx:b),1);
dFx=zeros();
for x=0:dx:b
```

```matlab
    if W_vel == 0
    angle_induced_wind=90/180*pi;
    else
    angle_induced_wind=abs(atan(V_y/(W_vel*x))); %the absolute value was added because
a negative normal angle is positive for AOA
    end
    V_rel=sqrt((W_vel*x)^2+(V_y)^2);
    AOA(d,i)=angle_induced_wind-angle_pitch; %in radians
    Re(d,i)=rho*abs(V_rel)*c/mu;% unit less

    %This creates the functions for lift and drag coeff. based on imported
    %data
    if Re(d,i)>=100000
    Re_look_up=round(Re(d,i),-5); %rounds the Reynolds number to a value used to
calculate Cl & Cd within files
    Column=find(Cl_data_high(1,:)==Re_look_up); %Finds the column that contains the Cd
& Cl values
    Cd_values=Cd_data_high(2:32,Column);
    Cl_values=Cl_data_high(2:32,Column);
    AOAs=(-5:25)';
    aoa_crit_test=5:0.01:20;
    elseif Re(d,i)>=15000 && Re(d,i)< 100000 %if the Reynolds number is between 10000
and 1000000 then these values are used
    Re_look_up=round(Re(d,i),-4); %rounds the Reynolds number to a value used to
calculate Cl & Cd within files
    Column=find(Cl_data_med(1,:)==Re_look_up); %Finds the column that contains the Cd
& Cl values
    Cd_values=Cd_data_med(2:32,Column);
    Cl_values=Cl_data_med(2:32,Column);
    AOAs=(-5:25)';
    aoa_crit_test=5:0.01:15; %test values to find the critical AOA
    elseif Re(d,i)<15000  %if the Reynolds number is below 10000 then these values are
used
    Cd_values=Cd_data_low(1:56,1);
    Cl_values=Cl_data_low(1:56,1);
    AOAs=(-5:50)';
    aoa_crit_test=40:0.01:50; %test values to find the critical AOA
    end

    Cl_function=fit(AOAs, Cl_values, 'smoothingspline'); %Creates a function of Cl for
an imput AOA
    Cd_function=fit(AOAs, Cd_values, 'smoothingspline');%Creates a function of Cd for
an imput AOA

    %tests the AOA for stall
    Dif=1;
    f=1;
    while Dif>0
        Dif=round(differentiate(Cl_function,aoa_crit_test(f)),3);
        if Dif==0
            critical_AOA=aoa_crit_test(f);
        end
        f=f+1;
    end

    if AOA(d,i)>(critical_AOA*pi/180) %keep it in radians
        Cl_function=fit((19:60)', Cl_stall(1:42,1), 'poly2'); %Creates a function of
Cl for an imput AOA
        Cd_function=fit((19:60)', Cd_stall(1:42,1), 'poly1');%Creates a function of Cd
for an imput AOA
    end
```

```
    AOA_deg=rad2deg(AOA(d,i)); %the Cl and Cd functions are determined by AOAs in
degrees
    Cl=Cl_function(AOA_deg); %Cl value used for analysis
    Cd=Cd_function(AOA_deg); %Cd value used for analysis

    dA=dx*c;% differential area of the blade
    dL=0.5*rho*dA*Cl*V_rel^2;
    dD=0.5*rho*dA*Cd*V_rel^2;

    %Horizontal forces
    dThor(d)=x*(-dD*cos(AOA(d,i))+dL*sin(AOA(d,i)));

    %Vertical forces
    dFx(d)=(dL*cos(AOA(d,i))+dD*sin(AOA(d,i)));
    d=d+1;
end
T=3*sum(dThor);
Fy_blade=sum(dFx);
F_drogue= 0.5*rho*C_d*A*Vo^2;
accel_y=F_drogue/m+n*Fy_blade/m+g; %g is negative so its added to the force equation

V_y=Vo+accel_y*dt;
Height=Ho+V_y*dt+0.5*accel_y*dt^2;

Vo=V_y;
Ho=Height;

ang_accel=T/I; % calculates the angular acceleration using torque and moment of
inertia
W_vel=Wo+ang_accel*dt;

Wo=W_vel; %set the calculated angular velocity of blades as the initial angular
velocity for the next iteration

F_auto(i)=Fy_blade;
V_auto(i)=V_y; %collects decent velocity data
Height_auto(i)=Height;
accel_auto(i)=accel_y;
Rotational_speed(i)=W_vel;
Torque(i)=T;
i=i+1;
end

%% Autorotation Descent
figure(1)
yyaxis left
plot((0:1:i-2)*dt,accel_auto(1,:), 'LineWidth', 1);
xlabel('Time (s)'); ylabel('Acceleration(m/s^2)'); title('Acceleration and Velocity
during decent');

%figure(3)
yyaxis right
plot((0:1:i-2)*dt,V_auto, 'LineWidth',1);
ylabel('Velocity (m/s)')

figure (2)
%yyaxis left
plot((0:1:i-2)*dt,Height_auto,'LineWidth',1);
ylabel('Height (m)'); xlabel('Time (s)'); title('Height of Rocket During Decent');

%% Whole Descent
%free fall
T_ff=0:dt:time_freefall;
```

```matlab
accel_ff=g*ones(1,numel(T_ff));
V_o=0;
V_ff=V_o+g.*T_ff;
H_ff=h+V_o.*T_ff+1/2.*accel_ff.*T_ff.^2;

%Entire decent motion
T_descent=0:dt:(time_freefall+time_drogue+(i)*dt);
accel_descent=[accel_ff,accel_d,accel_auto];
V_descent=[V_ff, V_d,V_auto];
Height_descent=[H_ff,H_d,Height_auto];

figure(1)
yyaxis left
plot(T_descent,accel_descent, 'LineWidth', 1);
xlabel('Time (s)'); ylabel('Acceleration(m/s^2)'); title('Acceleration and Velocity
during Descent with Drogue Parachute');

yyaxis right
plot(T_descent,V_descent, 'LineWidth',1);
ylabel('Velocity (m/s)');
xline(time_freefall,'--r','Drogue
Deployment','LabelVerticalAlignment','top','LabelOrientation','horizontal');
xline(time_drogue+time_freefall,'--k','Autorotation
Deployment','LabelVerticalAlignment','bottom','LabelOrientation','horizontal');

figure (2)
plot(T_descent,Height_descent,'LineWidth',1);
ylabel('Height (m)'); xlabel('Time (s)'); title('Height of Rocket During Descent with
Drogue Parachute');
xline(time_freefall,'--r','Drogue
Deployment','LabelVerticalAlignment','top','LabelOrientation','horizontal');
xline(time_drogue+time_freefall,'--k','Autorotation
Deployment','LabelVerticalAlignment','bottom','LabelOrientation','horizontal');
```

7.5.   Appendix E: Motor Comparison

Below is a table comparing a list of motors that were considered for the baseline and innovative design propulsion system.

Class	Motor	Total Impulse (N-s)	Motor Length (m)	Diameter (m)	Propellant Mass (g)	Avg. Thrust (N)	Thrust/Mass	Impulse/Mass	Thrust/Weight (15lbs assumption)	Mfr.	Rocket Configuration
I	I216	636	0.367	0.038	601	216	0.36	1.06	3.24	Cesaroni	Baseline (Stage 1)
H	H400	255	0.186	0.038	283	398.6	1.41	0.90	5.97	Cesaroni	Innovative (Stage 1)
I	I212	364	0.245	0.038	475	212.7	0.45	0.77	6.77	Cesaroni	Innovative (Stage 2)
I	I170	382	0.245	0.038	392	170	0.43	0.97	2.55	Cesaroni	
H	H238T-14A	263.4	0.194	0.029	202	238	1.18	1.30	3.57	Aerotech	
H	H170M-14	319.9	0.193	0.038	330	170	0.52	0.97	2.55	Aerotech	
H	H999N-P	320	0.193	0.038	331	972	2.94	0.97	14.57	Aerotech	
H	H268R-14	320	0.333	0.029	346	268	0.77	0.92	4.02	Aerotech	
H	H100W	234	0.155	0.038	261	100	0.38	0.90	1.50	Aerotech	
I	I200W-14A	324.5	0.333	0.029	364	200	0.55	0.89	3.00	Aerotech	
H	H130-14	210	0.152	0.038	237	130	0.55	0.89	1.95	Aerotech	
H	H669N-P	221	0.145	0.038	252	669	2.65	0.88	10.03	Aerotech	
H	H250G-14	219.5	0.229	0.029	256	250	0.98	0.86	3.75	Aerotech	
H	H242T-14	231.7	0.145	0.038	279	242	0.87	0.83	3.63	Aerotech	
I	I170G-14A	418.5	0.151	0.054	528	170	0.32	0.79	2.55	Aerotech	
I	I599N-P	404.9	0.156	0.054	512	559	1.09	0.79	8.38	Aerotech	
I	I229T-14	410.9	0.156	0.054	520	229	0.44	0.79	3.43	Aerotech	
H	H123W-14	223.6	0.145	0.038	293	123	0.42	0.76	1.84	Aerotech	
I	I215R-14A	397	0.156	0.054	527	215	0.41	0.75	3.22	Aerotech	
I	I115W-14	409.3	0.156	0.054	580	115	0.20	0.71	1.72	Aerotech	
H	H112J-10	261.1	0.193	0.038	385	112	0.29	0.68	1.68	Aerotech	
G	G69N-P	136.3	0.097	0.038	201	72.3	0.36	0.68	1.08	Aerotech	
I	I117FJ-14A	364.9	0.156	0.054	580	117	0.20	0.63	1.75	Aerotech	
G	G339N-P	110	0.097	0.038	181	339	1.87	0.61	5.08	Aerotech	
G	G61W-14	110.5	0.097	0.038	194	61	0.31	0.57	0.91	Aerotech	
G	G67R-14	110	0.097	0.038	201	67	0.33	0.55	1.00	Aerotech	
I	I284W	607.3	0.288	0.038	568	284	0.50	1.07	4.26	Aerotech	
I	I600R	597.3	0.335	0.038	617	600	0.97	0.97	8.99	Aerotech	
I	I364FJ	570.1	0.335	0.038	678	364	0.54	0.84	5.46	Aerotech	
I	I540	634	0.367	0.038	598	540	0.90	1.06	8.09	Cesaroni	

7.6. Appendix F: Chemical Equilibrium Solver

Below is the MATLAB script written in order to execute the chemical equilibrium solver from

Cantera and the one-dimensional isentropic nozzle flow equations.

```matlab
%Upload cti file containing NH4ClO4 species
gas = Solution('input-Copy.cti', 'gas');

%Identify major combustion products
O2 = speciesIndex(gas,'O2');
H2O = speciesIndex(gas,'H2O');
N2 = speciesIndex(gas,'N2');
HCL = speciesIndex(gas,'HCL');
CL2 = speciesIndex(gas,'CL2');
AL = speciesIndex(gas,'AL');

%Set the state of the reaction: temperature (K), pressure (Pa) and composition of
%reactants
% set(gas, 'Temperature', 293.15, 'Pressure', 1.379e7,'MassFractions', 'NH4CLO4:0.8,
AL:0.2')
set(gas, 'Temperature', 298.15, 'Pressure', 101325,'MassFractions', 'NH4CLO4:0.8,
AL:0.2')
% use 'equilibrate' function from Cantera to solve for chemical equilibrium
equilibrate(gas,'UV');
% Identify the mole fractions of all combustion products
composition = moleFractions(gas);
mole_fraction = moleFractions(gas);
%Mole fractions of each major combustion product
O2_comp = composition(O2,1);
H2O_comp = composition(H2O,1);
N2_comp = composition(N2,1);
HCL_comp = composition(HCL,1);
CL2_comp = composition(CL2,1);
AL_comp = composition(AL,1);
%Concatenate mole fraction scalars to form one vector
Z_mole = [O2_comp; H2O_comp; N2_comp; HCL_comp; AL_comp];

%Identify the mass fractions of all combustion products
O2_mole_num = mole_fraction(O2,1);
H2O_mole_num = mole_fraction(H2O,1);
N2_mole_num = mole_fraction(N2,1);
HCL_mole_num = mole_fraction(HCL,1);
CL2_mole_num = mole_fraction(CL2,1);
AL_mole_num = mole_fraction(AL,1);
%Concatenate mole fraction scalars to form one vector
Z_mole = [O2_mole_num; H2O_mole_num; N2_mole_num; HCL_mole_num; AL_mole_num];

%Properties of the reaction
```

```matlab
    T_equil = temperature(gas); %chemical equilibrium temperature (K)
    P_chamb = pressure(gas); %Chamber pressure (Pa)
    rho_chamb = density(gas); %Density (kg/m^3)
    Number_of_products = nnz(composition); %Total # of products
    max_Temp = maxTemp(gas); %Max temperature of reaction (K)
    Cp = cp_mass(gas); %Mass basis specific heat at constant pressure (J/kg-K)
    Cv = cv_mass(gas); %Mass basis of specific heat at a constant volume (J/kg-K)
    Mm = meanMolecularWeight(gas); %Mean molecular weight of mixture (kg/kmol)
    k = Cp/Cv; %Specific heat ratio of mixture

    %Plot results
    bar(Z_mole)
    xlabel('Species'); ylabel('Mole Fraction');
    title('Mole Fractions for Primary Combustion Products')
    ylim([0 0.34])
    name = {'O_2';'H_2O';'N_2';'HCL';'AL'};
    set(gca,'xticklabel',name)
    text(1:length(Z_mole),Z_mole,num2str(Z_mole),'vert','bottom','horiz','center');
    R = 8314; %Gas Constant (J/kg-K)
    g = 9.81; %gravity (m/s^2)
    P_a = 101325; %Ambient pressure (Pa)
    Ae_At = 5; %Expansion ratio
    exit_radius = 0.008; %Exit radius of nozzle (m)
    A_e = pi*exit_radius^2; %Exit area of nozzle (m^2)

    %Use matlab command 'flowisentropic' which uses isentropic flow equations
    %to calculate properties of the flow. Note: T is temperature ratio T2/T1, P
    %is pressure ratio P2/P1 and rho is density ratio rho2/rho1
    [mach, T, P, rho, area] = flowisentropic(k, Ae_At, 'sup');

    M_e = mach; %Exit Mach Number
    T_e = T*T_equil; %Exit Temperature (K)
    P_e = P*P_chamb; %Exit Pressure (Pa)
    rho_e = rho*rho_chamb; %Exit density (kg/m^3)

    u_e = sqrt((2*k/(k-1))*(R/Mm)*T_equil*(1-P)^((k-1)/k)); %Exit Velocity (m/s)
    m_dot = rho_e*u_e*A_e; %Mass flow rate (kg/s)
    c_star       =       1/((k*sqrt((2/(k+1))^((k+1)/(k-1))))/(sqrt(k*R*T_equil/Mm)));
%Characterstic velocity (m/s)


    % Isp = (u_e/g) + (P*Ae_At*c_star/g) %Specific Impulse (s)
    Isp = (u_e/g) %Specific Impulse (s)
    Thrust = m_dot*u_e + (P_e - P_a)*A_e %Thrust (N)
```

7.7. Appendix G: Table of Values for Analytical Aerodynamic Modeling

Symbol	Definition/Description	Function
Constants		
L	Reference length, diameter of body tube	-
A_T	Planform area of one fin; area of fin when viewed from above (lift direction)	-
A_r	Reference area; cross sectional area of body tube	-
S	Exposed fin semi-span, measured from root chord	-
r_L	Fin leading edge radius; approximated as a cylinder with radius r_L	$r_L = 1.1019 \left(\dfrac{t_r^2}{c_r} \right)$
Γ_L	Leading edge sweep angle	-
A_{B_f}	Base area of one fin; at root	-
c_r	Fin root chord	-
h_r	Root fin trailing edge thickness, 0 for tapered trailing edge	-
t_r	Root fin thickness	-
Γ_c	Mid-chord line sweep angle	-
f_B	Body fineness ratio, length of rocket divided by width of rocket	$f_B = \dfrac{length\ of\ rocket}{width\ of\ rocket}$
f_N	Nose fineness ratio, length of nose cone divided by its base diameter	$f_N = \dfrac{length\ of\ nosecone}{width\ of\ nosecone}$
A_{W_B}	Total body wetted area	-
A_B	Base area at tail, equivalent to reference area, A_r	-
A_{B_N}	Nose base area, equivalent to reference area, A_r	-
A_{W_N}	Nose wetted area	-
A_W	Total wetted area	-
AR	Aspect ratio of exposed fin	$AR = \dfrac{S^2}{A_T}$
A_f	Total area of one fin	-
User Inputs		
u	Velocity	-
u_{sound}	Speed of sound	$u_{sound} = \sqrt{\gamma R T}$

M	Mach number	$$M = \frac{V}{u_{sound}}$$
ρ	Air density	-
μ	Air viscosity	-
N	Number of fins; 3 or 4	-
α	Angle of attack	-
Axial Calculations		
R_e	Reynolds number	$$R_e = \frac{\rho u L}{\mu}$$
C_D	Total drag coefficient	$$C_D = C_{D_{T_T}} + C_{D_{T_B}}$$
$C_{D_{T_T}}$	Tail drag component	$$C_{D_{T_T}} = C_{D_{f_T}} + C_{D_{L_T}} + C_{D_{B_T}} + C_{D_{TT}}$$
$C_{D_{f_T}}$	Tail skin friction drag coefficient	$$C_{D_{f_T}} = 2NC_{f_c}\left(\frac{A_T}{A_r}\right)$$
$C_{D_{L_T}}$	Tail leading edge drag coefficient	$$C_{D_{L_T}} = 2N\left(\frac{Sr_L}{A_r}\right)\cos^2 \Gamma_L (\Delta C_D)$$
$C_{D_{B_T}}$	Tail trailing edge drag coefficient	$$C_{D_{B_T}} = \frac{0.135N\left(\frac{A_{B_f}}{A_r}\right)}{\sqrt[3]{C_{f_B}}\sqrt{K - M^2 \cos^2 \Gamma_c}}$$
$C_{D_{TT}}$	Tail thickness drag	$$C_{D_{TT}} = 4NC_{f_c}\left(\frac{A_T}{A_T}\right)[\left(\frac{t_r}{c_r}\right)\cos^2 \Gamma_c$$ $$+ \frac{30\left(\frac{t_r}{c_r}\right)^4 \cos^2 \Gamma_c}{\left(\sqrt{K - M^2 \cos^2 \Gamma_c}\right)^3}]$$
$C_{D_{T_B}}$	Body component of drag	$$C_{D_{T_B}} = C_{D_P} + C_{D_{BB}}$$
C_{D_P}	Body pressure drag	$$C_{D_P} = \frac{6A_{W_B}C_{f_c}}{f_B^3 A_r (K - M^2)^{0.6}}$$
$C_{D_{BB}}$	Body base drag	$$C_{D_{BB}} = \frac{0.29\left(\frac{A_B}{A_r}\right)}{\sqrt{C_{f_c}\left(\frac{A_W}{A_B}\right)(K - M^2)}}$$
Normal calculations		
C_{N_a}	Normal force coefficient derivative	$$C_{N_a} = C_{N_{a_B}} + C_{N_{a_{T_B}}} + C_{N_{a_{B_T}}}$$
$C_{N_{a_B}}$	Body normal force coefficient derivative	$$C_{N_{a_B}} = 2\left(\frac{A_{B_N}}{A_r}\right)$$
$C_{N_{a_{T(B)}}}$	Tail interference factor	$$C_{N_{a_{T(B)}}} = C_{N_{a_T}}K_{TB}$$
$C_{N_{a_{B(T)}}}$	Body interference factor	$$C_{N_{a_{B(T)}}} = C_{N_{a_T}}K_{BT}$$
Other calculations		

C_f	Incompressible Skin Friction Coefficient	$$C_f = \frac{1.328}{\sqrt{R_e}}$$
C_{f_c}	Compressible Skin Friction Coefficient	$$C_{f_c} = C_f(1 - 0.12M^2)$$
ΔC_D	Drag Coefficient of Leading Edge	$$\Delta C_D = (1 - M^2)^{-0.417} - 1$$
C_{f_B}	Incompressible Skin Friction Coefficient of Body	$$C_{f_B} = 2C_f\left(\frac{c_r}{h_r}\right)$$
K_1	Trailing Edge Drag Correction Constant	$$K_1 = \left(1 + \frac{18C_{f_c}\left(\frac{t_r}{h_r}\right)^2}{N(1 - 0.52)\left(\frac{A_{B_f}}{A_r}\right)}\right)\left(\frac{0.135N\left(\frac{A_{B_f}}{A_r}\right)}{C_{f_c}^{\frac{1}{3}}}\right) + \cos^2 \Gamma_c$$
K_{cone}	Body Pressure Drag Correction Constant	$$K_{cone} = 1 + \left[\frac{6.82A_{W_B}C_{f_c}(f_N + 0.7)^{1.29}}{(f_B^3 A_r)}\right]^{\frac{5}{3}}$$
K_2	Body Base Drag Correction Constant	$$K_2 = 1 + \frac{1}{\left[6.38 + 39.7\left(\frac{h_r}{c_r}\right)\right]C_{f_c}\left(\frac{A_W}{A_B}\right)}$$
B	Compressibility factor	$$B = \sqrt{1 - M^2}$$
r_t	Body Radius at Tail	-
K_{TB}	Interference Constant 1	$$K_{TB} = \frac{2}{\pi\left(1 - \frac{1}{\tau}\right)^2}\{(1 + \frac{1}{\tau^4})[\frac{1}{2}\tan^{-1}\frac{1}{2}\left(\tau - \frac{1}{\tau}\right)] - \frac{1}{\tau^2}[\left(\tau - \frac{1}{\tau}\right) + 2\tan^{-1}\left(\frac{1}{\tau}\right)]\}$$
L_r	Reference Length, diameter of body tube	-
X_{TB}	Longitudinal tail center of pressure	-
X_{CG}	Location of Center of Gravity, measured from nose tip	-
Δx	Distance between aerodynamic center of tail and center of gravity	$$\Delta x = X_{TB} - X_{CG}$$
q	Pitch Rate	-
C_m	Pitch Moment Coefficient	$$C_M = C_{N_{a_{T_B}}}\left(\frac{\Delta_x^2}{L_r}\right)\left(\frac{q}{V}\right)$$

7.8. Appendix H: Numerical Model Dynamic Pressure Contours

The following contours represent cases run at the maximum velocity (137.15 m/s). At this velocity, they provide the best visual representation of the dynamic pressure contours for both rockets. Both sets of contours show the 2D pressure distribution in the X-Y plane. In order to capture the effect of all fins on the innovative rocket, views of a plane rotated 45° about the Y-axis are included with the innovative rocket contours. A catalog of all contours produced from the numerical model was submitted as a separate document. As a reminder to the reader, the dynamic pressure is defined as the increase in the surrounding air's pressure due to motion compared to its pressure when static. Therefore, a value of zero implies that the surrounding air is static.

7.8.1 Baseline Rocket
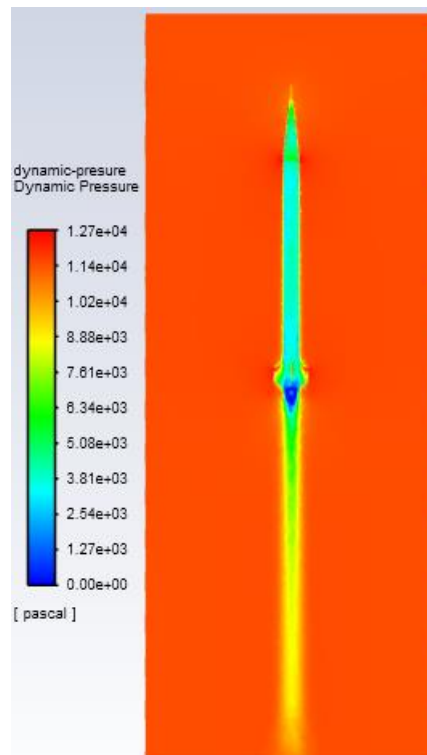
Figure 168: Dynamic pressure contour at 0 deg AoA
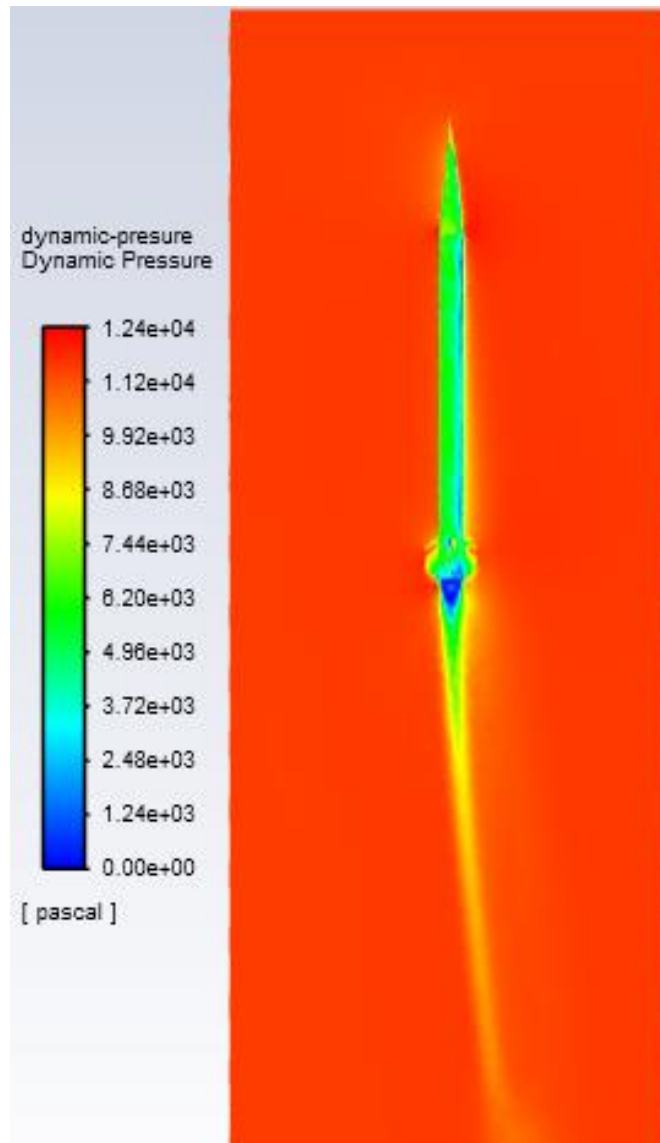
Figure 169: Dynamic pressure contour at 10 deg AoA
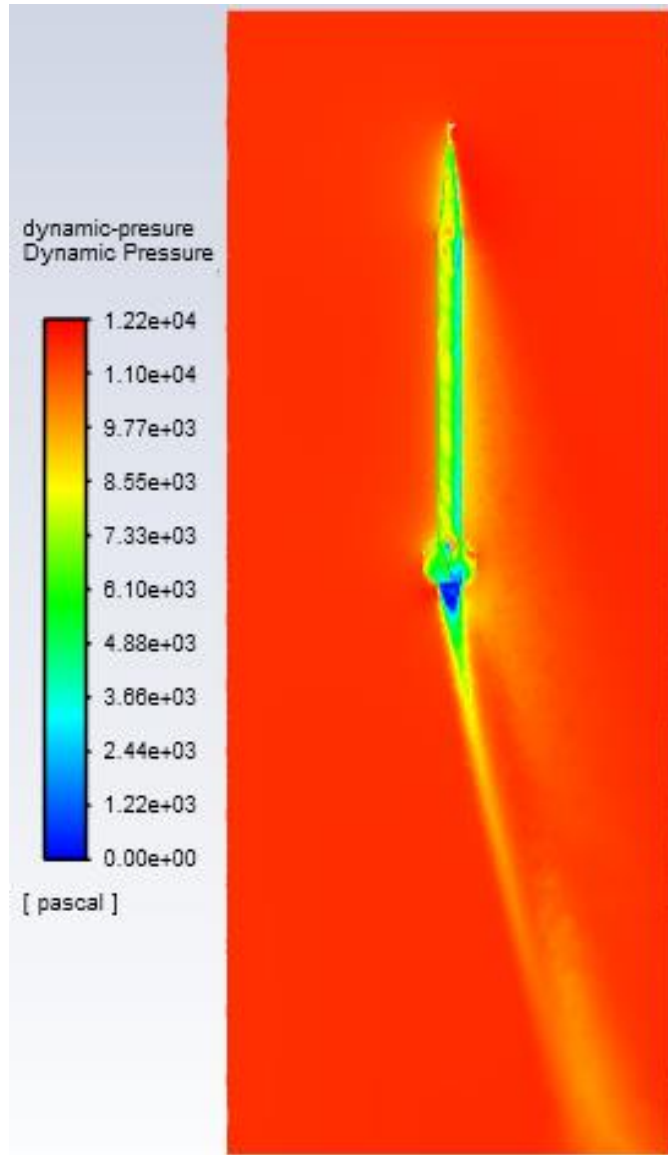
Figure 170: Dynamic pressure contour at 20 deg AoA
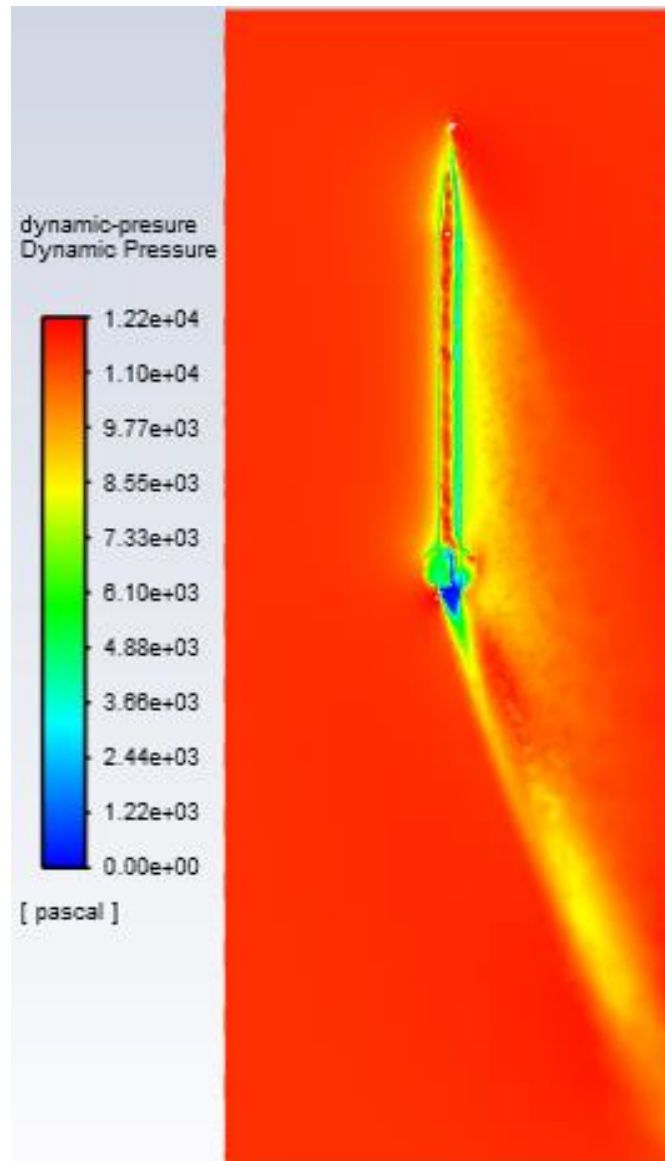
Figure 171: Dynamic pressure contour at 30 deg AoA
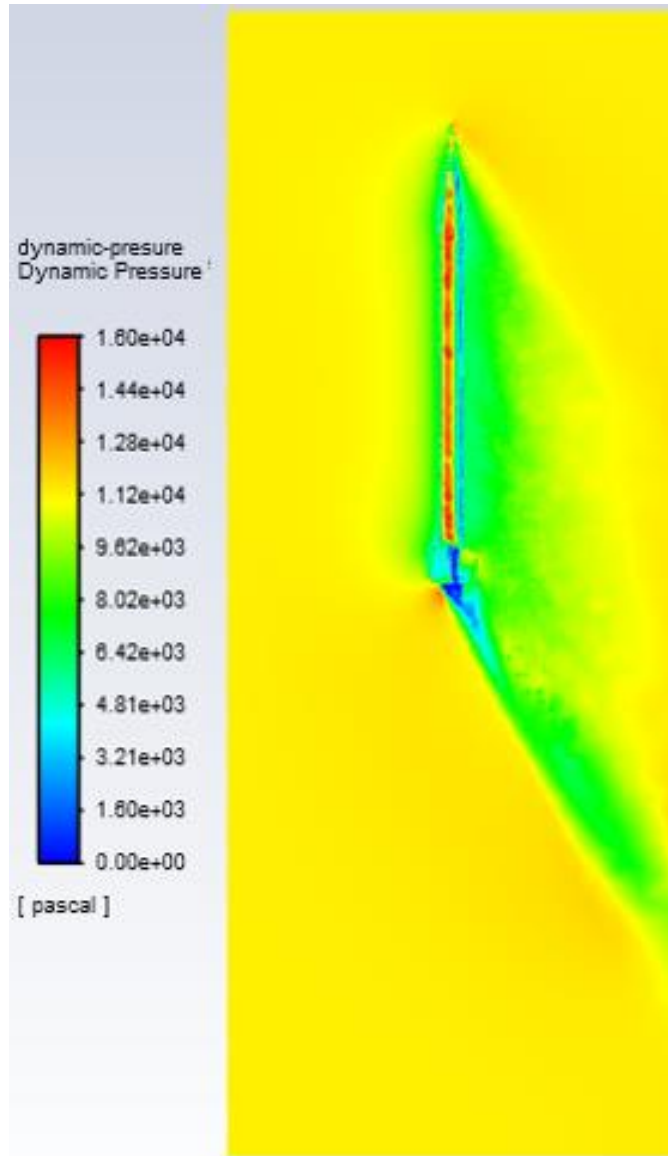
Figure 172: Dynamic pressure contour at 40 deg AoA
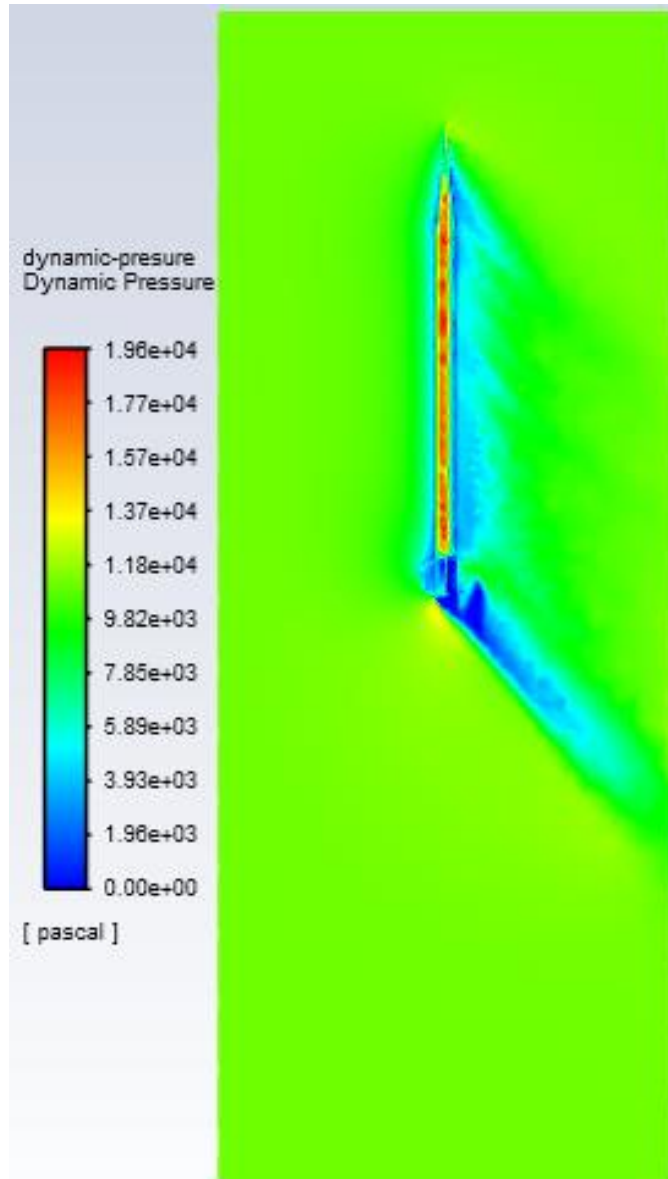
Figure 173: Dynamic pressure contour at 50 deg AoA
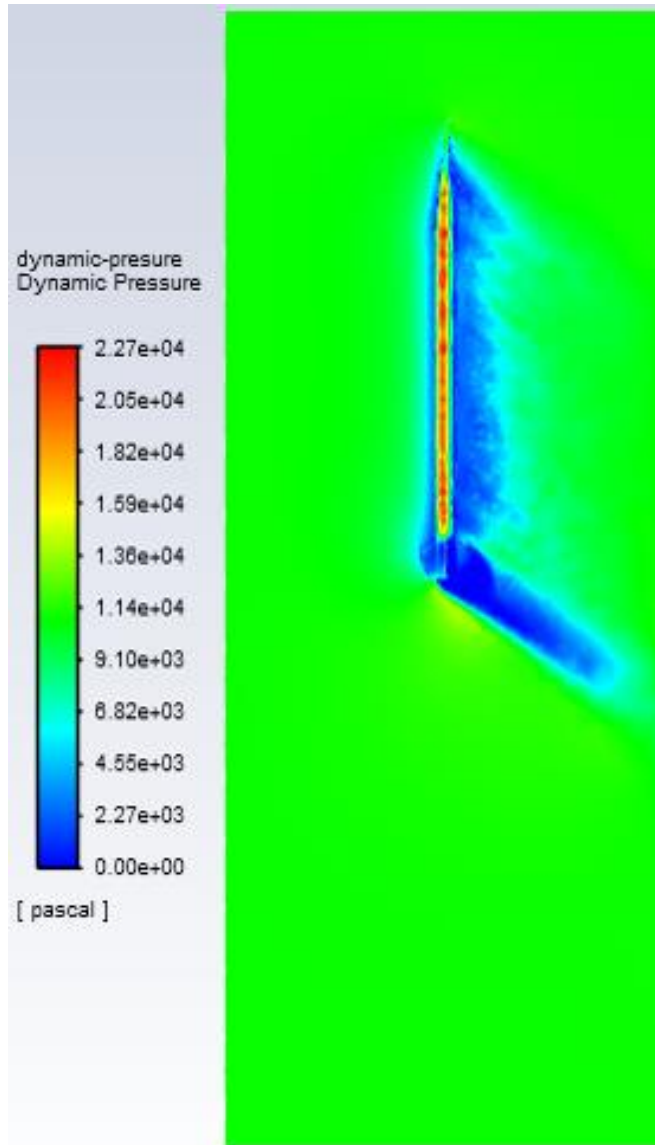
Figure 174: Dynamic pressure contour at 60 deg AoA
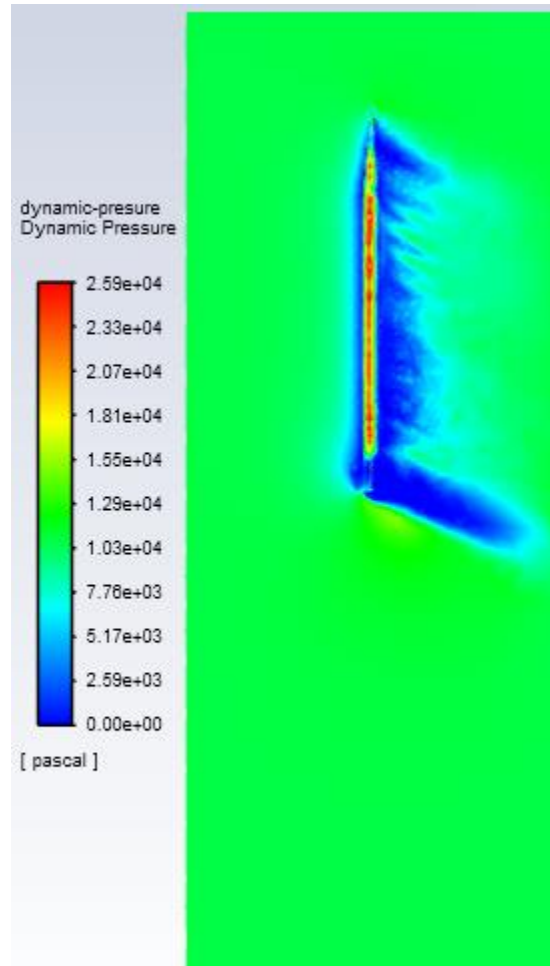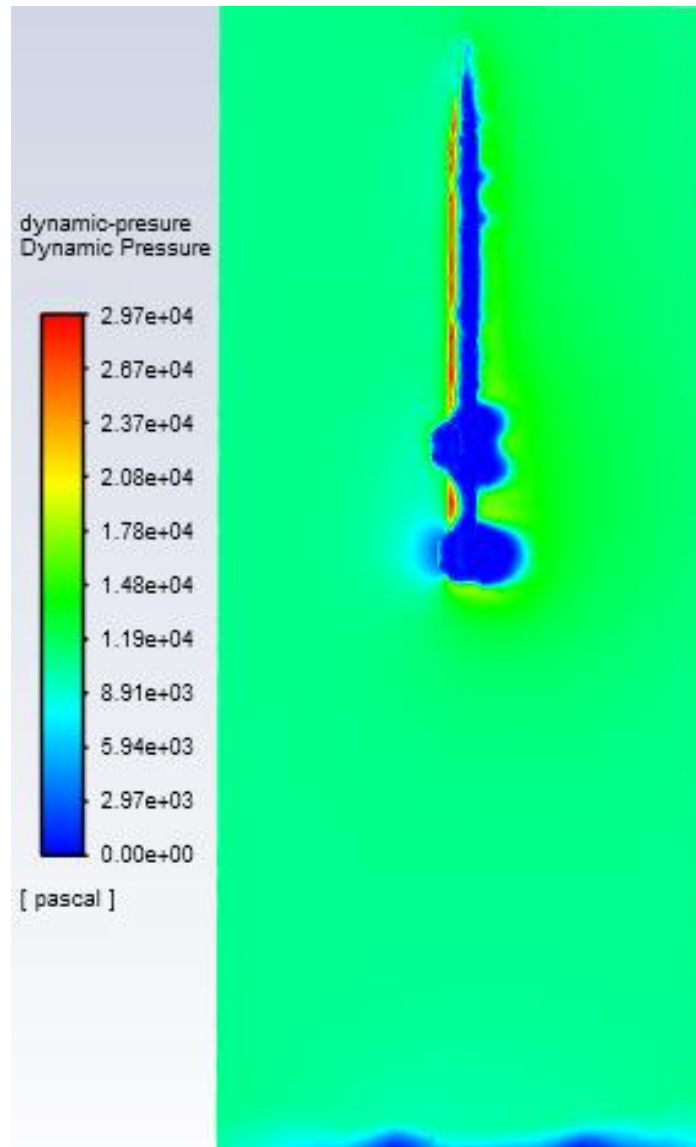
Figure 175: Dynamic pressure contour at 70 deg AoA
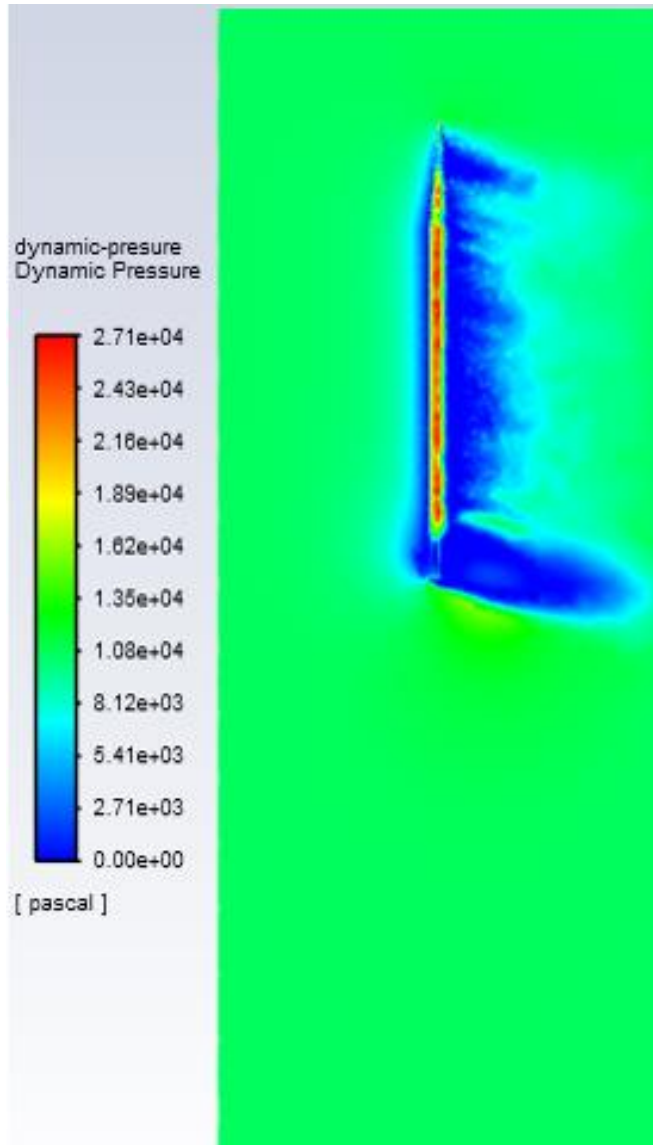
Figure 176: Dynamic pressure contour at 80 deg AoA
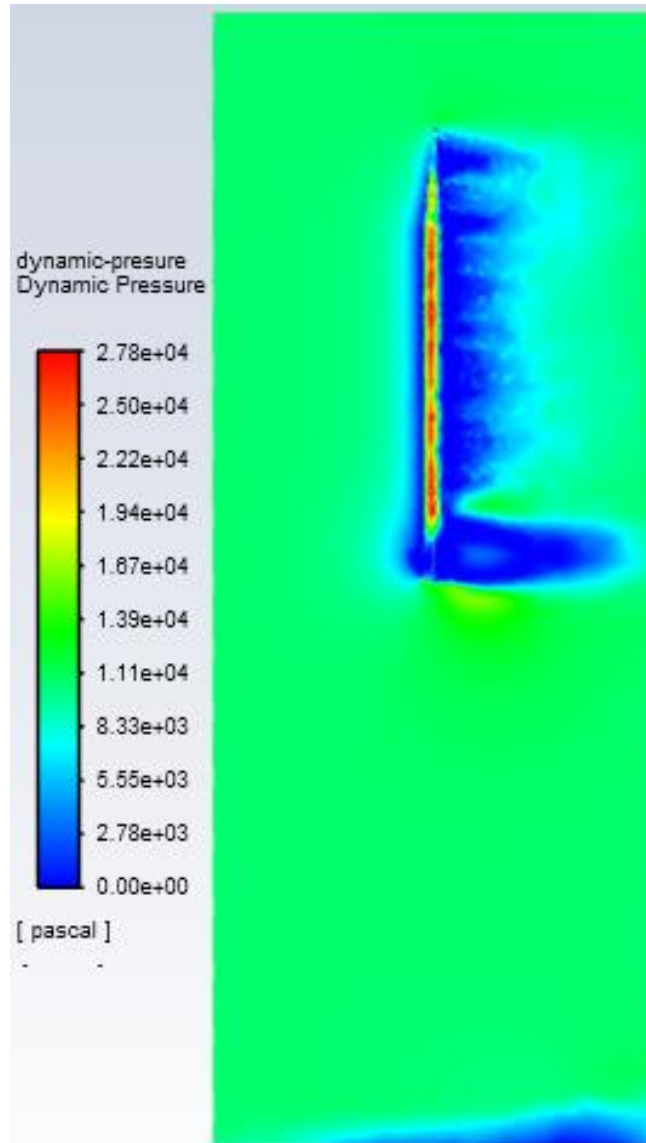
Figure 177: Dynamic pressure contour at 90 deg AoA

7.8.2 Innovative Rocket
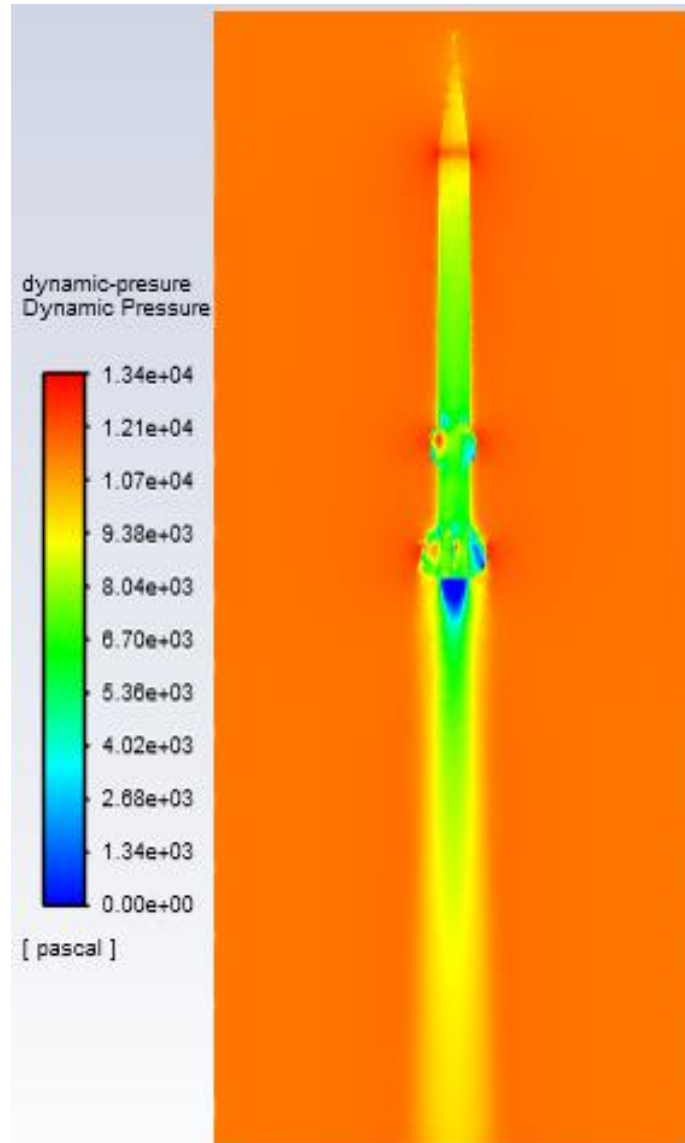
Figure 178: Dynamic pressure contour at 0 deg AoA
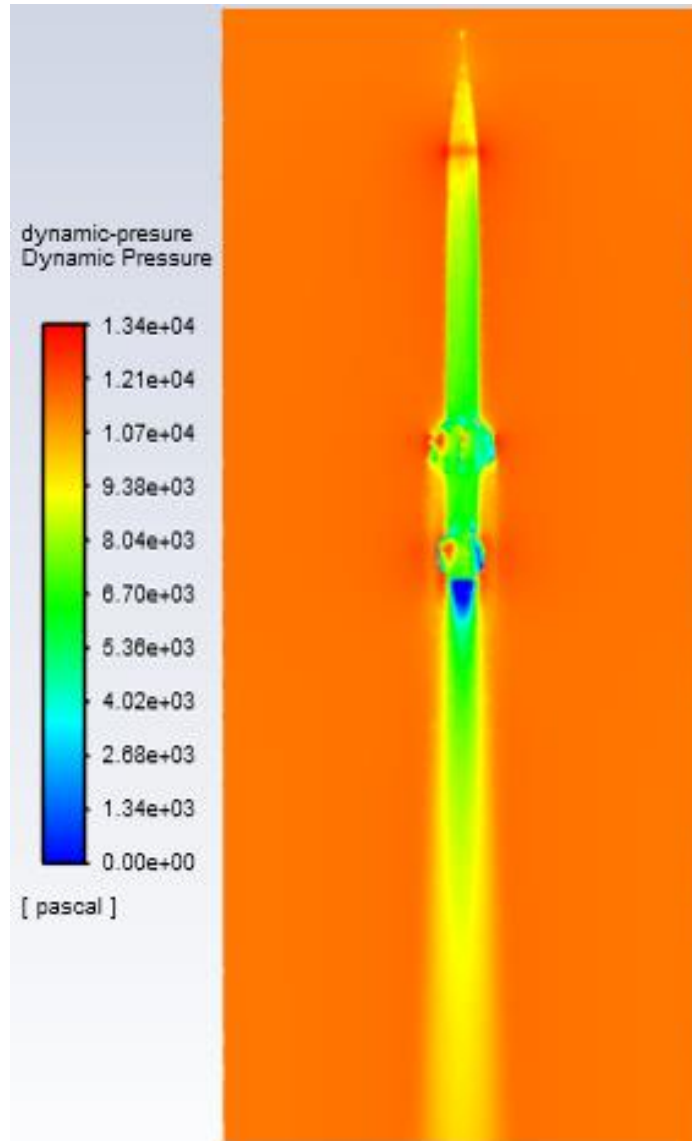
Figure 179: Dynamic pressure contour at 0 deg AoA, 45 deg out of XY plane
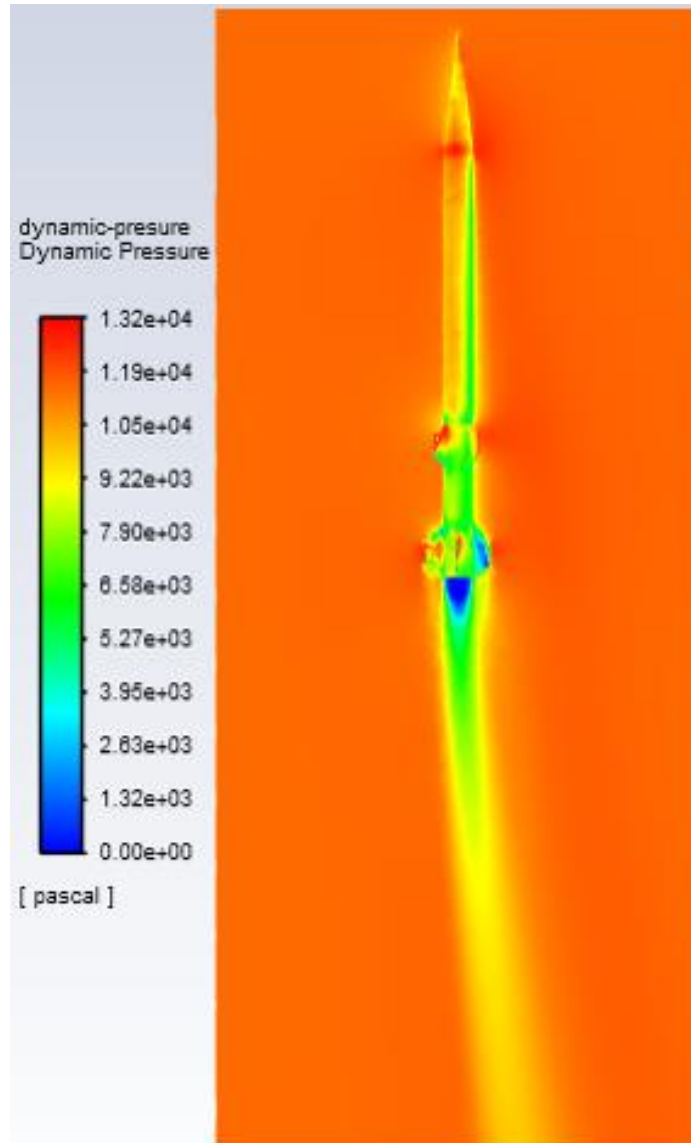
Figure 180: Dynamic pressure contour at 10 deg AoA
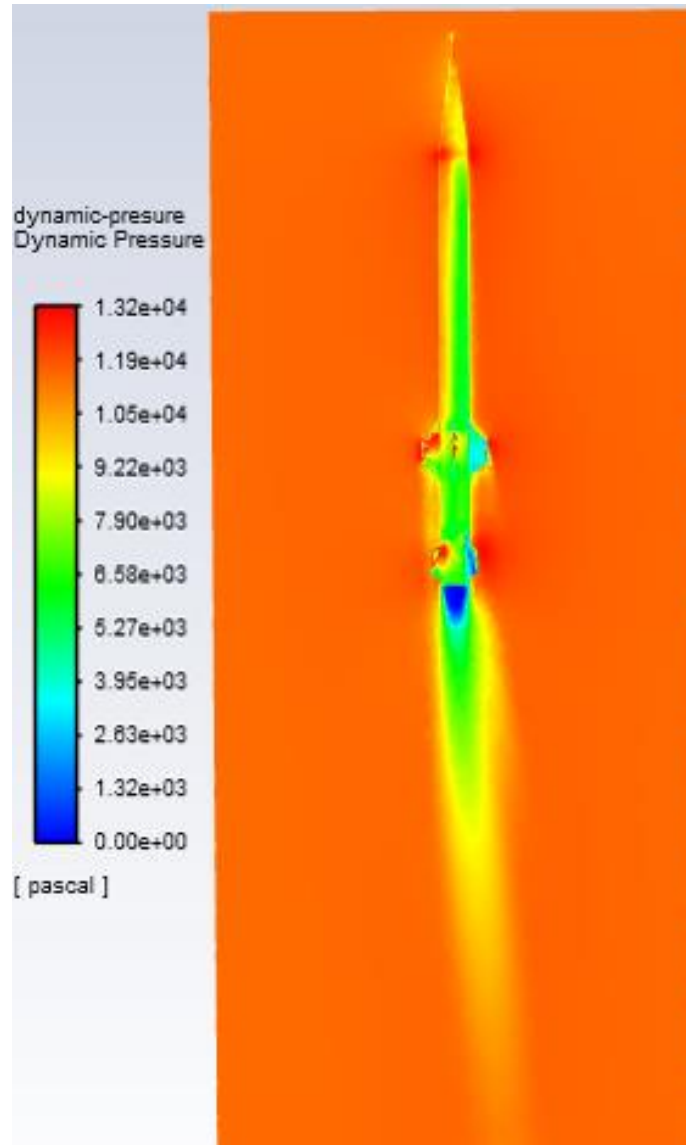
Figure 181: Dynamic pressure contour at 10 deg AoA, 45 deg out of XY plane
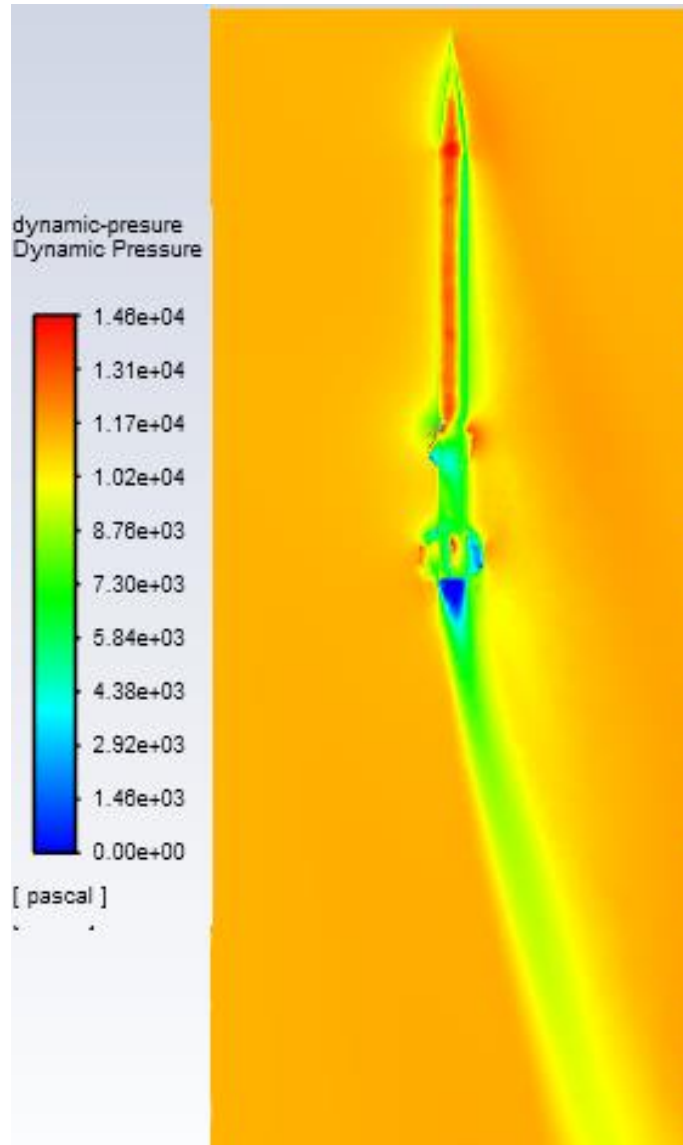
Figure 182: Dynamic pressure contour at 20 deg AoA
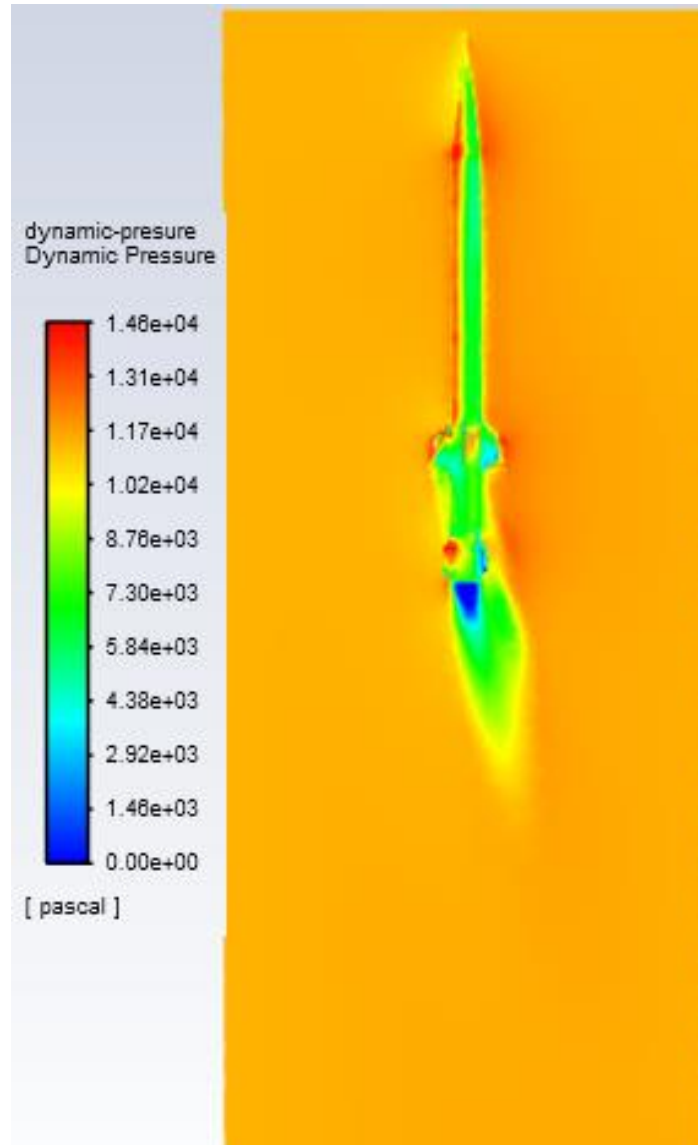
Figure 183: Dynamic pressure contour at 20 deg AoA, 45 deg out of XY plane
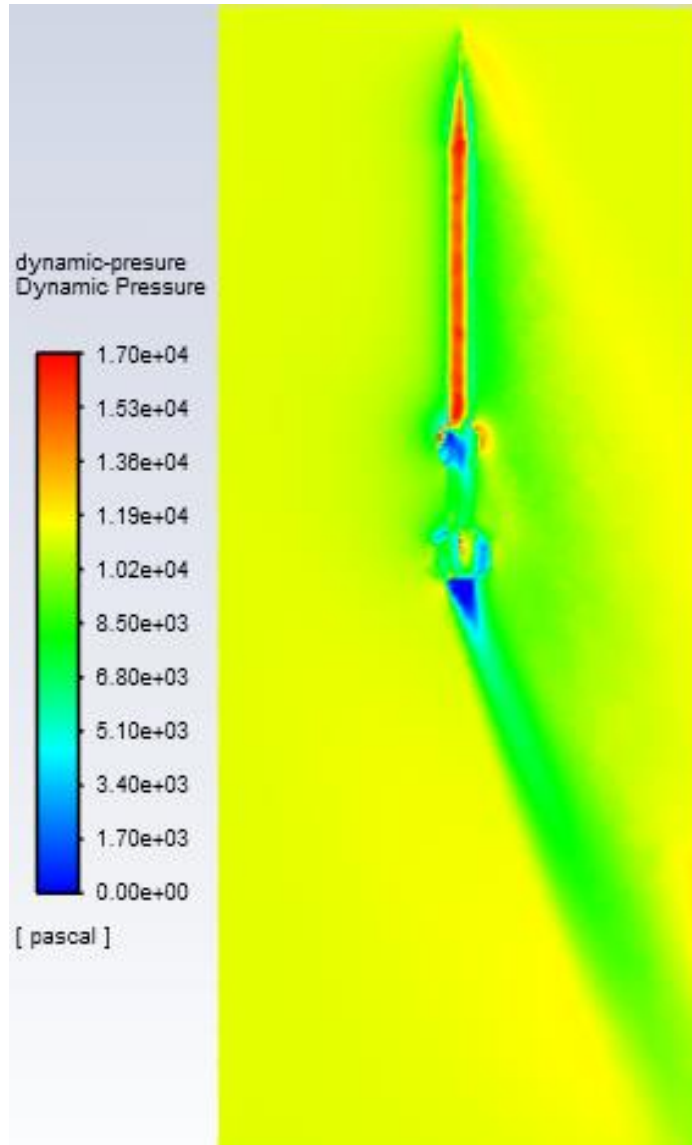
Figure 184: Dynamic pressure contour at 30 deg AoA
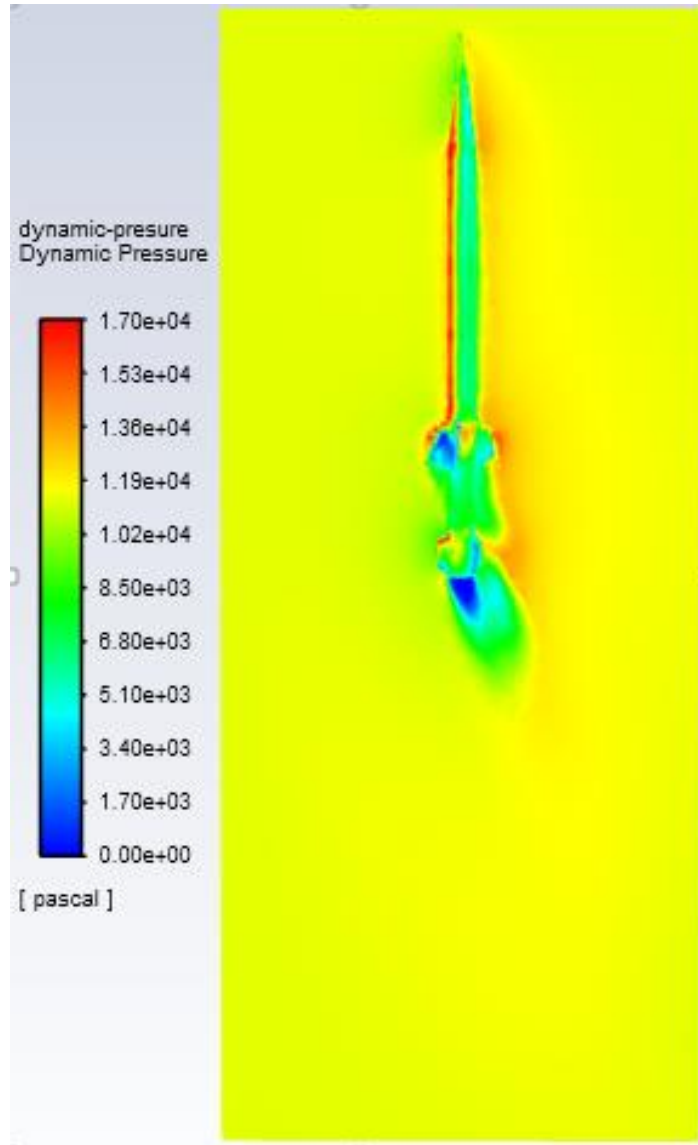
Figure 185: Dynamic pressure contour at 30 deg AoA, 45 deg out of XY plane
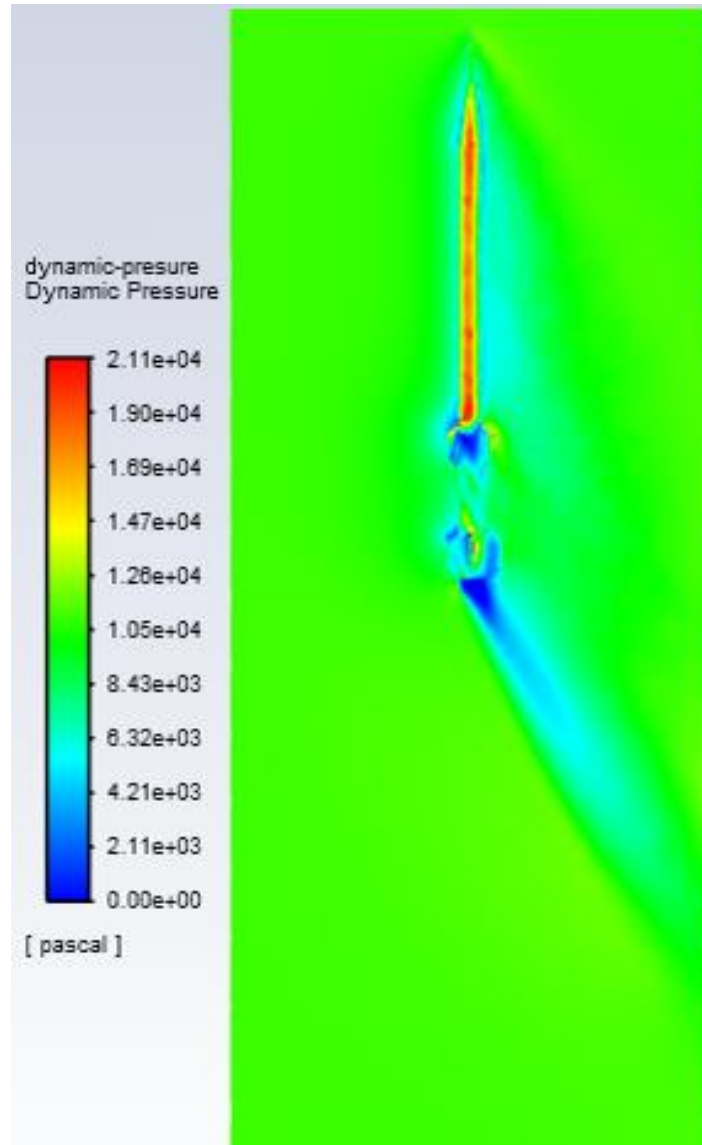
Figure 186: Dynamic pressure contour at 40 deg AoA
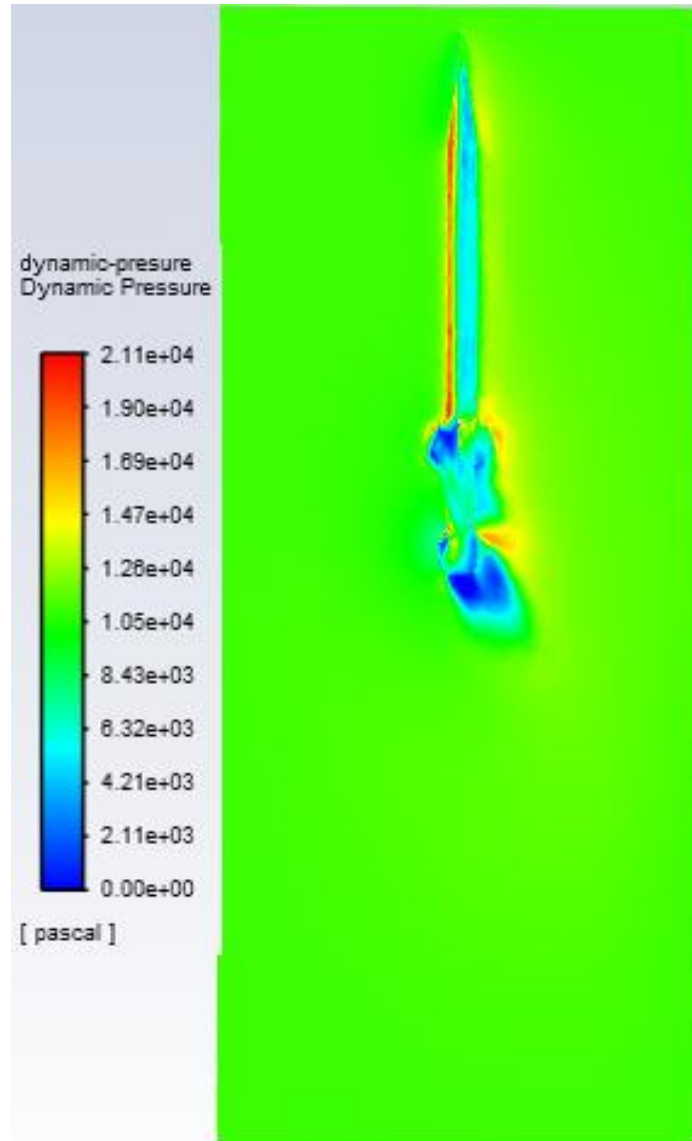
Figure 187: Dynamic pressure contour at 40 deg AoA, 45 deg out of XY plane
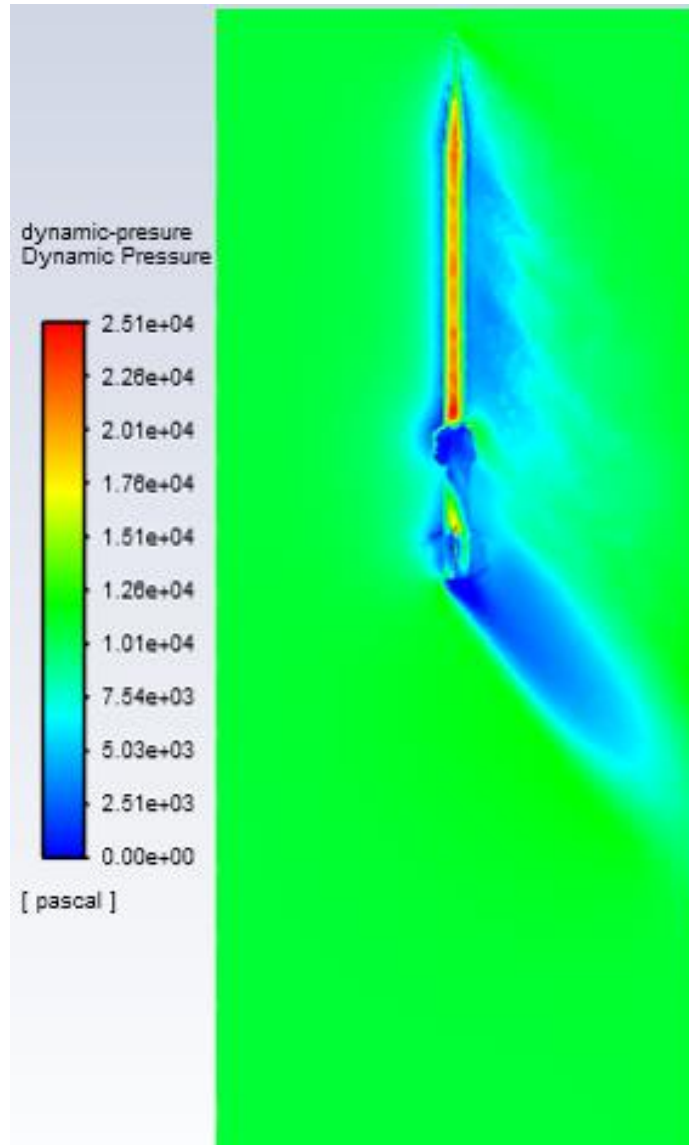
Figure 188: Dynamic pressure contour at 50 deg AoA
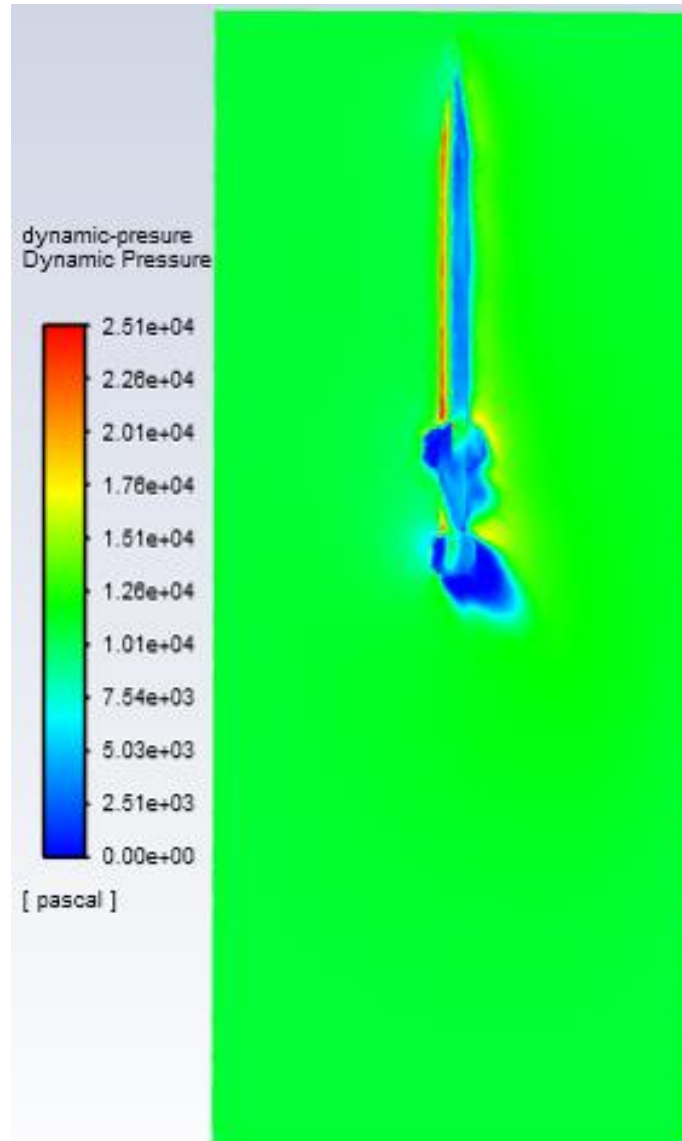
Figure 189: Dynamic pressure contour at 50 deg AoA, 45 deg out of XY plane
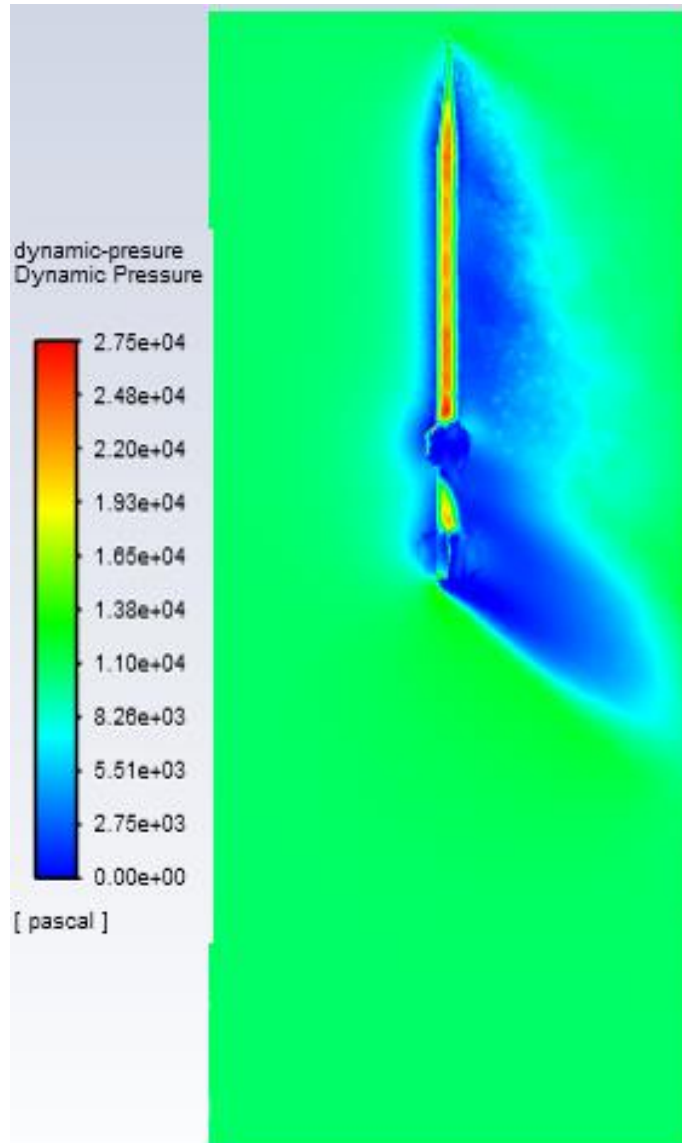
Figure 190: Dynamic pressure contour at 60 deg AoA
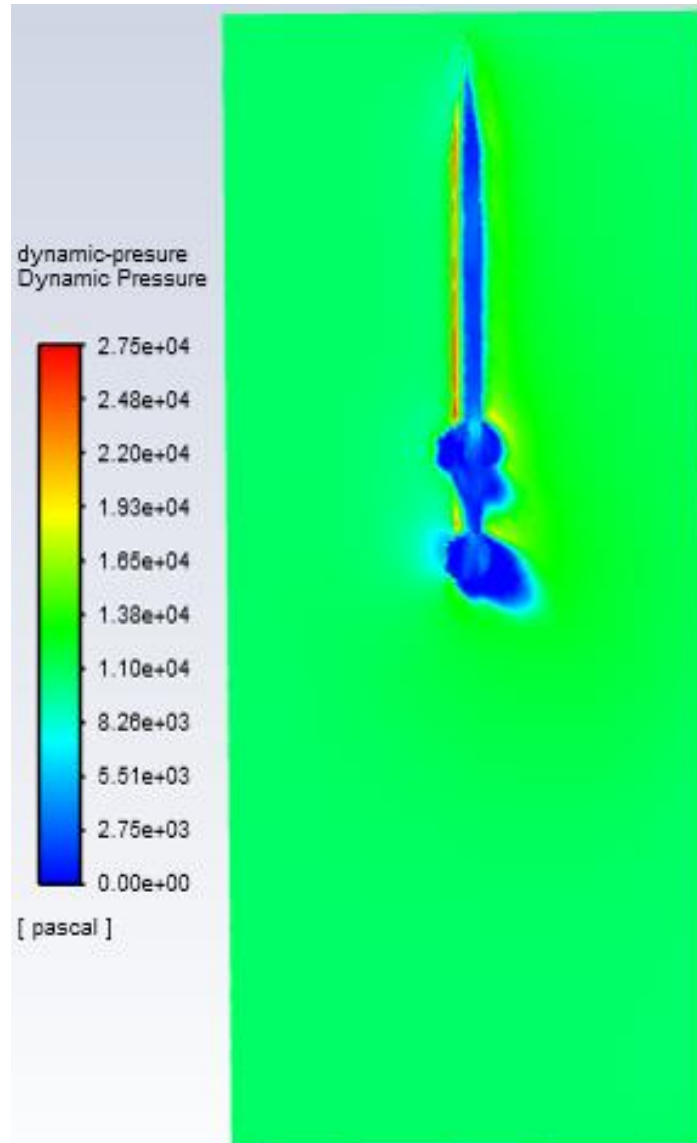
Figure 191: Dynamic pressure contour at 60 deg AoA, 45 deg out of XY plane
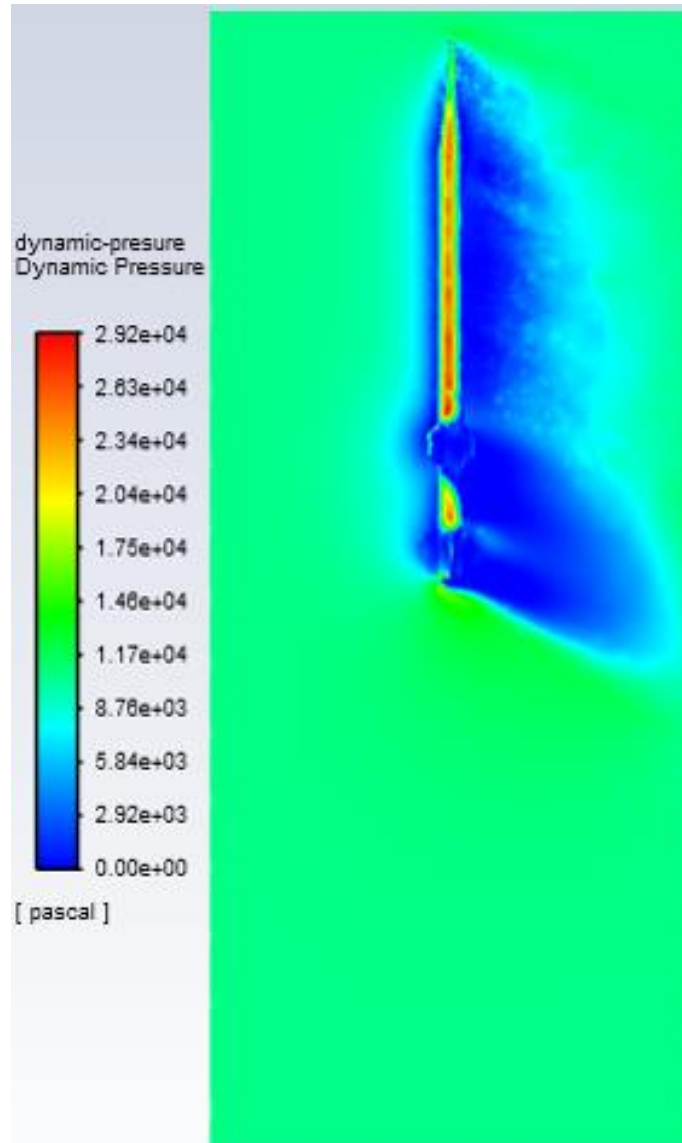
Figure 192: Dynamic pressure contour at 70 deg AoA
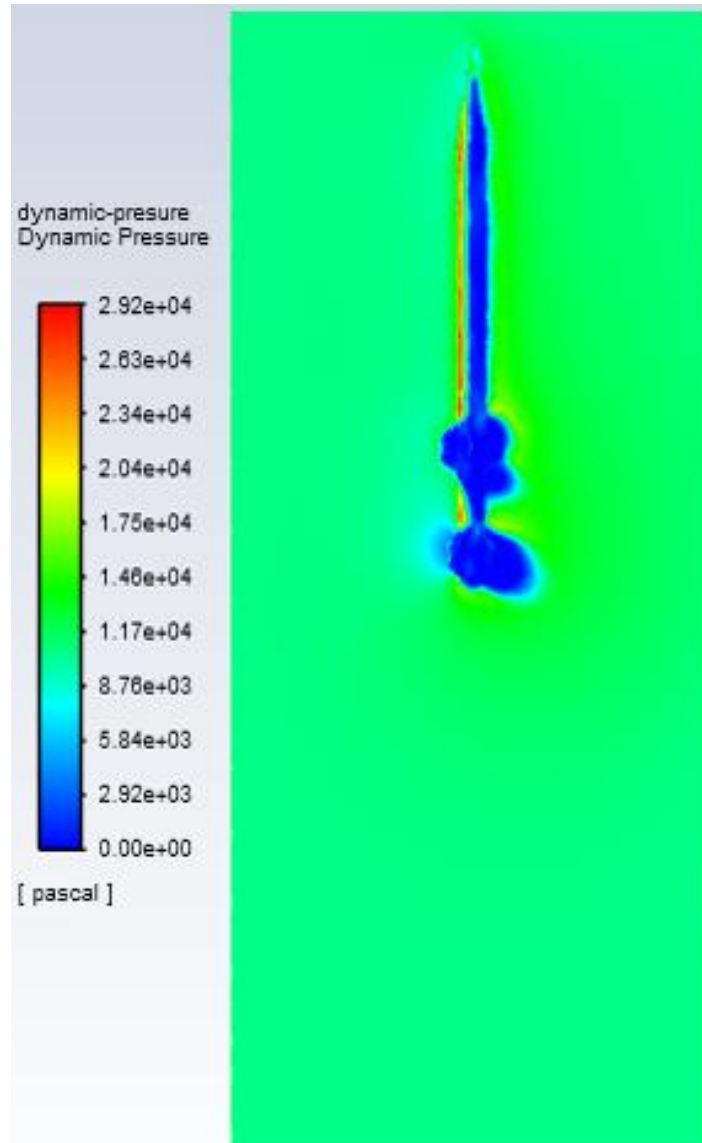
Figure 193: Dynamic pressure contour at 70 deg AoA, 45 deg out of XY plane
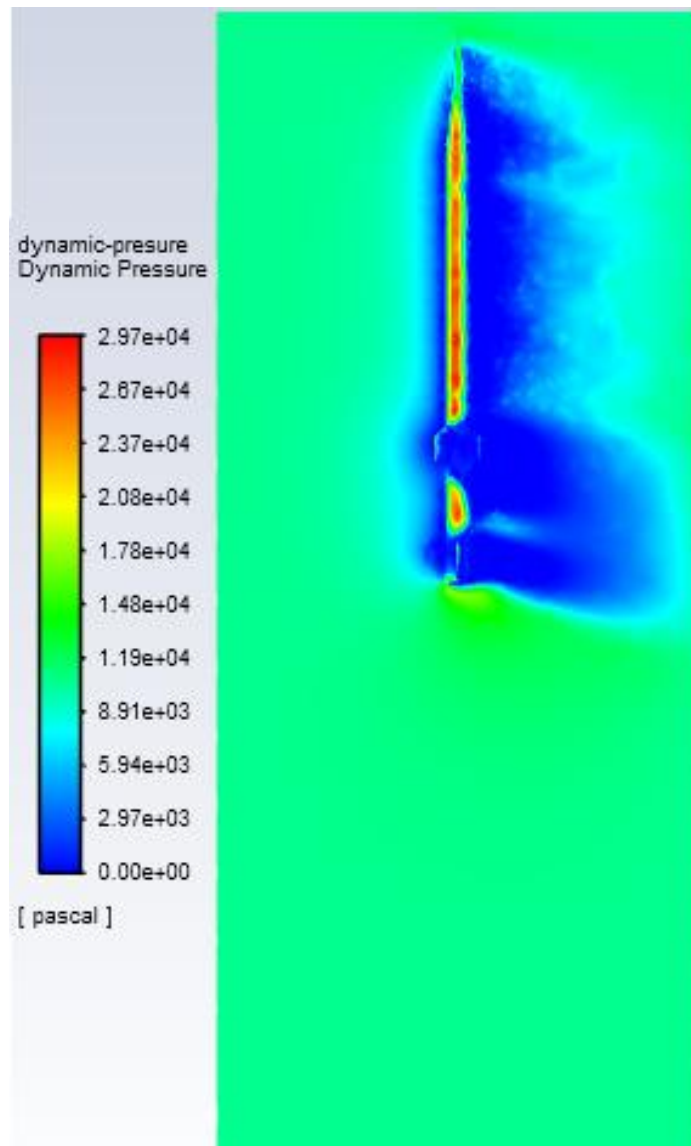
Figure 194: Dynamic pressure contour at 80 deg AoA
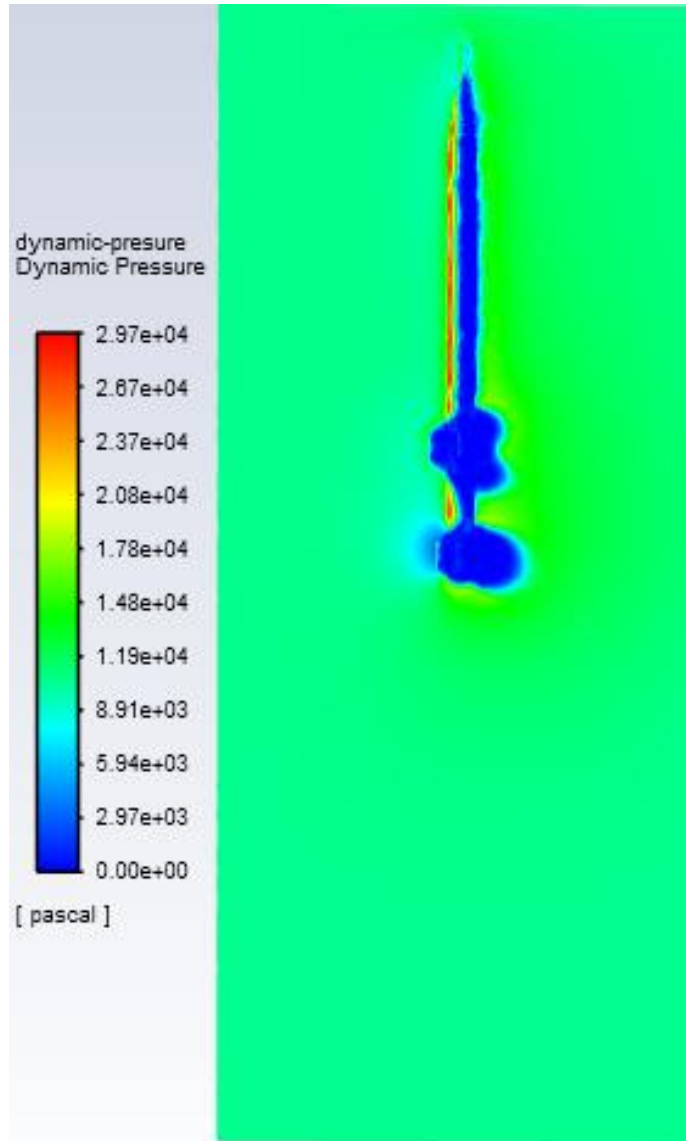
Figure 195: Dynamic pressure contour at 80 deg AoA, 45 deg out of XY plane
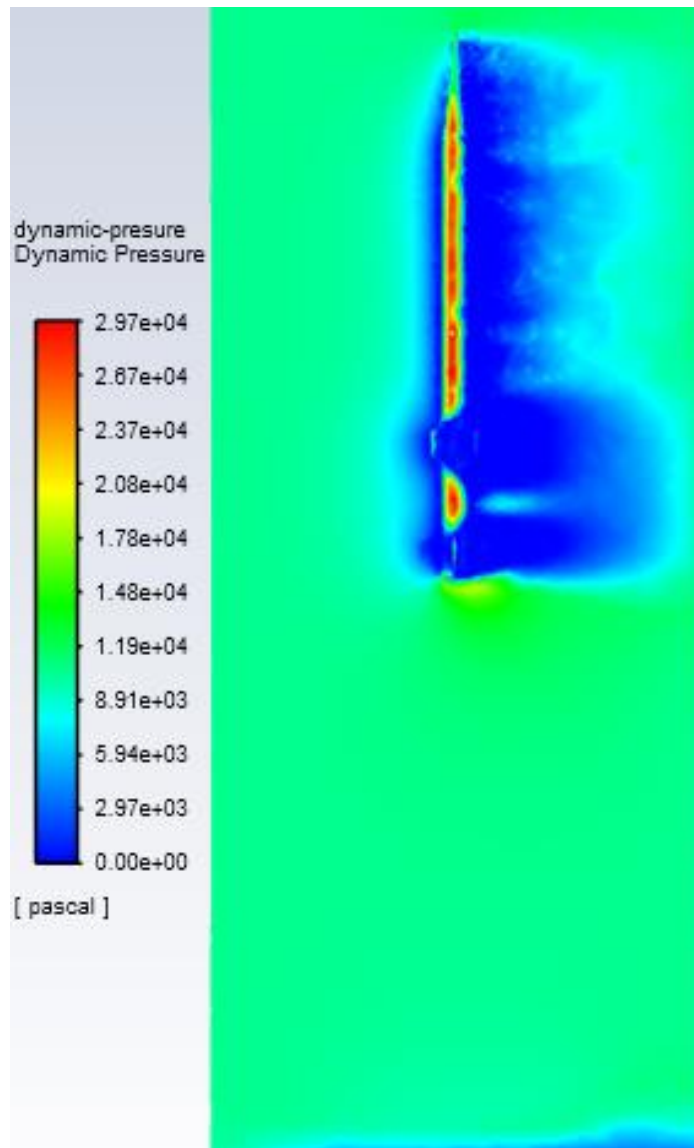
Figure 196: Dynamic pressure contour at 90 deg AoA

Figure 197: Dynamic pressure contour at 90 deg AoA, 45 deg out of XY plane

7.9. Appendix I: Numerical Model Aerodynamic Loads Data & Plots
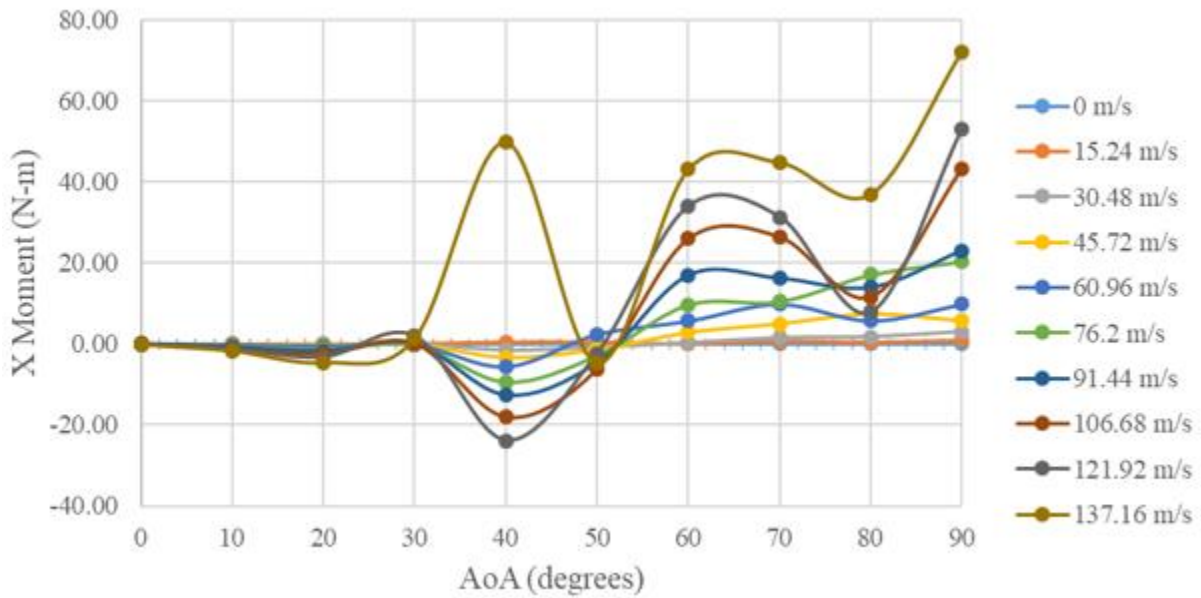
7.9.1 Baseline Rocket
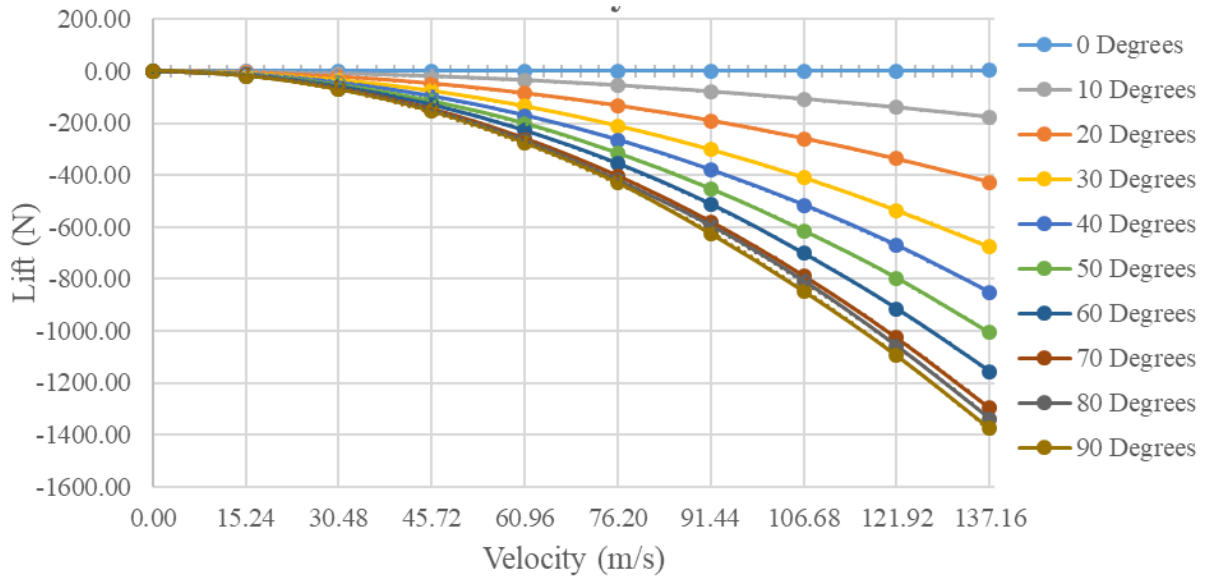
Figure 198: Plot of Velocity vs. Lift
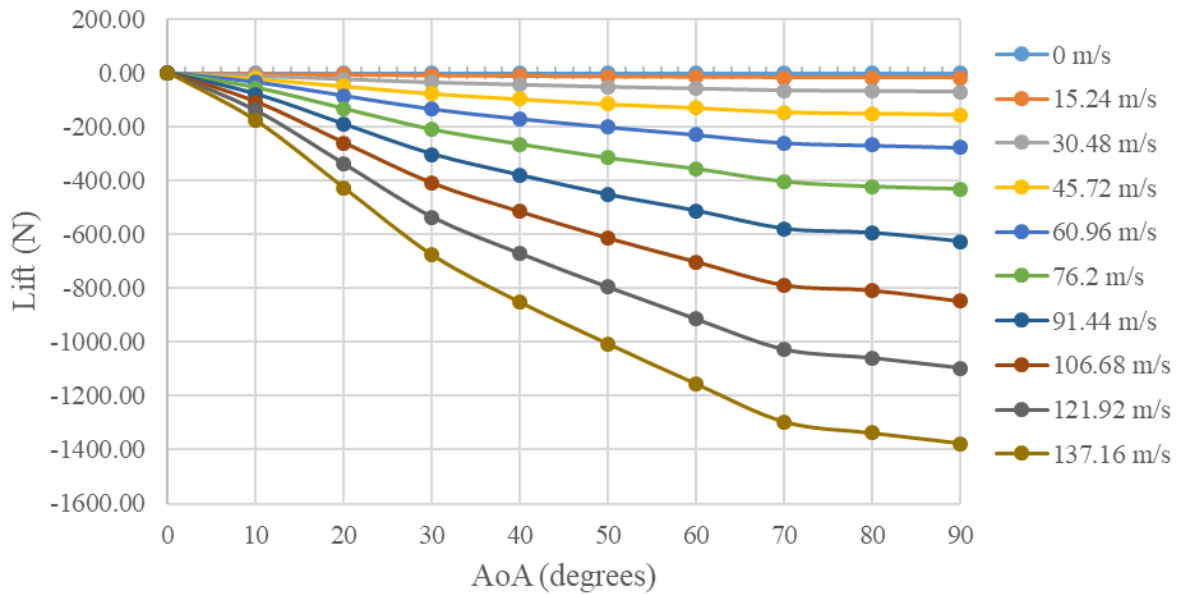
Figure 199: Plot of Angle of Attack vs. Lift
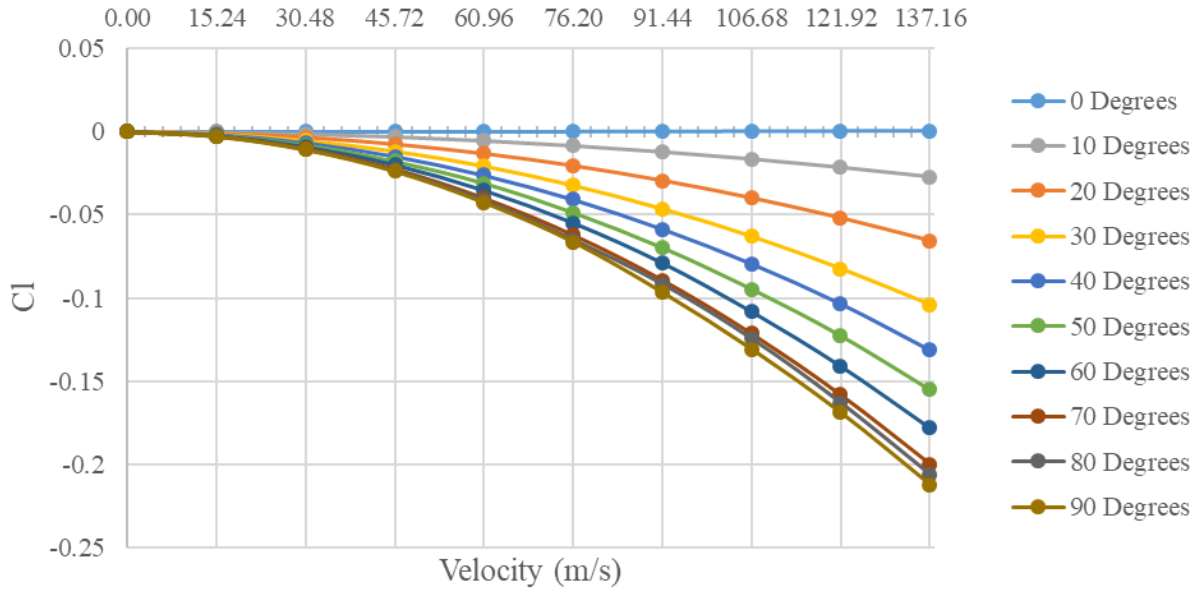
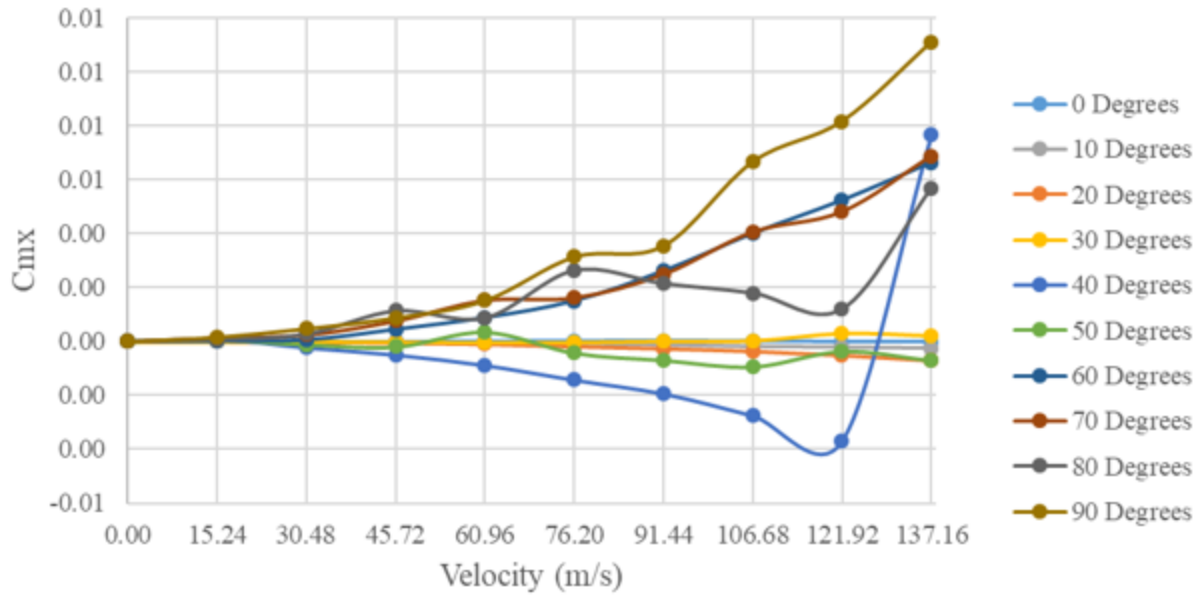Figure 200: Plot of Velocity vs. Lift Coefficient
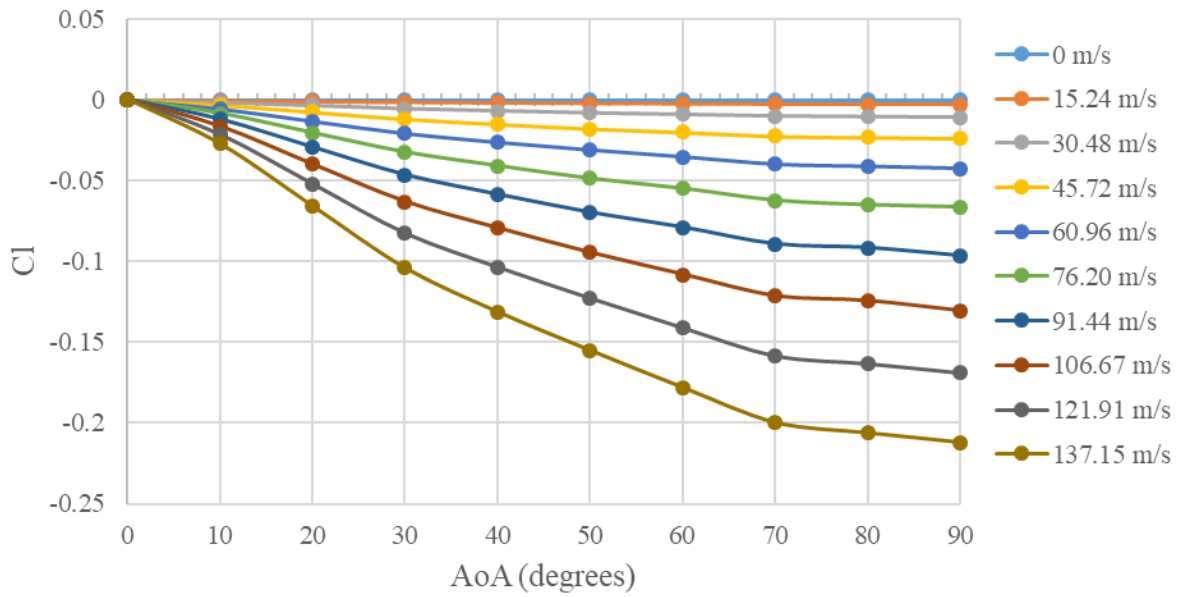
Figure 201: Plot of Angle of Attack vs. Lift Coefficient
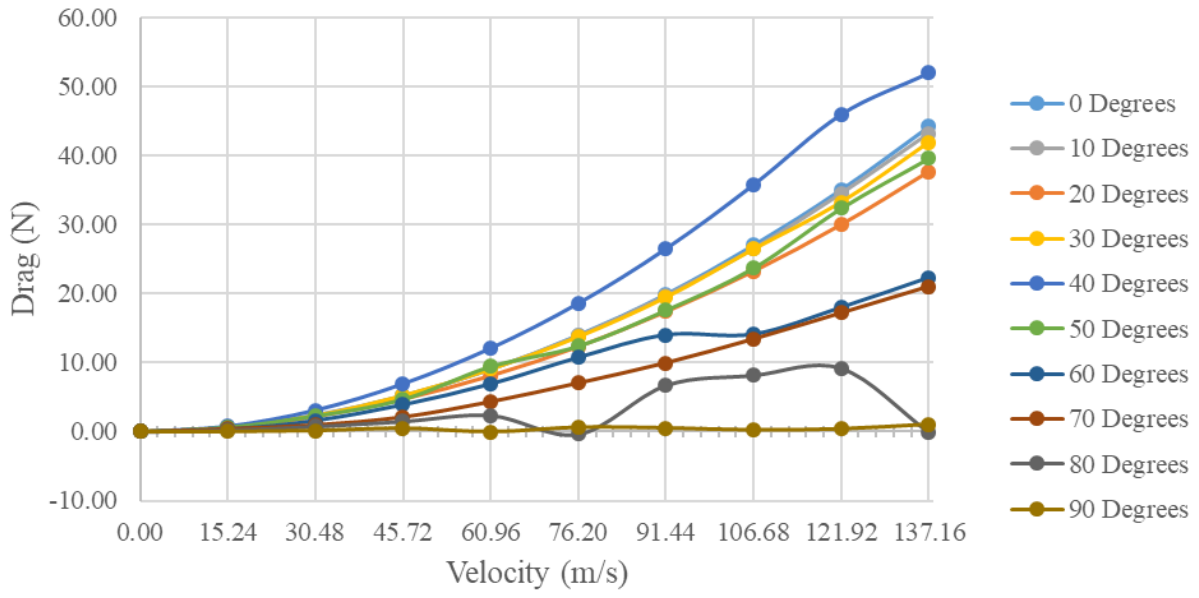
Figure 202: Plot of Velocity vs. Drag
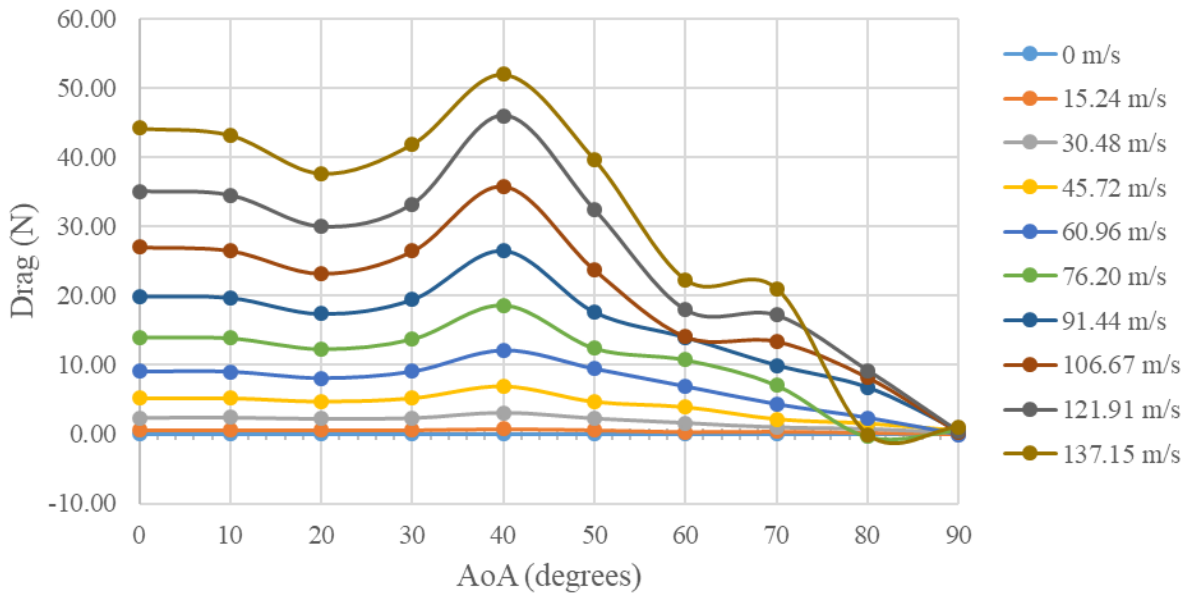
Figure 203: Plot of Angle of Attack vs. Drag
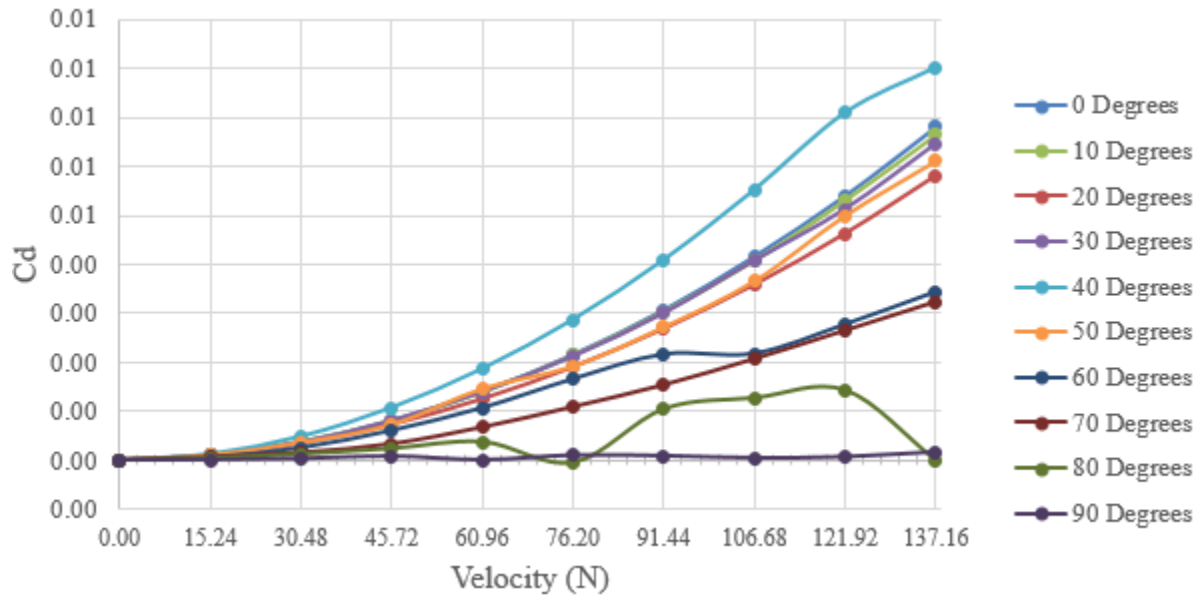
Figure 204: Plot of Velocity vs. Drag Coefficient
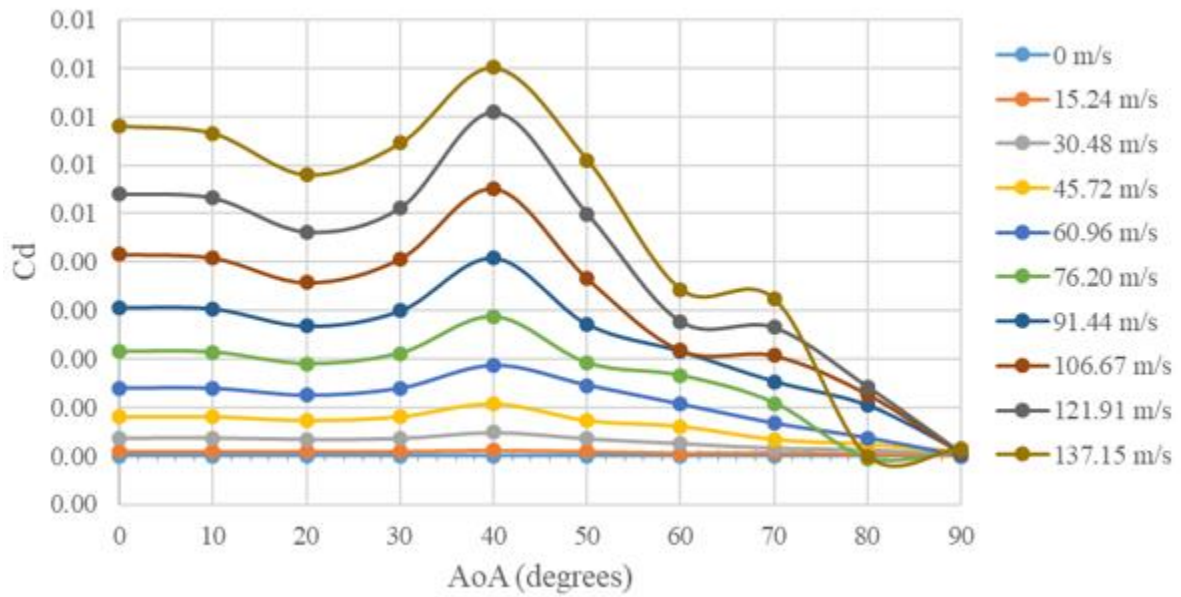
Figure 205: Plot of Angle of Attack vs. Drag Coefficient

316
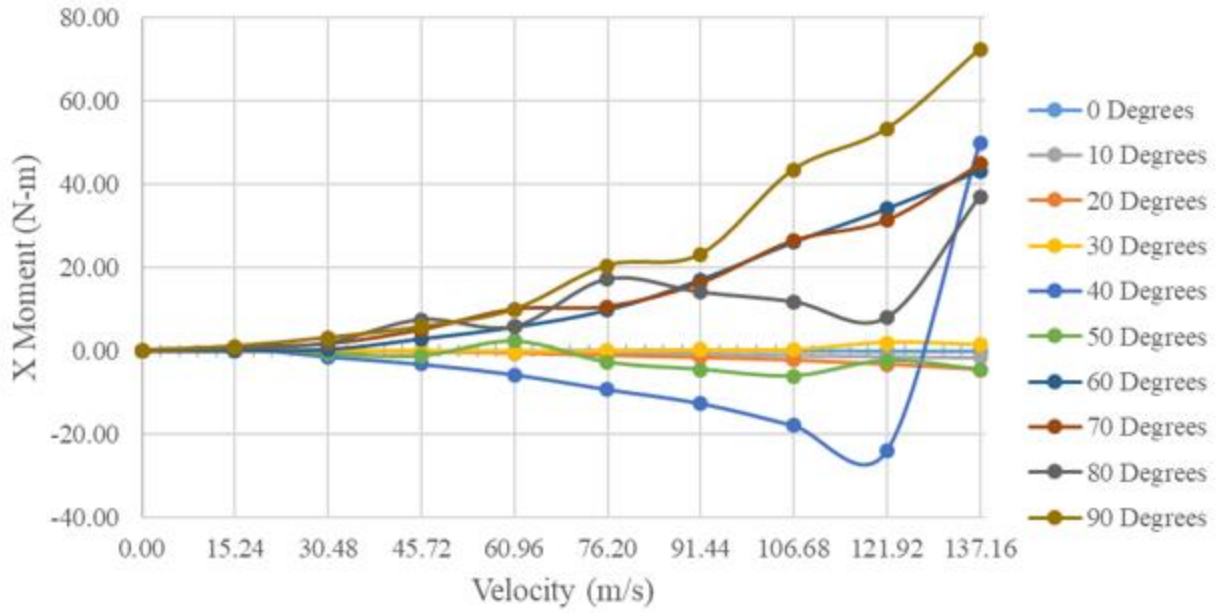
Figure 206: Plot of Velocity vs. X Moment

Figure 207: Plot of Angle of Attack vs. X Moment
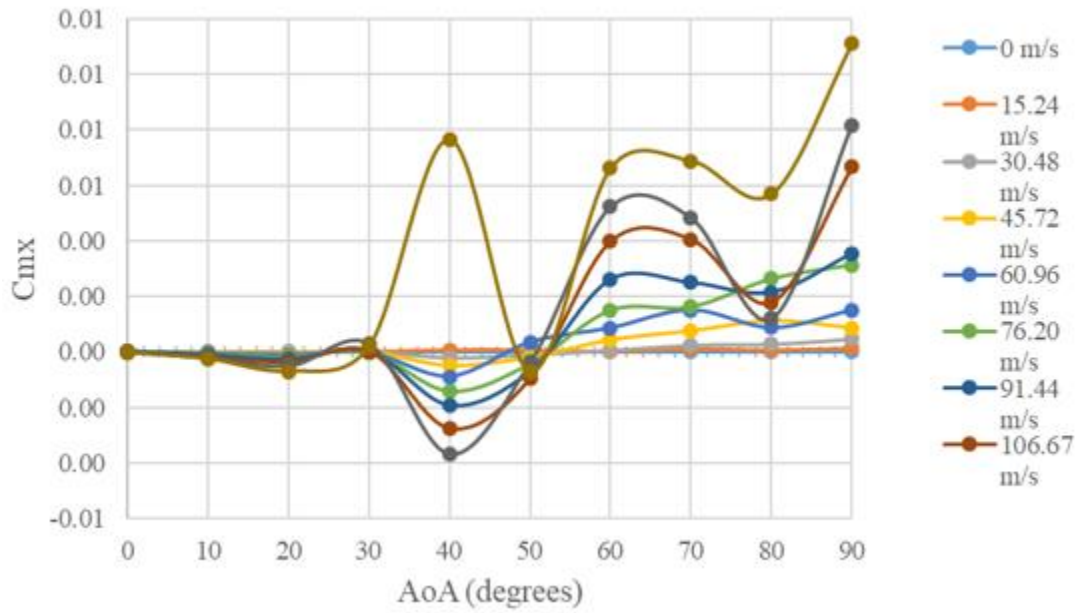
Figure 208: Plot of Velocity vs. X Moment Coefficient

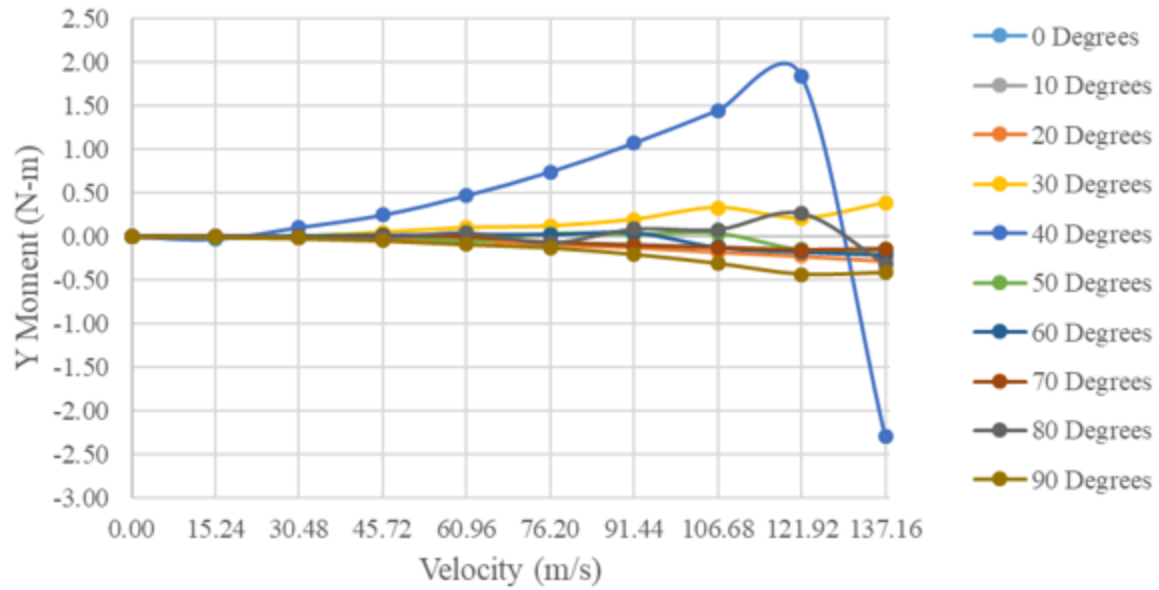Figure 209: Plot of Angle of Attack vs. X Moment Coefficient
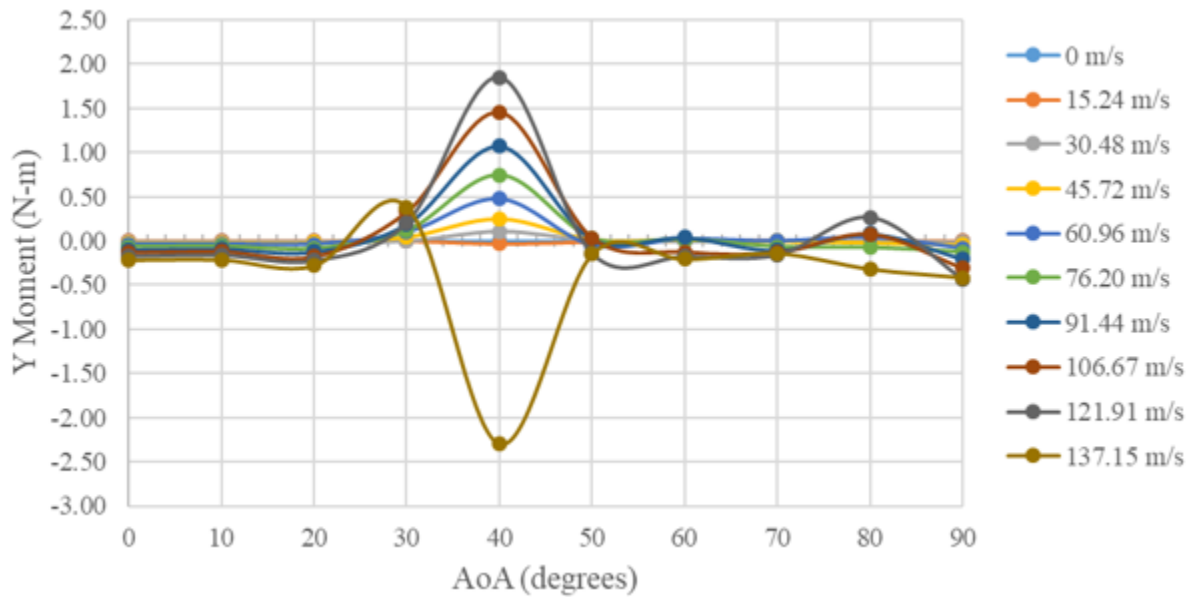
Figure 210: Plot of Velocity vs. Y Moment

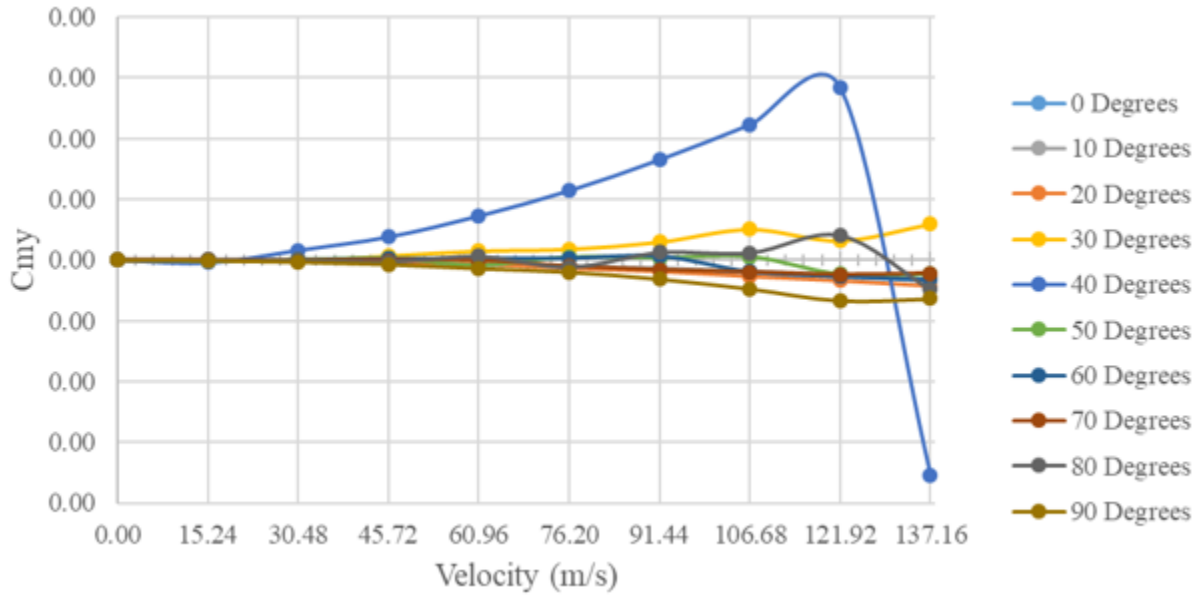Figure 211: Plot of Angle of Attack vs. Y Moment

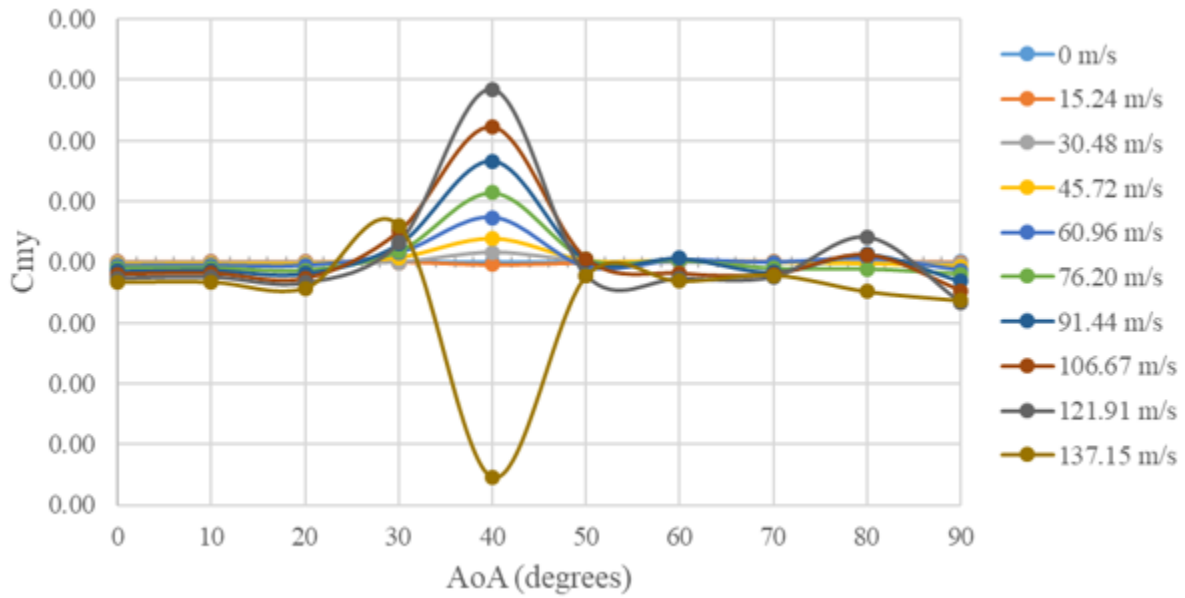Figure 212: Plot of Velocity vs. Y Moment Coefficient

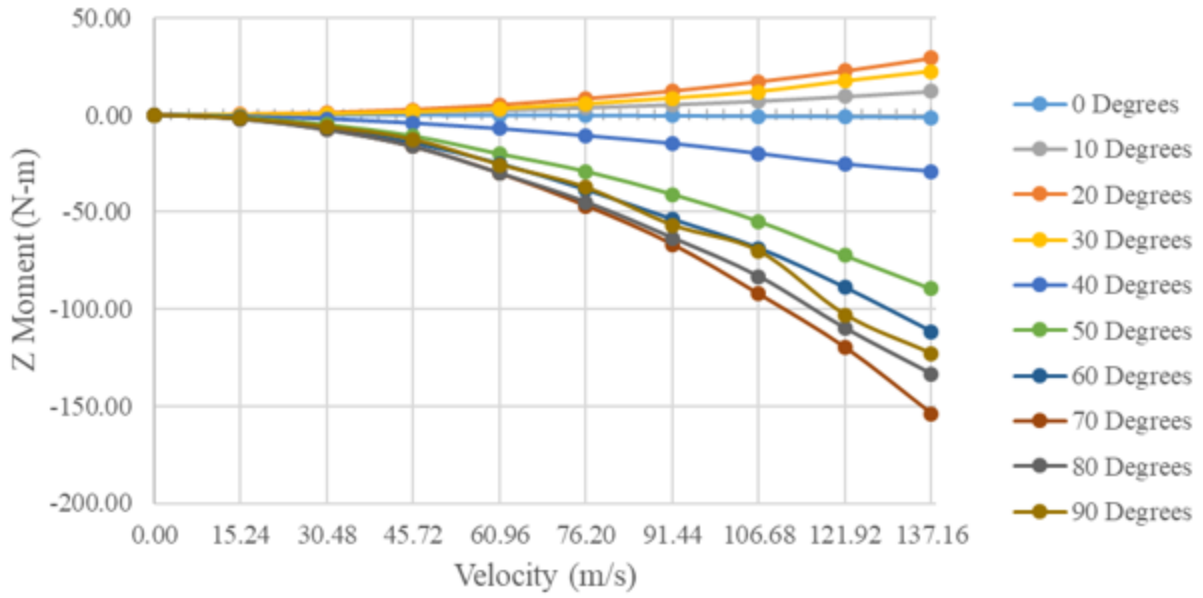Figure 213: Plot of Angle of Attack vs. Y Moment Coefficient

Figure 214: Plot of Velocity vs. Z Moment

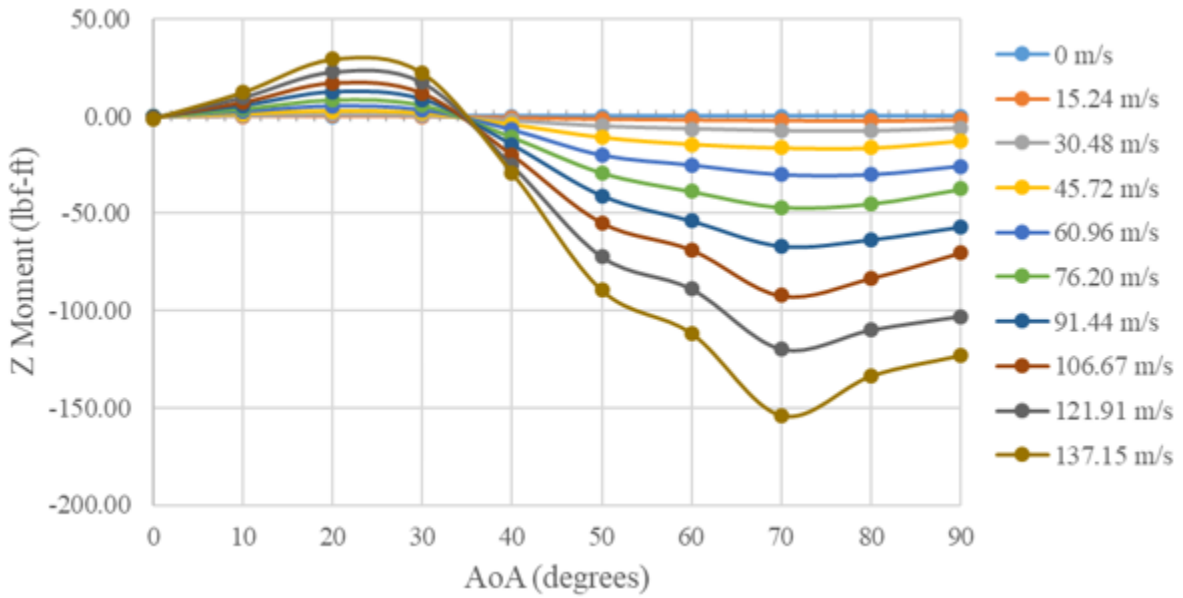

Figure 215: Plot of Angle of Attack vs. Z Moment

Figure 216: Plot of Velocity vs. Z Moment Coefficient

Figure 217: Plot of Angle of Attack vs. Z Moment Coefficient

7.9.2 Innovative Rocket
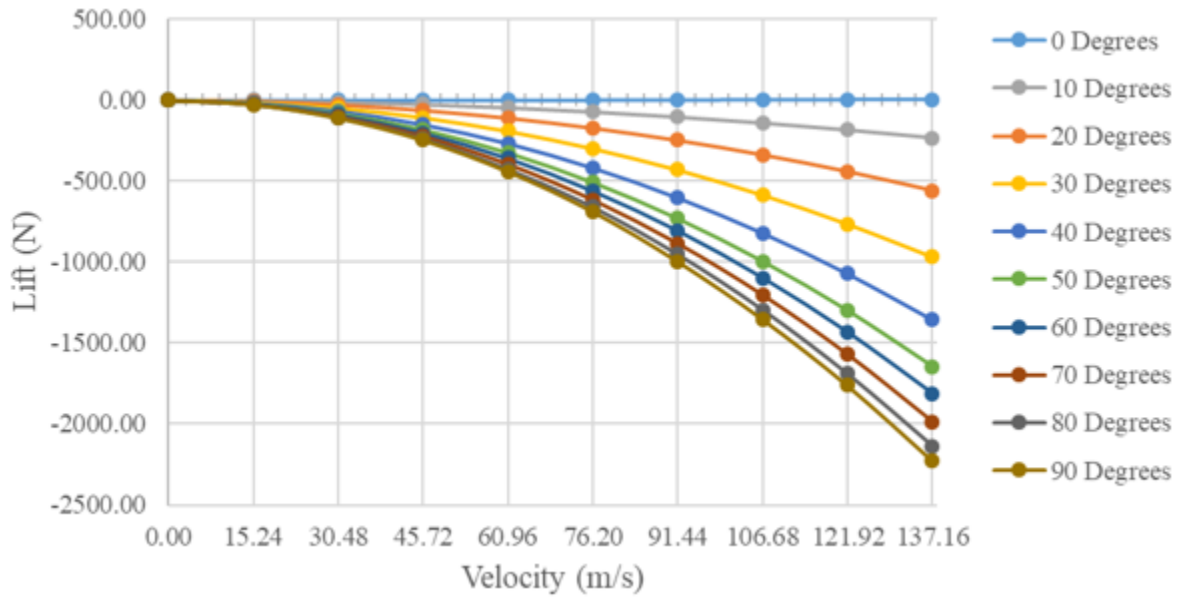
Figure 218: Plot of Velocity vs. Lift
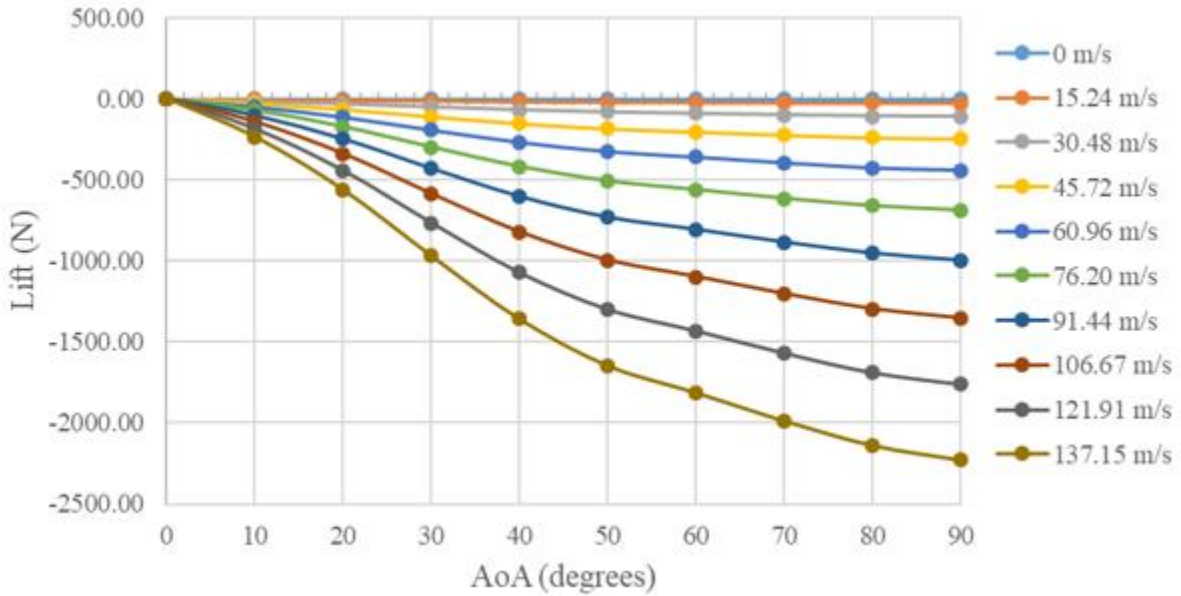
Figure 219: Plot of Angle of Attack vs. Lift
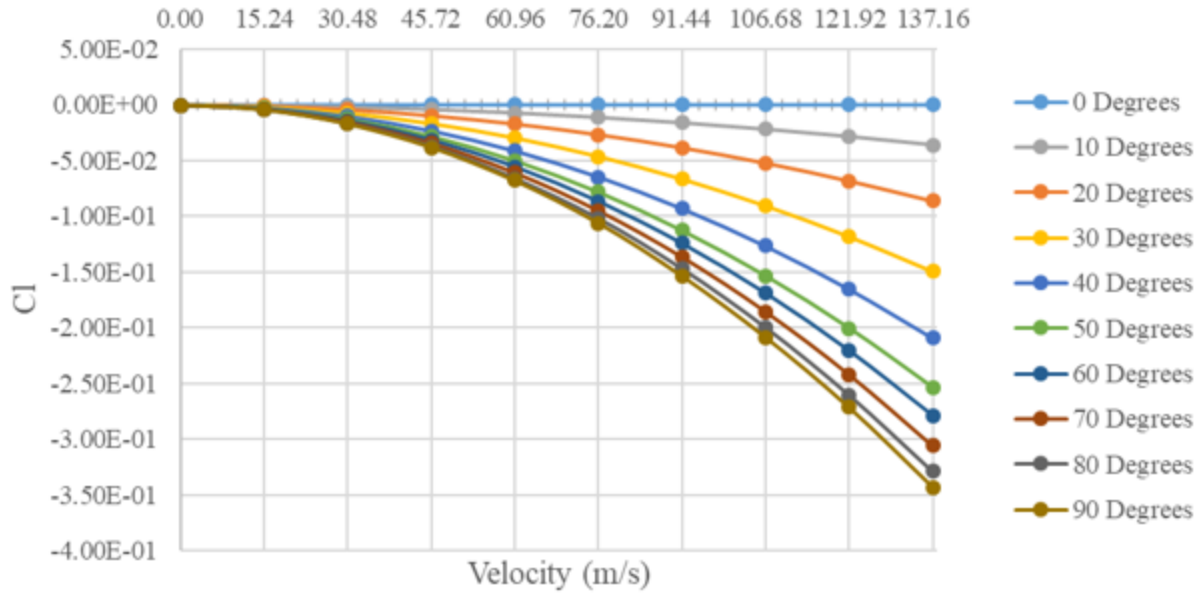
Figure 220: Plot of Velocity vs. Lift Coefficient
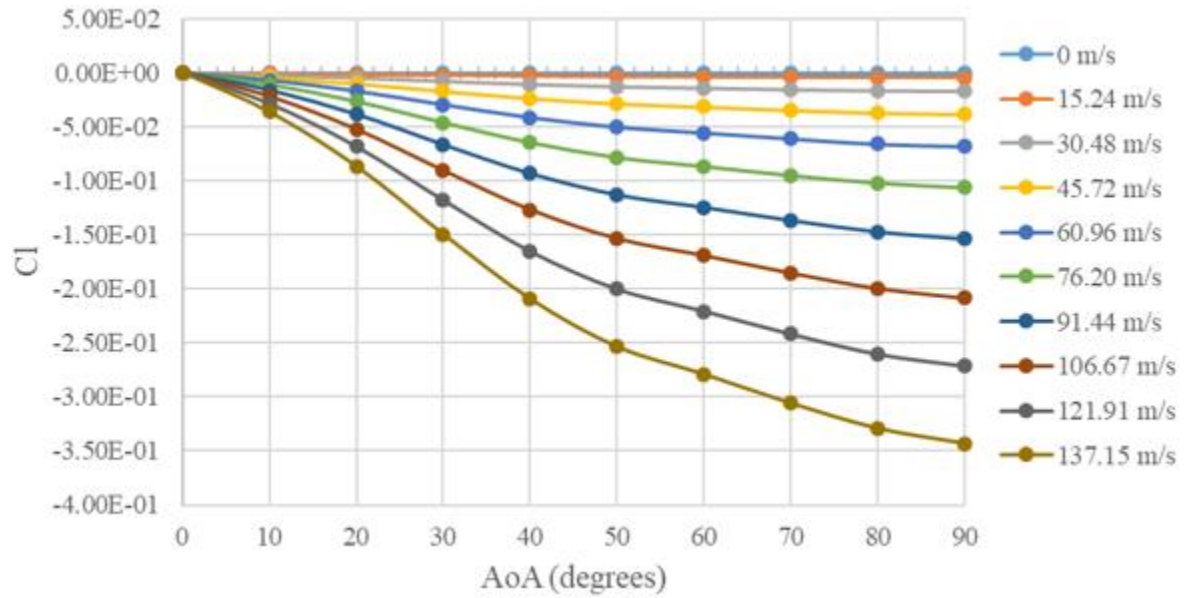
Figure 221: Plot of Angle of Attack vs. Lift Coefficient
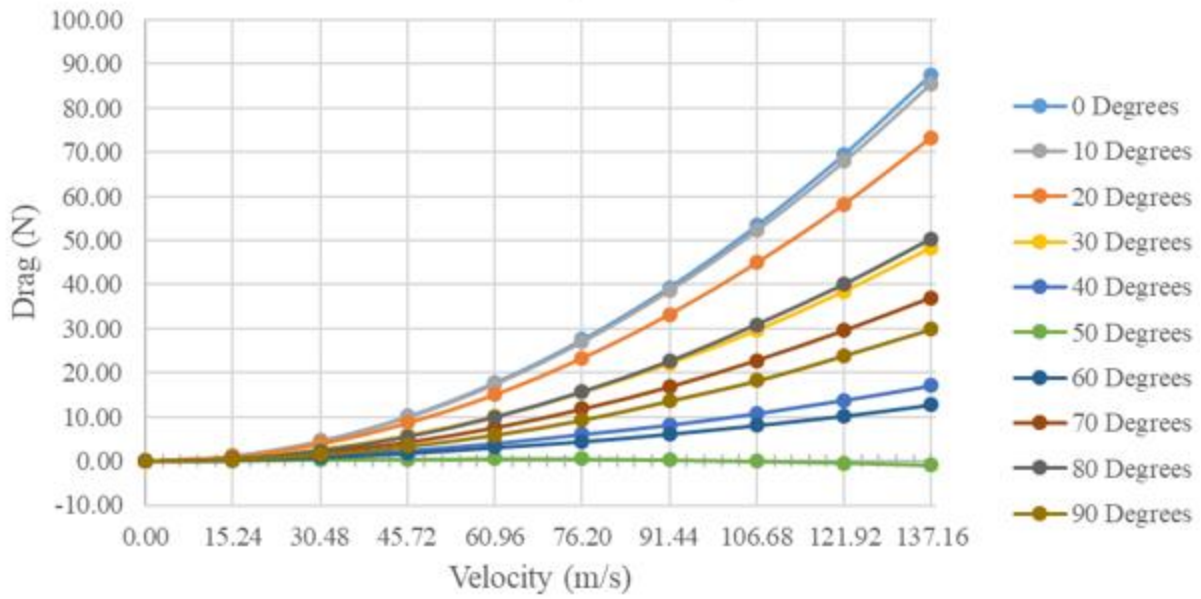
Figure 222: Plot of Velocity vs. Drag
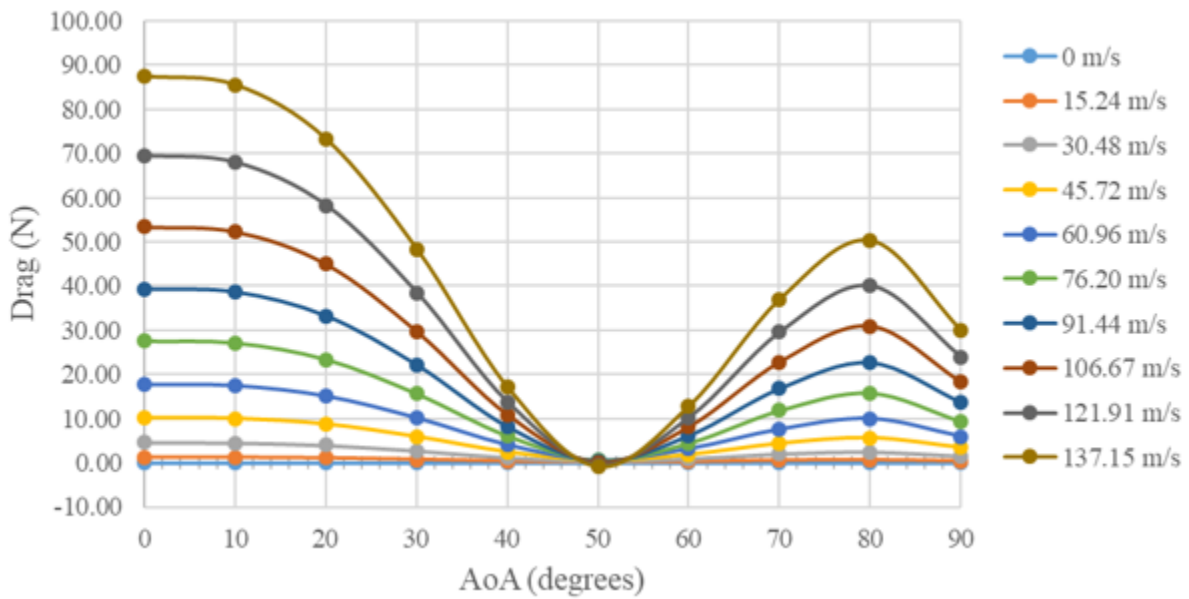
Figure 223: Plot of Angle of Attack vs. Drag
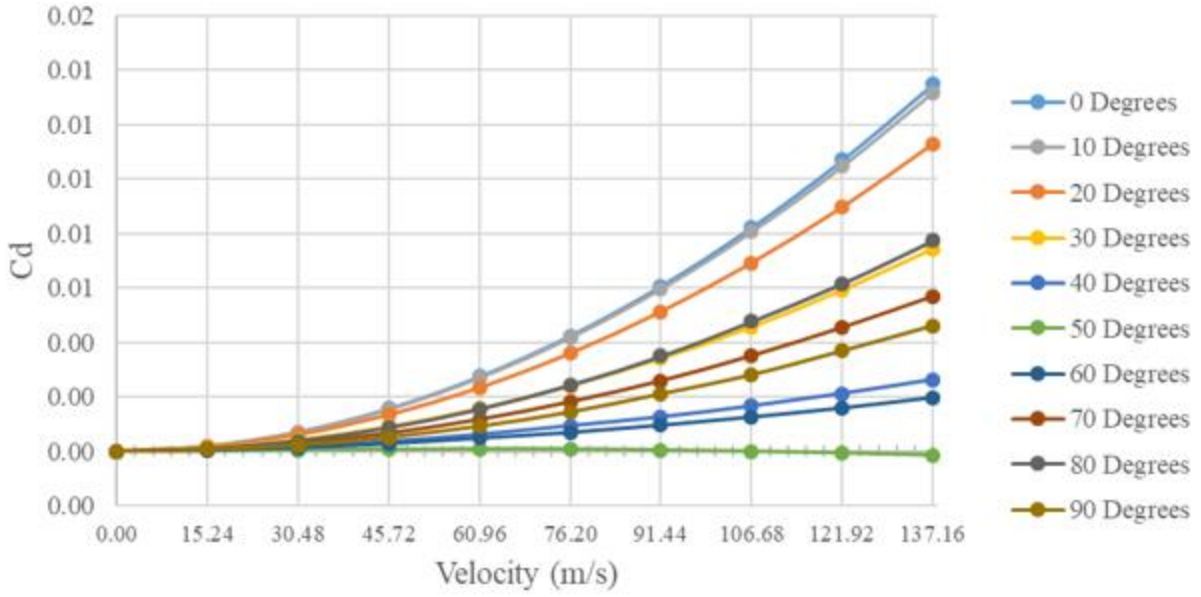
Figure 224: Plot of Velocity vs. Drag Coefficient
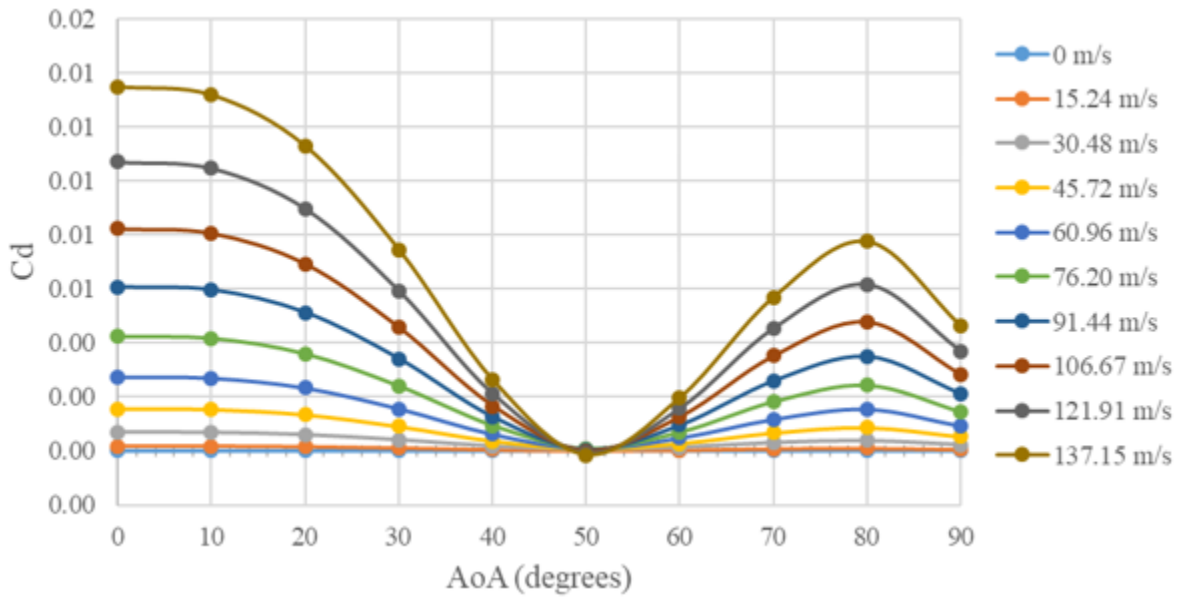
Figure 225: Plot of Angle of Attack vs. Drag Coefficient
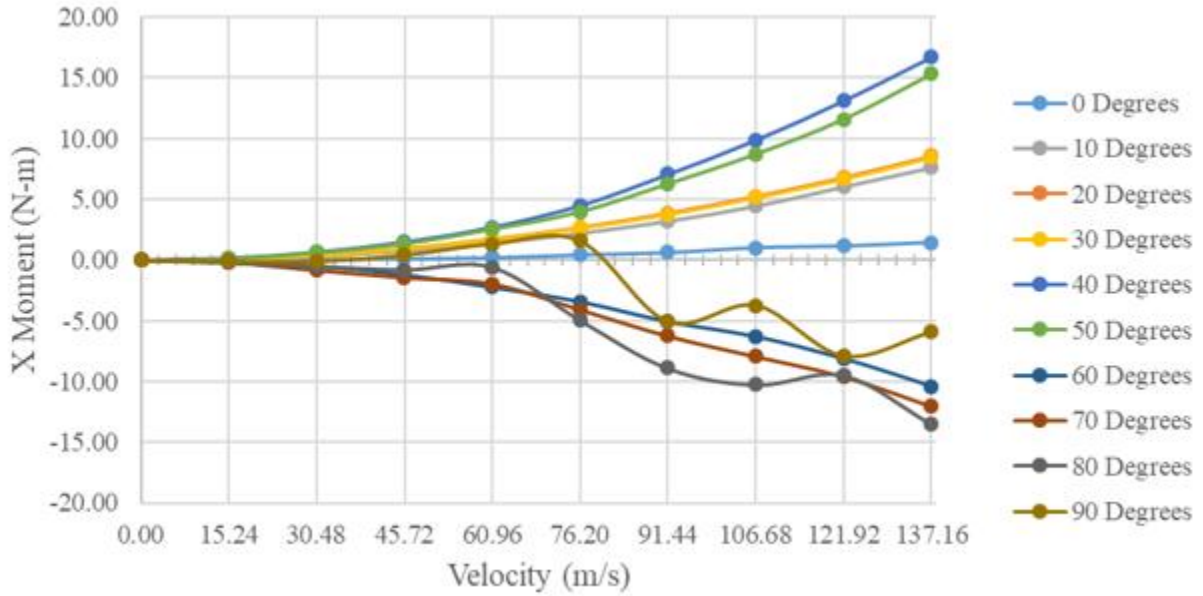
Figure 226: Plot of Velocity vs. X Moment
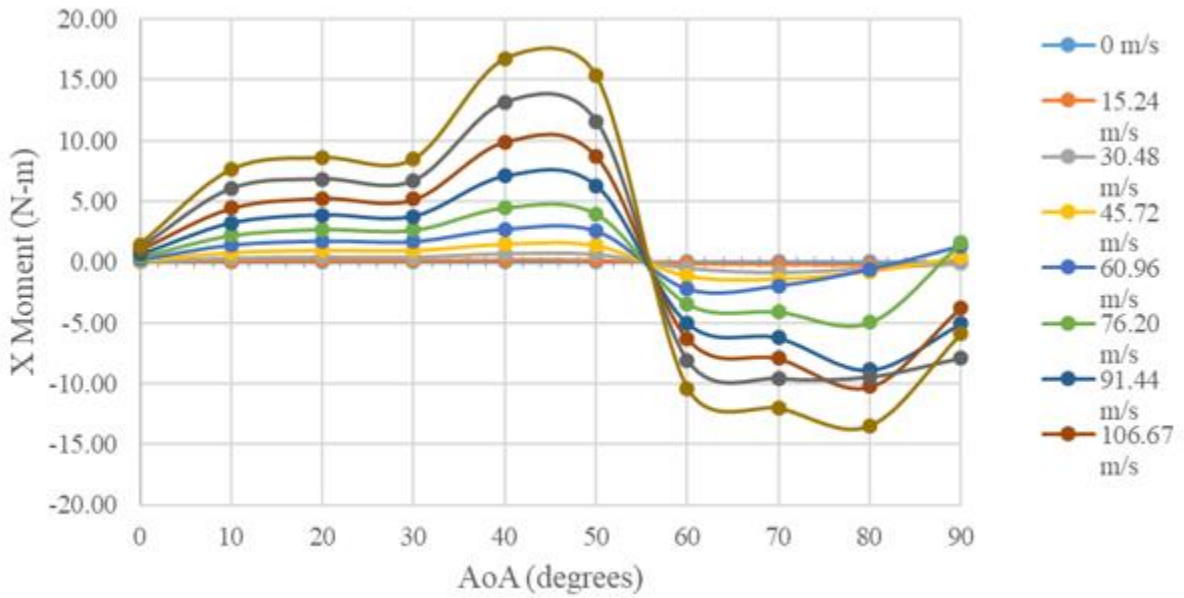
Figure 227: Plot of Angle of Attack vs. X Moment

Figure 228: Plot of Velocity vs. X Moment Coefficient
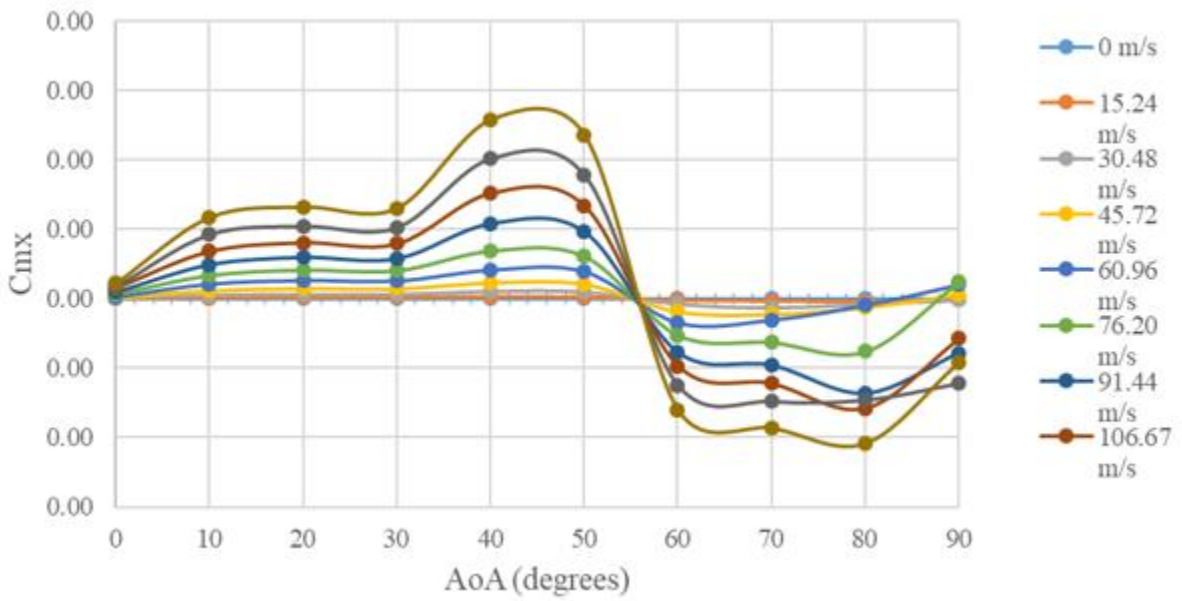
Figure 229: Plot of Angle of Attack vs. X Moment Coefficient
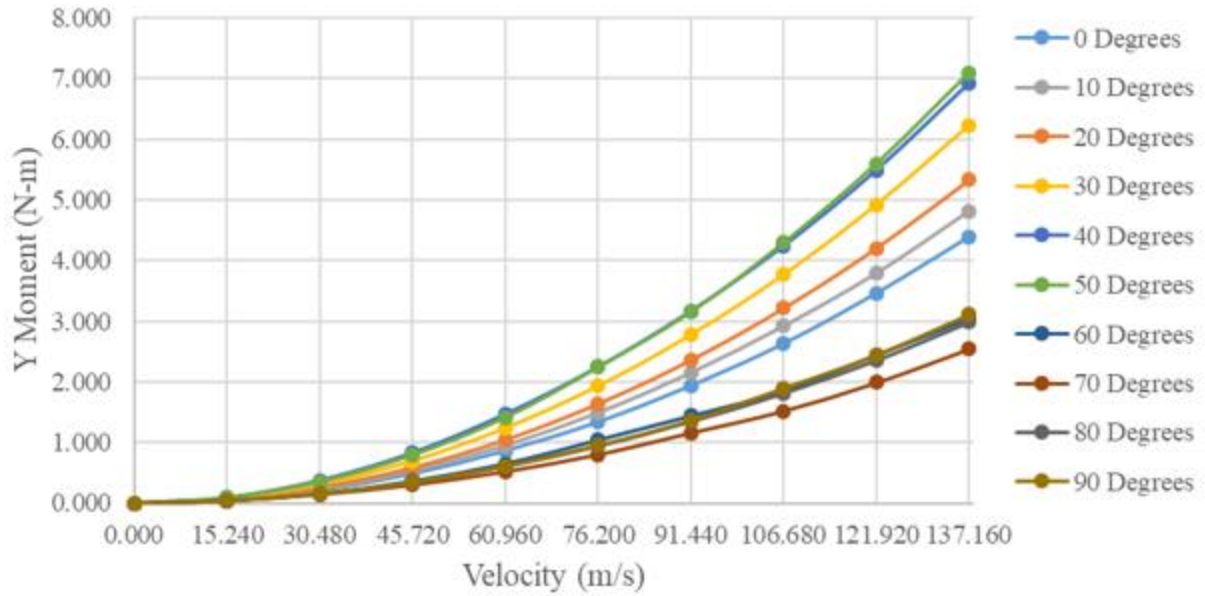
Figure 230: Plot of Velocity vs. Y Moment
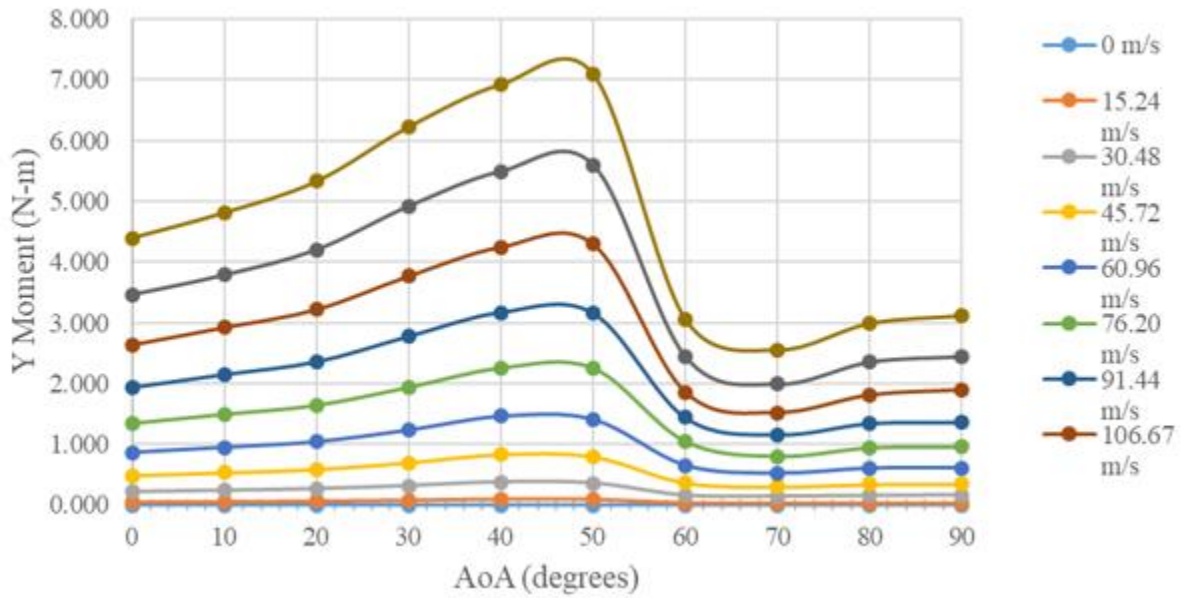
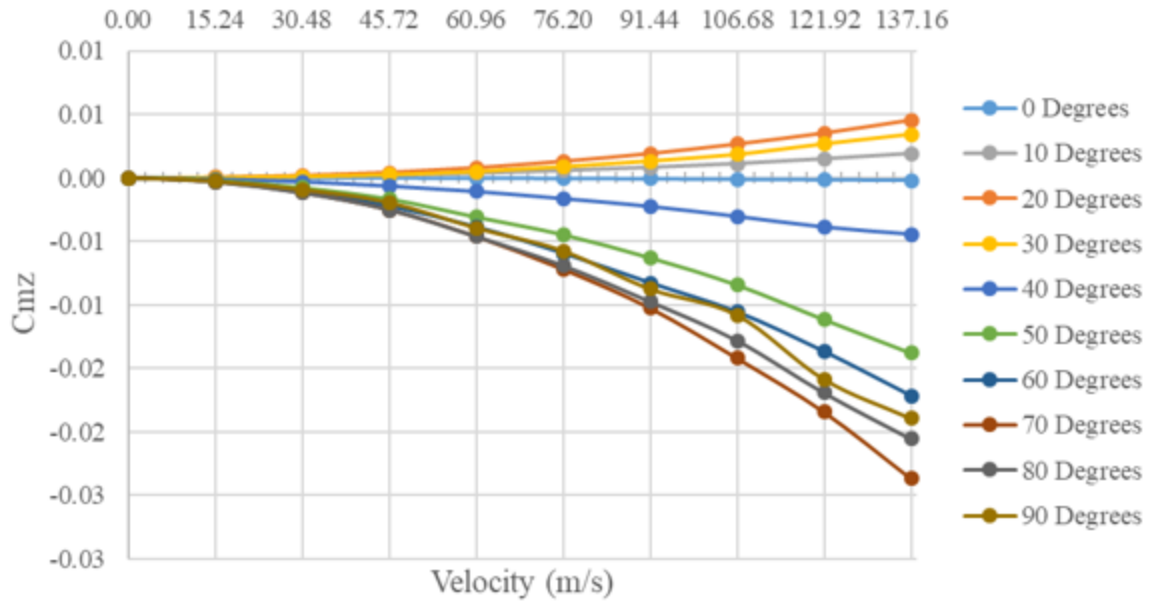Figure 231: Plot of Angle of Attack vs. Y Moment
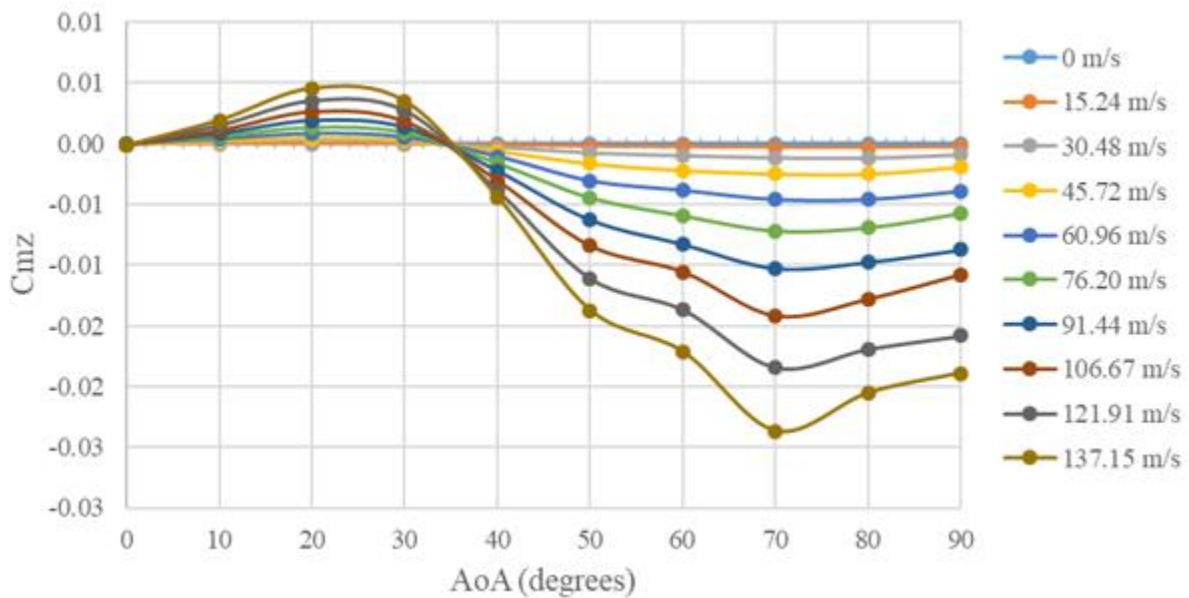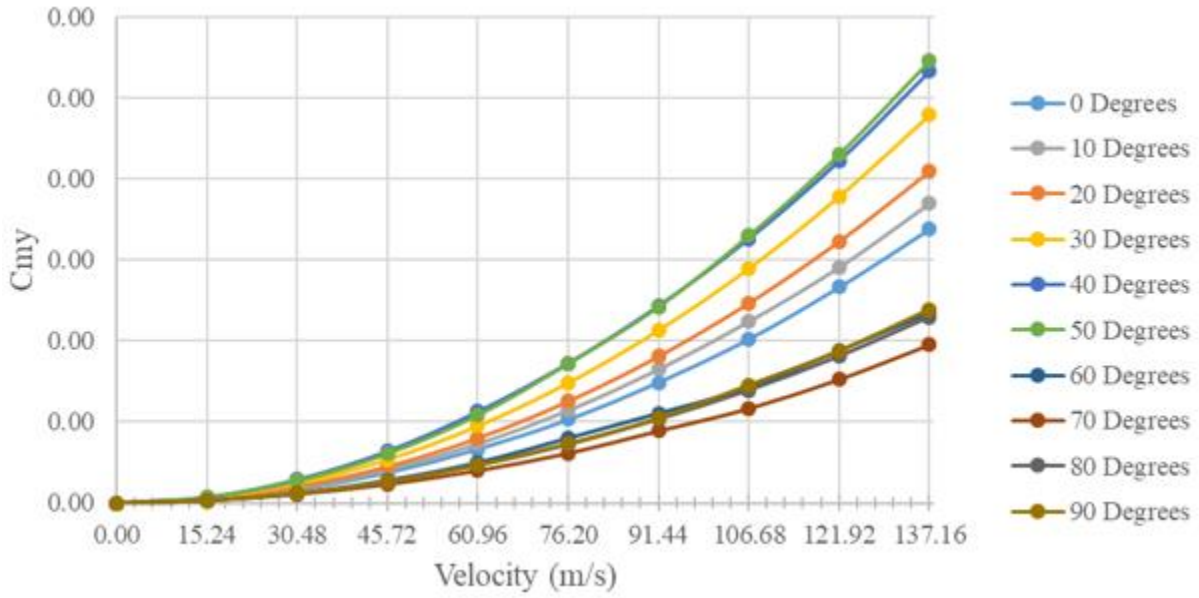
Figure 232: Plot of Velocity vs. Y Moment Coefficient
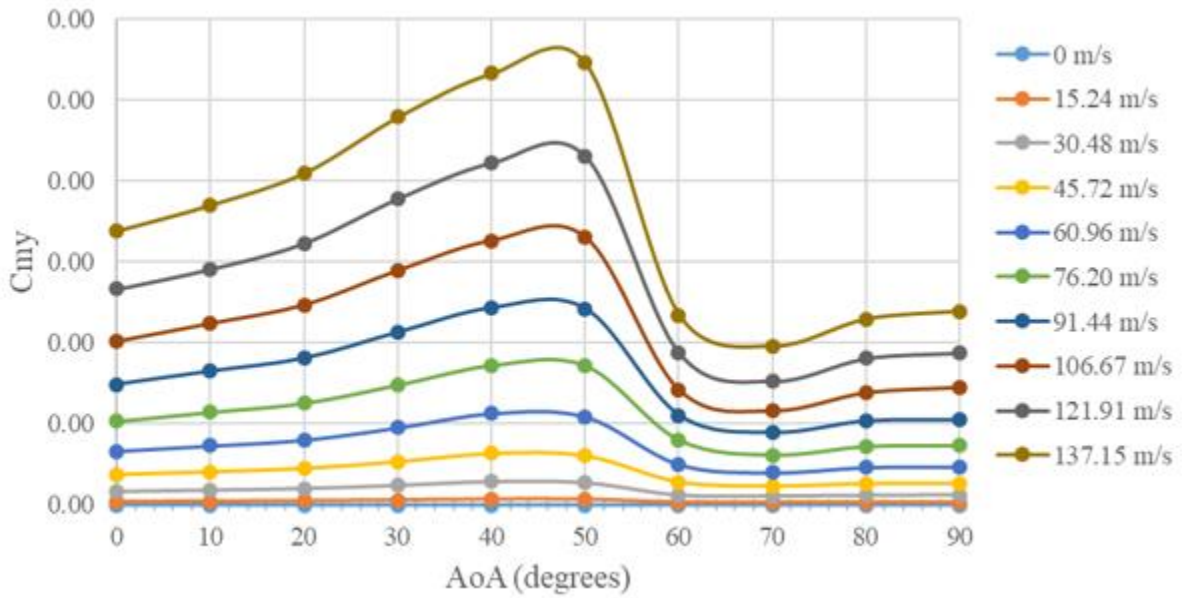
Figure 233: Plot of Angle of Attack vs. Y Moment Coefficient
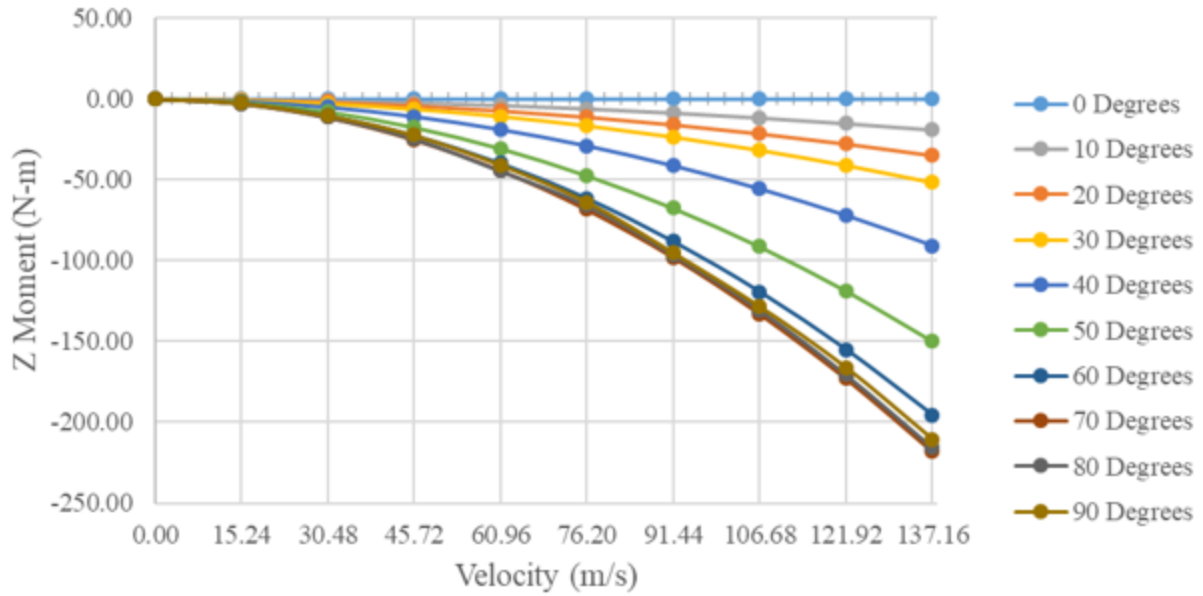
Figure 234: Plot of Velocity vs. Z Moment
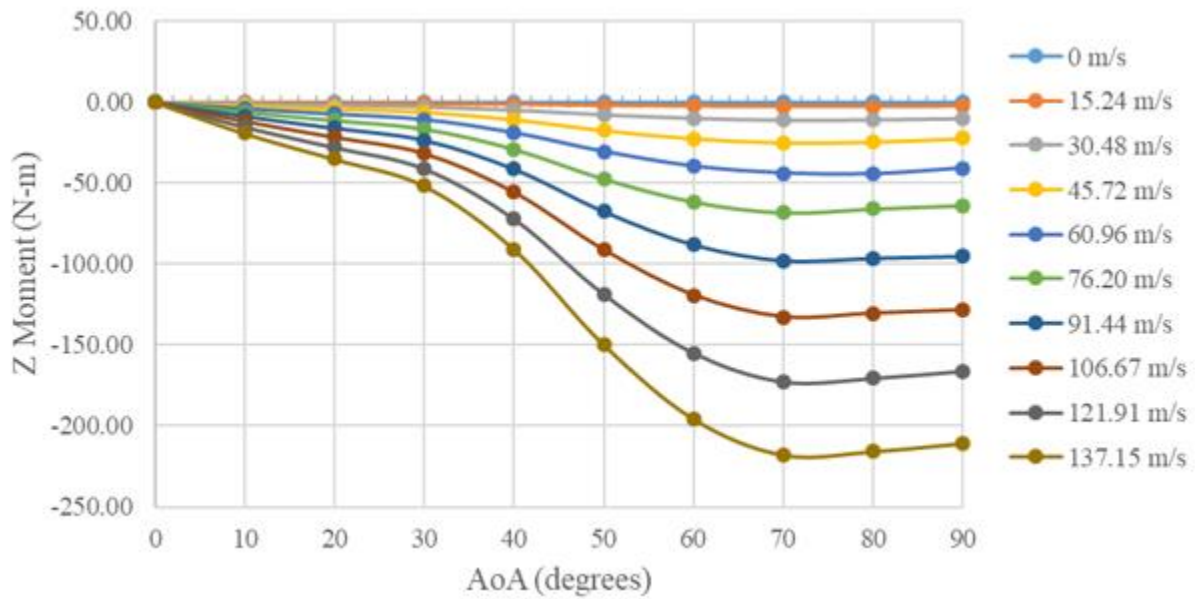
Figure 235: Plot of Angle of Attack vs. Z Moment
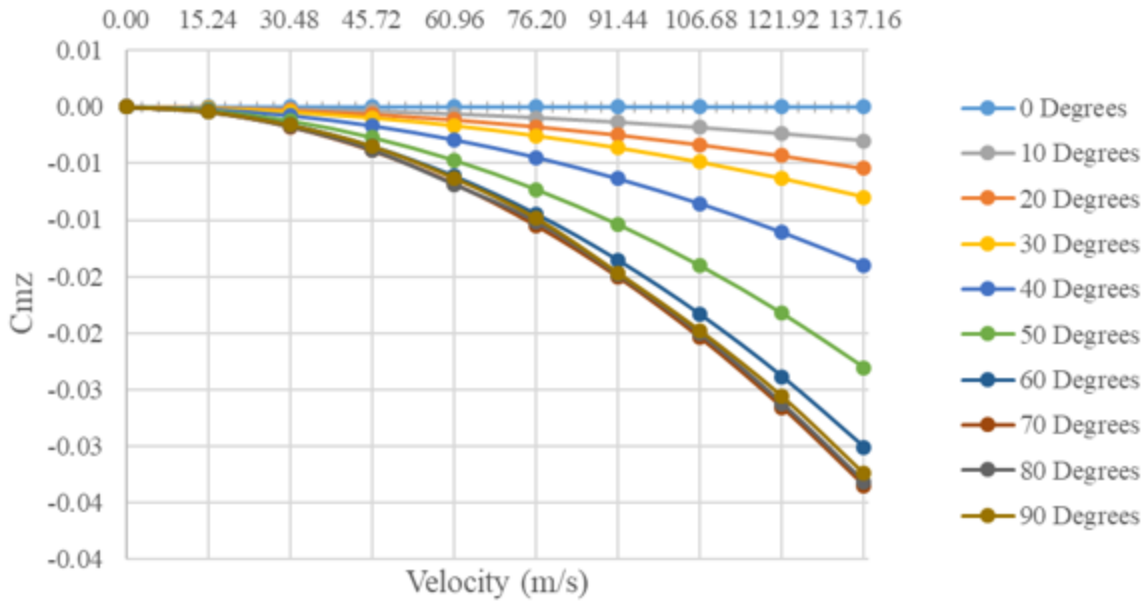
Figure 236: Plot of Velocity vs. Z Moment Coefficient
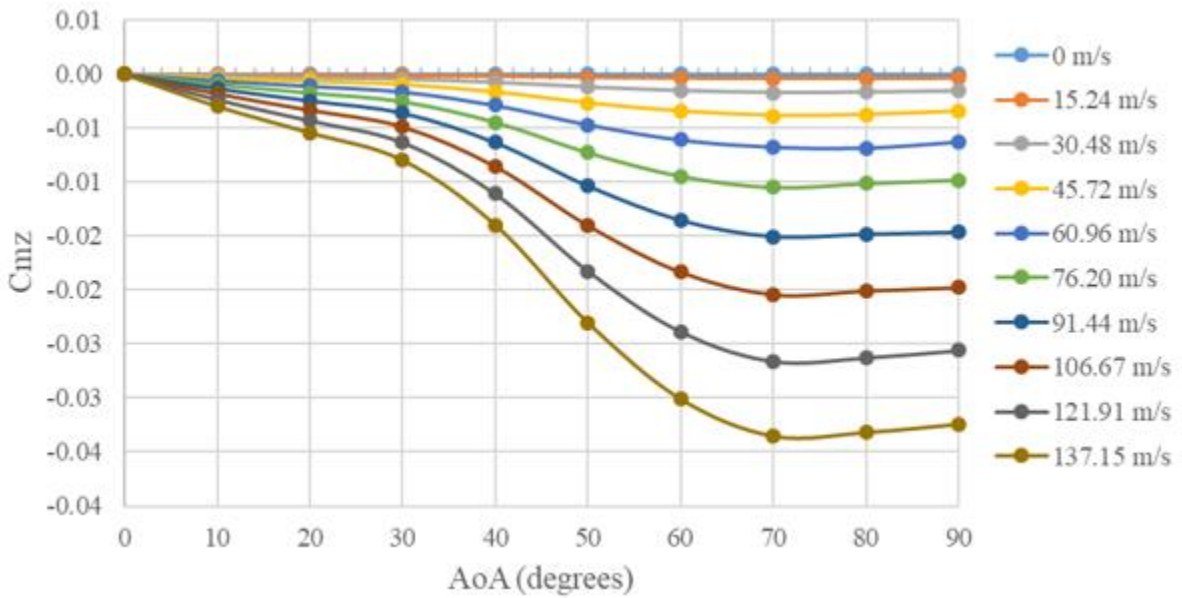
Figure 237: Plot of Angle of Attack vs. Z Moment Coefficient

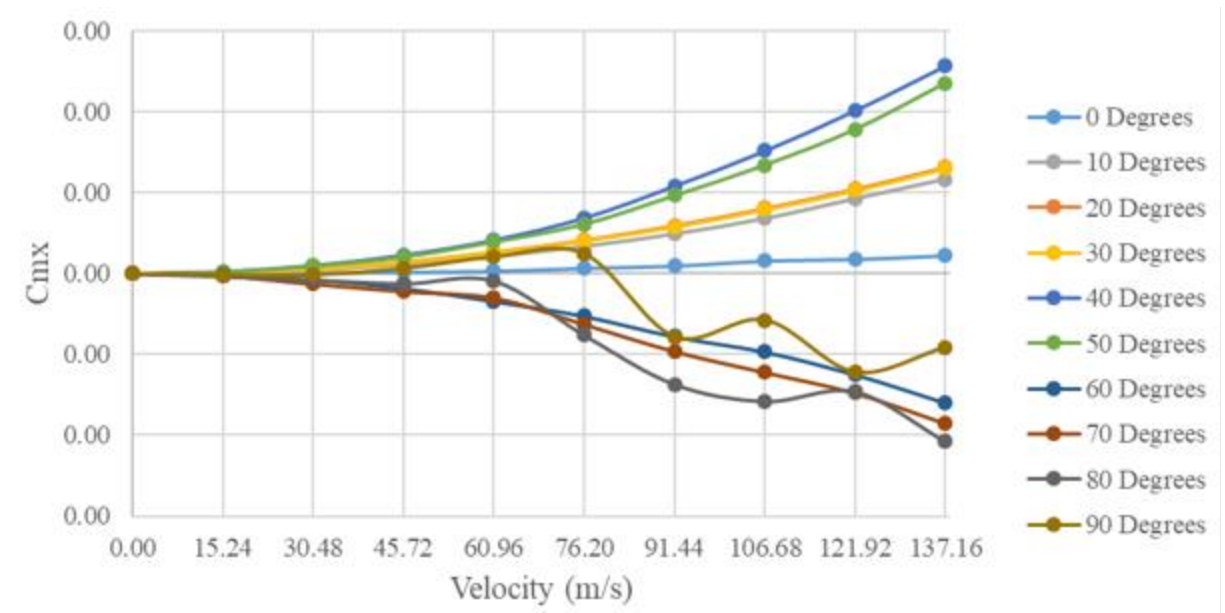## 7.10. Appendix J: Rigid Body Flight Simulation Algorithm

Figure 238 describes an algorithm for rocket flight simulation which solves for both the rocket's trajectory and orientation. This was originally created for FDA Analysis Task 4, and was based on the work of Box et al. This appendix briefly discusses this algorithm's method and original purpose.

Given an initial state, the vehicle trajectory equations could first be integrated numerically across a time step assuming a constant orientation. Then, the attitude dynamics equations could be similarly integrated through the same time step while maintaining the current position. This process could be repeated until a condition for reaching apogee was satisfied, at which point, the current position and linear momentum would be passed as initial conditions to a completely new set of equations representing only the vehicle's trajectory during parachute descent. These would be integrated until the simulated rocket reached the ground.

As shown Figure 238, initial conditions allow for the calculation of the current rocket orientation, as well as the state derivatives relevant to translational motion, those being the rate of change of position and angular momentum. Next, the velocity of the center of mass as well as that of the center of pressure (due to the rocket's angular velocity) combine to give the rocket's apparent velocity and angle of attack. The latter two values could be used with the results of FDA Analysis Task 2 to find normal, axial, and roll aerodynamic coefficients. Thus, we could arrive at the sum of all external forces acting on the rocket at a given time. Newton's Second Law applied to this net force acting on the rocket mass could be integrated to move the rocket through a portion of its trajectory across a time step and acquire its position and linear momentum at the end of this time step. Assuming apogee has not been reached, a similar procedure is then taken to find the net

Initial conditions

$t_0, \bar{X}_0, \bar{Q}_0, \bar{L}_0, \bar{P}_0,$
$I_{xx}, I_{yy}, I_{zz}, T(t), M(t), X_{cm},$
$C_{da}(t), C_A(\alpha, V), C_N(\alpha, V),$
$C_R(\alpha, V), \bar{W}(z), \rho,$
X_{RB}, A_{RB}, X_f, r_f

Orientation

$\bar{Q} = [s, \bar{v}] \rightarrow \mathbb{R}$
$\mathrm{s} = \cos(\Theta/2)$
$v_x = \sin(\Theta/2)a_x$
$v_y = \sin(\Theta/2)a_y$
$v_z = \sin(\Theta/2)a_z$
$\bar{Y}_A = \mathbb{R}\bar{Y}_{A,0}^T, \ \bar{P}_A = \mathbb{R}\bar{P}_{A,0}^T, \ \bar{R}_A = \mathbb{R}\bar{R}_{A,0}^T$

$$\mathbb{R} = \begin{bmatrix} 1 - 2v_y^2 - 2v_z^2 & 2v_xv_y - 2sv_z & 2v_xv_z + 2sv_y \\ 2v_xv_y + 2sv_z & 1 - 2v_x^2 - 2v_z^2 & 2v_yv_z - 2sv_x \\ 2v_xv_z - 2sv_y & 2v_yv_z + 2sv_x & 1 - 2v_x^2 - 2v_y^2 \end{bmatrix}$$

Some state derivatives
(in initial orientation)

$\dot{\bar{X}} = \bar{P}/M$
$\bar{\omega} = \mathbb{R}\mathbb{I}_0\mathbb{R}^T\bar{L}^T$

$$\mathbb{I}_0 = \begin{bmatrix} I_{xx} & 0 & 0 \\ 0 & I_{yy} & 0 \\ 0 & 0 & I_{yy} \end{bmatrix}$$

$\dot{\bar{Q}} = [\dot{s}, \dot{\bar{v}}]$
$\dot{s} = \frac{1}{2}(\bar{\omega} \cdot \bar{v})$
$\dot{\bar{v}} = \frac{1}{2}(s\bar{\omega} + (\bar{\omega} \times \bar{v}))$

Velocities and angle of attack

$\bar{V}_{cm} = \dot{\bar{X}} + \bar{W}(z)$
$\bar{V}_\omega = \bar{X}\sin[\cos^{-1}(\bar{R}_A \cdot \hat{\omega})](\bar{R}_A \times \bar{\omega})$
$\bar{X} = X_{cp} - X_{cm}$
Apparent velocity: $\bar{V} = \bar{V}_{cm} + \bar{V}_\omega$
$\alpha = \cos^{-1}(\hat{V} \cdot \bar{R}_A)$

Table lookup

Aerodynamic coefficients
C_A, C_N, C_R

Net force on rocket (t_0)
$\bar{F} = \bar{F}_T + \bar{F}_g + \bar{F}_A + \bar{F}_N$

$\bar{F} = m\bar{a}$ (Numerical integration over dt)

Part of current state
$\bar{X}_i, \bar{P}_i, t_i$

Force computations

$|\bar{F}_A| = \frac{1}{2}\rho|\bar{V}|^2 A_{RB}C_A$
$\bar{F}_A = -|\bar{F}_A|\bar{R}_A$
$|\bar{F}_N| = \frac{1}{2}\rho|\bar{V}|^2 A_{RB}C_N$
$\bar{F}_N = |\bar{F}_N|[\bar{R}_A \times (\bar{R}_A \times \hat{V})]$
$\bar{F}_T = -T\bar{R}_A$
$\bar{F}_g = [0, 0, -Mg]^T$

$P_{zi} = 0?$ — Yes → **Output to parachute model** $(\bar{X}_i, \bar{P}_i \rightarrow \bar{X}_0, \bar{P}_0)$

No

Torque computations

$\bar{\tau}_N = |\bar{F}_N|\bar{X}(\bar{R}_A \times \hat{V})$
$\bar{\tau}_{da} = -C_{da}\mathbb{R}\mathbb{M}\mathbb{R}^{-1}\bar{\omega}$

$$\mathbb{M} = \begin{bmatrix} 1 & 0 & 0 \\ 0 & 1 & 0 \\ 0 & 0 & 0 \end{bmatrix}$$

$\bar{\tau}_R = (\frac{1}{2}\rho V_f^2 A_{RB}C_R r_f)\bar{R}_A$

Net torque on rocket (t_0)
$\bar{\tau} = \bar{\tau}_N + \bar{\tau}_{da} + \bar{\tau}_R$

$\bar{\tau} = I\ddot{\bar{\theta}}$
(Integrate over same dt)

Rest of current state
$\bar{Q}_i, \bar{L}_i$
$T(t_i), M(t_i), C_{da}(t_i), \bar{W}(z_i)$

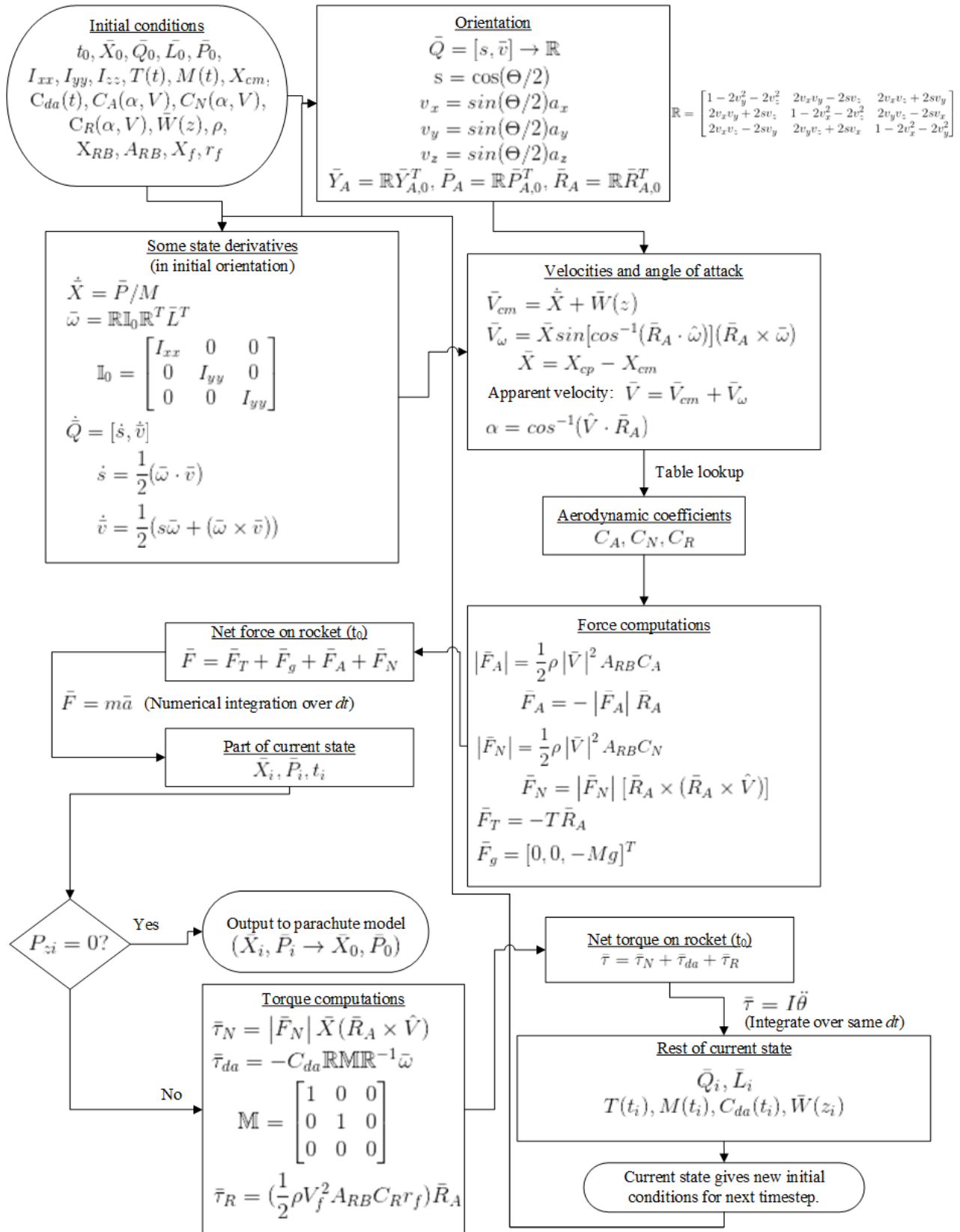**Current state gives new initial conditions for next timestep.**

Figure 238: Rigid body flight simulation algorithm

torque acting on the rocket, integrating of the Euler rigid body dynamic equations to turn the rocket to its end-of-time step orientation and find its updated angular momentum. Other time-dependent parameters are updated, and the current state becomes the initial state for the next time step.

If apogee is reached at the end of a time step, the current position and linear momentum of the rocket are passed to the parachute descent algorithm as initial conditions, which is performed until the z-component of position reached zero. This algorithm is identical to the previous, except that it uses: a constant, perfectly vertical orientation with no torque integration; zero thrust; and an equation representing the drag force on the parachute in place of equations for normal and axial aerodynamic forces which is

$$F_D = C_P A_P \frac{\rho V^2}{2},$$

wherein C_P represents the drag coefficient of the main and drogue parachutes, A_P their area, ρ the standard density of air at sea level, and V the downwards velocity of the descending rocket.

The originally planned products of this model were: a simulation of the rocket's trajectory for several cases, capturing the effects of statistically randomized variation in wind speed and direction; the evaluation of forces and moments acting on the vehicle, given its design, attitude, and velocity when subject to wind disturbances; and the effect of these disturbances on trajectory. These results were to be used to: generate landing probability distribution plots; compare stability and performance of the innovative fin design to the baseline fin design; estimate the perturbation of vehicle attitude when subjected to transient wind disturbances; and estimate the upper limit of wind disturbances that can occur while maintaining stable flight.

7.11. Appendix K: Point-Mass Model Flight Simulation Code

7.11.1 trajectory_solver.m: 2D rocket trajectory found with ODE45

```matlab
close all; clear all; clc

% Rocket description
global I_sp A_RB A_Pa A_Pm A_Pn g thrust drag
I_sp = 208; % motor specific impulse, sec
A_RB = (10.2/100)^2 * pi; % cross-sectional body area, m^2
A_Pa = 36/(12*3.28)^2; % apogee parachute area, m^2
A_Pm = 54/(12*3.28)^2; % main body parachute area, m^2
A_Pn = 36/(12*3.28)^2; % nose cone and payload parachute area, m^2
g = 9.809; % average accleration due to gravity, m/s^2

% Thrust (N) indexed as a function of time for I216 baseline motor (sec)
thrust = [0 0; 0.017 35; 0.03 300; 0.035 345; 0.05 325; 0.07 275;
    0.14 292; 0.26 296; 0.8 280; 1.1 280.4; 1.62 255; 1.8 226; 2.105 210;
    2.2 195; 2.45 80; 2.75 36; 3.1 0];

% Body drag coefficient indexed as a function of velocity (m/s), assuming
% zero angle of attack (partial results of Analysis Task 2)
vel_indx = [0:50:450]' * 3.28;
drag_indx = [0; 9.54798E-05; 0.000364973; 0.000798255; 0.00139439;...
    0.002155245; 0.003067682; 0.004163585; 0.005403134; 0.006809757];
drag = [vel_indx drag_indx];

% Initial Conditions
x_0 = 0; % horizontal position at launch, m
z_0 = 0; % altitude at launch, m
V_0 = 1; % vertical launch velocity, m/s
M_0 = 4.744; % initial wet mass at launch, kg
theta_0 = deg2rad(3); % polar angle at launch, radians
S0 = [x_0, z_0, V_0, M_0, theta_0]; % function input array

% Timespan of integration, seconds
dt = 0.01;
tspan = 0:dt:500;

% Use options to make solver terminate at apogee
options = odeset('Events', @terminate1);

% Solve system of ODEs for ascent of rocket
[t1,S1] = ode45(@(t, S) flight(t, S), tspan, S0, options);

% Output solutions at apogee as initial conditions for parachute descent
x_a = S1(length(t1),1);
z_a = S1(length(t1),2);
V_a = S1(length(t1),3);
M_a = S1(length(t1),4);
theta_a = S1(length(t1),5);
```

```matlab
S_a = [x_a, z_a, V_a, M_a, theta_a];

% New options make solver terminate upon landing
options = odeset('Events', @terminate2);

% Solve system of ODEs for descent of rocket
[t2,S2] = ode45(@(t, S) descent(t, S, S_a), tspan, S_a, options);

% Plotting results

burnout_state = interp1(t1,S1,3.1,'spline');
chute_state = interp1(S2(:,2),S2,700/3.28,'spline');
chute_time = interp1(S2(:,2),t2,700/3.28,'spline')+max(t1);

% Plot full trajectory
figure()
plot(S1(:,1),S1(:,2),'-',S2(:,1),S2(:,2),'--
',burnout_state(1),burnout_state(2),'*r',x_a,z_a,'*m',chute_state(1),chute_state(2),'*g');
title('Full rocket trajectory, launch angle 3 degrees from zenith')
xlabel('Downrange distance [m]');
ylabel('Altitude [m]');
leg = legend('Ascent path','Parachute descent path','Motor burnout','Apogee (first parachute
release)','Nosecone and main body parachute release','Location','Best');
axis square

% Plot altitude profile
figure()
plot(t1,S1(:,2),'-',max(t1)+t2,S2(:,2),'--
',3.1,burnout_state(2),'*r',max(t1),z_a,'*m',chute_time,chute_state(2),'*g');
title('Altitude profile, launch angle 3 degrees from zenith')
xlabel('Time from launch [seconds]');
ylabel('Altitude [m]');
leg = legend('During ascent','During descent','Motor burnout','Apogee (first parachute
release)','Nosecone and main body parachute release','Location','Best');

% Plot downrage distance profile
figure()
plot(t1,S1(:,1),'-',max(t1)+t2,S2(:,1),'--
',3.1,burnout_state(1),'*r',max(t1),x_a,'*m',chute_time,chute_state(1),'*g');
title('Downrange profile, launch angle 3 degrees from zenith')
xlabel('Time from launch [seconds]');
ylabel('Downrange distance traveled [m]');
leg = legend('During ascent','During descent','Motor burnout','Apogee (first parachute
release)','Nosecone and main body parachute release','Location','Best');

% Plot velocity profile
figure()
plot(t1,S1(:,3),'-',max(t1)+t2,S2(:,3),'--
',3.1,burnout_state(3),'*r',max(t1),V_a,'*m',chute_time,chute_state(3),'*g');
title('Velocity profile, launch angle 3 degrees from zenith')
xlabel('Time from launch [seconds]');
ylabel('Airspeed [m/s]');
leg = legend('During ascent','During descent','Motor burnout','Apogee (first parachute
release)','Nosecone and main body parachute release','Location','Best');
```

```
% Plot mass profile
figure()
plot(t1,S1(:,4),'-',max(t1)+t2,S2(:,4),'--
',3.1,burnout_state(4),'*r',max(t1),M_a,'*m',chute_time,chute_state(4),'*g');
title('Mass profile, launch angle 3 degrees from zenith')
xlabel('Time from launch [seconds]');
ylabel('Rocket mass [m/s]');
leg = legend('During ascent','During descent','Motor burnout','Apogee (first parachute
release)','Nosecone and main body parachute release','Location','Best');

% Plot flight angle profile
figure()
plot(t1,S1(:,5)*180/pi,'-',max(t1)+t2,S2(:,5)*180/pi,'--
',3.1,burnout_state(5)*180/pi,'*r',max(t1),theta_a*180/pi,'*m',chute_time,chute_state(5)*180/pi,'
*g');
title('Flight angle profile, launch angle 3 degrees from zenith')
xlabel('Time from launch [seconds]');
ylabel('Polar angle, counter-clockwise to zenith [degrees]');
leg = legend('During ascent','During descent','Motor burnout','Apogee (first parachute
release)','Nosecone and main body parachute release','Location','Best');
```

7.11.2 flight.m: Equations of state during ascent

```
function dS_dt = flight(t, S)

global I_sp A_RB g drag thrust

% Definition of state vector
% x = S(1) horizontal position
% z = S(2) vertical position
% Vx = S(3) horizontal velocity component
% Vz = S(4) vertical velocity component
% M = S(5) mass of rocket
% theta = S(6) angle between zenith and rocket's primary axis

% Find atmospheric density from altitude
rho = standard_atmosphere(S(2)); % standard atmospheric density, kg/m^3

% Find coefficient of drag from airspeed (assume zero angle of attack)
C_D = interp1(drag(:,1), drag(:,2), S(3), 'spline');

% Determine thrust from thrust curve data
if t < 3.1
    T = interp1(thrust(:,1), thrust(:,2), t, 'spline');
else
    T = 0;
end

% Define equations of state as time derivatives of state vector
dS_dt(1,1) = S(3) * sin(S(5));
dS_dt(2,1) = S(3) * cos(S(5));
```

```matlab
dS_dt(3,1) = (T - 0.5*rho*S(3)^2*A_RB*C_D - S(4)*g*cos(S(5))) / S(4);
if t < 3.1
    dS_dt(4,1) = - T / (g*I_sp);
else
    dS_dt(4,1) = 0;
end
dS_dt(5,1) = g * sin(S(5)) / S(3);
```

7.11.3 descent.m: Equations of state during descent

```matlab
function dS_dt = descent(t, S, S_a)

global A_Pa A_Pm A_Pn g

% Definition of state vector
% x = S(1) horizontal position
% z = S(2) vertical position
% Vx = S(3) horizontal velocity component
% Vz = S(4) vertical velocity component
% M = S(5) mass of rocket
% theta = S(6) angle between zenith and rocket's primary axis

% Find atmospheric density from altitude
rho = standard_atmosphere(S(2)); % standard atmospheric density, kg/m^3

% Parachute coefficient of drag (body drag assumed negligible
C_D = 0.8;

% Define equations of state as time derivatives of state vector
dS_dt(1,1) = S(3) * sin(S(5));
dS_dt(2,1) = S(3) * cos(S(5));
if 700/3.28 < S(2) < S_a(2)
    dS_dt(3,1) = (-0.5*rho*S(3)^2*A_Pa*C_D - S(4)*g*cos(S(5))) / S(4);
elseif 0 < S(2) <= 700/3.28
    dS_dt(3,1) = (-0.5*rho*S(3)^2*(A_Pa+A_Pm+A_Pn)*C_D - S(4)*g*cos(S(5))) / S(4);
end
dS_dt(4,1) = 0;
dS_dt(5,1) = g * sin(S(5)) / S(3);
```

7.11.4 terminate1.m: Events function that terminates ODE solver at apogee

```matlab
function [value,isterminal,direction] = terminate1(t,S)

% Value of interest (vertical velocity component)
value = S(3)*cos(S(5));

% Terminate solver at zero of "value"
isterminal = 1;
```

```
% Locate all zeroes of "value"
direction = 0;
```

7.11.5 terminate2.m: Events function that terminates ODE solver upon landing

```
function [value,isterminal,direction] = terminate2(t,S)

% Value of interest (vertical velocity component)
value = S(2);

% Terminate solver at zero of "value"
isterminal = 1;

% Locate all zeroes of "value"
direction = 0;
```

7.11.6 standard_atmosphere.m: Standard atmospheric density calculator

```
function rho_h = standard_atmosphere(h)

% Sea level temperature and density
T_sl = 288.16; %K
rho_sl = 1.225; %kg/m^3

% Temperature gradient
a_1 = -6.5*10^-3; %K/m
% Average gravitational acceleration
g = 9.809; %m/s^2
% Specific gas constant
R = 287; %J/(kg*K)

if h <= 11000
    % Standard atmosphere model, 0 to 11km altitude
    T_h = T_sl + a_1*h; %K
    rho_h = rho_sl * (T_h/T_sl)^(-1-g/(a_1*R)); %kg/m^3
else
    % Standard atmosphere model, 11 to 25km altitude
    T_h = T_sl + a_1*11000; %K
    rho_h = (rho_sl * (T_h/T_sl)^(-1-g/(a_1*R)))...
        * exp(-g*(h-11000)/(R*T_h)); %kg/m^3
end

end
```